

**Developing and applying the DO<sub>3</sub>SE-Crop model to assess ozone impacts on wheat**

Pritha Pande

PhD

University of York

Department of Environment and Geography

December 2023

## Abstract

This PhD thesis investigates the impact of ground-level ozone ( $O_3$ ) pollution on wheat yields, focusing on areas in Europe, Asia, and particularly in China's productive arable regions. The research employs a mechanistic photosynthesis-stomatal conductance model ( $A_{net}g_{sto}mech$ ), DO<sub>3</sub>SE-crop, integrated with an  $O_3$  damage module to develop a new flux-based dose-response relationship for wheat crops in Europe, utilizing a comprehensive dataset from European  $O_3$  fumigation experiments. The model's robustness ( $R^2 = 0.82$ ) is demonstrated, showing its effectiveness in simulating stomatal conductance ( $g_{sto}$ ) and photosynthesis ( $A_{net}$ ) under high  $O_3$  concentrations and in predicting yield loss determinants such as the timing of senescence.

The thesis further extends the DO<sub>3</sub>SE-crop model, integrating it with the JULES-Crop. This integrated DO<sub>3</sub>SE-crop model successfully simulates crop development and yield, reflecting the differential impact of  $O_3$  on tolerant and sensitive wheat cultivars with high accuracy when evaluated for 2007, 2008, and 2009, with an  $R^2$  of 0.73 and an RMSE of 58.41 g/m<sup>2</sup>. Moreover, the thesis identifies the variance in yield reduction as primarily due to premature senescence and reduced carbon assimilation under elevated  $O_3$  levels, advancing leaf senescence by 7-9 days.

The DO<sub>3</sub>SE-Crop model, when calibrated for different Chinese agro-ecological zones (AEZs), exhibited an acceptable level of precision in simulating crop phenology, with estimated emergence and maturity dates aligning within a margin of 2.5 weeks of the observed data. The model also effectively simulates crop yield, with an accuracy range of  $\pm 84$  g/m<sup>2</sup> as a mean yield by AEZ. However, the study also reveals the importance of accounting for regional climatic conditions in  $O_3$  damage assessment, highlighting the disproportionate impact of early  $O_3$  flux accumulation on certain AEZs. The study underscores the necessity of considering regional differences in AEZs for accurate parameterization of crop models, aiming to enhance their relevance and improve  $O_3$  damage assessment across varied international contexts.

# List of Contents

## Contents

<b>Abstract</b> .....	2
<b>Acknowledgement</b> .....	13
<b>Author declaration</b> .....	14
<b>1. Introduction</b> .....	15
1.1 Global food security.....	15
1.2 Global trends in ozone formation, transport, deposition and removal .....	20
1.2.1 Formation of tropospheric ozone .....	21
1.2.2 Ozone removal processes .....	22
1.2.3 Background versus peak ozone concentrations.....	23
1.2.5 Diurnal and seasonal ozone cycles in urban and rural locations .....	25
1.2.6 Hemispheric transport.....	26
1.3 Trends in ozone precursor emissions.....	27
1.4 Ozone impacts on crops .....	29
1.4.1 Ozone effects on stomatal conductance ( <i>g<sub>sto</sub></i> ).....	30
1.4.2 Ozone effects on <i>Anet</i> .....	31
1.4.3 Ozone effects on carbon allocation and yield .....	31
1.4.4 Ozone effect on senescence .....	32
1.5 Determinants of ozone sensitivity by plants .....	34
1.6 Approaches for modelling ozone exposure, uptake and damage.....	35
1.6.1 Experimental studies.....	35
1.6.2 Metrics of O <sub>3</sub> exposure .....	39
1.8 Policies.....	45
1.9 Aims and Objectives.....	47
<b>2. Ozone dose-response relationships for wheat can be derived using photosynthetic-based stomatal conductance models</b> .....	50
2.1 Abstract .....	50
2.2 Introduction .....	51
2.3 Methods.....	54
2.3.1 Stomatal conductance ( <i>g<sub>sto</sub></i> ) models .....	54
2.3.2 Estimation of O <sub>3</sub> uptake ( <i>f<sub>st</sub></i> ) and <i>POD<sub>y</sub></i> .....	58
2.3.3. Datasets.....	59
2.3.4 Parameterisation for the <i>g<sub>sto</sub></i> models.....	59

2.4 Results.....	65
2.4.1 Leaf physiology.....	65
2.4.2 Leaf Senescence.....	68
2.4.3 Flux-response relationships.....	71
2.5 Discussion.....	73
2.6 Conclusion .....	77
SI.1 Supporting Material.....	78
SI.1.1 Boundary line analysis of relative <i>gsto</i> data with VPD .....	78
SI.1.2 Multiplicative model equations.....	78
SI.1.3 Relationship between leaf <i>fphen</i> , <i>fLS</i> and <i>fLA</i> and thermal time intervals .....	83
SI.1.4. Dataset details: .....	84
SI.1.5 Parameters: Multiplicative model .....	87
SI.1.6. Parameters used for the estimation of the estimation of O <sub>3</sub> uptake <i>f<sub>st</sub></i> in <i>gstoemp</i> and <i>Anet</i> models .....	87
SI.1.7. Literature findings: <i>Vcmax25</i> and <i>Jmax25</i> data .....	88
SI.1.8. Flag leaf senescence .....	90
SI.1.9. Training and Test datasets.....	92
SI.1.10. Flux-response relationships for relative wheat yield derived using the <i>Anetgstomech.</i> .....	102
SI.1.11. Diurnal and maximum <i>Anet</i> .....	105
<b>3.The development, parametrisation and evaluation of the DO<sub>3</sub>SE Crop model for Xiaoji, China</b> .....	<b>108</b>
3.1 Abstract .....	108
3.2 Introduction .....	109
3.3.....	112
Methods: DO <sub>3</sub> SE-Crop Model development, calibration and Evaluation.....	112
3.3.1 DO <sub>3</sub> SE Crop Phenology .....	114
3.3.2 DO <sub>3</sub> SE-Crop leaf-level physiology.....	116
3.3.3 DO <sub>3</sub> SE-Crop canopy .....	122
3.3.4 Canopy irradiance .....	123
3.3.5 Canopy [O <sub>3</sub> ] concentration .....	124
3.3.6 Canopy maximum carboxylation capacity ( <i>Vcmax</i> ) .....	125
3.3.7 Canopy Photosynthesis ( <i>Anetc</i> ).....	126
3.3.8 Canopy Stomatal Conductance ( <i>gstoi</i> ).....	126
3.3.9 Crop biomass, LAI, height and yield variables.....	127
3.3.10 DO <sub>3</sub> SE-Crop model calibration .....	131
3.4.....	136

Results .....	136
3.4.1 Crop Phenology .....	136
3.4.2 Within canopy stomatal O <sub>3</sub> profile .....	136
3.4.3 Leaf physiology variables ( <i>Anet</i> , <i>gsto</i> ) .....	138
3.4.4 Crop growth and yield .....	139
3.4.5 Instantaneous and long-term O <sub>3</sub> impact .....	140
3.4.6 Senescence .....	141
3.4.7 Simulations across years and between cultivars .....	142
3.5 Discussion .....	145
3.6 Conclusions .....	150
SI.2 Supporting material .....	151
SI.2.1 Resistance and diffusivity of gases across leaf boundary layers .....	151
SI.2.2 Diffusivities of gases for stomatal conductance ( <i>gsto</i> ) .....	152
SI.2.3 Irradiance absorption by the canopy .....	152
SI.2.3.1 Total Photosynthetic Active Radiation ( <i>PAR<sub>tot</sub></i> ) .....	153
SI.2.3.2 Total irradiance absorbed as shaded leaves ( <i>Ilsh (LAI)</i> ) per unit leaf area are calculated as; .....	153
SI.2.4 O <sub>3</sub> Resistance .....	155
SI.2.5 The timing of crop emergence, anthesis and harvest .....	157
SI.2.6 Chinese FACE-O <sub>3</sub> dataset Scatter plot: Modelled grain dry matter (g/m <sup>2</sup> ) against experimental dataset for the year 2008 .....	157
SI.2.7 DO <sub>3</sub> SE-Crop variables .....	158
SI.2.8 DO <sub>3</sub> SE-Crop parameters for wheat .....	162
SI.2.9 DO <sub>3</sub> SE-crop phenology parameters .....	170
SI.2.10 Methodology for gap-filling and standardisation of data for AgMIP Ozone .....	170
<b>4.</b> .....	<b>174</b>
<b>The ozone impact on wheat growth and yield is influenced by agro-ecological zone and cultivar sensitivity in China.</b> .....	<b>174</b>
4.1 Abstract .....	174
4.2 Introduction .....	175
4.3 Methods .....	179
4.3.1 DO <sub>3</sub> SE Crop Model .....	179
4.3.2 WRF-Chem model .....	181
4.3.3 Calibration of DO <sub>3</sub> SE-Crop for O <sub>3</sub> damage in China .....	183
4.3.3.1 Calibration of DO <sub>3</sub> SE-Crop for phenology and yield under ambient O <sub>3</sub> in China .....	185
4.3.4 Evaluation of the DO <sub>3</sub> SE Crop model across China .....	190
4.4 Results .....	192

4.4.1 WRF-Chem modelled versus observed M7-O <sub>3</sub> .....	192
4.4.2 Seasonal variation in modelled and observed M7.....	194
4.4.3 Zone wise crop phenology versus observed.....	195
4.4.4 Scattered plot Observed (SPAM2010 data) vs calibrated DO <sub>3</sub> SE-crop modelled yield (g/m <sup>2</sup> ).....	196
4.4.5 Observed (SPAM2010 data) vs calibrated DO <sub>3</sub> SE-crop modelled yield (g/m <sup>2</sup> ).....	198
4.4.6 Comparison Observed (SPAM2010 data) vs calibrated DO <sub>3</sub> SE-crop modelled yield (g/m <sup>2</sup> ).....	199
4.5 Discussion.....	204
4.6 Conclusions.....	208
SI.3 Supporting material.....	209
SI.3.1 WRF-Chem model.....	209
SI.3.2 Data required to run the DO <sub>3</sub> SE-Crop model.....	211
SI.3.3. Statistical measures used to assess the WRF-Chem and DO <sub>3</sub> SE-Crop models.....	215
SI.3.4 Results.....	216
<b>5.</b> .....	221
<b>Thesis Discussion</b> .....	221
5.1 Choice of <i>gsto</i> model for PODy estimates. ....	221
5.2 Ozone damage module: Does the DO <sub>3</sub> SE-crop model capture O <sub>3</sub> damage mechanisms correctly? .....	223
5.3 The importance of leaf vs canopy stomatal O <sub>3</sub> uptake on damage.....	224
5.4 Model Calibration - Manual vs. Automated Methods. ....	226
5.5 AEZs and Cultivar-Specific Parametrization .....	228
5.6 Future work .....	232
5.7 Policy recommendations .....	233
<b>References</b> .....	237

## List of Tables

Table 1. Atmospheric lifetime of the O <sub>3</sub> precursors and O <sub>3</sub> in the atmospheric boundary layer and free troposphere. ....	26
Table 2. The table outlines 7 studies on the impact of ozone exposure on wheat cultivars, conducted at different locations in China. Each study differs in its experimental setup, ranging from field experiments with ethylene diurene urea (EDU) treatments, open top chamber (OTC)treatments and free air ozone and carbon dioxide enrichment (FAOCE). These studies collectively highlight the varying sensitivity of wheat cultivars to ozone exposure and the significant potential for yield loss, underscoring the importance of considering ozone levels in agricultural management and breeding programs for ozone tolerance. ....	36
Table 3. delineates various ozone metrics, their purposes, algorithms, and references, serving as a crucial tool for understanding and managing ozone concentrations in different environments. These metrics, providing a robust scientific foundation for their application in environmental monitoring and policy-making. ....	43
Table 4. presents a detailed overview of the parameters, ranges and optimised values after calibration that are employed in calibrating. Anetgsto models, which are critical in understanding plant physiological responses. ....	61
Table 5. This table provides a detailed comparison of the deviation in days for the Start of Senescence (SOS) and End of Senescence (EOS) across various treatments from the observed values, presented as <i>bias</i> . For each listed location and year, the table places different treatments like CF (Controlled Fertilization), NF+++ (Nitrogen Fertilization with additional nutrients), LB (Low Biomass), and VHP (Very High Pollution), followed by their 24-hour mean concentrations in ppb. The "SOS bias" and "EOS bias" columns indicate the deviation in days at the start (SOS) and end of the season (EOS) respectively, from an observed dataset, for both empirical and mechanistic approaches. Positive values denote a delay, while negative values signify an advancement in seasonal timing relative to observed data. PODy at SOS" and "PODy at EOS" columns measure the Phytotoxic Ozone Dose at the season's start and end, respectively, in mmol per square meter (mmol m <sup>2</sup> ), indicating the cumulative ozone exposure above a harmful threshold to vegetation. .	69
Table 6. Hourly meteorological and O <sub>3</sub> data measured at Xiaoji required to run the DO <sub>3</sub> SE-Crop .....	131
Table 7. The modelled % Yieldgrain loss compared to a pre-industrial O <sub>3</sub> scenario divided between that Yieldgrain loss caused by the direct and instantaneous effect of O <sub>3</sub> on Anet and that due to the long-term O <sub>3</sub> impact on senescence. The dataset extends over a three-year period, encompassing the years 2007, 2008, and 2009. Within this framework, the analysis is applied to two wheat crop cultivars, tolerant (Y15 and Y16) and sensitive (Y2 and Y19). ....	140

Table 8. Emissions and meteorological input data used to run the WRF-Chem model for the derivation of O <sub>3</sub> concentrations for year 2017/2018.....	182
Table 9. The key parameterisation of the DO <sub>3</sub> SE-Crop model after calibration against the Xiaoji experimental dataset (Zhu et al., 2011). .....	184
Table 10. The range in timings of key phenology stages (sowing, emergence, anthesis and maturity) for winter wheat across China, given in Julian day (DOY) divided by four agro-ecological zones (AEZs- as Zone1, Zone2, Zone3 and Zone 4). Also shown are the number of SPAM2010 and associated WRF-Chem sample sites used to perform a manual parameterisation of the DO <sub>3</sub> SE-Crop model.....	187
Table 11. Initial default and range (in brackets) of parameter values for the calibrated DO <sub>3</sub> SE-Crop phenology model. ....	188
Table 12. Initial default and range (in brackets) of parameter values for the calibrated DO <sub>3</sub> SE-Crop yield model. ....	189

### List of Supporting Material Tables

Table. SI. 1 Definitions of Parameters for a Multiplicative Stomatal Conductance Model .....	79
Table. SI. 2. Details of the ozone fumigation/filtration experiments used to derive flux-response relationships using the various g <sub>sto</sub> models.....	85
Table. SI. 3. Parameters used for g <sub>stoemp</sub> model (Mapping Manual, 2017) .....	87
Table. SI. 4. Parameters used for the estimation of the estimation of O <sub>3</sub> uptake (f <sub>st</sub> ) in g <sub>stoemp</sub> , Anetg <sub>stoemp</sub> , and Anetg <sub>stomech</sub> for three different biogeographic regions (Atlantic, boreal and continental).....	87
Table. SI. 5. The SOS and EOS of the flag leaf determined from break-point analysis of the UK (Mulika and Skyfall,2015) and Swedish (Dragon,1997 and 1999) datasets .....	92
Table. SI. 6. Composition of Training and Test Data Samples (Sets 1-5) Derived via Bootstrap Resampling. Each dataset entry follows the format: CountryCode_Year_CultivarAbbreviation_TreatmentType. For instance, BE_1994_Mi_CF denotes a dataset from Belgium in the year 1994, involving the Minaret cultivar, subjected to carbon-filtered treatment. ....	92
Table. SI. 7. Empirically derived constant conductance (mol TLA m <sup>-2</sup> s <sup>-1</sup> ) (and resistance (PLA s/m)) values for heat and gas (H <sub>2</sub> O, CO <sub>2</sub> and O <sub>3</sub> ) from a single leaf surface.....	151
Table. SI. 8. Conversion factors for H <sub>2</sub> O, CO <sub>2</sub> and O <sub>3</sub> .....	152
Table. SI. 9. Variables and parameters, their definitions and units used to calculate the multi-layer canopy irradiance after De Pury and Farquhar (1997). ....	154
Table. SI. 10. DO <sub>3</sub> SE-Crop variables, their description and units. ....	158

Table. SI. 11. DO <sub>3</sub> SE-Crop parameters for wheat. Highlighted are the parameters (and their associated ranges) which require calibration when applying DO <sub>3</sub> SE-Crop to varying environmental conditions. ....	162
Table. SI. 12. DO <sub>3</sub> SE-crop phenology parameters description and relation to the thermal time .	170
Table. SI. 13 Input data required by the DO <sub>3</sub> SE-Crop model and made available via the implementation of WRFChem (version 4.2). ....	211
Table. SI. 14. Final calibrated parameters by zone used for the DO <sub>3</sub> SE-Crop model runs across China. Other parameters used are same as in Table 17. ....	212

## List of Figures

- Fig. 1. Geography of wheat production (estimated M kcal energy produced by wheat per pixel. ca 10 x 10 km<sup>2</sup>). Prepared using SPAM 2010 and other sources (Reynolds et., 2022). Here, the global map highlighting the food calorie supply from wheat production in different regions of the world. The color-coded legend on the bottom of the map indicates the amount of food calories supplied in millions of kilocalories, with a spectrum ranging from light grey for less than 1 million kcal, to dark red for regions supplying over 100 million kcal ..... 16
- Fig. 2. is derived from the IPCC's Fifth Assessment Report (AR5), illustrates anticipated changes in global agricultural output due to alterations in temperature and precipitation patterns, predicting a notable reduction in crop production worldwide. Furthermore, it suggests that climate change will likely lead to greater year-to-year fluctuations in crop yields in various regions. Part A of the figure provides an overview of the estimated effects of climate changes from 1960 to 2013 on four principal crops across different global regions, with the number of studies referenced for each crop type indicated in parentheses. Part B offers a synthesis of future yield projections throughout the 21st century, considering various greenhouse gas emission scenarios and factoring in the potential impacts in both temperate and tropical regions, with and without the implementation of adaptation strategies. .... 19
- Fig. 3. A schematic view of the sources and sinks of O<sub>3</sub> formation and transport in the atmosphere. (Young et al., 2018). This diagram illustrates the complex interactions of ozone (O<sub>3</sub>) within Earth's troposphere and its exchange with the stratosphere. It depicts the photochemical reactions driven by sunlight (hν) that produce ozone from precursor molecules like nitrogen oxides (NO<sub>x</sub>), carbon monoxide (CO), and volatile organic compounds (VOCs) from both natural and anthropogenic sources. The schematic also shows the transport mechanisms, such as advection, which move these compounds and ozone throughout the atmosphere, as well as the mixing and deposition processes. Highlighted are the dynamic processes between land, ocean, and atmosphere that contribute to the atmospheric life cycle of ozone, a critical component in air quality and environmental health ..... 22
- Fig. 4. The mechanism which ozone and its Reactive Oxidant Species (ROS) result in crop damage (Emberson et al., 2018). The figure depicts a complex interplay between ozone and its reactive derivatives with crop physiological processes, highlighting the dual nature of ozone-induced injuries: acute and chronic. It maps out the movement of ozone and its by-products (open arrows) and the plant's defensive responses (#1-11), alongside mechanisms possibly hindering ozone entry (hatched arrows). Feedback loops influencing stomatal conductance (g<sub>sto</sub>), critical in controlling ozone influx, are marked by dotted arrows (#A-E). This review encapsulates the intricate responses and adaptations of crops to ozone stress, underpinning the significance of understanding these interactions to mitigate the adverse impacts on crop vitality and yield. .... 34

Fig. 5. Scatter plots for Background and peak O<sub>3</sub> treatments for Mulika and Skyfall wheat cultivars, fumigated in Bangor over the 2015 and 2016 growing seasons were used to plot a) Observed against modelled gsto values estimated using the three different gsto models. In each plot, the red solid line represents the regression line, showing the relationship or fit between the modelled and observed values. The black dashed line represents the 1:1 line, which would indicate a perfect match between the modelled and observed values. Data points are scattered across each plot, and the coefficient of determination (R<sup>2</sup>) is provided for the regression, indicating the proportion of variance explained by the model. The closer the data points and the red regression line are to the black dashed line; the better the model's prediction matches the observed data. b) Average daily maximum gsto values simulated over the flag leaf life span by each of the three gsto models and observed maxima gsto data were also shown. Error bars, indicating the standard error of the observed data, are included and shown with black lines extending from the red observed points, providing a visual representation of uncertainty in the measurements..... 67

Fig. 6. Leaf senescence profiles of O<sub>3</sub> induced leaf senescence for cv Mulika for the low background and very high peak O<sub>3</sub> treatments in the UK dataset. The timing of the SOS and EOS (vertical dotted black lines) determined by applying the break point method to the CCI (red circle with standard errors )are shown in relation to the empirical (minimum of fO<sub>3</sub> and leaf fphen) and fLS simulations of senescence. .... 69

Fig. 7. The figures depict flux-response relationships for relative wheat yield using three different stomatal conductance to ozone (gsto) models—namely gstoemp, Anetgstoemp and Anetgstomech—to simulate the POD<sub>6</sub> (Phytotoxic Ozone Dose above a threshold of 6 nmol O<sub>3</sub> m<sup>-2</sup> PLA s<sup>-1</sup>). The plots show the modelled POD<sub>6</sub> on the x-axis against the relative grain yield on the y-axis, with a clear negative trend indicating that as ozone exposure increases, the relative grain yield decreases. The 95% confidence intervals are indicated by the dotted lines surrounding the best-fit line, providing a visual representation of the uncertainty around the estimated response. Each figure should include the coefficient of determination (R<sup>2</sup> value), which quantifies the proportion of variance in the relative grain yield that can be predicted from the modelled POD<sub>6</sub> using the respective gsto model. This value is a statistical measure of how well the regression line approximates the real data points..... 72

Fig. 8. Schematic of DO<sub>3</sub>SE-Crop model..... 113

Fig. 9. The division of thermal time defined periods (TT<sub>emr</sub>, TT<sub>veg</sub>, TT<sub>rep</sub> and TT<sub>leaf</sub> and the relationship with fLA and fLS). This diagram illustrates the stages of crop development in relation to thermal time and the effects of vernalization and photoperiod. Thermal time, a measure of accumulated heat, is divided into periods of emergence (TT<sub>emr</sub>), vegetative growth (TT<sub>veg</sub>), reproduction (TT<sub>rep</sub>), and leaf lifespan (TT<sub>leaf</sub>). TT<sub>leaf</sub> encompasses the thermal time from a canopy leaves full expansion to its senescence, split into active (tlep) and senescing (tlse)

phases. Vernalization and photoperiod can alter  $TT_{veg}$ , affecting the timing of flowering. Crop development correlates with the Developmental Index (DVI), ranging from -1 at sowing, 0 at emergence, 1 at anthesis, to 2 at maturity, with total leaf lifespan distributed between DVI 0 and 2. The impact of ozone ( $O_3$ ) on the maximum rate of carboxylation ( $V_{cmax25}$ ) is indicated by short-term effects ( $f_{LA}$ ) and long-term impacts ( $f_{LS}$ )..... 120

Fig. 10. Plot showing variation in key  $O_3$  deposition terms as daily maxima by canopy layer (N.B.  $i = 1$  is the top canopy layer,  $n = 4$ ) a).  $[O_3]$ , b).  $rb, O_3$ , c).  $PAR_{sun}$  and d).  $gO_3$  for the duration of the flag leaf period for the Y2 cultivar E- $O_3$  treatment in 2008. .... 138

Fig. 11.  $DO_3SE$ -Crop modelled diurnal profile of a).  $gO_3$ , and b).  $Anet$  for a fully-expanded flag leaf prior to the start of senescence  $t_{lep}$  for the ambient ozone and seasonal profile of daily maxima, with data points plotted as open circles connected by a line, representing the average daily pattern c).  $gO_3$ , and d).  $Anet$  for the flag leaf between  $t_{lep}$  and  $t_{lse}$  for the ambient ozone treatments. Black line showing the Start of senescence (SOS). The black line in the plot c and d shows the start of anthesis. .... 139

Fig. 12. a). the partition fractions of the daily accumulated NPP partitioned to roots, stems, leaves, and grains for modelled (solid lines) vs the JULES Crop model (dashed line after (Osborne et al., 2015)) plotted against DVI, which shows a crop development, ranging from -1 at sowing, 0 at emergence, 1 at anthesis, to 2 at maturity, with total leaf lifespan distributed between DVI 0 and 2 and b). the Grain DM of daily accumulated NPP partitioned to roots, stems, leaves, and grains plotted against DVI, the observed grain dry matter (in  $g\ m^{-2}$ ) is shown as a filled red circle..... 140

Fig. 13. Leaf senescence profiles of  $O_3$  induced leaf senescence for the Y2 cultivar for the a). ambient (AA) and b). elevated (E- $O_3$ )  $O_3$ . The timing of the SOS (solid black line) and EOS (dashed black line) were determined by applying the break point method to the CCI data and are shown in relation to the  $f_{LS}$  simulations of senescence (grey line). The observed relative CCI data are also shown (open symbols). DVI is development vegetative index, which shows a crop development, ranging from -1 at sowing, 0 at emergence, 1 at anthesis, to 2 at maturity, with total leaf lifespan distributed between DVI 0 and 2. .... 142

Fig. 14. The figure presents a detailed comparison of the grain dry matter yield of wheat under two distinct ozone treatments: ambient (AA) and elevated (E- $O_3$ ). The boxplots graphically summarize the distribution of both observed and simulated yield data for four wheat cultivars, categorized by their tolerance to ozone. Crosses denote the 0.01 and 0.99 percentiles, capturing the extreme values in the data set. The edges of the boxes represent the 25th and 75th percentiles, with the line inside the box depicting the median. The solid squares indicate the mean yield, offering a direct measure of central tendency. The left cluster of boxplots under "Ambient treatment" contrasts observed yields with those simulated for ozone-tolerant cultivars Y15 and Y16, and ozone-sensitive cultivars Y2 and Y19. The right cluster, labelled "Elevated

treatment," follows the same structure but under conditions of increased ozone exposure. This juxtaposition across treatments and cultivar responses—coupled with multiple years of data (2007, 2008, and 2009) provides a comprehensive view of the impact of ozone on wheat yield, illustrating the variability within and across cultivars and ozone treatments. .... 144

Fig. 15. This scatter plot delineates the relationship between observed and modeled grain dry matter yields for wheat, aggregating data across four cultivars over three different years—2007, 2008, and 2009—as part of the Xiaoji dataset. Each year is color-coded: black for 2007, blue for 2008, and red for 2009, with respective data points plotted to illustrate the comparison on an annual basis. The dashed line represents the 1:1 correspondence between observed and modeled yields, serving as a reference for perfect model accuracy. The solid diagonal line indicates the actual regression fit between the observed and modeled data, evidencing the model's performance. The coefficient of determination ( $R^2 = 0.73$ ) suggests a substantial degree of correlation, indicating that the model can explain around 73% of the variability in observed yields. The root means square error (RMSE = 58.41) quantifies the model's prediction error, offering insight into the average magnitude of the model's residuals or prediction errors. .... 145

Fig. 16. Winter wheat distribution across China according to SPAM2010 (Yu et al. 2020). The map divides the country into four distinct agro-ecological zones (AEZs) for winter wheat production, labeled as I, II, III, and IV. Within these zones, 32 locations were manually selected for calibration, while 107 were chosen for automated calibration of the DO3SE-Crop model, as indicated by the respective symbols. These calibration points were extracted from the SPAM2010 database to refine the DO3SE-Crop model, ensuring it accurately reflects the conditions affecting winter wheat growth across the different ecological regions of China. .... 187

Fig. 17. Spatial plot showing (a). WRF-Chem modelled and observed M7 (09.00-16.00)  $O_3$  concentrations  $\mu\text{g}/\text{m}^3$  and (b). bias between modelled and observed M7 (09.00-16.00)  $O_3$  concentrations  $\mu\text{g}/\text{m}^3$  at observation sites. All M7 values are calculated for the period November to mid-May (rural locations only) for 2017/18..... 194

Fig. 18. (a). Seasonal variation in modelled (teal) and observed (black) M7 (mean 09.00 to 16.00 hrs) mean (line) and 1 standard deviation (shading)  $O_3$  concentrations,  $\mu\text{g}/\text{m}^3$  (for the period November 2017 to May 2018). (b-d) Modelled (teal) and observed (black) diurnal variations in hourly mean (line) and 1 standard deviation (shading)  $O_3$  concentrations,  $\mu\text{g}/\text{m}^3$  for (b). November, (c). March and (d). May, across the winter wheat growing region of China..... 195

Fig. 19. Boxplots (crosses: 0.01 and 0.99 percentiles; box: 0.25 quartile, median and 0.75 quartile; square: mean) comparing crop emergence, anthesis, and maturity phases of winter wheat in agro-ecological zones (AEZs) (zones I, II, III and IV; labelled black boxes) with data collected from observational studies (red boxes). Observed data are predominantly for zones II and IV..... 196

Fig. 20. This composite figure presents the analytical comparison between wheat yield data in two contexts: a. The left panel depicts the correlation between observed yield data from SPAM2010 and yield estimates modelled by the calibrated DO<sub>3</sub>SE-crop model across 89 randomly selected sites spanning four Agro-Ecological Zones (AEZs), distinguished by unique colours. The site-specific data points, identified by highlighted numbers, are earmarked for in-depth analysis later in the paper. The R<sup>2</sup> value displayed suggests a strong correlation between observed and modelled yields, with the regression line serving as a visual benchmark of their concordance..... 198

Fig. 21. Box plots comparing the (a). absolute yield under ambient O<sub>3</sub> for 2017/18 vs observed SPAM2010 yield and (b). relative yields (i.e. current compared to pre-industrial O<sub>3</sub> for the tolerant cultivar for the four different AEZs. All for irrigated winter wheat. The mean value of the yield is indicated by the square box inside each plot, while the median value is represented by the dashed line within the box. The "whiskers" extend from the box to show the range, which includes the maximum and minimum yield values. Outliers, which are data points that differ significantly from the rest of the dataset, are marked with crosses. It is noteworthy that Zone III has only a single data point for the observed yields, due to limited data availability. This single data point is represented as an outlier, which may affect the interpretation of the results for that zone..... 199

Fig. 22. Comparison of WRF-Chem (a. and b.) and experimental (c. and d.) O<sub>3</sub> concentration and meteorological data on crop phenology, growth and yield at Xioaji for the tolerant cultivar for key variables (a. and c.) of O<sub>3</sub> concentration, surface air temperature (T<sub>air</sub>), canopy stomatal ozone flux (canopy f<sub>st</sub>), fLS and grain yield and (b. and d.) canopy f<sub>st</sub>O<sub>3</sub>, LAI and accumulated stomatal ozone flux (acc\_f<sub>st</sub>) for the period of 1<sup>st</sup> Oct (Day of Year 274) to end of June (Day of Year 540). ..... 201

### List of Supporting material Figures

Fig. SI. 1. Boundary line analysis of relative g<sub>sto</sub> in response to vapor pressure deficit (VPD). The dataset includes points from various field and open top chamber studies conducted in Europe, illustrating the decreasing g<sub>sto</sub> with increasing VPD. The solid line represents the VPD function used in this paper for Anetg<sub>sto</sub> models (LRTAP,2017) and dashed line represents the hyperbolic VPD function used in (Leuning, 1995) ..... 80

Fig. SI. 2. a -e. Functional Relationships in Wheat Modeling. (a) Wheat f<sub>temp</sub> relationship shows the relative conductance (g) response to temperature, comparing the g<sub>stoemp</sub> model function to datasets from Bunce (2000) and Danielsson (2003);(b) Wheat f\_VPD relationship shows the relative conductance decline with increasing Vapour Pressure Deficit (VPD), with empirical data from Weber (1996), Teubner (1985), and Bunce (2000) alongside the g<sub>stoemp</sub> model's function; (c) Wheat f<sub>light</sub> relationship depicts the relationship between relative conductance and irradiance

(PPFD), including empirical observations from Machado (1994), Gruters (1995), and Bunce (2000), contrasted with the New EMEP or gstoemp model's output function; (d) Spring wheat Canopy  $f_{phen}$  and leaf  $f_{phen}$  profiles within growing season" outlines the phenological development of wheat, marking the canopy and leaf  $f_{phen}$  from sowing date to end of growing season (EGS), highlighting critical growth stages like anthesis; (e)  $f_{O_3}$  function profile alongside thermal time. It shows the decline in  $f_{O_3}$  as the thermal time increase (depicting the crop growing season) ..... 82

Fig. SI. 3. Relationship between gstoemp model leaf phenology (leaf  $f_{phen}$ ) and the Anetgstomech leaf senescence (fLS) and leaf age (fLA). fLA and fLS are unitless and Thermal time is in °C day 95

Fig. SI. 4. Data extracted from literature showing the range of  $V_{cmax25}$  in Atlantic (A) and Continental (C) and Mediterranean (M) biogeographic region, and variability in the ratio of  $V_{cmax25} : J_{max25}$ .  $V_{cmax25}$  and  $J_{max25}$  data extracted from the literature grouped by biogeographic region (Mediterranean (M), 11 datapoints from Spain & Italy; Atlantic (A) and Continental (C), 238 datapoints from UK, Germany, Slovakia and Hungary). The higher number of datapoints in A&C are due to a large number coming from two published studies conducted in the UK on 64 (Silva-Pérez et al., 2020) and >80 wheat varieties respectively (McAusland et al., 2020). The Continental region shows the most extensive range in values (51-186  $\mu\text{mols CO}_2 \text{ m}^{-2} \text{ s}^{-1}$ ) ((Olsovska et al., 2016)(Harnos et.al, 2002); (Tcherkez et al., 2020)whereas, the Mediterranean region showed the least range in values (88.3-122  $\mu\text{mols CO}_2 \text{ m}^{-2} \text{ s}^{-1}$ ) with some outliers from an Italian study (Dikhoshi., 2015), where  $V_{cmax25}$  values were 190 and 240 for cultivars *Triticum durum*. ..... 90

Fig. SI. 5. (a) The first figure presents a comparison of  $V_{cmax25}$  values in wheat cultivated under irrigated and rainfed conditions. The box plots display a clear demarcation of central tendency and variability, with the red line representing the mean, the black line within the boxes indicating the median, and the box edges showing the 25th and 75th percentiles. Whiskers mark the range of data, extending to the maximum and minimum values, and there are no outliers indicated..... 91

Fig. SI. 6. This diagram outlines the process of a systematic literature review focused on physiology parameters ( $V_{cmax25}$  and  $J_{max25}$ ) related to wheat. The flowchart begins with a broad systematic literature review and narrows down through various stages of filtering and search string specificity, such as " $V_{cmax}$  and wheat and Europe" and related terms. The search is conducted using Google Scholar, starting with an initial result pool of 12,120 articles. This number is refined first to 436 after further criteria are applied, and finally to 238 articles that meet the specific inclusion criteria for the review. Each step is a successive refinement, aimed at isolating the most relevant studies for the physiological parameters in question..... 91

Fig. SI. 7. This graph demonstrates the application of the breakpoint method to determine the onset of senescence in a Bangor low background ozone treatment study. The data points are plotted over time, with a noticeable breakpoint at the x-value of 195. This value indicates the transitional phase that signifies the start of senescence according to the model's prediction. The

lines represent the fitted model's segments, both before and after the breakpoint, capturing the change in trend associated with the senescing process ..... 92

Fig. SI. 8. Leaf senescence profiles (Ostad, Sweden) simulated by the empirical (minimum of  $f_{O_3}$  and leaf  $f_{phen}$ )  $f_{O_3}$  and mechanistic (fLS) approaches compared to the start (SOS and end (EOS) of senescence as determined by the breakpoint method. Higher  $O_3$  treatment brought forwards SOS by 6 days and EOS by 12 days. .... 93

Fig. SI. 9. Flux-response relationships for relative wheat yield derived using the Anetgstomech to simulate the POD6 metric. .... 104

Fig. SI. 10. The background and peak  $O_3$  treatments dataset for Mulika and Skyfall wheat cultivars fumigated in Bangor over the 2015 and 2016 growing season were used to plot a) observed against modelled Anet values estimated using the two different Anetgsto models The black dashed line is the 1:1 line, where a best match between modelled and observed values would lie. The coefficient of determination ( $R^2$ ) is provided for each model, with an  $R^2$  of 0.86 for the background and an  $R^2$  of 0.83 for the background and  $R^2$  of 0.32 and  $R^2$  of 0.56 for the peak treatments respectively for the Anetgstoemp, (left) and Anetgstomech (right). b) Average daily maxima Anet values simulated over the flag leaf life span by the two Anetgsto models and observed maxima Anet values were also shown. Red circles represent the observed data points and black vertical lines connected to the red circles illustrate the standard error associated with the observed data..... 107

Fig. SI. 11. Average diurnal gsto values simulated over the flag leaf life span by each of the three gsto models for the background and peak ozone treatments for Mulika and Skyfall wheat cultivars fumigated in Bangor over the 2015 and 2016 growing season. Also shown are observed gsto data collected and averaged over the same period. The observed gsto values are indicated by red dots, with the standard error represented by the vertical black lines. Predicted gsto values are plotted as blue and purple dashed lines, corresponding to the empirical (Anetgstoemp) and mechanistic (Anetgstomech) stomatal conductance models, respectively. .... 108

Fig. SI. 12. Average diurnal plots of Anet for the days 167-205 ( $n=32$ ) for background  $O_3$  treatments and 167-211 for peak  $O_3$  treatments ( $n= 112$ ) each of the two Anetgsto models. The observed Anet values are indicated by red dots, with the standard error represented by the vertical black lines. Predicted Anet values are plotted as blue and purple dashed lines, corresponding to the empirical (Anetgstoemp) and mechanistic (Anetgstomech) stomatal conductance models, respectively..... 109

Fig. SI. 13. The Chinese FACE- $O_3$  dataset were used to plot modelled phenological stages against experimental dataset for the year a) 2008 (training set) and b) 2007 and 2009 (testing set). The straight line shows the 1:1 line. .... 159

Fig. SI. 14. The Chinese FACE-O <sub>3</sub> dataset were used to plot modelled grain dry matter (g/m <sup>2</sup> ) against experimental dataset for the year 2008 for tolerant (Y16) and sensitive cultivar (Y2) (training set). The dotted black line is the regression line.....	159
Fig. SI. 15. Scatter plot showing M7 (09.00-16.00) O <sub>3</sub> concentrations µg/m <sup>3</sup> comparison of observed vs modelled for rural locations only. All M7 values are calculated for the period November to mid-May (rural locations only) for 2017/18. ....	218
Fig. SI. 16. (a.) Mean and (b.) sum observed vs simulated yields (g/m <sup>2</sup> ) for tolerant cultivars for each of the four AEZs. ....	218
Fig. SI. 17. Comparison of (a). zone I (88_186; with an overestimated O <sub>3</sub> induced yield loss) and (b). zone II (62_192; with a negligible O <sub>3</sub> induced yield loss) for variables canopy fstO <sub>3</sub> , LAI and accumulated stomatal ozone flux (acc_f <sub>st</sub> ) for the period of 1st Oct (Day of Year 274) to end of June (Day of Year 540). ....	219
Fig. SI. 18. Comparison of (a). zone II (92_218; with a low absolute yield and a negligible O <sub>3</sub> effect on yield) and (b). zone II (87_245; with a high absolute yield and a substantial O <sub>3</sub> induced yield loss) for variables canopy fstO <sub>3</sub> , LAI and accumulated stomatal ozone flux (acc_f <sub>st</sub> ) for the period of 1st Oct (Day of Year 274) to end of June (Day of Year 540). ....	220
Fig. SI. 19. Comparison of (a). zone I (88_186; with a medium absolute yield and an overestimated O <sub>3</sub> effect on yield) and (b). zone II (87_245; with a high absolute yield and a substantial O <sub>3</sub> induced yield loss) for variables O <sub>3</sub> , T <sub>air</sub> , f <sub>st</sub> , f <sub>LS</sub> and grain for the period of 1st Oct (Day of Year 274) to end of June (Day of Year 540). ....	221

## Acknowledgement

This thesis could not have been completed without the help of numerous individuals.

I extend my deepest gratitude to my supervisor, Prof Lisa Emberson, for her unwavering support and guidance throughout the research project. Her enthusiasm and willingness to assist have been invaluable. She has provided deep insights into plant physiology, and adeptly assisted me in navigating through some challenging tasks during the development of the DO3SE-crop model.

I would sincerely like to thank Hakan Pleijel and Felicity Hays for their assistance in understanding the European datasets used in this study and for their insights into crop phenology and physiology.

I am grateful to my co-supervisors, Kevin Hicks, and Chris Malley, for their guidance with the literature at the beginning of my PhD and for making me feel welcome at SEI-York.

A special thanks to my team member, Sam Bland, for his help in developing the DO3SE-crop model; to Nathan Booth for his statistical advice; to Jo Cook for constructive discussions about the model's canopy module; to Connie O'Niell for her insights into Chinese Agricultural Emissions; and to Ailish Graham for assistance with the WRF-Chem dataset.

Finally, I thank my family for their constant love and support. My parents have been a pillar of support in all my endeavours. My brother has always been there for me in everything I do. I am indebted to my friends, particularly Jenny, for her companionship and culinary skills. And a heartfelt thank you to my partner Lavi, whose unwavering support in the final stages of this Ph.D. journey has been greatly appreciated.

## Author declaration

I declare that this thesis is a presentation of original work, and I am the sole author. This work has not previously been presented for an award at this, or any other, University. All sources are cited in the text and acknowledged as references.

The following research paper has been produced from this body of work and has been submitted for publication, in a peer-reviewed journal:

Pande, P., Hayes, F., Bland, S., Booth, N., Pleijel, H., Emberson, L.D. (submitted).

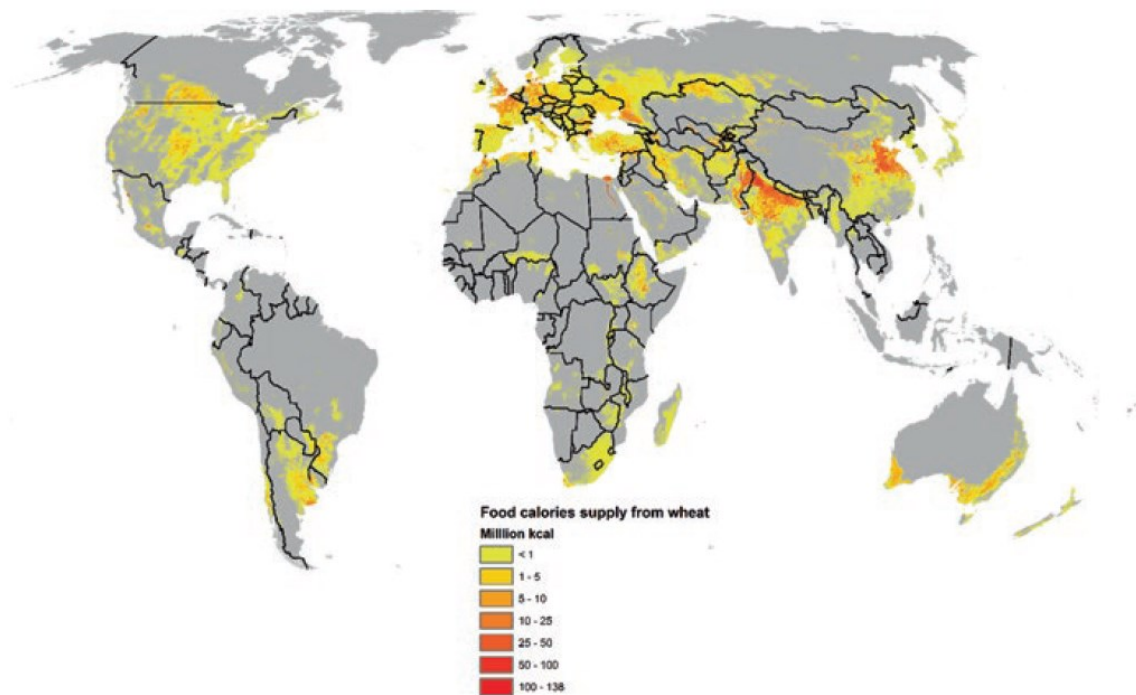
Ozone dose-response relationships for wheat can be derived using photosynthetic-based stomatal conductance models. *Agricultural and Forest Meteorology*

## 1. Introduction

### 1.1 Global food security

Global food security is a pressing issue, especially considering the projected growth in world population from 7.4 billion in 2017 to 9.7 billion in 2050 (Fukase and Martin, 2020). This surge in population demands a significant increase in agricultural output. By 2050, an expected increase of 70% in agricultural production from current levels is required to ensure food security, including raising annual cereal production to 3 billion tonnes (FAO,2009; Muhie, 2022). Cereal grains, especially rice and wheat, meet the global populations' calorific needs (Reynolds et al., 2022). In developing countries, cereals provide between 60%-80% of daily calories compared to 30% in developed countries (Reynolds et al., 2022). Wheat offers essential calories and is a crucial source of dietary protein, serving as a staple for 35% of the global population (Grote et al., 2021). Moreover, it is, therefore, a vital crop for global food security; the current global distribution of wheat production as M kcal of energy produced is shown in Fig 1 (Reynolds et al., 2022).

Fig. 1. Geography of wheat production (estimated M kcal energy produced by wheat per pixel. ca 10 x 10 km<sup>2</sup>) prepared using SPAM 2010 and other sources (Reynolds et., 2022). Here, the global map highlighting the food calorie supply from wheat production in different regions of the world. The color-coded legend on the bottom of the map indicates the amount of food calories supplied in millions of kilocalories, with a spectrum ranging from light grey for less than 1 million kcal, to dark red for regions supplying over 100 million kcal.



Wheat's adaptability to various growing conditions also makes it a versatile crop and, hence, one that is cultivated around the globe as a staple crop. For instance, in 2009/2010, 226 million hectares were used for wheat cultivation, yielding 650 million metric tons (MMT) of grain (Reynolds et al., 2022). This production increased to 750 MMT in 2016-2018, as reported by FAO in 2019. The global wheat production in 2020 is 760 MMT, with China, India, and Russia accounting for 41% of this total (Reynolds et al., 2022); these countries have been significant wheat producers since the 1960s. However, China and India have increased wheat production tenfold from some 10+ MMT each in the early 1960s to each surpassing 100 MMT currently (Reynolds et al., 2022). This has led China and India to become the top two global producers of wheat (Reynolds et al., 2022). Asia also stands out as the primary aggregate consumer of wheat, with 53% of global wheat consumption. By contrast, Europe comprises 26% of global wheat consumption, with the Americas and Africa each taking approximately 10% of the share in consumption (Reynolds et al., 2022).

Future agricultural production and output are very likely to be vulnerable to climate change and air pollution. Crop yields, particularly for wheat, rice, and maize, will decrease by 5-10% in the next 30 years in China as a result of climatic changes (Xiao et al., 2005). An increase in extreme temperature with increasing mean temperatures can severely affect critical crops (Liu et al., 2016). 1-degree Celsius increase into the more

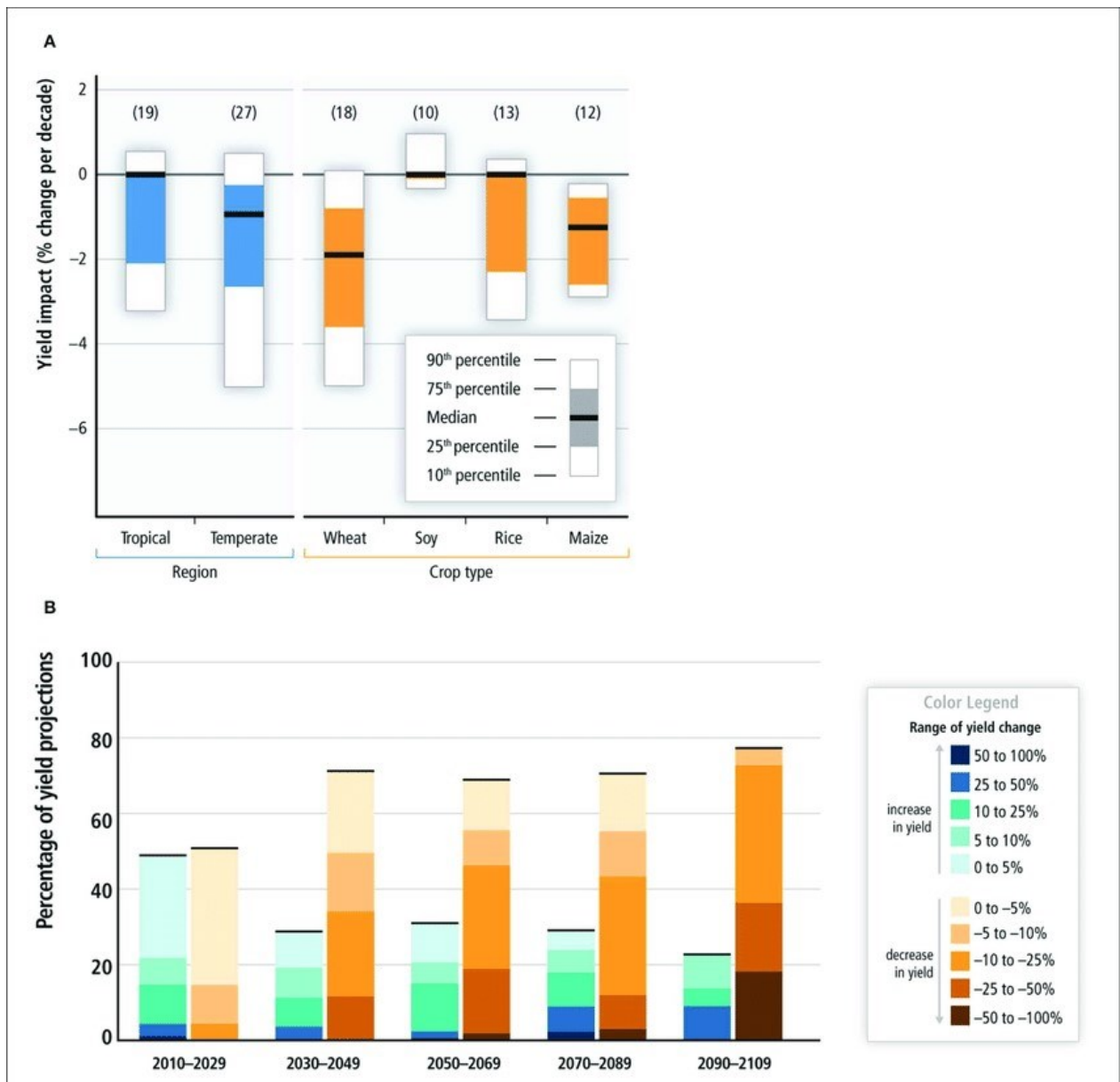
extreme temperatures above a threshold of 30°C leads to a 0.3-0.58 % decrease in wheat grain filling duration in irrigated wheat (Ishaque et al., 2023). Furthermore, another modelling study has estimated that global wheat yields would decrease by 6% with a 1-degree Celsius rise in global mean temperature (Asseng et al., 2015). Temperature changes will also affect wheat phenology; crop modelling studies have found that higher mean growing season temperatures affect phenology, usually resulting in faster growth rates and shorter growing and reproductive seasons of up to 25 days (Ishaque et al., 2023). Such studies have also predicted that anthesis would occur earlier (Ishaque et al., 2023). There is a consensus that drought reduces crop yield. For example, drought has contributed to a significant yield loss of 1.28% per year in main wheat-growing regions in China (Chen et al., 2016) between 1964 and 2015, droughts and heatwaves reduced EU wheat yields by 11.3% (Brás et al., 2021). Ground-level ozone (O<sub>3</sub>) is arguably the most important air pollutant known to pose a phytotoxic threat to arable productivity (Pleijel et al., 2022). Low levels of tropospheric O<sub>3</sub> concentration exist naturally in the environment and are termed 'natural' or 'background' O<sub>3</sub> concentrations (Emberson, 2020a). However, O<sub>3</sub> precursor gases (e.g., nitrogen oxides (NO<sub>x</sub>) and volatile organic compounds (VOCs)) are emitted due to anthropogenic activities related to industry, transport, and power generation and lead to elevated O<sub>3</sub> concentrations (Yadav et al., 2019; Li et al., 2020). The resulting O<sub>3</sub> pollution is considered the air pollutant most damaging to arable productivity (Zhao et al., 2020). This is primarily due to the high phytotoxicity of O<sub>3</sub> and its high concentrations over rural (and hence agricultural) regions due to the secondary nature of O<sub>3</sub> pollution (i.e., it is formed from primary 'precursor' air pollutant emissions under hot, sunny conditions prevalent during crop growing seasons (Emberson et al., 2018).

The Intergovernmental Panel on Climate Change's Fifth Assessment Report (AR5) predicts a significant rise in global surface temperatures throughout the 21st century across all examined scenarios for greenhouse gas emissions (Challinor et al., 2014; Konduri et al., 2020). This warming is expected to significantly increase the frequency, intensity, and duration of extreme weather phenomena, including heatwaves and heavy rainfall, in many parts of the world.

The IPCC AR5 Working Group 2's report on Food Security and Food Production Systems includes graphics (referred to as Fig. 2 A and B) that compile findings from multiple studies on the effects of climate change on four key crops worldwide (Konduri et al.,

2020). The synthesis of these studies predominantly indicates a downward trend in crop yields during the historical period from 1960 to 2013, as illustrated in Figure 1A (Challinor et al., 2014; Konduri et al., 2020) . Furthermore, many of these studies forecast significant yield reductions in various global regions, particularly as the twenty-first century progresses, as depicted in Figure 1B (Challinor et al., 2014; Konduri et al., 2020). This anticipated decrease in yields towards the century's end underscores the potential challenges in maintaining food security amid changing climate conditions.

Fig. 2. is derived from the IPCC's Fifth Assessment Report (AR5), illustrates anticipated changes in global agricultural output due to alterations in temperature and precipitation patterns, predicting a notable reduction in crop production worldwide. Furthermore, it suggests that climate change will likely lead to greater year-to-year fluctuations in crop yields in various regions. Part A of the figure provides an overview of the estimated effects of climate changes from 1960 to 2013 on four principal crops across different global regions, with the number of studies referenced for each crop type indicated in parentheses. Part B offers a synthesis of future yield projections throughout the 21st century, considering various greenhouse gas emission scenarios and factoring in the potential impacts in both temperate and tropical regions, with and without the implementation of adaptation strategies (Challinor et al., 2014; Konduri et al., 2020).



Short-term predictions from the IPCC indicate potential yield increases in Europe and North America, where warmer conditions could prolong the growing seasons at higher latitudes, and elevated CO<sub>2</sub> levels may enhance crop growth (Godde et al., 2021). However, in lower latitudes and particularly in the tropics, the benefits of increased CO<sub>2</sub> are unlikely to outweigh the adverse effects of climate change, with yields expected to diminish (Godde et al., 2021). The impact on wheat, rice, and maize across tropical and temperate zones is anticipated to be harmful once local temperatures rise by 2°C or more from late 20th-century levels, barring any adaptive measures (Godde et al., 2021). While some areas might see benefits, the overall projection indicates a mix of outcomes, with

some models suggesting yield increases of over 10% and others forecasting losses greater than 25% between 2030 and 2049 relative to late 20th-century benchmarks. A global temperature rises of approximately 4°C or more, coupled with an increasing demand for food, presents a substantial threat to food security on both global and regional scales, underscoring the critical need for effective adaptation strategies to safeguard future food supplies (Godde et al., 2021).

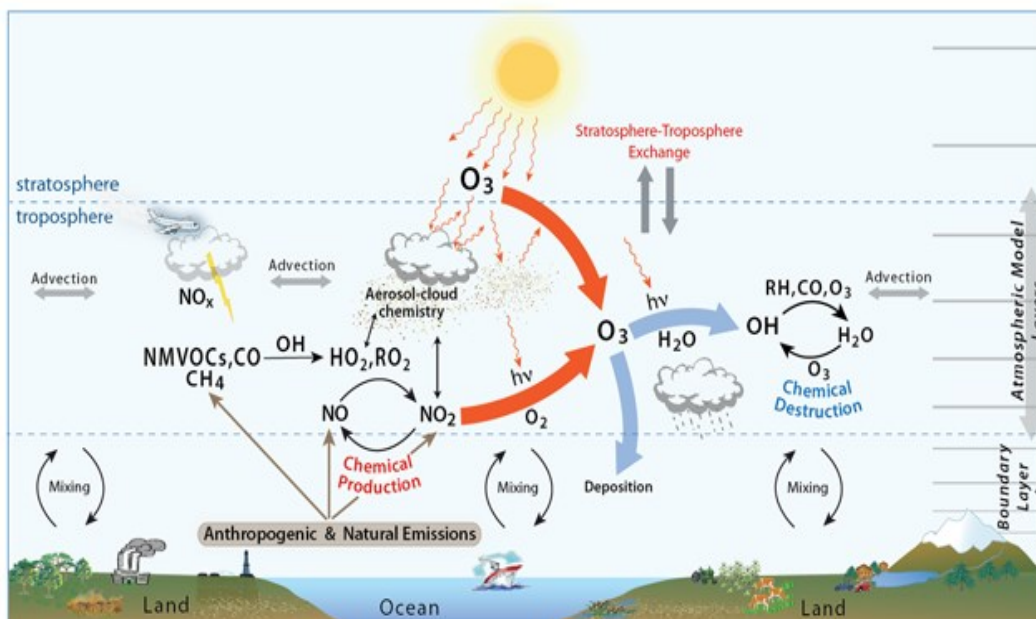
Using a modelled approach, the study estimated that under the climate and CO<sub>2</sub> conditions prevalent in the 2000s, wheat productivity suffered a loss due to O<sub>3</sub> of 1.1-13.3%. The loss is projected to increase to 6.5-21.8% in the 2020s across the region examined (Tao et al., 2017). Meta-analytical experiments have shown that wheat yields may decrease by 3-50% when O<sub>3</sub> levels, defined as a 7-hour daylight average over the growing season, vary between 5-115 parts per billion (ppb) (Mills, Sharps, Simpson, Pleijel, Broberg, et al., 2018). Utilizing dose-response relationships from such experiments for risk assessments (Pleijel et al., 2007), it is estimated that O<sub>3</sub>-related yield reductions globally range from a mean 9.9% in the northern hemisphere and 6.2% in the southern hemisphere, resulting in a production decline of about 85 MMT (Mills, Sharps, Simpson, Pleijel, Broberg, et al., 2018). In the future, increasing global atmospheric CO<sub>2</sub> and temperature trends will lead to a significant change in climate. Such changes can directly affect O<sub>3</sub> concentration; additionally heat waves can increase the probability of extreme O<sub>3</sub> concentration events (Guarin et al., 2019). These studies help to exemplify the interconnectedness between climate change and O<sub>3</sub> air pollution stressors to global arable agriculture.

## 1.2 Global trends in ozone formation, transport, deposition, and removal

As a secondary pollutant O<sub>3</sub> is intricately linked to the emissions of precursor pollutants and the chemical rates of production in the atmosphere, as well as any chemical destruction and deposition processes Fig. 3. is formed as precursors undergo photochemical reactions with light of wavelengths <430 nm in the atmosphere (Sharma et al., 2016). These O<sub>3</sub> precursors, namely VOCs, CO, NO<sub>x</sub> (NO and NO<sub>2</sub>), and methane (CH<sub>4</sub>) can be either natural or anthropogenic. NO<sub>x</sub> and VOCs, in particular, are considered chief O<sub>3</sub> precursors near the ground surface, while CO and CH<sub>4</sub> contribute towards O<sub>3</sub> formation mainly in the free troposphere (10-20 km), but in high concentrations, they also contribute to near-surface O<sub>3</sub> production (Reid et al., 2008; Lu et al., 2019). Understanding these processes and their implications is crucial for us, as it

empowers us to make informed decisions and take necessary actions to mitigate the impact of O<sub>3</sub> air pollution on global arable agriculture.

Fig. 3. A schematic view of the sources and sinks of O<sub>3</sub> formation and transport in the atmosphere. (Young et al., 2018). This diagram illustrates the complex interactions of ozone (O<sub>3</sub>) within Earth's troposphere and its exchange with the stratosphere. It depicts the photochemical reactions driven by sunlight (hν) that produce ozone from precursor molecules like nitrogen oxides (NO<sub>x</sub>), carbon monoxide (CO), and volatile organic compounds (VOCs) from both natural and anthropogenic sources. The schematic also shows the transport mechanisms, such as advection, which move these compounds and ozone throughout the atmosphere, as well as the mixing and deposition processes. Highlighted are the dynamic processes between land, ocean, and atmosphere that contribute to the atmospheric life cycle of ozone, a critical component in air quality and environmental health.

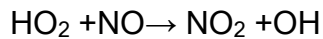
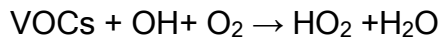


### 1.2.1 Formation of tropospheric ozone

Ozone is a secondary pollutant formed in the air through a complex set of sunlight-initiated reactions of its precursors. The main ozone precursors are NO<sub>x</sub> (NO<sub>2</sub>, NO) gases and VOCs (hydrocarbons, aldehydes, and alcohols) (Tibrewal et al., 2019).

The significant catalytic reactions that lead to O<sub>3</sub> formation are summarised in the steps below. Initially, VOCs react with a hydroxyl (OH) radical and oxygen molecule to produce

hydroperoxyl radicle ( $\text{HO}_2$ ) (or organic analog ( $\text{RO}_2$ )). The  $\text{HO}_2$  radicles further react with  $\text{NO}$  to produce  $\text{NO}_2$ , and  $\text{OH}$  radicles  $\text{NO}_2$  in the presence of sunlight ( $\lambda < 420$ ) release oxygen radicles, which combine with oxygen molecules in the next step of the catalytic reaction to form  $\text{O}_3$  (Kleinman et al., 2001).



### 1.2.2 Ozone removal processes

The primary mechanism for  $\text{O}_3$  removal within the planetary boundary layer is called dry deposition, which involves the transfer of  $\text{O}_3$  to the Earth's surface and comprises approximately 20-25% of total  $\text{O}_3$  removal from the troposphere globally. Notably,  $\text{O}_3$  dry deposition rates on terrestrial surfaces are about ten times higher than on marine surfaces (Barten et al., 2021). In terrestrial ecosystems, dry deposition is predominantly influenced by stomata, responsible for facilitating  $\text{O}_3$  uptake, accounting for a substantial portion, ranging from 30% to 90% of the total  $\text{O}_3$  absorbed by ecosystems (Ainsworth et al., 2012; Emberson, 2020).

The magnitude of  $\text{O}_3$  dry deposition is controlled by the combined effects of all removal pathways, which include stomatal and non-stomatal uptake to vegetation and deposition to soils or any other external surface (Huang et al., 2016). Stomatal uptake is the primary mechanism for  $\text{O}_3$ -associated damage within plants (Emberson, 2020). The non-stomatal sinks for  $\text{O}_3$  removal include  $\text{O}_3$  deposition onto plant cuticles, other surfaces, and the soil (Emberson, 2020). The effectiveness of stomatal and non-stomatal processes depends on various factors, such as leaf and soil moisture levels, soil composition, and the structure of the plant canopy, which changes diurnally and seasonally (Osborne et al., 2019). The non-stomatal processes for  $\text{O}_3$  removal do not harm plants; on the contrary, they mitigate the overall damaging impact of  $\text{O}_3$  by reducing its concentration in the atmosphere (Emberson, 2020). However, stomatal  $\text{O}_3$  uptake above a threshold determined by a plant's ability to detoxify  $\text{O}_3$  is thought to lead to biochemical and

physiological changes, including inhibition of carbon assimilation from photosynthesis ( $A_{net}$ ) that can result in reduced agricultural yields (Huang et al., 2016).

### 1.2.3 Background versus peak ozone concentrations

Ozone is naturally present in the environment, but industrialization has steadily increased  $O_3$  concentration (Emberson, 2020) to the extent that 30% of the present-day tropospheric  $O_3$  burden is attributable to human activity (Gaudel et al., 2018). The Industrial Revolution, which occurred at different times across the globe, saw countries experience rapid economic growth and urbanization, which resulted in higher energy demands and an increase in traffic pollution. This caused increases in various air pollutants associated with emissions from the burning of fossil fuels, including  $O_3$  (Chen et al., 2022). Since the industrial revolution,  $O_3$  levels have steadily increased from average  $O_3$  concentrations of less than 20 ppb in pre-industrial times to current levels of 30-50 ppb in Northern mid-latitude regions (Emberson, 2020). Since the 1950s to 2010s, mean  $O_3$  concentrations have been growing at 1-5 ppb/decade in the Northern Hemisphere (NH) and by 2 ppb/decade in the Southern Hemisphere (Cooper et al., 2014; Emberson, 2020a). Over recent decades, there have been efforts to reduce  $O_3$  precursor emissions. However  $O_3$  levels remain high in many rural and urban areas of Europe, North America, and Japan (Osborne et al., 2019). Ozone concentration profiles have also been changing recently such that the frequency of peak  $O_3$  values tends to show a declining trend while background  $O_3$  concentrations are increasing (Fuhrer, 2009; Emberson, 2020). Such persistently high background  $O_3$  levels have been recorded over key agricultural regions; 18% of the agricultural land area in Europe, which totals approximately 401,000 square kilometres, experienced  $O_3$  concentrations above the target thresholds of 886 ppb.hr set for the protection of vegetation (European Environment Agency, 2023). Additionally, both background and peak  $O_3$  levels are rising in South Asia's Indo-Gangetic plains (IGP) (Shah et al., 2019) and the North China Plain in East Asia (Wang et al., 2009; Liu et al., 2016). For example, a five-year study from 2010 to 2015 in the IGP region of India recorded a 19.2% rise in the annual average  $O_3$  levels. Additionally, the study measured the daytime ozone peak, observing an initial level of  $48.6 \pm 22.3$  ppb in the IGP that rose to  $55.5 \pm 23.2$  ppb by 2015, indicating a 14.2% growth from the figures reported in 2010 (Kumari et al., 2020). Similarly, urban  $O_3$  concentrations in mainland China reached peaks of 90 ppb in 2018, and the annual mean  $O_3$  concentration was  $77 \mu\text{g}/\text{m}^3$  from 2015 to 2020 (Yao et al., 2023). Another

important agricultural region, the Yangtze Delta region of China, observed a decrease in the average O<sub>3</sub> concentration but an increase in the daily amplitude of the diurnal variation in O<sub>3</sub> concentrations due to increasing frequencies at both high and low ends of the O<sub>3</sub> distribution profile, the most likely cause was believed to be an increase in NO<sub>x</sub> concentrations across the region (Xu et al., 2016).

#### 1.2.4 Ozone precursors: Variability by global region

Ozone formation dominates in rural areas of industrialised countries, experiencing moderate NO<sub>x</sub> pollution levels (Emberson, 2020). These areas also tend to include major crop-growing regions of the world such locations where the rate of O<sub>3</sub> formation increases with increasing NO<sub>x</sub> are referred to as NO<sub>x</sub>-limited regions. By contrast, where O<sub>3</sub> formation is inhibited by increasing NO<sub>x</sub> (since this leads to NO<sub>x</sub> titration) in urban locations with very high NO<sub>x</sub> levels (e.g., approximately 1000 ppt), O<sub>3</sub> is referred to as VOC limited (Liu and Shi, 2021). Titration refers to the process where nitrogen oxides (NO<sub>x</sub>) react with ozone (O<sub>3</sub>) in the atmosphere, often leading to the reduction of ozone levels in certain conditions. This process is particularly relevant in urban and polluted environments where NO<sub>x</sub> emissions are significant. The primary mechanism involves the reaction between nitrogen dioxide (NO<sub>2</sub>), a component of NO<sub>x</sub>, and ozone. The reaction can be simplified as follows  $NO + O_3 \rightarrow NO_2 + O_2$ . This reaction suggests that nitrogen oxide (NO) reacts with ozone to form nitrogen dioxide (NO<sub>2</sub>) and oxygen (O<sub>2</sub>) (Nguyen et al., 2022). These dynamics can vary significantly by region and are influenced by many factors, including local emissions, weather patterns, and geography. For instance, during winter, a more significant proportion of the globe (7%) falls under this VOC-limited regime compared to summer (3%), as indicated by (Liu et al., 2022). Currently, North America, Europe, and East Asia primarily face VOC- limited O<sub>3</sub> formation regimes. However, future projections suggest a shift towards NO<sub>x</sub> limitations in North America and Europe are primarily due to decreasing NO<sub>x</sub> emissions (Liu et al., 2022). The study also compared current and future ozone levels under SSP3-7.0 (Shared Socioeconomic Pathway 3 with a radiative forcing of 7.0 W/m<sup>2</sup> by 2100) scenarios, finding a 4% increase in ozone burden with a 0.7-0.9 ppb rise, a 7% decrease with a 3.2-5.2 ppb drop, and a 5% decrease in methane alone decreased by 438 ppb compared to the present. Therefore, methane reduction effectively decreases ozone despite a higher ozone mixing ratio in the future under low methane. This highlights the critical need for a thorough understanding of how shifts in VOC and NO<sub>x</sub> levels impact O<sub>3</sub> concentrations under various

environmental scenarios; this will be a key consideration in formulating region-specific emissions reduction strategies in the future (Liu et al., 2022).

### 1.2.5 Diurnal and seasonal ozone cycles in urban and rural locations

Another critical aspect of O<sub>3</sub> pollution related to vegetation impacts is the diurnal and seasonal cycle. The diurnal variation of O<sub>3</sub> concentration in O<sub>3</sub> levels is influenced by a combination of various elements that either contribute to its creation (e.g., local photochemical reactions and horizontal or vertical transport) and depletion (e.g., deposition or chemical reactions (Zhu et al., 2015). During the day, the O<sub>3</sub> concentration profile shows substantial diurnal variations at lowland sites where O<sub>3</sub> destruction dominates during the night, and vertical mixing with photochemical activity causes the highest levels in the afternoon (Ma et al., 2021). For instance, in the Northwest-Shandong Plain of China, at a relatively low elevation, 28 m above sea level (a.s.l), peak ozone concentration, 128.4 ppb, is highest at 16:30 (Zhu et al., 2015). In North China Plain, for the site, Raoyang National, 18m a.s.l, the O<sub>3</sub> concentration was found maximum at around 16:00 LT (120ppb) from July 2 to 8 and around 14:00 LT (100ppb) from July 13 to 16 (Xu et al., 2020).

Given this variation in the O<sub>3</sub> diurnal profile, it is important to consider the diurnal variation in key plant physiological variables that determine O<sub>3</sub> sensitivity (such as  $g_{sto}$  and  $A_{net}$ ) and use O<sub>3</sub> damage assessment methods that incorporate this type of variation. The seasonal O<sub>3</sub> cycle also correlates with local climate conditions and varies by geographic region (Boleti et al., 2020). Seasonal O<sub>3</sub> concentrations generally peak during the late spring and early summer months, coinciding with the wheat grain filling period. For instance, research indicates that O<sub>3</sub> concentrations in some of the main Chinese agricultural regions (Tibetan Plateau, Yangtze River Delta, Hainan, Guangdong, Guangxi) are highest during wheat's grain-filling phase (which occurs between March and May) (Li et al., 2022). The impact of seasonal O<sub>3</sub> fluctuations on crops varies, influenced by crop type and planting timing. Adjusting sowing dates can mitigate high O<sub>3</sub> exposure, particularly during grain filling. This approach, tested using modelling studies, compares yields of early-sown versus traditionally sown crops, demonstrating potential benefits as discussed in section 5.7 (Porter, 1984; Ghosh et al., 2020; Yadav et al., 2021).

### 1.2.6 Hemispheric transport

In the atmospheric boundary layer, O<sub>3</sub> has an atmospheric lifetime of a few hours to days, and its precursor's lifetimes range from a few to several weeks to months (as seen in Table 1).

Table 1. Atmospheric lifetime of the O<sub>3</sub> precursors and O<sub>3</sub> in the atmospheric boundary layer and free troposphere.

Trace gas (O <sub>3</sub> precursors and O <sub>3</sub> )	Approximate lifetime in the atmosphere boundary layer	Approximate lifetime in the free troposphere	Reference
NO <sub>2</sub>	hours	Days	(Pommier, 2023)
CH <sub>4</sub>	10 years	10 years	(Monks et al., 2015)
VOCs	Hours to months	Hours to months	(Ragothaman and Id, 2017)
CO	Weeks to months	Weeks to months	(lii and Cheung, 1960)
O <sub>3</sub>	Hours to days	Weeks to months	(Monks et al., 2015)

Therefore, due to strong upwelling in the tropics, hemispheric transport of O<sub>3</sub> precursors is quite common (Singla et al., 2011). In-situ and satellite data have shown that O<sub>3</sub> pollution plume transfer is not only from one part of the hemisphere to another but can circle the entire globe (Wang et al., 2022). This means that background O<sub>3</sub> and its precursors, once released, are not confined to their area of origin but can be carried across continents by atmospheric currents. In the case of East Asia, a substantial amount of ozone in the higher atmospheric layers comes from distant sources, particularly during spring when the westerlies are strong, facilitating the movement of ozone from Asia towards Europe more directly than via North America (Archibald et al., 2020). Observations have shown that Asian outflows can contribute tropospheric O<sub>3</sub> mixing ratios of 3.5 to 6.6 ppb into Europe, with the highest inflow recorded in Mace Head (Ireland) (Derwent et al., 2004).

The phenomenon of ozone traveling vast distances is evidenced by the observed intercontinental transport of ozone from Asia to North America; Asian O<sub>3</sub> outflow

contributions to the western United States are in the range of 3 to 10 ppb (Yienger et al., 2000), and then to Europe. This global interchange highlights how emissions in one part of the world can influence air quality in distant regions, underlining the interconnectedness of our atmospheric systems (Archibald et al., 2020).

The mechanisms governing the movement of ozone are intricate, varying with seasons and influenced by meteorological phenomena such as the East Asian monsoon. This seasonal pattern affects the vertical distribution of ozone in the atmosphere over East Asia, showcasing the dynamic and complex nature of atmospheric transport processes (Han et al., 2019).

### 1.3 Trends in ozone precursor emissions

The importance of various O<sub>3</sub> precursors to the overall pollution burden varies globally. In North America, key O<sub>3</sub> precursors are primarily nitrogen oxides (NO<sub>x</sub>) and VOCs, which have shown varying trends over recent decades due to the impact of air quality policies and other factors (Wolff et al., 2001; U.S. EPA., 2020). Studies indicate a general decrease in O<sub>3</sub> concentrations across most of the United States from the mid-1980s to the mid-1990s, with mixed trends in Canada, where some urban sites experienced O<sub>3</sub> concentration increases. In contrast, most regionally representative sites showed decreases or no significant change (Wolff et al., 2001). Ozone precursor emissions originate largely from the energy and surface transportation sectors; policies implemented to reduce NO<sub>x</sub> and VOC emissions from these sectors significantly contributed to the decrease in summertime O<sub>3</sub> concentration in the United States from 1995 to 2019, though winter levels increased partly due to weakened NO<sub>x</sub> titration processes and contributions from aviation, shipping emissions, and transpacific transport of O<sub>3</sub> from Asia (Li et al., 2023). In addition, biogenic sources significantly contribute to VOC emissions. Biogenics are particularly important in parts of Eastern North America and Southern Europe, indicating the influence of natural sources alongside human activities in O<sub>3</sub> formation (Pun et al., 2002; U.S. EPA., 2020). Traffic-related O<sub>3</sub> concentrations in Europe also highlight the significant role of the transportation sector in contributing to O<sub>3</sub> precursor emissions (Mertens et al., 2024).

Furthermore, CH<sub>4</sub>, predominantly emitted from the agricultural sector from a variety of sources (e.g., rice cultivation, field burning of agricultural residues, enteric fermentation, and manure management (Li et al., 2023), has contributed a steady increase to globally well-mixed VOC concentrations over the past few decades.

Since the pre-industrial era, the levels of atmospheric methane have risen by approximately 150% (Karlsson et al., 2017). Over the course of the industrial age, from 1750 to 2014, variations in emissions of precursors and methane concentrations have resulted in alterations in ground-level ozone ( $O_3$ ), an increase in the tropospheric ozone burden, and an augmentation in ozone's radiative forcing by +8 ppbv, +76 Tg, and +0.3  $W m^{-2}$  respectively (Turnock et al., 2019). Furthermore, the long-term impact of air quality policies in North America and Europe has reduced anthropogenic emissions of  $O_3$  precursors since the 1990s, contributing to lower tropospheric  $O_3$  trends in northern mid-latitudes (Sicard et al., 2021). This reduction contrasts with equatorial regions, where emissions have continued to increase (Sicard et al., 2021). The complexity of these trends is further influenced by factors such as the relatively long lifetime of tropospheric  $O_3$ , hemispheric transport of  $O_3$ , and other sources of  $O_3$  precursors such as tropical biogenic and biomass burning emissions (Russo et al., 2023).

It is important to understand the role that  $O_3$  precursors play in contributing to the formation of  $O_3$  pollution. These can help understand the likely future trends in  $O_3$  pollution as emission compositions change under varying meteorological climates. Although declines in  $O_3$  precursor emissions and associated  $O_3$  concentrations have been observed in North America and Europe in recent decades (Chang et al., 2017),  $O_3$  concentrations continue to rise in developing regions, especially in the East and South Asia (Xu et al., 2016; Lu et al., 2018).

An increase in  $O_3$  precursor emissions in India and a major increase in  $CH_4$  emissions globally are the main reasons for rising future trends in South Asian  $O_3$  concentrations. A global spatial analysis of  $O_3$  concentrations and associated impacts was recently conducted (Hsu et al., 2012), and it was found that the highest  $O_3$  concentrations and potential  $O_3$  impact were found in the northern hemisphere. Different global atmospheric chemistry transport models (CTMs) have been used to predict the influence of  $O_3$  precursor emissions on  $O_3$  concentrations under different RCP scenarios (Sicard et al., 2017). AOT40 metrics (the accumulated ozone concentration above a 40-ppb threshold; designed to emphasise peak  $O_3$  concentrations) reveal trends for three RCP scenarios. Representative Concentration Pathways (RCPs) are scenarios in climate modelling that describe different greenhouse gas concentration trajectories. The "worst-case" scenario often refers to RCP 8.5, which assumes high greenhouse gas emissions and significant climate change by the end of the century (Thomson et al., 2011). This scenario is

characterized by continued population growth, high energy demand, and a heavy reliance on fossil fuels. On the other hand, the intermediate scenario, often related to RCP 4.5 or 6.0, assumes moderate changes in emissions without significant new climate policies (Thomson et al., 2011). Another, RCP 2.6, is a scenario that represents a pathway where global warming is likely to be limited to below 2°C above pre-industrial levels (Thomson et al., 2011). These scenarios project a stabilization of climate change, although still with significant impacts. RCP 8.5 is used for highlighting the risks of inaction, while RCP 4.5 and 6.0 offer more moderate outcomes, and the RCP 2.6 scenario is characterized by aggressive mitigation strategies leading to a substantial decrease in greenhouse gas emissions (Thomson et al., 2011).

RCP 8.5 predicted an increase in O<sub>3</sub> concentration of between 4-5 ppb; on the contrary, a decrease in O<sub>3</sub> (2-10ppb) is predicted by RCP 2.6 (Szopa et al., 2013). Similarly, another study showed that under RCP 2.6, a decrease in O<sub>3</sub> concentration of approximately 0.07 ppbv/year would be seen in the Northern Hemisphere, whilst an increase in O<sub>3</sub> concentrations in some tropical regions such as India and China would be likely. Under the RCP 8.5 scenario, significant increases in O<sub>3</sub> burden (+30Tg from 2010 to 2100) were estimated (Szopa et al., 2013). Globally, all O<sub>3</sub> precursor emissions decreased after 2030 in RCP 8.5 except for CH<sub>4</sub>. CH<sub>4</sub> was, therefore, found to be the primary cause of future increasing O<sub>3</sub> precursors across the globe (Szopa et al., 2013). Regional O<sub>3</sub> concentration changes have also been modelled for South Asia. For example, although RCP 4.5 and RCP 6 follow a similar emission trajectory, spatial differences are evident; RCP 6 showed an increase in O<sub>3</sub> concentrations in China and Indonesia, whereas RCP 4.5 showed a decrease in O<sub>3</sub> concentrations in China and an increase in the O<sub>3</sub> burden in India (Szopa et al., 2013).

#### 1.4 Ozone impacts on crops

Ozone has been found to have detrimental impacts on crops where it occurs at elevated concentrations over agricultural regions worldwide. Ozone can alter the physiology, morphology, and biochemical characteristics of various crops (Feng et al., 2008; Emberson et al., 2018; Feng et al., 2022). It can either lead to acute or chronic leaf injury. Programmed and unregulated cell death are considered acute responses, where symptoms like lesions, rashes, stippling, etc., on leaf surfaces, could be seen within a few hours of plants being exposed to relatively high O<sub>3</sub> concentrations (Tamaoki, 2008). Conversely, chronic injury symptoms developed after only a few days or weeks of

exposure to low O<sub>3</sub> concentrations and have been found to accelerate leaf senescence, among other effects (Feng et al., 2022). These effects can impact the overall development and growth of the crop as they modify biochemical processes, reduce carbon assimilation, and hence affect yield (Emberson et al., 2018; Yadav et al., 2020). Ozone mainly harms plants when it enters through the stomatal pores (Emberson et al., 2018). However, O<sub>3</sub> can also settle on external plant cuticular surfaces; this is usually minor, if any, damage. However, once inside a leaf, O<sub>3</sub> rapidly transforms into reactive oxygen species (ROS) like hydroxyl, peroxy, and superoxide radicals. This process activates the plant's defence mechanisms, notably increasing the activity of antioxidants such as superoxide dismutase and peroxidases. These antioxidants help protect against oxidative damage in the apoplast, the space outside the plant's cells (Rai and Agrawal, 2012; Mina et al., 2019). Some plants react to O<sub>3</sub> stress by producing isoprene, which can neutralize O<sub>3</sub> before it converts into harmful ROS (Mina et al., 2010). However, these defence responses require significant metabolic resources, consuming carbon, and other nutrients. This often leads to heightened mitochondrial respiration in plants, especially crops, due to increased metabolic demands (Ainsworth et al., 2012; Emberson, 2020a). ROS can oxidize essential proteins and lipids in the plasma membrane if these protective measures are overwhelmed, leading to dysfunction (Paoletti et al., 2019). This can trigger a cascade of harmful reactions, including the formation of toxic compounds, visible leaf damage, impaired  $A_{net}$ , and leaf senescence (Emberson et al., 2018). The damage mechanisms are shown in Fig. 3.

#### 1.4.1 Ozone effects on stomatal conductance ( $g_{sto}$ )

Experiments with wheat and other plants have demonstrated that exposure to O<sub>3</sub> reduces  $g_{sto}$ . This reduction is primarily attributed to ozone's effect on  $A_{net}$ , possibly due to increased internal CO<sub>2</sub> concentration in the palisade mesophyll cells. For instance, research by (Feng et al., 2008) found that elevated O<sub>3</sub> levels led to comparable decreases in both photosynthetic rates and  $g_{sto}$  in wheat crops, of around 20% and 22% respectively. However, the connection between  $A_{net}$  and  $g_{sto}$  in wheat is complex and not entirely linear and can vary depending on the experimental conditions and species involved (Gago et al., 2016). This happens because the initial increases in  $g_{sto}$  can proportionally boost  $A_{net}$  due to higher CO<sub>2</sub> availability; excessive stomatal opening may not significantly enhance  $A_{net}$  but may increase water loss. These findings suggest a

need for models that can more accurately simulate the complex relationship between  $g_{sto}$  and  $A_{net}$ .

#### 1.4.2 Ozone effects on $A_{net}$

Several studies have revealed that high levels of  $O_3$  suppress photo-assimilate accumulation, and such reduction varies with species and cultivars (Yadav et al., 2020). The central biochemical processes controlling  $A_{net}$  are, the maximum carboxylation efficiency ( $V_{c_{max}}$ ), which reflects *in vivo* activity of Rubisco (Rogers & Humphries, 2000), and the maximum rate of RuBP regeneration ( $J_{max}$ ). Many physiological studies have shown damages in photosynthetic machinery due to  $O_3$  leading to a progressive loss of Rubisco activity and reduction in carbon fixation even in the absence of any visible injury (Feng et al., 2008; Feng et al., 2011). These studies showed that leaf area index (LAI) and specific leaf area (SLA) were not significantly affected by elevated  $O_3$ , whereas a 20% decrease in leaf photosynthetic rate and a 21% increase in leaf dark respiration rate were induced. Lower photosynthetic rates may have resulted from the combined effects of decreases in Rubisco activity,  $V_{c_{max}}$ , and  $g_{sto}$ , and a large decrease in chlorophyll content (by up to 40%) and light use efficiency (by up to 11%) (Feng et al., 2008). Along with the decrease in leaf Fv/Fm (variable to maximal fluorescence), which shows the reflects the maximum light energy conversion efficiency of the PS reaction center (Meng et al., 2012), leaf photosynthetic light and dark reaction capacity was decreased, which should have resulted in less available carbon for growth and grain formation when exposed to elevated  $O_3$ . The effects of growth at elevated  $O_3$  were due primarily to a lower  $V_{c_{max}}$  (Biswas et al., 2013).

#### 1.4.3 Ozone effects on carbon allocation and yield

Ozone exposure in plants leads to elevated levels of soluble sugars and carbohydrates in the leaves, which are essential for the plant's defence, maintenance, and repair mechanisms (Singh Yadav et al., 2020; Feng et al., 2024). However, this increased retention of sugars and carbohydrates results in lower availability of carbon compounds for the development of biomass, affecting both aboveground and belowground parts of the plant (Hansen et al., 2019). Additionally, ozone's detrimental effect on cellular membranes disrupts the transport of photosynthates via the phloem (Hansen et al., 2019). This disruption reduces the production of photosynthates and hampers the

transfer of carbon from the source (leaves) to the sink (grains), adversely affecting carbon fixation during the crucial grain-filling phase (Hansen et al., 2019). Consequently, this impairment in the reproductive phase of crop growth can lead to the reduction in both the number of grains and the weight of a thousand kernels, culminating in diminished grain yields (Feng et al., 2024). However, it's worth noting that certain studies have indicated that while the grain's weight may be affected, the actual number of grains produced in wheat crops may remain unchanged (Broberg et al., 2015). Further studies have shown that O<sub>3</sub> exposure increases the carbon-to-nitrogen (C: N) ratio in straw, with a slight but non-significant decrease in the grain C:N ratio at harvest compared to normal conditions (Brewster et al., 2024). This change in C:N ratios indicate that O<sub>3</sub> exposure alters nutrient distribution within different parts of the wheat plant (Brewster et al., 2024). One of the primary reasons for this alteration is premature aging or early onset of senescence, a typical response of wheat to O<sub>3</sub> stress (Feng et al., 2024). This premature senescence, characterized by a shortened grain filling period, limits the time for carbon and nutrient translocation to the grains, thus reducing yields and nutritional quality (Feng et al., 2024).

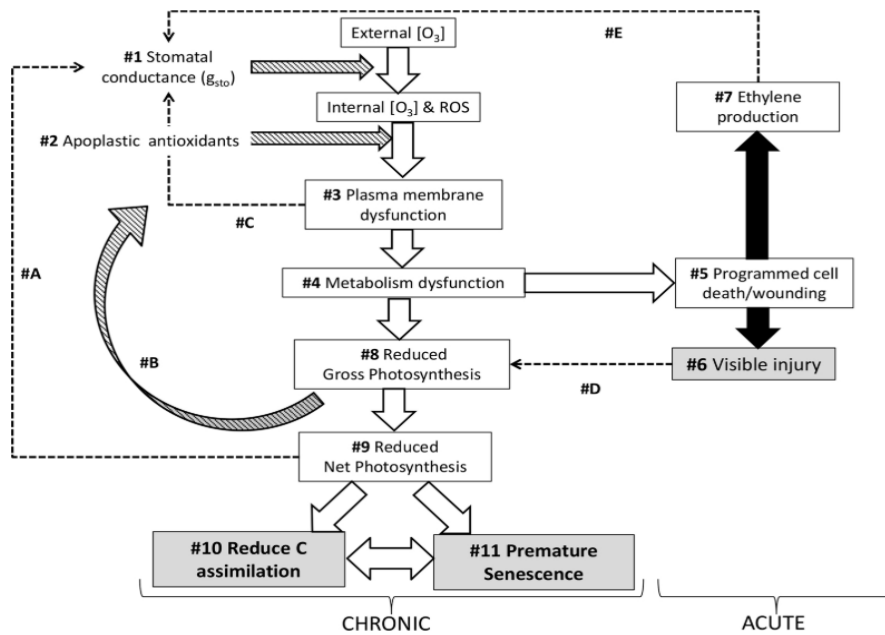
#### 1.4.4 Ozone effect on senescence

It has been proposed that the primary effect of O<sub>3</sub> on plants is the degradation of enzymes linked with advancing senescence (Feng et al., 2016; Feng et al., 2022). A prominent indicator of leaf aging is leaf yellowing, also known as chlorosis (Kittipornkul et al., 2021). While not always a part of the senescence process, yellowing can occur due to the bleaching of chlorophyll, even without senescence (Kittipornkul et al., 2021). Leaf senescence encompasses a variety of degradative processes beyond just chlorophyll breakdown and is marked by distinct shifts in metabolic activity, including changes in the activity of essential enzymes (Grandjean and Grandjean, 1989). Adverse growth conditions during the post-anthesis period can affect metabolic activity, potentially reducing the carbohydrate supply available for grain development and leading to earlier leaf senescence in crops like wheat (Buchner et al., 2015).

Research has shown that increased O<sub>3</sub> concentrations can lead to an earlier onset of leaf senescence (by approximately 20 days) compared to control or non-filtered treatments (Chen et al., 2020). Leaf aging is characterized by a significant decrease in chlorophyll content (evidenced by measurements of 'chlorophyll a' fluorescence), which indicates

reduced photochemical efficiency and quantum yield of Photosystem II under light conditions; accelerations in this process have been found as a consequence of growth under elevated O<sub>3</sub> levels, varying with the O<sub>3</sub> dose and type of crop species (Feng et al., 2011). Additionally, this acceleration in leaf aging is linked to alterations in protein content and metabolic activities, as identified in studies by (Heyneke et al., 2019; Feng et al., 2022). Commonly, senescence includes a reduction in Rubisco activity and other assimilatory enzymes coupled with a temporary rise in the activities of degradative enzymes. In this context, the activity of GDH (glutamate dehydrogenase) was monitored due to its known increase during senescence, which mainly relies on the de novo synthesis of at least one GDH protein (Liu et al., 2008). Findings indicate that the typical increase in GDH protein activity during senescence is evident and is especially significant in flag leaves exposed to higher levels of O<sub>3</sub> (Grandjean and Grandjean, 1989). Therefore, senescence accelerated by increased O<sub>3</sub> levels is marked by shifts in metabolic activities, potentially involving new protein synthesis. These findings support the notion that chronic O<sub>3</sub> exposure may reduce leaf lifespan in crops, a phenomenon also observed in various crop studies (Feng et al., 2011; Feng et al., 2022). O<sub>3</sub> has also been shown to impact the timing of flag leaf maturity, (Shi et al., 2009) observed an 8-day earlier maturation in elevated O<sub>3</sub> conditions (50% higher than ambient) compared to treatments with ambient O<sub>3</sub> levels.

Fig. 4. The mechanism by which ozone and its Reactive Oxidant Species (ROS) result in crop damage (Emberson et al., 2018). The figure depicts a complex interplay between ozone and its reactive derivatives with crop physiological processes, highlighting the dual nature of ozone-induced injuries: acute and chronic. It maps out the movement of ozone and its by-products (open arrows) and the plant's defensive responses (#1-11), alongside mechanisms possibly hindering ozone entry (hatched arrows). Feedback loops influencing stomatal conductance ( $g_{sto}$ ), critical in controlling ozone influx, are marked by dotted arrows (#A-E). This review encapsulates the intricate responses and adaptations of crops to ozone stress, underpinning the significance of understanding these interactions to mitigate the adverse impacts on crop vitality and yield.



### 1.5 Determinants of ozone sensitivity by plants

Research on different crop cultivars' sensitivity to O<sub>3</sub> has been conducted on a range of staple crops, including wheat (Feng et al., 2016), soybean (Chutteang et al., 2016), mung bean (Kittipornkul et al., 2021), and rice (Sinha et al., 2015). This has led to the categorization of cultivars into three distinct groups: tolerant, intermediate, and sensitive (Feng et al., 2016; Singh et al., 2018). A key factor in determining a crop and crop cultivars tolerance to O<sub>3</sub> is its genetic ability to maintain high ratios of ascorbate to dehydroascorbate enzymes (Yoshida et al., 2006). For instance, in wheat, the ability to endure O<sub>3</sub> stress is linked to reducing O<sub>3</sub> uptake through stomatal closure and, more crucially, sustaining carbon assimilation rates under such stress (Feng et al., 2022).

Interestingly, studies have shown that modern wheat cultivars tend to be more sensitive to O<sub>3</sub>, with an average yield reduction of 7-10% found for more recent cultivars grown in the northern hemisphere compared to old/ traditional wheat cultivars (which has (Brewster et al., 2019; Sarkar et al., 2021). The study Brewster et al., 2019 examined a high-yielding wheat variety named 'Skyfall' introduced in 2014 (*T. aestivum* L., cv. Skyfall), alongside an older variety named 'Maris Dove' that was released in 1971 (*T. aestivum* L., cv. Maris Dove). Their findings indicated that 'Maris Dove' exhibited a lower sensitivity to ozone compared to 'Skyfall'. Furthermore, 'Skyfall' was previously identified to be more susceptible to ozone damage than varieties introduced during the 1980s and 1990s, based on assessments of seed head biomass and the weight of a thousand grains. This increased sensitivity in newer cultivars has been primarily attributed to their

higher  $g_{sto}$ , which allows for greater O<sub>3</sub> uptake (Yadav et al., 2020). However, high  $g_{sto}$  is essential for high yield, making it a critical factor from an agronomic crop breeding perspective. Therefore, the focus needs to shift towards comparing modern high  $g_{sto}$  varieties to uncover alternative sources of tolerance that do not rely on restricting O<sub>3</sub> flux into leaves through lower  $g_{sto}$  (Biswas et al., 2008). This approach aims to balance the need for high productivity with the necessity of developing O<sub>3</sub>-resistant crop varieties.

Furthermore, the way crops are managed, including irrigation timing and planting to coincide with adequate rainfall, plays a significant role in modulating the impact of O<sub>3</sub> (Teixeira et al., 2011). Ozone's impact on crops accumulates throughout the growing season and can intensify during discrete O<sub>3</sub> episodes, often characterized by elevated O<sub>3</sub> levels during spring and summer (Feng et al., 2022). These episodes typically occur when climatic conditions conducive to O<sub>3</sub> formation coincide with significant emissions of O<sub>3</sub> precursors, as detailed by Wilkinson et al. (2012). This pattern underscores the complex interaction between crop management, environmental factors, and O<sub>3</sub> sensitivity, highlighting the need for a nuanced approach to agriculture in the face of changing atmospheric conditions (Wilkinson et al., 2012).

## 1.6 Approaches for modelling ozone exposure, uptake, and damage

To estimate the impact of O<sub>3</sub> on yield and other physiological characteristics, O<sub>3</sub> experimental studies and O<sub>3</sub> modelling-based risk assessment studies have been conducted, the latter for crops across large regions (e.g. national, regional, and global domains). These studies have tended to use concentration based O<sub>3</sub> exposure metrics Table 2 to characterise the levels of O<sub>3</sub> causing impacts on crops. These studies can be divided into experimental and model-based studies.

### 1.6.1 Experimental studies

- 1) Ethylene di-urea (EDU) studies involves crops being treated with EDU, which is a chemical protectant that reduces O<sub>3</sub> toxicity inside the plant. These studies provide data from which the relative yield of crop cultivars at different O<sub>3</sub> concentrations can be inferred. This can be used to define the sensitivity of different cultivars (see Table 2).
- 2) Open top chambers studies, which include a) filtration and b) fumigation methods, where plants are grown in chambers either provided with O<sub>3</sub>-filtered air with low or

negligible O<sub>3</sub> concentrations as compared to ambient conditions or with elevated O<sub>3</sub> compared to ambient conditions respectively (see Table 2).

3) Ozone - Free air concentration enrichment studies enabled the ozone exposure studies to be conducted in the field, thereby facilitating the dose-response relationships to be derived from the field experiments without the chamber's effect. The dose-response relationships for wheat can be utilised to forecast the effects of increased O<sub>3</sub> levels in China and India. FACE-Ozone presents a distinct chance for studying underlying mechanisms. By exposing the whole vegetation to elevated O<sub>3</sub> levels while maintaining the integrity of both the above and below-ground environments, it becomes possible to examine how plant processes react to O<sub>3</sub> as a component of the broader ecosystem responses (Kobayashi, 2015) (see Table 2).

Table 2. The table outlines 7 studies on the impact of ozone exposure on wheat cultivars conducted at different locations in China. Each study differs in its experimental setup, ranging from field experiments with ethylene diurene urea (EDU) treatments, open-top chamber (OTC)treatments, and free air ozone and carbon dioxide enrichment (FAOCE). These studies collectively highlight the varying sensitivity of wheat cultivars to ozone exposure and the significant potential for yield loss, underscoring the importance of considering ozone levels in agricultural management and breeding programs for ozone tolerance.

Reference	Study site	Experimental type, (growth period) -field/pot- ozone monitoring method	Year	Cultivar (data points)	M7/M12 Ozone concentration in ppb	AOT40 ppm h	Relative Yield loss (range shows for different cultivars)
Feng et al., 2018	XiaoTangShan town (40° 19' N, 116° 13' E), Changping District, Northwest of Beijing, China	Field; EDU, Ambient	2016	15 cultivars winter wheat	40-60ppb (hourly average for the experimental period)	0-17.4	6.5-40.2%
Wang et al., 2007	Shuangqiao Farm (31° 53'N, 121° 18'E) Jiaxing City, Zhejiang Province	Field; EDU, Ambient	2005	Yangmei 185		No data	12.7%
Feng et.al., 2003	Gucheng (39°08'N, 115°48'E)	Pot CF, NF, 50,100,200ppb	1999		No data	No data	4.7-58.6%
Wang et.al., 2012	Jiaxing (31°53'N, 121°18'E)	Field; 2006 ozone exposure is diurnal	2004, 2006, 2007, 2008	Yangmai185(2004-2005), Jia002(2006-2008);	No data	0-61.91,0-24.22,0-9.17,0-27.67 for	8.5-58% 40-73%

		Ozone 1 (75 or 100ppb) Ozone 2 (150-200ppb)				the year 2004 to 2008 in ppm h	
Tong et. Al.,2011	Changping (40°12'N, 116°08'E)	Field; NF, NF+30, NF+60, NF+90ppb	2010				
Zhu et al., 2011	Jiangsu (32°35'N, 119°42'E)	Open air O3 fumigation system-Field-Ozone analyser A-O3 E-O3- 50% higher than ambient	2007,2008,2009	Yannong 19 (Y19), Yangmai 16 (Y16), Yangmai 15 (Y15), Yangfumai 2 (Y2)	46.4,46,44 56.9,57.6,57.3	7.8,8.3,6.8 14.7,16.4 ,15.1	10.2-33.6 (loss relative to ambient)
Feng et al., 2012	Jiangsu (32°35'N, 119°42'E)	Open air O3 fumigation system-Field-Ozone analyser A-O3 E-O3- 50% higher than ambient	2006-2007, 2007-2008, 2008-2009 and 2009-2010	Yannong 19 (Y19), Yangmai 16 (Y16), Yangmai 15 (Y15), Yangfumai 2 (Y2) Datapoints: 24	No data	4.2-13pph	POD-20-58% AOT40-10-48%

## 1.6.2 Metrics of O<sub>3</sub> exposure

### 1.6.2.1 Concentration based metrics

Concentration-based metrics that have been commonly used to estimate O<sub>3</sub> responses are 1) M7 and 2) M12, 3) W126, 4) SUMO6, which were developed in North America, and 4) AOT40, which was developed in Europe (see Table 3). The AOT40 European metric is deemed more suitable to estimate the effects of moderate to high O<sub>3</sub> concentrations whereas the North American metrics are better suited to estimate the O<sub>3</sub> impact on crops at more chronic O<sub>3</sub> concentrations (Mauzerall and Wang, 2001). Other metrics developed are 5) the seasonal percentile metric, which is basically used to study the long-term variations of O<sub>3</sub> and avoids potential misinterpretation in a risk analysis using mean O<sub>3</sub> concentration (Avnery et al., 2011). All these metrics are well recognised and can help inform a precautionary approach to state the need for measures to control O<sub>3</sub> precursors, but they lack the ability to accurately estimate the impact of O<sub>3</sub> on crops as they assume that the plant is exposed to the same amount of O<sub>3</sub> concentration to which it is exposed in the atmosphere. This is not always the case, as certain environmental conditions, such as soil water stress, high temperature, and vapour pressure deficits, can lead to stomatal closure and decouple the levels of ambient O<sub>3</sub> concentration from the amount of stomatal O<sub>3</sub> uptake (Emberson et al., 2018).

These metrics can be defined as follows, and further details with references are provided in Table 3.

**M7 and M12 metrics:** These are mean concentration metrics that represent the average of the daily maximum 7-hour (M7) and 12-hour (M12) ozone concentrations over a specified period, usually during the growing season when crops are most sensitive to ozone damage. M7 and M12 are designed to capture the peak ozone levels that occur during daylight hours, which are most relevant for plant exposure (Mauzerell and Wang 2001).

**W126 metric:** This is a weighted cumulative exposure index used in the United States. The W126 index integrates all hourly ozone concentrations over a defined period (typically the growing season) but weights the concentrations so that higher levels have a disproportionately larger impact on the index. This weighting reflects the non-linear response of plant damage to ozone concentrations; higher ozone levels are more damaging than lower levels, even over the same exposure time (Mauzerell and Wang,

2001).

SUM06: This metric sums all hourly ozone concentrations above 0.06 parts per million (ppm) during daylight hours over the growing season. It is used to estimate the cumulative exposure of plants to ozone concentrations that are likely to cause damage. By focusing on higher ozone concentrations, the SUM06 metric aims to represent the potential for significant plant injury (Mauzerell and Wang, 2001).

AOT40 metrics: Developed in Europe, the AOT40 (Accumulated Ozone exposure over a Threshold of 40 parts per billion) metric sums all hourly ozone concentrations above 40 parts per billion (ppb) during the daylight hours (typically from 8:00 to 20:00 local time) over a specified period, which is often the growing season for crops. AOT40 is specifically designed to estimate the effects of moderate to high ozone concentrations on sensitive vegetation and is widely used in European ozone risk assessments (Mauzerell and Wang, 2001).

Seasonal percentile metrics: This metric looks at the distribution of ozone concentrations over a season and identifies a certain percentile (e.g., the 95th percentile) to assess ozone levels that occur less frequently but may have significant impacts. This approach helps in understanding long-term variations in ozone exposure and avoids potential misinterpretation that could arise from using mean ozone concentrations. It is particularly useful in risk analysis for evaluating the extremes of ozone exposure that are not captured by average-based metrics (Xu et al., 2008; Lefohn et al., 2018).

#### 1.6.2.3 Flux based metrics

To address this problem, the flux-based approach was developed, which assesses O<sub>3</sub> impacts based on the O<sub>3</sub> taken up through the stomates. The Deposition of Ozone for Stomatal Exchange (DO<sub>3</sub>SE) model was developed to estimate O<sub>3</sub> impacts on vegetation using this flux-based approach (Emberson et al., 2000). The DO<sub>3</sub>SE model has been incorporated into the European Monitoring and Evaluation Programme (EMEP) photo-oxidant CTM, which is used by the United Nations Economic Commission for Europe (UNECE) in their air pollution impact assessments (UNECE, 2017). DO<sub>3</sub>SE considers various resistances to O<sub>3</sub> deposition to a vegetated surface from an O<sub>3</sub> concentration at some height in the atmosphere. Resistances include a) Aerodynamic resistance, b) the quasi-laminar resistance above the canopy, c) the surface resistance, which further divides into stomatal and non-stomatal resistances. Non-stomatal resistance represents

canopy aerodynamic resistance and the soil resistance to decomposition to soil surface (Emberson et al., 2001). The stomatal resistance (the inverse of which is stomatal conductance) is calculated using a multiplicative  $g_{sto}$  approach (and used to estimate stomatal  $O_3$  flux to a representative leaf of the upper sunlit canopy Emberson et al., 2000). Accumulated stomatal  $O_3$  flux for a period over the course of the crop growing season has been found to be a useful metric to characterise the effect of  $O_3$  on crop yield losses (Danielsson et al., 2003; Pleijel et al., 2007). Flux-based (empirical) and concentration-based approaches have been used to develop dose-response relationships for the European region (Pleijel et al., 2007). These dose-response relationships provide a link between a pollutant dose and a crop response of concern and are ideally developed from coordinated standardised experimental trials (LRTAP, 2017). Such dose-response relationships have been used to define 'critical levels' of  $O_3$  (the level below which no statistically significant effect of  $O_3$  is expected to occur) (UNECE, 2017). Dose-response relationships can also be used in risk assessments to estimate crop yield losses across broad geographical regions (Emberson et al., 2018). The flux-based approaches are considered more biologically meaningful than the concentration-based approach (Mills et al., 2011, 2018) but still lack some detail on how crucial processes important in determining  $O_3$  impacts play out, which include: - 1) Detoxification of the incoming  $O_3$  flux in cell wall 2) the effect of  $O_3$  on carbon allocation patterns, mostly important for crops and trees.

#### 1.6.2.4 Mechanistic $A_{net}g_{sto}$ models

Building on this understanding, there has been a notable shift in the process of crop development, i.e., with the development of mechanistic  $A_{net}g_{sto}$  models, specifically tailored for wheat. This approach innovatively connects  $A_{net}$  a crucial determinant of plant development rate to  $g_{sto}$ . The strength of such models lies in their foundation in leaf physiology, enabling a more accurate estimation of  $O_3$  flux and its impact on crop yield (Schauberger et al., 2019). These models consider various environmental conditions, like light, temperature, and soil water, which are known to influence crop development, growth, and yield (Emberson et al., 2018).

Several models have delved into the interactive effects of  $O_3$  and climate variables. Notably, the LPJml model by (Schauberger et al., 2019), a process-based big leaf model,

stands out as the first to simulate the interactive effects of O<sub>3</sub> with temperature, water stress, phenology, and CO<sub>2</sub> on global wheat crops. The MCWLA-Wheat model by (Tao et al., 2017), more region-specific than LPJml and parametrized for eight Chinese provinces, assesses the interactive effects of climate change, O<sub>3</sub>, and CO<sub>2</sub> on crop growth and productivity. Additionally, the LINTULLC2 model, as researched by (Feng et al., 2022), focuses on the impact of ozone at the canopy level and has been parametrized for both sensitive and tolerant German wheat species.

Further progress in this study includes the development of the DO<sub>3</sub>SE-crop model, an adaptation of the DO<sub>3</sub>SE model's stomatal deposition component. This modification is crucial as it allows the model to simulate both CO<sub>2</sub> uptake for carbon assimilation and ozone uptake through the stomata. The UK JULES crop model, a part of the UK Earth System Model (UKESM), complements this by distributing assimilated carbon to various plant parts based on the crop's developmental stage. This model also factors in the impact of ozone on  $A_{net}$ , leaf senescence and the timing of crop maturity, employing algorithms from (Ewert and Porter, 2000). This integration is vital for comparing the UK JULES Crop model, based on (Sitch et al., 2007), with the alternate ozone damage mechanisms within DO<sub>3</sub>SE-crop. It plays a key role in assessing biogeochemical cycles, including ozone, between the atmosphere and the land surface. The development of the DO<sub>3</sub>SE-crop model encompasses various elements: phenology, processes at the leaf scale, scaling up to the canopy level, and carbon allocation. It has been calibrated and parametrized for European and 47 Chinese sites. Such models are capable of simulating key physiological variables, crop development, biomass, yield, and ozone deposition across canopy layers. Importantly, it facilitates the development of dose-response relationships and critical levels for regional scale risk assessments.

#### 1.6.2.5 Flux- response relationships

One of the primary applications of this model lies in its use for flux-response relationships. Currently, these relationships are often developed using an empirical approach, specifically the multiplicative  $g_{sto}$  model, as cited in the LRTAP Convention of 2017. This methodology is employed to calculate the stomatal O<sub>3</sub> flux for crops, particularly those grown in European filtration and fumigation experiments (Osborne et al., 2019). By utilizing these experimental datasets, it is possible to compute the accumulated stomatal O<sub>3</sub> flux (PODy) over a crop's growing season (Emberson et al., 2018). This flux can then be plotted against the relative yield loss observed under various

experimental ozone treatments (Emberson et al., 2018). From this, a response relationship can be derived, usually through statistical linear regression of these pooled data points, as indicated by research from (Pleijel et al., 2022). In Europe, specifically, the flux-response relationships for wheat have been established based on data gathered from four European countries (LRTAP, 2017). This data encompasses a period of nine years and includes observations from five different wheat cultivars, as documented in the LRTAP Convention of 2017.

However, there is a growing consensus that flux-response relationships developed using Mechanistic  $A_{net}g_{sto}$  models could be more beneficial (Emberson et al., 2018). These models are more closely aligned with the plant's primary physiological requirements for gas exchange (Schauberger et al., 2019). This includes the uptake of CO<sub>2</sub> for carbon assimilation through  $A_{net}$  and understanding the mechanisms of the ozone damage. Such an approach would likely provide a more accurate and meaningful basis for the development of flux-response relationships (Schauberger et al., 2019). By focusing on these mechanistic models, researchers can gain a deeper understanding of how environmental factors like O<sub>3</sub> impact crop health and productivity, leading to more effective strategies for crop management and protection.

Table 3. delineates various ozone metrics, their purposes, algorithms, and references, serving as a crucial tool for understanding and managing ozone concentrations in different environments. These metrics provide a robust scientific foundation for their application in environmental monitoring and policymaking.

Metrics	Purpose	Algorithms	References
AOT40 (12-h(8am-7pm) for growing season)	Suitable for moderate or high O <sub>3</sub> concentration	$AOT40 = \sum_{i=1}^n [C_{o3} - 40]_i$ for $[C_{o3}] \geq 40$ ppb, during daylight hours; units ppbh	Mauzerell and Wang 2001  Mapping Manual 2017
W126 (12-h weighted average for growing season)	Suitable for moderate or high O <sub>3</sub>	$W126 = \sum_{i=1}^n C_i * w_i$ where $w_i = 1 / (1 + 4403 * \exp(-0.126 * C_i))$ ; units ppbh	Mauzerell and Wang 2001

	concentration		
SUMO6 (	Suitable in urban areas where summer smog and O <sub>3</sub> -related health issues are more prevalent.	$SUM06 = \sum_{i=1}^n [C_{O_3}]_i$ for $[C_{O_3}] \geq 60$ ppb; units ppbh	Mauzerell and Wang 2001
Seasonal Percentiles (median, 5th, 25th, 75th, 95th, 98th, and 99th) of hourly average O <sub>3</sub> values	Used during summer		(Xu et al., 2008; Lefohn et al., 2018)
Daily 12-hand 7-h average for various months and daily periods	Suitable for low to moderate O <sub>3</sub> concentration	$M7, M12 = \frac{1}{n} \sum_{i=1}^n [C_{O_3}]_i$ From hours includes 0900 to 1559 h for M7 metrics; and 8:00-19:59 for M12 metrics	Mauzerell and Wang 2001

## 1.8 Policies

Various global regions have implemented diverse strategies to evaluate and mitigate the effects of O<sub>3</sub> on vegetation. These strategies typically encompass monitoring O<sub>3</sub> concentrations, establishing exposure limits, and enforcing measures to diminish O<sub>3</sub> pollution. To quantitatively evaluate the influence of ground-level O<sub>3</sub> on crops, different exposure-based metrics have been developed through use of data collected from open-

top field chamber (OTC) and free atmospheric concentration enrichment (FACE) experiments.

In Europe, the Convention on Long-Range Transboundary Air Pollution (LRTAP), initiated in 1979, has been pivotal in developing O<sub>3</sub> exposure indices (Pleijel et al., 2022). Initially, indices focused on averaging daylight hourly O<sub>3</sub> concentrations over a growing season (i.e., the M7 (7-hour) or M12 (12-hour) indices) (Mills et al., 2007). The LRTAP Convention later adopted the AOT40 index, which accumulates hourly O<sub>3</sub> concentrations that exceed 40 ppb during daylight hours over the growing season. This index was found to provide statistically robust predictions of changes in yield with changes in AOT40 (Mills et al., 2007). The M7 and M12 metrics still tend to be the preferred metrics for use in the United States. These metrics were in the US EPA's National Crop Loss Assessment Network (NCLAN) (Mauzerall and Wang, 2001).

Nevertheless, these methods have their shortcomings. Conventional O<sub>3</sub> indices, which rely on external ambient O<sub>3</sub> concentrations, are not always able to provide a true characterisation of O<sub>3</sub> damage (Schauberger et al., 2019). This is because plant responses to O<sub>3</sub> are more directly related to the internal concentration of O<sub>3</sub>, which is controlled by  $g_{sto}$  (Emberson et al., 2018). This insight led to the development of the flux-based metric—this new metric estimates the internal O<sub>3</sub> 'dose,' considering the environmental conditions that influence  $g_{sto}$  and hence stomatal O<sub>3</sub> uptake (Emberson et al., 2018). The flux-based approach has proven more adept at forecasting plant responses (Mills et al., 2011) and has been integrated into the chemical transport model used by the European Monitoring and Evaluation Programme (EMEP) (Simpson et al., 2012) so that regional scale estimates of stomatal O<sub>3</sub> uptake can be simulated.

Increasing harmful pollutants and environmental degradation have gained the government's attention in China (Li et al., 2020). The Ministry of Environment Protection developed a nationwide network to monitor urban and suburban air pollution, which has been operational since 2013 (Li et al., 2020). This network's data and the Tropospheric Ozone Assessment Report (TOAR) data have informed revisions to China's O<sub>3</sub> standards (Li et al., 2020). However, these standards focus on human health, with no specific standards set for vegetation (Li et al., 2020). Recent studies in Asia, including work on dose-response relationships for crops such as wheat, have tended to use AOT40 metrics but have highlighted the need for flux-response relationships and a standard critical limit for vegetation (Yadav et al., 2021; Feng et al., 2022).

Capturing the variation in O<sub>3</sub> sensitivity among different species and cultivars presents an additional challenge. Concentration-based indices like AOT40 can be adjusted for varying sensitivity levels by modifying the critical level below which adverse effects on different plant species would be expected to occur (Pleijel et al., 2022). By contrast, flux-based models can address this variation in species sensitivity to O<sub>3</sub> by applying species-specific maximum rates of  $g_{sto}$  and thresholds for hourly stomatal O<sub>3</sub> flux accumulation; such variations can be used to simulate the accumulated stomatal ozone flux above a threshold over the course of a growth period, resulting in the PODY metric (Yadav et al., 2021). Another approach, proposed by (Massman, 2004), combines estimated O<sub>3</sub> uptake through stomata with the plant's detoxification capability to produce the 'effective ozone dose.' However, modelling or estimating a plant's detoxification capacity remains a challenge (Paoletti et al., 2019).

These different metrics can be used to develop dose-response relationships. Once established, dose-response relationships can then be used to define Air Quality Standards (in Europe, these are referred to as 'Critical Levels') which provide a target for emission reductions in that achieving the AQG should eliminate any adverse effects of pollutant concentrations on vegetation (Emberson et al., 2018). Therefore, these air quality standards therefore aid policymakers in their efforts to reduce harmful emissions (Emberson et al., 2018). Exceedance of these AQG standards would be expected to oblige policymakers to develop local, regional, and national action plans to reduce emissions, targeting emission reductions to specific locations where AQGs are exceeded, therefore optimizing emission reductions according to an 'effects-based' approach (Emberson et al., 2018).

### 1.9 Aims and Objectives

In summary, there is substantial evidence that ground-level O<sub>3</sub> is causing damage to vegetation and in particular, sensitive crop species, affecting crop development, growth, and yield. It is also clear that the severity of such O<sub>3</sub> damage is dependent upon prevailing environmental conditions and other abiotic stresses (e.g., temperature and water stress) as well as the sensitivity of different cultivars to O<sub>3</sub> stress. Current O<sub>3</sub> concentrations remain high across many parts of Asia, and projections of likely emission trajectories would suggest that these O<sub>3</sub> concentrations may remain high in the coming decades. At the same time, climate change is also projected to cause stress on crop productivity, especially in relation to temperature and water stress. A key limitation of the

current concentration- or flux-based risk assessment models is that they are unable to incorporate the full effects of different abiotic stresses acting in combination. They are also limited in their ability to simulate O<sub>3</sub> damage outside the range of environmental conditions under which the data used to develop dose-response relationships have been collected. As such, there is a need to develop new approaches for O<sub>3</sub> risk and damage assessment that can provide additional information to optimise emission reduction efforts and potentially to identify adaptation options for agricultural management that might limit O<sub>3</sub> damage under a range of future abiotic stresses.

To date, flux-based methods have relied on multiplicative  $g_{sto}$  models, which are rather empirical by nature and require rather extensive parameterisation for different vegetation types (Osborne et al., 2019). Mechanistic  $A_{net}$ -based  $g_{sto}$  models ( $A_{net}g_{sto}$ ), could provide an alternative estimate stomatal ozone flux and at the same time provide a more direct relationship between O<sub>3</sub> uptake, carbon assimilation, allocation, and hence growth and yield as well as crop development. The development of robust  $A_{net}g_{sto}$  flux-response relationships could prove that this type of  $g_{sto}$  model is suitable for O<sub>3</sub> damage assessment and provide a segway to the development of photosynthetic-based crop modelling approaches that incorporate O<sub>3</sub> damage. Developing the DO<sub>3</sub>SE model (which has been used extensively for vegetation assessment in Europe) to incorporate such crop modelling approaches is also helpful since it incorporates important O<sub>3</sub> deposition terms (required to estimate canopy height concentrations from atmospheric chemistry output) and maintains a connection and ability to apply other approaches for O<sub>3</sub> risk assessment for comparative purposes.

Finally, given the threat that elevated O<sub>3</sub> concentrations pose in Asia, both currently as well as most likely into the future, it also makes sense to focus on the development and calibration of such a new crop modelling method for Chinese conditions.

Therefore, the overall aim of this PhD thesis is the development and application of the newly developed DO<sub>3</sub>SE-crop model to understand and predict ozone (O<sub>3</sub>) induced yield losses in crops, with a specific focus on Europe and China Agro-Ecological Zones. This involves a comprehensive evaluation of different stomatal conductance models ( $g_{sto}$  models) for their ability to develop robust dose-response relationships, the integration of these models with the JULES-Crop model to simulate site-specific ozone-induced yield loss, and the application of the integrated model across different agro-ecological zones in China to estimate yield losses due to ozone exposure.

In essence, the thesis aims to enhance the understanding of how ozone impacts crop yields and to provide a robust modelling framework that can be used to simulate these effects with high accuracy across diverse conditions. This could serve as a valuable tool for agricultural scientists, policymakers, and farmers for planning and mitigating the impacts of ozone on food production.

This PhD thesis, therefore, has the following research objectives: -

1. Can the  $A_{net}g_{sto}$  model be used to develop robust dose-response relationships?

This research question is addressed in Chapter 2, which compares the ability of three different  $g_{sto}$  models (i.e., the DO<sub>3</sub>SE multiplicative  $g_{sto}$  model ( $g_{sto}emp$ ), ii. an empirical  $A_{net}g_{sto}$  model ( $A_{net}g_{sto}emp$ ), and iii. a mechanistic  $A_{net}g_{sto}$  model ( $A_{net}g_{sto}mech$ ) to derive robust dose-response relationships. To evaluate model performance, we use a dataset which describes O<sub>3</sub>-induced yield losses for a number of cultivars, years and experimental fumigation sites across Europe.

2. Can the DO<sub>3</sub>SE model (including a mechanistic  $A_{net}g_{sto}$  model) be combined with the JULES Crop model to simulate site-specific O<sub>3</sub> induced yield loss in China.

This research question is addressed in Chapter 3, which describes the development, calibration, and evaluation of a new model, DO<sub>3</sub>SE-Crop. Development of this model involves bringing together the various aspects of DO<sub>3</sub>SE that are useful for both O<sub>3</sub> deposition and stomatal O<sub>3</sub> flux and interfacing the  $A_{net}g_{sto}$  models carbon assimilation with the JULES crop models carbon allocation algorithms, ensuring alignment of crop development.

3. Can DO<sub>3</sub>SE-Crop be applied across China to estimate O<sub>3</sub>-induced yield losses for different agro-ecological zones?

Chapter 4 addresses this research questions by describing the calibration of the DO<sub>3</sub>SE-Crop model for the main winter wheat-producing agro-ecological zones in China. Here, we focus on the effectiveness of methods to calibrate phenology and yield across China and use model results to understand potential climatic differences that might influence O<sub>3</sub> damage and the importance of cultivar sensitivity to yield loss estimates.

## 2. Ozone dose-response relationships for wheat can be derived using photosynthetic-based stomatal conductance models.

### 2.1 Abstract

Ground-level ozone ( $O_3$ ) pollution occurs across many important agricultural regions in Europe, North America, and Asia, negatively impacting  $O_3$ -sensitive crops such as wheat. Risk assessment methods to quantify the magnitude and spatial extent of  $O_3$  pollution have often used dose-response relationships. In Europe, the dose metrics used in these relationships have evolved from concentration- to flux-based metrics since stomatal ozone flux has been found to correlate better with yield losses. Estimates of  $g_{sto}$  have, to date, used an empirical multiplicative model. However, other more mechanistic approaches are available, namely the coupled photosynthetic-stomatal conductance ( $A_{net}g_{sto}$ ) model. This study used a European  $O_3$  OTC and solardome fumigation experimental dataset (comprising 7 cultivars, 4 countries, and 12 years) to develop a new flux-based dose-response relationship for wheat yield using the mechanistic  $A_{net}g_{sto}$  model ( $A_{net}g_{sto}mech$ ). The  $A_{net}g_{sto}mech$  model was found to be equally robust ( $R^2 = 0.82$ ) compared to the flux-response models derived from empirical  $g_{sto}$  models. In addition, the mechanistic  $A_{net}g_{sto}$  model was found to be better at predicting the effect of high  $O_3$  concentrations on diurnal and seasonal profiles of  $g_{sto}$  and  $A_{net}$ . It was also better able to simulate changes of up to, 7 and 12 days respectively, in the start (SOS) and end (EOS) of senescence, an important determinant of yield loss, over a range of  $O_3$  treatments. We conclude that mechanistic  $A_{net}g_{sto}$  models can be used to derive robust flux-response relationships.

## 2.2 Introduction

Empirical evidence from Europe, North America, and Asia shows that O<sub>3</sub> is causing a range of impacts on staple crops such as wheat (Hansen et al., 2019; Feng et al., 2022; Büker et al., 2015). These impacts include altered  $g_{sto}$  (Danielsson et al., 2003; Ghosh et al., 2020), reduced  $A_{net}$  (Ojanperä et al., 1998), and early and enhanced leaf senescence (Osborne et al., 2019; Gelang et al., 2000). Effects on leaf senescence can lead to a reduction in  $A_{net}$  and  $g_{sto}$  and a shorter grain-filling period (Gelang et al., 2000), thus decreasing yield (Pleijel et al., 2022) and biomass (Feng et al., 2021). Experimental meta-analyses have found that wheat yield losses can range from 3-50% when O<sub>3</sub> concentrations (described as a 7-hour daylight mean over the growing season) range from 5-115 ppb (Mills et al., 2018). Risk assessments performed on the application of dose-response relationships derived from such experimental data (Pleijel et al., 2007) estimate O<sub>3</sub>-induced yield losses of between 12 to 15 % globally, causing production losses of approximately 85 million tonnes (Mills et al., 2018). These losses in productivity are a cause for concern, given the importance of wheat as a staple crop for approximately 35% of the global population (Grote et al., 2021) and that the annual consumption of wheat worldwide is approximately 791 million tonnes (US Department of Agriculture, 2023). Evidence also suggests that the threat from O<sub>3</sub> pollution will continue into the future. Background O<sub>3</sub> concentrations have remained high over agriculturally important regions (Feng et al., 2019; Arnold et al., 2021; Boleti et al., 2020; Sicard et al., 2021) and in particular across Europe (Rega et al., 2020) and both background and peak O<sub>3</sub> are increasing in the Indo-Gangetic plains in south Asia (Shah et al., 2019), and the North China Plain in East Asia (Liu et al., 2016). Therefore, to estimate the threat from O<sub>3</sub> pollution, risk assessment modelling methods have been developed to assess the current and future effects of O<sub>3</sub> on crop growth and yield at national, regional, and global scales (Emberson et al., 2018). These methods often use experimental O<sub>3</sub> filtration/fumigation data to derive dose-response relationships and hence require the identification of a suitable dose metric capable of predicting O<sub>3</sub> damage (i.e., yield loss for crops). Metrics would ideally be able to incorporate the effects of species and cultivars as well as management practices (e.g., irrigation) that are known to alter sensitivity to O<sub>3</sub> pollution (Mills et al., 2018; Anav et al., 2016; Osborne et al., 2019). Metrics have evolved over the past decade, moving from concentration- to flux-based indices (Grulke and Heath, 2019; Pleijel et al., 2007; Mills et al., 2018) with the flux-based approach allowing O<sub>3</sub>

concentrations to be decoupled from O<sub>3</sub> exposure when conditions (e.g., high atmospheric or soil water deficits) limit stomatal O<sub>3</sub> uptake (Emberson et al., 2018; Tai et al., 2021) This capability of the flux-based approach has been shown to give more reliable estimates of the spatial extent of O<sub>3</sub> damage (Mills et al., 2011).

Consequently, the stomatal O<sub>3</sub> flux metric, denoted as Phytotoxic Ozone Dose (PODy), has been adopted by the UNECE Convention on Long-Range Transboundary Air Pollution (LRTAP) to develop dose-response relationships for the derivation of 'critical levels' for Europe; these are levels below which crop damage would not be expected to occur according to current knowledge (LRTAP Convention, 2017). These 'critical levels' have been used to establish national and regional air quality standards for the formulation of emission reduction policy (Massman et al., 2000; Emberson et al., 2000; Mills et al., 2011). Current flux-response relationships have been developed using an empirical multiplicative  $g_{sto}$  model (LRTAP Convention, 2017), a component of the DO<sub>3</sub>SE O<sub>3</sub> deposition model used in European scale modelling (Simpson et al., 2012) to calculate stomatal O<sub>3</sub> flux for crops grown in European filtration/fumigation experiments. This approach datasets allow accumulated stomatal O<sub>3</sub> flux (PODy) to be calculated over a growing season and plotted against relative yield loss for a range of experimental O<sub>3</sub> treatments. A response relationship can then be derived from statistical linear regression of these pooled data points (Pleijel et al., 2022). In Europe, flux-response relationships for wheat are based on data from 4 European countries, encompassing 14 years and 6 cultivars (LRTAP Convention, 2017).

An important criticism and limitation of existing flux-response relationships is that the estimate of  $g_{sto}$  is not related to the plant's main physiological requirement for gas exchange, which is the uptake of CO<sub>2</sub> for carbon assimilation by  $A_{net}$ . This creates a disconnect between O<sub>3</sub> stomatal uptake and critical physiological processes such as  $A_{net}$ , respiration, carbon accumulation and allocation, development, growth, and yield (Wang et al., 2009). Stomatal conductance models coupled to  $A_{net}$  were developed in the early 1990s (Leuning et al., 1995) and worked on a supply and demand basis whereby  $g_{sto}$  is determined according to the requirement of CO<sub>2</sub> for  $A_{net}$ . These models are more complex than the empirical multiplicative  $g_{sto}$  model since they require an estimate of  $A_{net}$ , which often involves applying a biochemical model to simulate plant physiological processes (Büker et al., 2007; Op De Beeck et al., 2010). However, using a multiplicative model requires more parameters and cannot consider the interaction of different

environmental variables at the same time. Using an  $A_{net}g_{sto}$  approach would also allow a more mechanistic representation of  $O_3$  effects on growth and yield to be explored (Emberson et al., 2018; B ker et al., 2007). This is important as  $O_3$  is thought to cause damage via both an instantaneous effect on  $A_{net}$  as well as a longer-term effect that induces early onset senescence, which may lead to earlier maturity and a shorter time period for grain filling (Ewert and Porter, 2000; Emberson et al., 2018).

In this chapter, we develop leaf-level  $A_{net}g_{sto}$  models suitable for quantifying stomatal  $O_3$  flux. The aims of this paper are (i) to assess the ability of the multiplicative  $g_{sto}$  ( $g_{sto}emp$ ),  $A_{net}g_{sto}$  models (an empirical  $A_{net}g_{sto}$  model ( $A_{net}g_{sto}emp$ ) and a mechanistic  $A_{net}g_{sto}$  model ( $A_{net}g_{sto}mech$ )) to simulate  $g_{sto}$  (and  $A_{net}$ ), (ii) to assess the ability of  $A_{net}g_{sto}$  models to simulate  $O_3$  damage to  $A_{net}$  and leaf senescence, and (iii) to compare the ability of ( $g_{sto}emp$ ) and  $A_{net}g_{sto}$  models to simulate yield loss and hence derive flux-response relationships. This will be achieved by re-analysis of the European wheat flux-response data used to derive the current UNECE LRTAP Convention flux response relationship (LRTAP Convention, 2017) along with additional data from the UK and Sweden, which provide further insight into the effects of  $O_3$  concentrations on leaf physiology and senescence. The three models described above were not designed to simulate dynamic crop growth or yield over time; rather, they simply associated the fluxes of ozone with the yields that were observed. However, they were tested with observed  $A_{net}$ ,  $g_{sto}$ , and Chlorophyll Content Index (CCI) data.

## 2.3 Methods

### 2.3.1 Stomatal conductance ( $g_{sto}$ ) models

#### 2.3.1.1 $g_{sto}emp$ model

The  $g_{sto}emp$  model is an empirical model that estimates  $g_{sto}$  according to environmental modifications to a species-specific maximum stomatal conductance value ( $g_{max}$ ) (Jarvis, 1976; Emberson et al., 2000; Pleijel et al., 2007) written as:

$$g_{sto} = g_{max} \cdot [min(leaf\ f_{phen}, f_{O_3}) \cdot f_{light} \cdot max\{f_{min}, (f_{temp} \cdot f_{VPD} \cdot f_{SWP})\}] \quad \text{Eq. 1}$$

Where  $g_{sto}$  is the flag leaf stomatal conductance ( $\text{mmol O}_3 \text{ m}^{-2} \text{ PLA s}^{-1}$  where PLA is the sunlit projected leaf area) and  $g_{max}$  is the species-specific maximum  $g_{sto}$ . The parameters  $leaf\ f_{phen}$ ,  $f_{O_3}$ ,  $f_{light}$ ,  $f_{temp}$ ,  $f_{VPD}$ , and  $f_{SWP}$  account for the effect of phenology,  $\text{O}_3$ , light, temperature, vapour pressure deficit (VPD), and soil water potential (SWP) on  $g_{max}$ .  $f_{min}$  is the fractional minimal daylight  $g_{sto}$ . These functions these functions can have values ranging from 0 to 1. Since wheat grown in the filtration/fumigation studies was always well-watered, we assume that  $f_{SWP}$  equals 1. The  $\text{DO}_3\text{SE}$  algorithms and parameters for these functions are described in Eq. SI. 1- Eq. SI. 5 and Table. SI. 3, respectively, after the (Grünhage et al., 2012) and LRTAP Convention (2017). Graphical representation of these factors is also shown in Fig. SI. 2. a-e.

#### 2.3.1.2 $A_{net}g_{sto}emp$ model

The coupled  $A_{net}g_{sto}emp$  model provides a consistent estimate of the exchange of  $\text{CO}_2$  (driven by supply and demand of  $\text{CO}_2$  for  $A_{net}$  and its products) on consideration of water loss controlled by  $g_{sto}$ . The  $A_{net}g_{sto}emp$  model consists of a combination of two separate models: a) the mechanistic and biochemical  $A_{net}$  model (Farquhar et al., 1980; Harley et al., 1992) that estimates net  $A_{net}$ , and b) the coupled  $A_{net}-g_{sto}$  model (Leuning, 1995) that estimates  $g_{sto}$ .

The  $A_{net}$  model assumes that  $A_{net}$  is limited, according to prevailing environmental conditions, by three different mechanisms: i. rubisco activity ( $A_c$ ); ii. the regeneration of ribulose-1,5-bisphosphate (RuBP), which is limited by the rate of electron transport ( $A_j$ ) and iii. the rate of transport of photosynthetic products ( $A_p$ ) (Sharkey et al., 2007). These influences on  $A_{net}$  are calculated by determination of the smaller of these theoretical  $\text{CO}_2$  assimilation rates less the rate of dark respiration ( $R_d$ ) (Harley et al., 1992), see Eq. 2-Eq. 6.

$$A_{net} = \min(A_c, A_j, A_p) - R_d \quad \text{Eq. 2}$$

Where,

$$A_c = \frac{(C_i - \Gamma^*) \cdot V_{cmax25} \cdot f_{O_3} \cdot leaf\ f_{phen}}{C_i + K_c \left(1 + \frac{O_i}{K_o}\right)} \quad \text{Eq.3}$$

$$A_j = J \cdot \frac{C_i - \Gamma^*}{a \cdot C_i + b \cdot \Gamma^*} \quad \text{Eq.4}$$

$$A_p = 0.5 \cdot V_{cmax25} \quad \text{Eq. 5}$$

Where  $V_{cmax25}$  is the maximum rate of RuBP carboxylation catalysed by the enzyme Rubisco at 25°C (leaf temperature),  $C_i$  and  $O_i$  are the intercellular CO<sub>2</sub> and O<sub>2</sub> concentrations respectively;  $K_c$  and  $K_o$  are the Rubisco Michaelis-Menten constants for CO<sub>2</sub> and O<sub>2</sub> respectively;  $\Gamma^*$  is the CO<sub>2</sub> compensation point in the absence of respiration.  $J$  is the electron transport rate, which increases linearly with incident photosynthetically active photon flux density ( $Q$ ,  $\mu\text{mol}/\text{m}^2/\text{s}$ ) until light saturation is reached, beyond which  $J$  approaches a maximum value known as  $J_{max}$ . In the photosynthetic model by Sharkey et al. (2007), the parameters 'a' and 'b' reflect conservative estimates for the electron transport rate during carboxylation and oxygenation, assumed to be 4 and 8 electrons respectively, which are pivotal for the regeneration of RuBP and consequently impact the formation of NADPH and ATP in the Calvin cycle (Sharkey et al., 2007).  $A_c$  is modified to include  $f_{O_3}$  and  $leaf\ f_{phen}$  to empirically define the effect of leaf age and O<sub>3</sub> induced senescence on  $g_{sto}$  (Ewert, Van Oijen and Porter, 1999). This allows  $V_{cmax25}$  to change throughout the growing season. Since O<sub>3</sub> primarily causes a limitation to Rubisco we do not include O<sub>3</sub> damage in estimates of  $A_j$  and  $A_p$ .

$g_{sto}$  is calculated from  $A_{net}$  using an empirical relationship between  $g_{sto}$ ,  $A_{net}$  and environmental variables following an approach first developed by (Ball et al., 1987) and modified by Leuning (1995) as described in Eq. 6.

$$g_{sto} = [f_{min} + m \cdot A_{net} \cdot f_{VPD} / (c_s - \Gamma)] \quad \text{Eq. 6}$$

Where  $f_{min}$  is the minimal daylight  $g_{sto}$  value (Leuning, 1995). The parameter  $m$  describes the sensitivity of  $g_{sto}$  to the carbon assimilation rate accounting for atmospheric water status (determined according to  $VPD$ ) and CO<sub>2</sub> concentration at the leaf surface.  $c_s$  is the CO<sub>2</sub> concentration at the leaf surface and  $\Gamma$  is the CO<sub>2</sub> compensation point and  $C_s$  is the humidity deficit. The use of the multiplicative  $g_{sto}$

models  $f_{VPD}$  relationship (Danielsson et al., 2003; Pleijel et al., 2007; LRTAP Convention, 2017) ensures consistency between the  $g_{stoemp}$  and  $A_{netg_{stoemp}}$  modelling methods used in this study see equation Eq. 7

$$f_{VPD} = \left(1 + \left(\frac{VPD}{VPD_0}\right)^8\right)^{-1} \quad \text{Eq. 7}$$

where  $VPD_0$  is the VPD threshold parameterised to reflect a more gradual decrease in  $g_{sto}$  with increasing VPD of the  $f_{VPD}$  relationship compared to that previously suggested by Leuning's (1995) hyperbolic function (Fig. Sl. 1).

### 2.3.3.3 $A_{netg_{sto}mech}$ model

The  $A_{netg_{sto}mech}$  model simulates the loss of instantaneous photosynthetic activity and the acceleration of leaf senescence using a mechanistic approach to modify the Rubisco-limited rate of photosynthesis ( $A_c$ ) following the approach of Ewert & Porter (2000) as described in Eq. 8

$$A_c = \frac{(C_i - \Gamma^*) \cdot V_{cmax} \cdot f_{O_{3,s}}(d) \cdot f_{LS}}{C_i + K_c \left(1 + \frac{\theta_i}{K_o}\right)} \quad \text{Eq. 8}$$

The short-term impact of  $O_3$  on  $A_c$  is calculated according to the  $f_{O_{3,s}}(d)$  term, the cumulative daylight hour effect of  $O_3$  on  $V_{cmax}$ , which allows for an instantaneous effect of  $O_3$  on  $A_{net}$  when stomatal  $O_3$  flux overwhelms detoxification and repair mechanisms (Betzberger et al., 2012; Feng et al., 2022).  $f_{O_{3,s}}(d)$  is estimated by calculating  $f_{O_{3,s}}(h)$  (representing the linear relationship between stomatal  $O_3$  flux ( $f_{st}$ )) and a decrease in  $A_c$  calculated for every hour as described in Eq. 9

$$\begin{aligned} f_{O_{3,s}}(h) &= 1; & \text{for } f_{st} &\leq \frac{\gamma_1}{\gamma_2} \\ f_{O_{3,s}}(h) &= 1 + \gamma_1 - \gamma_2 * f_{st} & \text{for } \frac{\gamma_1}{\gamma_2} &< f_{st} < \frac{1+\gamma_1}{\gamma_2} \\ f_{O_{3,s}}(h) &= 0; & \text{for } f_{st} &\geq \frac{1+\gamma_1}{\gamma_2} \end{aligned} \quad \text{Eq. 9}$$

where  $\gamma_1$  and  $\gamma_2$  are both short-term  $O_3$  damage coefficients, with  $\frac{\gamma_1}{\gamma_2}$  representing the  $O_3$  detoxification threshold below which no damage occurs to the photosynthetic system and  $\gamma_2$  determining the effect of  $f_{st}$  on  $A_c$ ;  $f_{O_{3,s}}(d)$  and  $f_{O_{3,s}}(d - 1)$  are calculated as described in Eq. 10

$$f_{O_{3,s}}(d) = f_{O_{3,s}}(h) * r_{O_{3,s}} \quad \text{for } PAR \leq 50 \mu\text{mol}/\text{m}^2/\text{s}$$

$$f_{O3,s}(d) = f_{O3,s}(h) * f_{O3,s}(d - 1) \quad \text{for } PAR > 50\mu\text{mol}/\text{m}^2/\text{s} \quad \text{Eq. 10}$$

where  $r_{O3,s}$  represents incomplete recovery from  $f_{st}$  overnight which depends on leaf age according to equation Eq. 11

$$r_{O3,s} = f_{O3,s}(d - 1) + (1 - f_{O3,s}(d - 1)) * f_{LA} \quad \text{Eq. 11}$$

Where  $f_{LA}$  defines leaf age and calculated as

$$\begin{aligned} f_{LA} &= 1; & \text{for } TT_{leaf} \leq tl, em \\ f_{LA} &= 1 - \frac{(tl - tl_{em})}{tl_{ma}}; & \text{for } tl, em < TT_{leaf} < tl \\ f_{LA} &= 0; & \text{for } TT_{leaf} \geq tl \end{aligned} \quad \text{Eq. 12}$$

The long-term impact of  $O_3$  on  $V_{C_{max25}}$  represented by the  $f_{LS}$  term represents the longer-term accumulation of stomatal  $O_3$  flux ( $acc_{fst}$ ) causing degradation to the Rubisco enzyme triggering early and enhanced senescence of mature leaves (Gelang et al., 2000; Osborne et al., 2019). The simulation of  $f_{LS}$  (and  $f_{LA}$  used in the short-term  $O_3$  effect) are related to thermal time defined periods over the course of the flag leaf life span defined as a mature ( $tl, ep$ ) and a senescing ( $tl, se$ ) stage which together comprise  $tl, ma$ , the full flag leaf life span equivalent to  $leafphen$  in the empirical models. The  $tl, ep$  stage defines the period between the start of anthesis and start of senescence (SOS). The  $tl, se$  stage simulates an abrupt decline in chlorophyll content and depicts the period between SOS and end of senescence (EOS). See 2.3.4 for the description of the SOS and EOS calculation.  $TT_{leaf}$  represents the cumulative thermal time, which varies on a daily basis. This value is determined by taking the mean of the temperature recorded hourly over a 24-hour period and then integrating it with the thermal time accumulated up to the previous day.

See Eq. SI. 5-Eq. SI. 6 for  $leafphen$  and  $tl, ma$  equations and Fig. SI. 3 to see the relationship between  $leafphen$ ,  $f_{LS}$  and  $f_{LA}$ . The  $O_3$  effect on  $f_{LS}$  is first simulated by estimating a weighted accumulated  $f_{st}$  ( $f_{O3,l}$ ) modified from Ewert and Porter (2000) by:

$$f_{O3,l} = 1 - \max(\min(\gamma_3 * acc_{fst}, 1), 0) \quad \text{Eq. 13}$$

where  $\gamma_3$  determines the reduction in  $tl, ma$  as  $acc_{fst}$  (in  $\mu\text{mol m}^{-2}$ ) increases. The SOS is determined by  $\gamma_4$ , with  $\gamma_5$  which determining maturity (or EOS),

$$tl_{epO_3} = tl_{ep} * (1 - ((1 - fO3_l) * \gamma4))$$

$$tl_{seO_3} = tl_{se} * (1 - ((1 - fO3_l) * \gamma5)) + zc \quad \text{Eq. 14}$$

$$zc = tl_{ep} - tl_{epO_3}$$

Where,  $tl_{epO_3}$  is  $tl_{ep}$  with an  $O_3$  effect which may bring senescence earlier, and  $tl_{seO_3}$  is  $tl_{se}$  with an  $O_3$  effect which may bring maturity earlier.  $f_{Ls}$  is estimated by,

$$f_{Ls} = 1; \quad \text{for } TT_{leaf} < tl, em + tl, ep$$

$$f_{Ls} = 1 - \frac{TT_{leaf} - tl_{em} - tl_{epO_3}}{tl_{seO_3}}; \quad \text{for } tl, em + tl, ep < TT_{leaf} < tl \quad \text{Eq. 15}$$

$$f_{Ls} = 0; \quad \text{for } TT_{leaf} \geq tl$$

### 2.3.2 Estimation of $O_3$ uptake ( $f_{st}$ ) and **PODy**

For all models used in this study  $f_{st}$  (in nmol  $O_3$  PLA  $m^{-2} s^{-1}$ ) are calculated as a function of  $O_3$  concentration at the leaf boundary layer,  $g_{sto}$ , and  $O_3$  deposition to the external leaf surface (see equations Eq. 16, Eq. 17, Eq. 18 following the LRTAP Convention (2017)).

$$f_{st} = [O_3] * (g_{sto}) * \left( \frac{leaf_{rc}}{(leaf_{rb} + leaf_{rc})} \right) \quad \text{Eq. 16}$$

$$leaf_{rb} = 1.3 * 150 * \text{sqrt} \left( \frac{Lm}{uh} \right) \quad \text{Eq. 17}$$

$$leaf_{rc} = leaf_{rc} = \frac{1}{(g_{sto} + g_{sto_{ext}})} \quad \text{Eq. 18}$$

Where  $O_3$  is the  $O_3$  concentration at the upper surface of the quasi-laminar boundary layer of the flag leaf (nmol/mol),  $g_{sto_l}$  is leaf stomatal conductance (m/s) as described in equation 6,  $leaf_{rb}$  is the quasi laminar leaf boundary layer resistance (s/m),  $Lm$  is the cross wind leaf dimension (m),  $uh$  is the windspeed at the canopy surface (m/s),  $leaf_{rc}$  is leaf surface resistance (s/m),  $g_{ext}$  is the external plant cuticle conductance (s/m). Here we assume that the  $O_3$  concentrations measured within the field chambers of the filtration/fumigation experiments represent a reasonable estimate of  $O_3$  at the leaf boundary layer due to the enhanced air circulation. Parameters value provided Table. Sl. 4.

This study uses the  $POD_y$  stomatal flux-based index currently used by the UNECE LRTAP Convention (2017) to assess damage to European wheat calculated using a  $y$  threshold value of  $6 \text{ nmol O}_3 \text{ m}^{-2} \text{ PLA s}^{-1}$  according to Eq. 19 for all three models.

$$POD_6 = \sum_{i=1}^n [f_{sti} - y] * \left( \frac{3600}{10^6} \right); \text{ for } f_{sti} \geq y \text{ nmol m}^2 \text{ PLA s}^{-1} \quad \text{Eq. 19}$$

where  $f_{sti}$  is the hourly mean  $\text{O}_3$  flux in  $\text{nmol O}_3 \text{ m}^{-2} \text{ PLA s}^{-1}$  (see equation [14]) and  $n$  is the number of hours within the accumulation period.  $y$  (equivalent to  $y \frac{y^1}{y^2}$ ), which is equal to  $6 \text{ (nmol m}^{-2} \text{ PLA s}^{-1})$  and is subtracted from each hourly averaged  $f_{st}$  ( $\text{nmol O}_3 \text{ m}^{-2} \text{ PLA s}^{-1}$ ) value only, when  $f_{st} > y$ , during daylight hours (when  $\text{PAR} > 50 \text{ W m}^{-2}$ ). The term  $(3600/10^6)$  converts to hourly fluxes and to  $\text{mmol O}_3 \text{ m}^{-2} \text{ PLA}$ .

### 2.3.3. Datasets

The  $g_{sto}$  models were applied to simulate  $POD_6$  for  $\text{O}_3$  filtration/fumigation experimental datasets conducted since the 1980s in Europe that described wheat yield losses due to different  $\text{O}_3$  treatments. These datasets represent 4 countries (Belgium, Sweden, Finland, and United Kingdom) 7 cultivars, and 12 years. These are predominantly the same data used to derive the UNECE LRTAP flux-response relationships (LRTAP Convention, 2017), exceptions being the exclusion of an Italian dataset due to experiments not being performed on the flag leaf), and the inclusion of new data from the UK and Sweden which have the benefit of also providing important physiological and chlorophyll content data. A detailed description of these datasets is given in the Table. SI. 1.

### 2.3.4 Parameterisation for the $g_{sto}$ models

The  $g_{stoemp}$  model uses the same parameters as described in the LRTAP Convention, 2017. Full details are provided in Table. SI. 3.

Both the  $A_{net}g_{stoemp}$  and  $A_{net}g_{stomech}$  models require parameterisation of  $V_{cmax25}$ ,  $J_{max25}$  and  $m$ . Parameters, such as  $fmin$ , representing the minimum stomatal conductance (set at  $0.01 \text{ } \mu\text{mol CO}_2 \text{ m}^{-2} \text{ s}^{-1}$ ), are sourced from (Ewert and Porter, 2000), while  $VPD_0$  (set at  $2.2 \text{ kPa}$  and detailed in section 2.3) are determined empirically.

However, the  $A_{net}g_{stomech}$  model also needs extra parameters for the damage module (represented by  $\gamma$  coefficients). On the other hand, the  $A_{net}g_{stoemp}$  model employs the

same  $f_{O_3}$  function as the multiplicative  $g_{sto}$  model for estimating ozone damage, without the need for calibration.

A systematic literature review was conducted to extract data to define the likely range and initial values (range mean) of  $V_{cmax25}$ ,  $J_{max25}$  and  $m$  values occurring in wheat across Europe, this approach is similar to that used to parameterise the  $g_{stoemp}$  model (LRTAP Coonvention,2017).  $V_{cmax25}$  and  $J_{max25}$  values were recorded for fully developed flag leaves growing under ambient atmospheric concentrations of  $O_3$  and  $CO_2$  for crops grown in the field/or large pots under a stress-free environment (see, Fig. SI. 4). Information describing the bio-geographic region and the prevalence of rainfed or irrigated management were also recorded (Fig. SI. 5). A diagrammatic representation of the systematic literature review is provided in Fig. SI. 6.

The parameterisation of  $m$  needs to be considered in relation to  $VPD_0$  since the slope of the relationship  $m$  found when plotting  $A_{net}$  against  $g_{sto}$  represents a compromise between the cost and benefit of  $g_{sto}$  relative to  $CO_2$  uptake for  $A_{net}$  vs. water loss affecting intrinsic water use efficiency (Medlyn et al., 2011). Here, the approach of Medlyn et al. (2011) was followed and calibrate  $m$  to ensure that the modelled maximum  $A_{net}$  against  $g_{sto}$  aligns accurately with the maximum observed  $A_{net}$  against  $g_{sto}$  values.

The parameters  $\gamma_3$ ,  $\gamma_4$ , and  $\gamma_5$  are exclusively utilised in the  $A_{net}g_{sto}mech$  damage module to simulate the rate of senescence. They were calibrated to ensure that the start and end of the senescence period matched observed senescence timings. These observations were derived from data describing the Chlorophyll Content Index (CCI) using the 'break point' analysis method (Mariën et al., 2019). This method determines the change in the seasonal pattern of the CCI (and hence senescence) as a function of day of the year through piecewise linear regressions. The first segment of the regression (i.e., leaf expansion to mid-anthesis) was constrained to zero since it is assumed the leaf does not undergo senescence during this period. The slope of the second segment (from mid-anthesis to harvest) was allowed to be greater than zero on the assumption that the senescence of the flag leaf will only occur after mid-anthesis. The slope with the lowest RMSE, indicating the smallest deviation between the measured CCI data points and the values estimated by the piecewise linear regression model, was assumed as the breakpoint for the SOS. Furthermore, a polynomial regression line, which delineates the period of senescence, was employed to determine the end of the season (EOS), as depicted in Fig. SI. 7. The SOS and EOS of the flag leaf determined from breakpoint

analysis of the UK (2015) and Swedish (1997 and 1999) datasets are given in the Table. SI. 5. The SOS and EOS of the flag leaf determined from break-point analysis of the UK (Mulika and Skyfall,2015) and Swedish (Dragon,1997 and 1999) datasets

Details of the initial values and the associated ranges for calibration of all  $A_{net}g_{sto}$  parameters are provided in Table 4.

Table 4. presents a detailed overview of the parameters, ranges and optimised values after calibration that are employed in calibrating  $A_{net}g_{sto}$  models, which are critical in understanding plant physiological responses.

Parameters	Description	Units	Initial Parameter	Range	Parameters used (This study)	Reference
$V_{cmax25}$	Maximum catalytic rate at 25°C	$\mu\text{mol CO}_2 \text{ m}^{-2} \text{ s}^{-1}$	90	60-180	88.91	(Büker et al., 2007) systematic literature review (this study)
$J_{max25}$	Maximum rate of electron transport at 25°C	$\mu\text{mol CO}_2 \text{ m}^{-2} \text{ s}^{-1}$	180	150-250	173.83	
$m$	Species-specific sensitivity to $A_{net}$	-	7	5-15	7.87	(Kosugi et al., 2003; Collatz et al., 1991; Baldocchi and Meyers, 1998; Miner et al., 2017)
$\gamma_1 *$	Short term $\text{O}_3$ impact coefficient	$\text{nmol O}_3 \text{ m}^{-2} \text{ s}^{-1}$	0.027	-	0.027	Ewert & Porter (2000)
$\gamma_2 *$	Short term $\text{O}_3$ impact coefficient		0.0045	-	0.0045	

$\gamma_3^*$	Long term O <sub>3</sub> impact coefficient	(nmol O <sub>3</sub> m <sup>-2</sup> s <sup>-1</sup> ) <sup>-1</sup>	0.1	0.1-0.7	0.11	Break point method (this study, see 2.3.4)
$\gamma_4^*$	Long term O <sub>3</sub> impact coefficient	( $\mu$ mol O <sub>3</sub> m <sup>-2</sup> ) <sup>-1</sup>	0.1	0.1-0.5	0.16	
$\gamma_5^*$	Long term O <sub>3</sub> impact coefficient		0.1	0.1-0.5	0.44	

\* $\gamma$  parameters only used for  $A_{net}g_{sto} + O_3 mech$

In constructing the  $A_{net}g_{sto}mech$  model, meticulous calibration has been applied to both the leaf physiological and ozone-related parameters. This comprehensive approach to calibration gives the model with the potential for enhanced precision and reliability in its analytical capabilities, mainly when applied to the datasets introduced in this investigation, notably the novel Bangor datasets from 2015 and 2016. Consequently, this refined calibration methodology is posited to confer a superior operational performance on the  $A_{net}g_{sto}mech$  model in comparison to its counterparts, the  $A_{net}g_{sto}emp$  model—which has undergone calibration solely in the context of leaf physiological parameters—and the  $g_{sto}emp$  models. In contrast, the calibration of the  $g_{sto}emp$  model and the ozone module within the  $A_{net}g_{sto}emp$  model adheres to the parameters delineated in the LRTAP 2017 framework. 2.3.5 Calibration of the  $A_{net}g_{sto}emp$  and  $A_{net}g_{sto}mech$  models

The parameters for the multiplicative model were applied as outlined in the LRTAP Convention, 2017, indicating that the model was utilised without any calibration adjustments in this study.

$A_{net}g_{sto}emp$  uses the same set of  $V_{cmax25}$ ,  $J_{max25}$  and  $m$  values as used in  $A_{net}g_{sto}mech$  after performing calibration (step1-3 below). Ozone damage parameters are used as outlined in the LRTAP Convention, 2017.

For  $A_{net}g_{sto}mech$ , calibration of the  $V_{cmax25}$ ,  $J_{max25}$  and  $m$  models for European conditions is performed in steps (as outlined below) using  $g_{sto}$ ,  $A_{net}$  and CCI data from various subsets of the fumigation/filtration dataset.

In the first step, initial values for  $V_{cmax25}$ ,  $J_{max25}$  and  $m$  are identified, aiming for a maximal  $g_{sto}$  of between 500-600 mmol O<sub>3</sub> m<sup>-2</sup> PLA s<sup>-1</sup> and maximum  $A_{net}$  of between 30-35 μmol CO<sub>2</sub> m<sup>-2</sup> s<sup>-1</sup>, consistent with the experimental dataset for Bangor and published studies across Europe (Uddling and Pleijel, 2006; Sharma et al., 2015). This step only uses low O<sub>3</sub> treatment data (n=14) to ensure leaf physiology is unaffected by O<sub>3</sub>.

In the second step, the focus is on establishing initial values for O<sub>3</sub> damage parameters (γ1 to γ5) using datasets from both low (n=11) and very high (n=10) O<sub>3</sub> treatments. The O<sub>3</sub> coefficients γ1 and γ2 were set to give a detoxification threshold of 6 nmol O<sub>3</sub> m<sup>-2</sup>s<sup>-1</sup>, while γ3, γ4, γ5 were calibrated based on the observed start and end of senescence data, identified through the breakpoint method discussed in section 2.3.4.

Moving to the third step, the model uses all O<sub>3</sub> treatment data, segmenting them into training and test sets as detailed in Supplementary Table 5. This uses a bootstrapping resampling technique (Hesterberg, 2011), using R software to create bootstrap samples (n=5) that randomly select dataset with replacement i.e., in a sample, there can be duplicates of the same dataset (Table. SI. 6). Such an approach ensures that the initial parameters from steps one and two, along with their defined ranges drawn from both these steps and existing literature, are robustly tested across diverse data combinations from the fumigation/filtration experiments.

The calibration process then proceeds with these training samples (n=5), aiming to calibrate the model to find the best parameters for  $V_{cmax25}$ ,  $J_{max25}$  and  $m$ , and O<sub>3</sub> damage parameters (γ3 to γ5). This calibration employs a computational genetic algorithm (Wang, 1997), an optimisation technique, with gradient descent to find the best parameters. The process requires an initial value and a range) and uses a combination of crossover strategy (selecting parameters randomly from parameter pairings) and mutation strategy (which takes a parameter range and uses incremental step changes) to identify the parameters with the highest R<sup>2</sup> and lowest RMSE value. Finally, the calibration outcomes from each training sample are aggregated using weighted averages following Eq. SI. 7, to establish the final set of parameters. These parameters are then used to construct the flux-response relationships, ensuring the model's applicability and accuracy.

The model's efficacy is then tested using test datasets (n=5), which apply these final parameters. The performance metrics for these tests, specifically the R<sup>2</sup> values for the flux-response relationships of  $A_{net}g_{sto}mech$ , ranged between 0.68-0.77 (Fig. SI. 9) and RMSE

between 0.003-1.7, underscoring the model's reliability and precision across different datasets.

## 2.4 Results

### 2.4.1 Leaf physiology

Leaf physiology data ( $g_{sto}$  and  $A_{net}$ ) from the UK were used to assess the ability of the different models to simulate key physiological variables necessary to estimate  $POD_y$  under both low background and peak  $O_3$  treatments over the course of the growing season.

Fig. 5. a. shows a scatter plot of model simulations of hourly mean  $g_{sto}$  values plotted against observed values for the 2015 and 2016 background and peak  $O_3$  treatments for Mulika and Skyfall wheat varieties. All  $g_{sto}$  models performed similarly under the background  $O_3$  treatments with  $R^2$  values of between 0.36 and 0.50, with the  $A_{net}g_{sto}mech$  model performing the best. All  $g_{sto}$  models performed less well under the peak  $O_3$  treatment with the  $R^2$  range between 0.07 to 0.44; with the  $A_{net}g_{sto}mech$  model performing the best for the peak  $O_3$  treatment, the  $A_{net}g_{sto}mech$  model tends to overestimate  $g_{sto}$  whilst the other two models tend to underestimate  $g_{sto}$  in relation to the 1:1 line. Similarly,  $A_{net}g_{sto}emp$  and  $A_{net}g_{sto}mech$  models provided simulations of  $A_{net}$  under background  $O_3$  treatments that corresponded closely with observed data, achieving  $R^2$  values ranging from 0.83 to 0.86 Fig. SI. 9 both the model the  $A_{net}g_{sto}emp$  and  $A_{net}g_{sto}mech$  models tends to underestimate maximum values of  $A_{net}$  by  $\sim 10 \mu\text{mol CO}_2 \text{ m}^{-2} \text{ PLA s}^{-1}$ .

All models were able to simulate the mean diurnal (see Fig. SI. 11) and mean daily maximum (see Fig. 5.b)  $g_{sto}$  values equally well for the background  $O_3$  treatment. For the peak  $O_3$  treatments, the  $A_{net}g_{sto}mech$  model tended to overestimate mean diurnal  $g_{sto}$  by about  $50 \text{ mmol O}_3 \text{ m}^{-2} \text{ PLA s}^{-1}$ , whilst the other two models tended to underestimate  $g_{sto}$  by the same margin. Similarly, models were able to simulate the mean diurnal (see Fig. SI. 12) and mean daily maximum  $A_{net}$  values (see Fig. SI. 10. b) equally well for the background  $O_3$  treatment. As for  $g_{sto}$ , all models struggled to predict  $A_{net}$  under the peak  $O_3$  treatments with a tendency to overestimate  $A_{net}$  in relation to the 1:1 line but to underestimate maximum  $A_{net}$  values.  $A_{net}$  was comparatively better predicted by the  $A_{net}g_{sto}mech$  model with  $R^2$  values of 0.56 compared to 0.32 for  $A_{net}g_{sto}emp$  model. Fig. SI. 10. shows that the  $A_{net}g_{sto}mech$  model exhibits enhanced performance in simulating the impact of peak  $O_3$  concentrations throughout the entire lifespan of the flag

leaf, thereby capturing the effects of senescence on stomatal conductance with a correlation coefficient ( $R^2$ ) of 0.56. This is in comparison to the  $A_{net}g_{sto}emp$  model, which demonstrated a lower  $R^2$  value of 0.32. By contrast the  $g_{sto}emp$  and  $A_{net}g_{sto}emp$  models simulated an overly sensitive senescence response of  $g_{sto}$  to  $O_3$  compared to the observations. Similar to the  $g_{sto}$  results, the  $A_{net}g_{sto}$  models overestimated the decline in  $A_{net}$  at the end of the growing season compared to the observations (see Fig. Sl. 10. a). However, the  $A_{net}g_{sto}mech$  model gave a closer fit to the observations than the  $A_{net}g_{sto}emp$  model.

Despite the  $A_{net}g_{sto}mech$  being parameterized for ozone parameters; it still exhibits biases when juxtaposed with the observed dataset. The root of these discrepancies lies in the model's dependency on the CCI dataset for estimating the Start of Senescence (SOS) and End of Senescence (EOS), which is derived from experimental studies. The CCI dataset, however, only provides values from mid-anthesis up to ten days before maturation, leading to a critical gap.

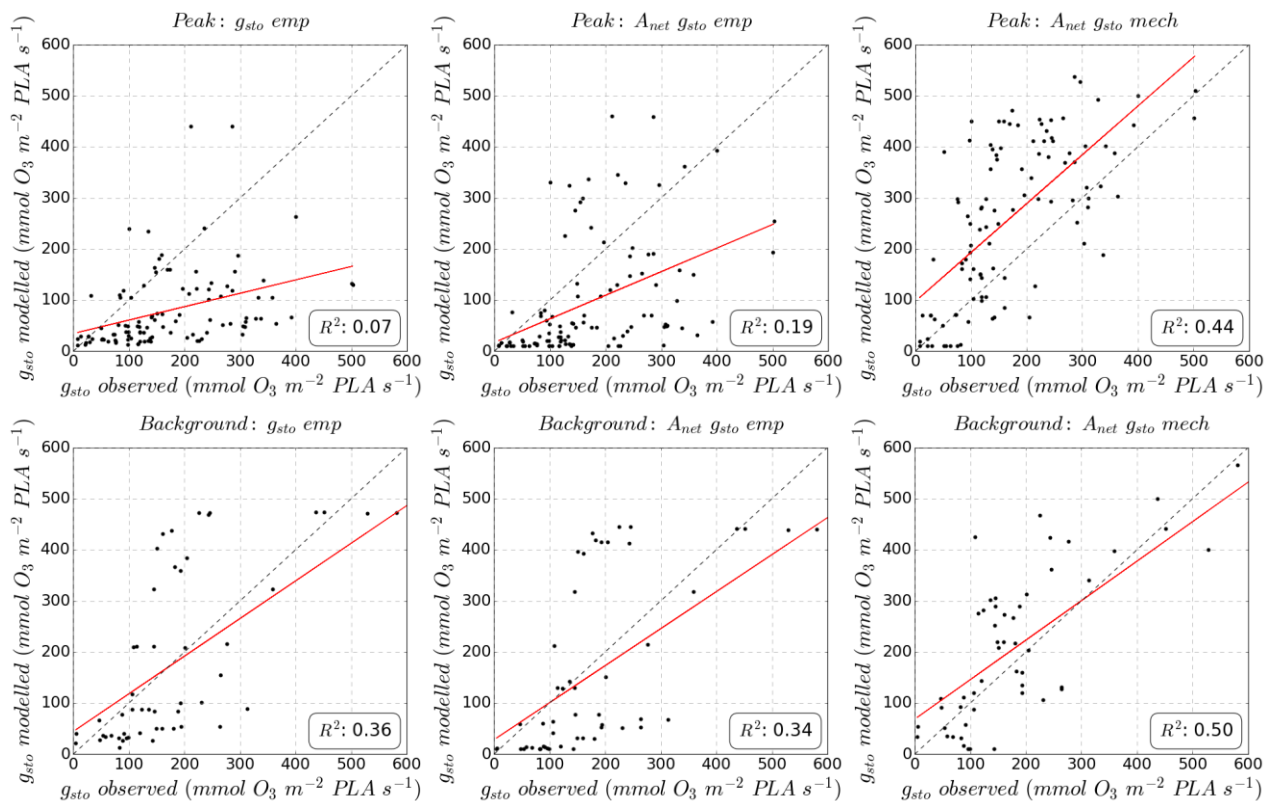
This limitation is especially concerning due to the lack of continuous data collection for the anthesis to complete leaf senescence (maturity) and the complete absence of data during the final stages of the growing season. This gap in data can lead to either an early or a late forecast of the start and end of senescence (SOS and EOS), which compromises the accuracy of the model.

Addressing this issue, therefore, hinges on the integration of additional datasets into the model. By incorporating data from both empirical studies and satellite observations, the model can be fortified against the inconsistencies born out of incomplete data coverage. This enrichment is poised to significantly bolster the robustness of the model's outcomes, providing a more reliable framework for understanding senescence dynamics.

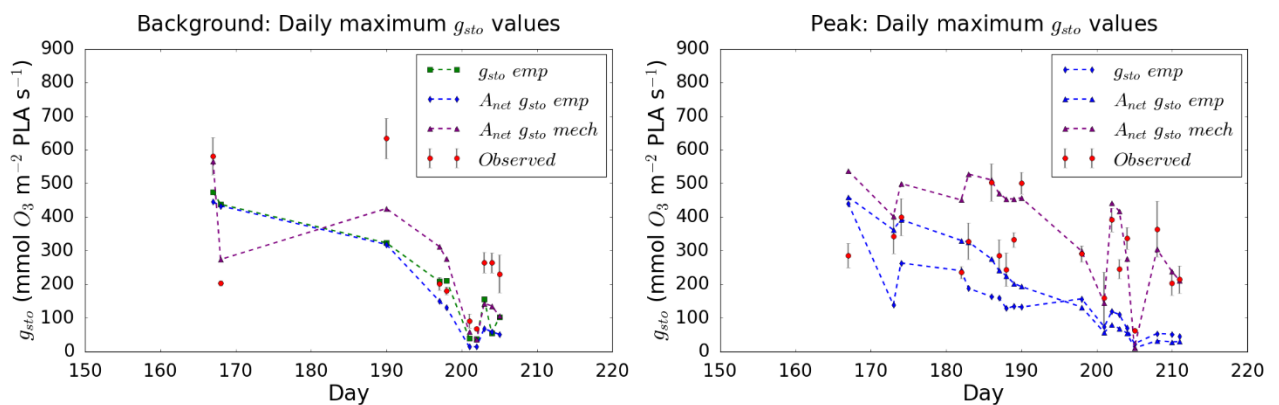
Fig. 5. Scatter plots for Background and peak  $O_3$  treatments for Mulika and Skyfall wheat cultivars, fumigated in Bangor over the 2015 and 2016 growing seasons, were used to plot a) Observed against modelled  $g_{sto}$  values estimated using the three different  $g_{sto}$  models. In each plot, the red solid line represents the regression line, showing the relationship or fit between the modelled and observed values. The black dashed line represents the 1:1 line, which would indicate a perfect match between the modelled and observed values. Data points are scattered across each plot, and the coefficient of determination ( $R^2$ ) is provided for the regression, indicating the proportion of variance

explained by the model. The closer the data points and the red regression line are to the black dashed line; the better the model's prediction matches the observed data. b) Average daily maximum  $g_{sto}$  values simulated over the flag leaf life span by each of the three  $g_{sto}$  models and observed maxima  $g_{sto}$  data were also shown. Error bars, indicating the standard error of the observed data, are included, and shown with black lines extending from the red observed points, providing a visual representation of uncertainty in the measurements.

a.)



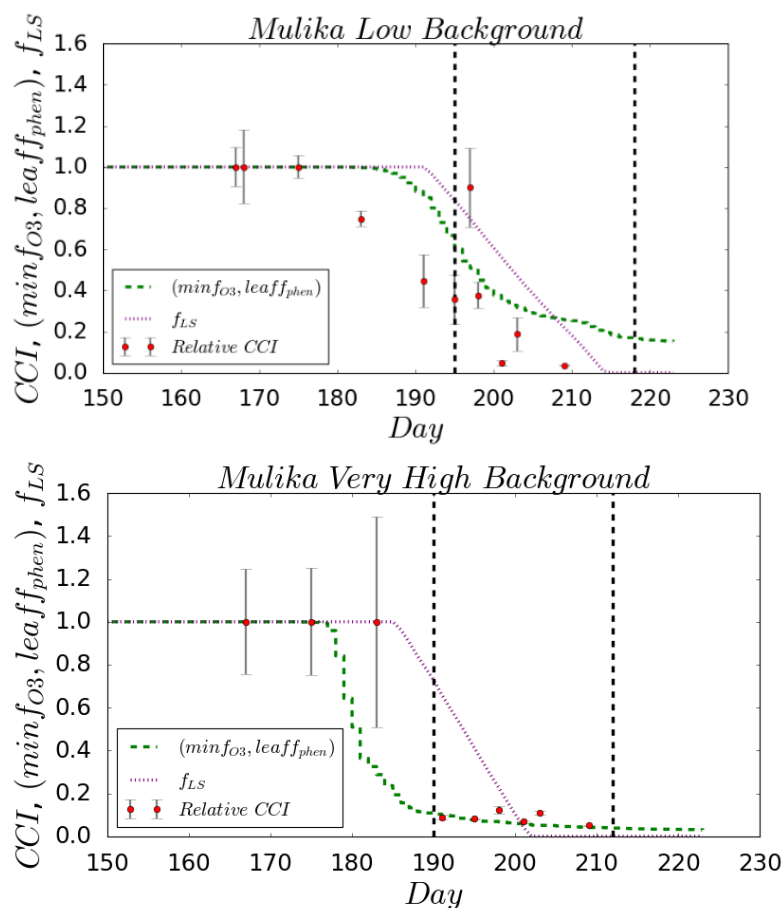
b.)



## 2.4.2 Leaf Senescence

The CCI data are available from the UK (*cv Mulika*) and Swedish (*cv Dragon*) filtration/fumigation datasets were used with the breakpoint method to estimate the start (SOS) and end (EOS) of senescence. Results in Fig. 6 show that the higher O<sub>3</sub> treatment (low background vs very high peaks for the UK) brought forwards the SOS by 7 days and EOS by 12 days. Similar results are found for Sweden (CF vs. NF++ experiment) for Sweden (Fig. SI. 8)

Fig. 6. Leaf senescence profiles of O<sub>3</sub> induced leaf senescence for *cv Mulika* for the low background and very high peak O<sub>3</sub> treatments in the UK dataset. The timing of the SOS and EOS (vertical dotted black lines) determined by applying the breakpoint method to the CCI (red circle with standard errors) are shown in relation to the empirical (minimum of  $f_{O_3}$  and  $leaf\ f_{phen}$ ) and  $f_{LS}$  simulations of senescence.



It is also useful to assess the senescence effects of the O<sub>3</sub> treatments applied in the datasets explored in this study and compared them against the observed datasets. Table 5 summaries this information by dataset for the extreme O<sub>3</sub> treatments (i.e., comparing lowest with highest). The difference in O<sub>3</sub> treatment causing these senescence effects is

indicated by the  $POD_6$  values for the flag leaf life span. The mechanistic approach used by the  $A_{netg_{sto}mech}$  model simulated SOS and EOS more closely to the observations.

Table 5. This table provides a detailed comparison of the deviation in days for the Start of Senescence (SOS) and End of Senescence (EOS) across various treatments from the observed values, presented as *bias*. For each listed location and year, the table places different treatments like CF (Controlled Fertilization), NF+++ (Nitrogen Fertilization with additional nutrients), LB (Low Biomass), and VHP (Very High Pollution), followed by their 24-hour mean concentrations in ppb. The "SOS bias" and "EOS bias" columns indicate the deviation in days at the start (SOS) and end of the season (EOS), respectively, from an observed dataset for both empirical and mechanistic approaches. Positive values denote a delay, while negative values signify an advancement in seasonal timing relative to observed data. "PODy at SOS" and "PODy at EOS" columns measure the Phytotoxic Ozone Dose at the season's start and end, respectively, in mmol per square meter ( $mmol\ m^{-2}$ ), indicating the cumulative ozone exposure above a harmful threshold to vegetation.

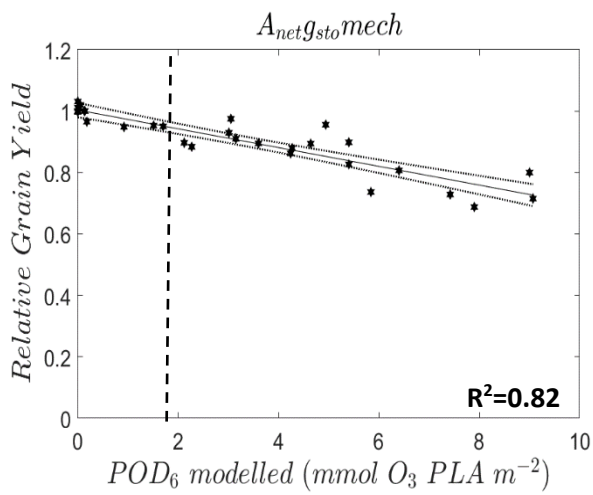
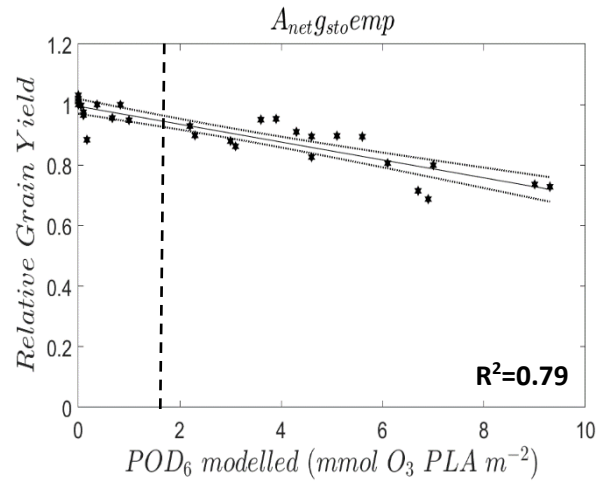
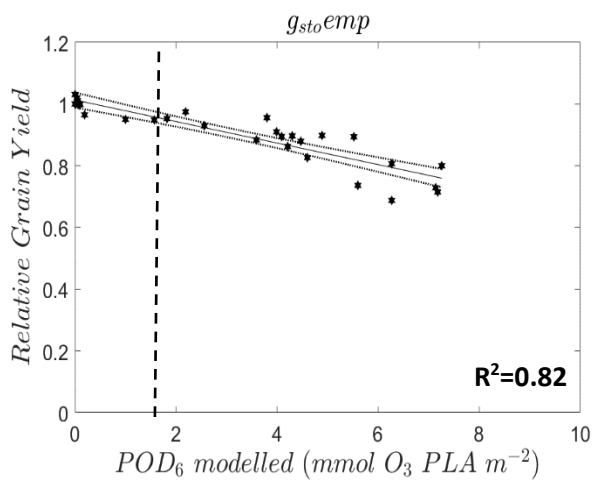
Location and Country	Year	Treatments comparison (24-h Mean in ppb)	$A_{netg_{sto}emp}$ SOS bias (in days)	$A_{netg_{sto}emp}$ EOS bias (in days)	$A_{netg_{sto}emp}$ PODy at SOS ( $mmol\ m^{-2}$ )	$A_{netg_{sto}emp}$ PODy at EOS ( $mmol\ m^{-2}$ )	$A_{netg_{sto}mech}$ SOS bias (in days)	$A_{netg_{sto}mech}$ EOS bias (in days)	$A_{netg_{sto}mech}$ PODy at SOS ( $mmol\ m^{-2}$ )	$A_{netg_{sto}mech}$ PODy at EOS ( $mmol\ m^{-2}$ )

Ostad, Sweden	1997	CF (11.5)	-6	7	0	0	-8	0	0.13	0.13
		NF+++ (22.2)	-9	1	3.3	6.26	3	-4	5.6	7.94
Ostad, Sweden	1999	CF (17.1)	-9	3	0	0	-16	3	0	0.01
		NF+ (35.2)	-14	-4	4.3	7.5	3	-8	6.9	9.2
Bangor, UK	2015	LB (26.94)	-12	6	2.07	3.3	-4	-1	3.1	4.07
		VHP (55.73)	-9	14	2.78	8.07	1	-4	8.5	11.4

### 2.4.3 Flux-response relationships

Each of the three  $g_{sto}$  models were used to develop flux-response relationships based on  $POD_6$  using the  $O_3$  filtration/fumigation data Fig. 7. The robustness of the flux-response relationship can be determined by the strength of the linear regression (i.e.,  $R^2$  value). The  $A_{net}g_{sto}mech$  model ( $R^2=0.82$ ) performed similarly to the  $g_{sto}emp$  model ( $R^2=0.82$ ) in deriving flux-response relationships. The  $A_{net}g_{sto}emp$  model performed slightly less well ( $R^2=0.79$ ). The slope of the relationships differs by -0.0323, -0.0305, and -0.03 for  $g_{sto}emp$ ,  $A_{net}g_{sto}emp$  and  $A_{net}g_{sto}mech$ . This is because the  $A_{net}g_{sto}$  models simulate higher  $g_{sto}$  values under elevated  $O_3$  and during senescence, which will increase the  $POD_y$  values. This demonstrates the importance of consistency in using the same  $g_{sto}$  method to estimate  $POD_y$  as is used to derive the flux-response relationship for yield loss estimates. Were 'critical levels' to be derived from these relationships using the methods described in the LRTAP Convention (2017) (i.e., a 5% reduction on grain yield of the effect based on the slope of the relationship) values of 1.4, 1.5, and 1.6 mmol  $O_3/m^2$  would be found for  $g_{sto}emp$ ,  $A_{net}g_{sto}emp$  and  $A_{net}g_{sto}mech$  models respectively (also shown as dotted lines in the respective plots in Fig. 7). The range of these values reflects the high  $g_{sto}$  values modelled using the  $A_{net}g_{sto}$  models.

Fig. 7. The figures depict flux-response relationships for relative wheat yield using three different stomatal conductance to ozone ( $g_{sto}$ ) models—namely  $g_{sto}emp$ ,  $A_{net}g_{sto}emp$  and  $A_{net}g_{sto}mech$ —to simulate the  $POD_6$  (Phytotoxic Ozone Dose above a threshold of 6 nmol  $O_3 m^{-2} PLA s^{-1}$ ). The plots show the modelled  $POD_6$  on the x-axis against the relative grain yield on the y-axis, with a clear negative trend indicating that as ozone exposure increases, the relative grain yield decreases. The 95% confidence intervals are indicated by the dotted lines surrounding the best-fit line, providing a visual representation of the uncertainty around the estimated response. Each figure should include the coefficient of determination ( $R^2$  value), which quantifies the proportion of variance in the relative grain yield that can be predicted from the modelled  $POD_6$  using the respective  $g_{sto}$  model. This value is a statistical measure of how well the regression line approximates the real data points.



## 2.5 Discussion

We found that the process-based  $A_{net}g_{sto}mech$  model can derive robust flux-based dose-response relationships (with an  $R^2$  value of 0.82), which are very similar to the empirical-based models ( $g_{sto}emp$  and  $A_{net}g_{sto}emp$ ). This suggests  $A_{net}g_{sto}$  models can be reliably used in the derivation of dose-response relationships and critical levels for regional scale risk assessments. However, the variability in the slope of the dose-response relationship (which is also reflected in a higher critical level value of 1.6 mmol  $O_3$   $m^2/s$ ) highlights the importance of consistency in application, i.e. that the same  $g_{sto}$  algorithm used to derive the flux ( $POD_y$ )-response relationship be used in the risk assessment. Our study also found that the  $A_{net}g_{sto}mech$  model was better able to simulate the diurnal and seasonal variation in observations of both  $A_{net}$  and  $g_{sto}$  found under low vs high  $O_3$  treatments in the Bangor experiment. This model attribute is particularly advantageous in estimating  $POD_y$ , given that  $O_3$  concentration profiles can vary substantially across the global wheat growing regions, with some experiencing more chronic  $O_3$  concentrations (e.g., Europe, Karlsson et al., 2017) while others will experience more extreme, episodic concentrations (e.g., Asia, Lei et al., 2012).

There are three important aspects to accurate  $A_{net}$  and  $g_{sto}$  estimates, firstly the parameterisation of the leaf level  $A_{net}$  model which is dependent upon  $V_{cmax25}$ ,  $J_{max25}$ ,  $m$  and  $D_0$ , secondly, the instantaneous effect of  $O_3$  on  $A_{net}$  and thirdly, the parameterisation of the module describing  $O_3$ -induced leaf senescence; the latter is especially important to estimate  $A_{net}$  and  $g_{sto}$  toward the end of the growing season, in wheat, this coincides with the grain-filling period and is therefore crucial in determining yield (Neghliz et al., 2016).

Parametrised values for  $V_{cmax25}$  and  $J_{max25}$  of 88 and 173  $\mu\text{mol CO}_2$   $m^2/s$ , respectively, in this study compare well to the values of 62-75 and 150-195  $\mu\text{mol CO}_2$   $m^2/s$  used for LINTULLC2 (Feng et al., 2022) and AFRCWHEAT (Oijen and Ewert, 1999) crop models which incorporate  $O_3$  damage modules for similar European wheat applications. We found limited evidence for variation in  $V_{cmax25}$  and  $J_{max25}$  with biogeographical regions with  $V_{cmax25}$  varying between 55-180, 53-185, and 90-120  $\mu\text{mol CO}_2$   $m^2$   $s^{-1}$  for Atlantic, continental and Mediterranean biogeographic regions, respectively; no statistical difference by region was found. This contrasts with the  $g_{max}$  value of the  $g_{sto}emp$  model that has lower values for Mediterranean wheat cultivars (by 70 mmol  $O_3$   $m^2$   $s^{-1}$ , LRTAP

Convention, 2017). This study only used data from Atlantic, Boreal, or Continental regions. Were Mediterranean data to have been included, the  $V_{cmax25}$  and  $J_{max25}$  values may have warranted further investigation to establish whether a different  $V_{cmax25}$  might be justified, especially since only 11 datapoints were retrieved for this region in our literature search (see Fig. SI. 4).

The ratio between  $V_{cmax25}$  and  $J_{max25}$  was found to vary between 0.2 and 0.8 (see Fig. SI. 4) and was calibrated to a value of 0.51 for this dataset. This is consistent with a study by (Wullschlegel, 1993), who found a ratio of 0.38-0.55 for wheat even as growth and temperature varied. However, other research found that the ratio may range from 1-3 (Camino et al., 2019; Day et al., 1982), which may be attributed to  $J_{max25}$  being more reliant on light than  $V_{cmax25}$  causing the ratio to decrease when light intensity decreases (Dai et al., 2004). The value of 7.87 for  $m$  used in this study is also within the range of 5 and 15 found for many different cultivars of wheat (Kosugi et al., 2003; Collatz et al., 1991; Baldocchi and Meyers, 1998; Miner et al., 2017). The  $VPD_0$  value is markedly different (2.2 kPa) from that of Luening et al. (1995) and means that  $A_{net}$  can be maintained under high values of VPD; this is consistent with the  $f_{VPD}$  relationship and observational data (Danielsson et al., 2003).

The validity of the  $A_{net}g_{stomech}$  model also depends on the appropriate parameterisation of the key  $O_3$  damage mechanisms. These damage mechanisms are assumed to have both an instantaneous ( $f_{O_3,s}(d)$ ) effect of  $O_3$  on  $A_{net}$  and a longer-term effect ( $f_{LS}$ ) of accumulated  $O_3$  uptake promoting earlier senescence. The instantaneous effect reduces carboxylation via a reduction in Rubisco activity, which may, in turn, lead to a reduction in carbon assimilation when Rubisco activity ( $A_c$ ) is limiting net  $A_{net}$ . This reduction in rubisco activity is assumed to repair overnight, but with repair effectiveness decreases as the leaf ages. According to (Farage et al., 1991), the instantaneous impact of  $O_3$  was only seen with a significant reduction in carboxylation efficiency (>50%), causing a reduction in carbon assimilation. This could happen when crops are exposed to elevated  $O_3$  concentrations for long periods or if repeated high  $O_3$  exposures were to take place causing the crop to lose its ability to recover (Feng et al., 2022). By contrast, the length of the leaf senescence period is essential for determining the crop development cycle (Ding et al., 2022). The onset of leaf senescence causes a substantial decrease in carbon assimilation ( $A_{net}$ ), primarily attributed to changes in chloroplast

structure and function, and hence the chlorophyll content in the flag leaf (Ding et al., 2022; Gelang et al., 2000; Ojanperä et al., 1998), and contributes to the reduction in dry ear weight, which directly affects yield loss (Gelang et al., 2000). The Chlorophyll Content Index (CCI) has been shown to be a good predictor of the onset of senescence (Mariën et al., 2019; Osborne et al., 2019). It can also be used as a proxy for  $V_{cmax25}$  (Croft et al., 2017), which is our modelling approach since we assume SOS will coincide with a reduction in  $V_{cmax25}$  and consequently  $A_c$  (see eq 8). We find that the  $A_{net}g_{sto}mech$  model can simulate SOS and EOS for the elevated  $O_3$  treatments in the UK and Sweden data better than the empirical models. For the UK, the flag leaf starts to senesce 6 days earlier in high (VHP) compared to low (LB)  $O_3$  treatment, and for Sweden, 7 days earlier in high (NF++) compared to carbon-filtered (CF) treatment. The number of days by which high  $O_3$  levels can bring forward the start of senescence is corroborated by other published studies (Pleijel et al., 1997; Grandjean and Fuhrer, 1989; Gelang et al., 2000) which found the flag leaf could senesce up to 25 days earlier in the very high  $O_3$  compared to the carbon filtered treatments.  $O_3$  was also found to cause differences in the time to maturity of the flag leaf; (Shi et al., 2009) reported 8 days earlier maturity in elevated  $O_3$  (50% higher than ambient) compared to ambient  $O_3$  treatments. Similar results were found in this study, with the flag leaf maturing 12 days earlier in VHP compared to LB treatments. Although our results seem consistent, they are based on a limited number of CCI data points (approximately 11 and 13 for each treatment for the UK and Sweden, respectively) only captured from mid-anthesis to 10 days before maturity). Additional CCI data spread more evenly over the crucial crop growth period would improve our understanding of how  $O_3$  affects senescence.

Parameters for the  $A_{net}g_{sto}$  models were found using an automated calibration method, the genetic algorithm (GA) optimisation technique since this approach is considered superior in performance to more traditional techniques (Kuo et al., 2000; Dai et al., 2009; Vazquez-Cruz et al., 2014). The GA method was also chosen since it works with a range of parameter searches from a population of points and employs probabilistic transition rules, i.e., uses random sets of parameters instead of using fixed sets, which makes the optimisation process more robust (Kuo et al., 2000). This study demonstrated the effectiveness of this approach with the five training samples that are used to form dose-response relationships, giving RMSE ranges from 0.99 to  $4.5 \times 10^{-5}$  for the  $A_{net}g_{sto}mech$  model. Such a good performance suggests that the parametrisation derived

can give robust values for the  $A_{net}g_{sto}$  models for use in other European O<sub>3</sub> risk assessment applications.

The calibration approach to parameterise the  $A_{net}g_{sto}$  models is different from that used to parameterise the  $g_{sto}emp$  model, which identifies  $g_{max}$  and  $f_{min}$  values (as average maximum and minimum values, respectively) and the  $f$  functions using a boundary line analysis method (LRTAP Convention, 2017). Since the  $A_{net}$  models are effectively calibrated to the output of a sub-set of all datasets, it can be argued that this may improve the ability of this model type compared to the  $g_{sto}emp$  model. As such, unequivocal claims that  $A_{net}g_{sto}$  models are better than  $g_{sto}emp$  models need to be made with caution.

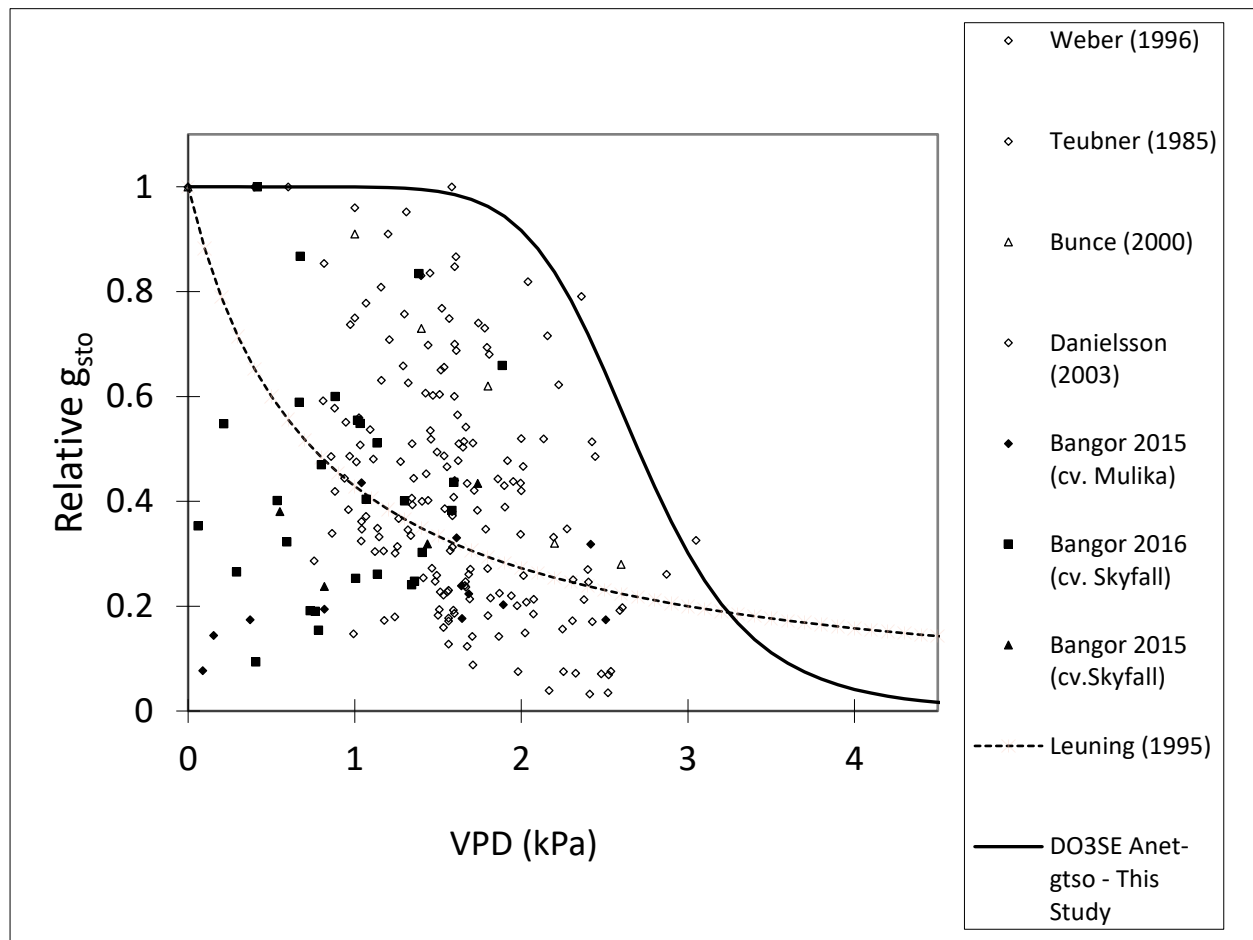
## 2.6 Conclusion

Overall, we find that the  $A_{net}g_{sto}mech$  model can be used to derive robust flux-response relationships when incorporating both short- and long-term O<sub>3</sub> damage processes. The  $A_{net}g_{sto}mech$  model also has the added benefit of estimating  $g_{sto}$  under variable O<sub>3</sub> concentrations and has a direct link to carbon assimilation. This study's establishment of the  $A_{net}g_{sto}mech$  flux-response relationship could be used to calibrate or constrain models that use the  $A_{net}g_{sto}$  approach (e.g.,  $A_{net}$  based crop models, land surface exchange models, biogeochemical cycling models, and earth system models), thus supporting a move towards more process-based assessments of O<sub>3</sub> damage and yield loss.

## SI.1 Supporting Material

### SI.1.1 Boundary line analysis of relative $g_{sto}$ data with VPD

Fig. SI. 1. Boundary line analysis of relative  $g_{sto}$  in response to vapor pressure deficit (VPD). The dataset includes points from various fields and open-top chamber studies conducted in Europe, illustrating the decreasing  $g_{sto}$  with increasing VPD. The solid line represents the VPD function used in this paper for  $A_{net}g_{sto}$  models (LRTAP,2017) and dashed line represents the hyperbolic VPD function used in (Leuning, 1995)



### SI.1.2 Multiplicative model equations

$$1. f_{temp} = \max(f_{min}, ((T - T_{min}) / (T_{opt} - T_{min})) * ((T_{max} - T) / (T_{max} - T_{opt}))^{bt}) \quad \text{Eq. SI. 1.}$$

$$\text{Where; } bt = \frac{T_{max} - T_{opt}}{T_{opt} - T_{min}}$$

$$2. f_{VPD} = \min\left(1, \max\left(f_{min}, \left((1 - f_{min}) * \frac{(VPD_{min} - VPD)}{(VPD_{min} - VPD_{max})}\right)\right) + f_{min}\right) \quad \text{Eq. SI. 2}$$

$$3. f_{light} = 1 - EXP(-light_a * PPF D) \quad \text{Eq. SI. 3}$$

$$4. f_{O3} = \left( \left( 1 + \left( \frac{POD_0}{14} \right)^8 \right) - 1 \right) \quad \text{Eq. SI. 4}$$

$$5. leaf f_{phen} = 1; \text{ for } mid\text{-anthesis}(\text{°Cdays}) \leq leaf f_{phen3ETS}$$

$$leaf f_{phen} = 1 - \frac{leaf f_{phen a}}{leaf f_{phen4ETS} - leaf f_{phen3ETS}} * (mid\text{-anthesis}(\text{°Cdays}) - leaf f_{phen3ETS});$$

for  $mid\text{-anthesis}(\text{°Cdays}) > leaf f_{phen3ETS}$  and  $mid\text{-anthesis}(\text{°Cdays}) \leq leaf f_{phen4ETS}$

$$leaf f_{phen} = 0, f_{phen b} - \frac{f_{phen b}}{leaf f_{phen5ETS} - leaf f_{phen4ETS}} * (mid\text{-anthesis}(\text{°Cdays}) - leaf f_{phen4ETS});$$

for  $(mid\text{-anthesis}(\text{°Cdays}) > leaf f_{phen4ETS})$  and  $mid\text{-anthesis}(\text{°Cdays}) \leq leaf f_{phen5ETS}$  )

Eq. SI. 5

Table. SI. 1 Definitions of Parameters for a Multiplicative Stomatal Conductance Model

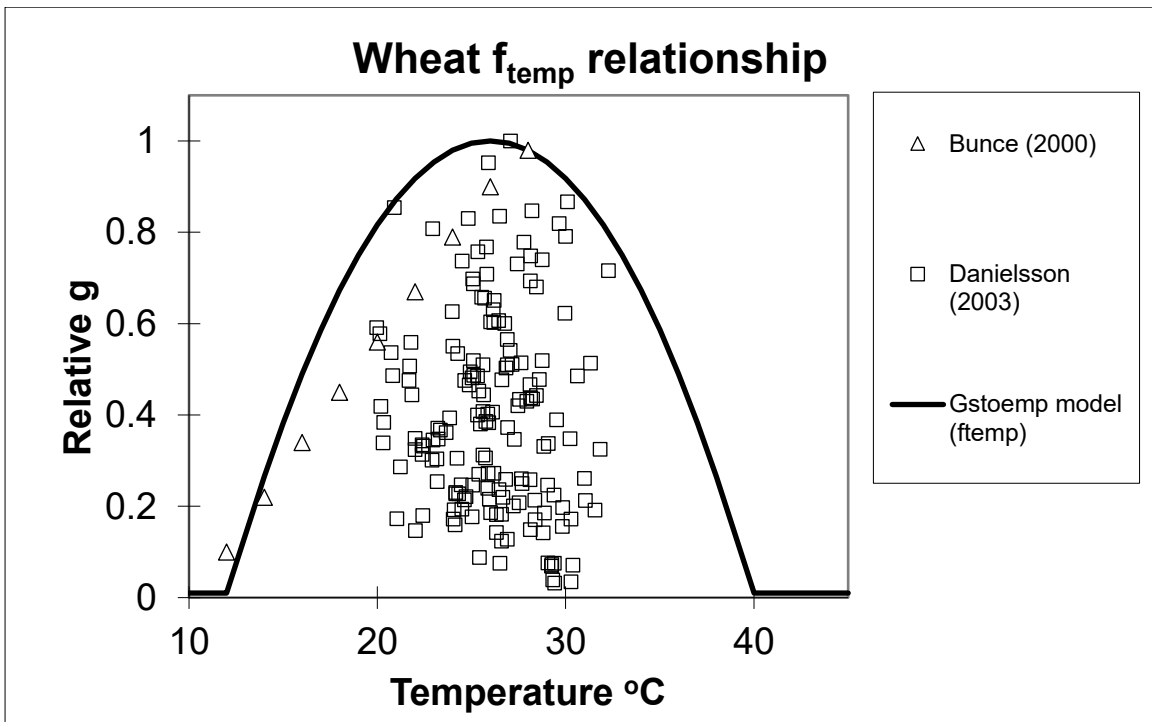
Parameters	Definition
$T_{min}$	Minimum temperature
$T_{opt}$	Optimum temperature
$T_{max}$	Maximum Temperature
$T$	Air Temperature
$f_{min}$	Minimum Stomatal conductance
$VPD$	Vapour Pressure deficit
$VPD_{min}$	Minimum VPD
$VPD_{max}$	Maximum VPD
$light_a$	Irradiance factor
$PPFD$	Photosynthetic photon flux density
$POD_0$	Phytotoxic Ozone Dose
$leaf f_{phen a}$	Thermal time at crop emergence
$leaf f_{phen3ETS}$	Thermal time between mid-anthesis to start of flag leaf ageing
$leaf f_{phen4ETS}$	Thermal time between mid-anthesis to start of flag leaf senescence
$leaf f_{phen5ETS}$	Thermal time between mid-anthesis to maturity

$f_{phen_b}$	Thermal time at double ridge stage
--------------	------------------------------------

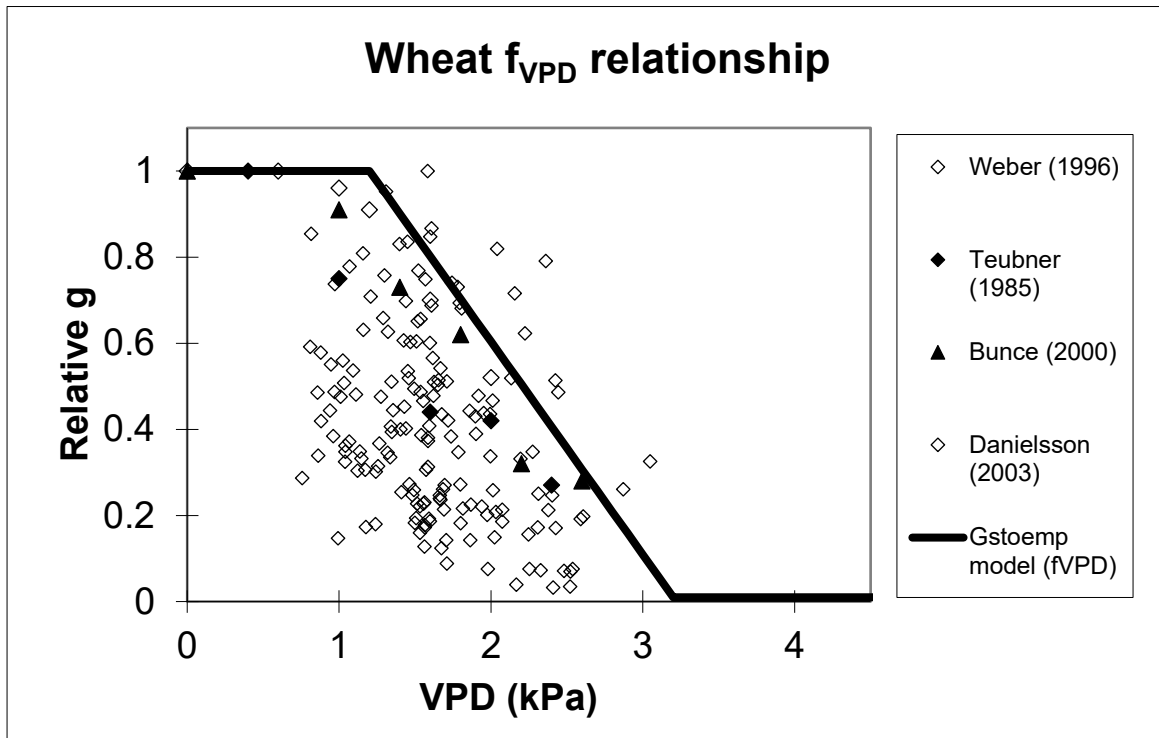
Plots for multiplicative functions

Fig. SI. 2. a -e. Functional Relationships in Wheat Modelling. (a) Wheat  $f_{temp}$  relationship shows the relative conductance ( $g$ ) response to temperature, comparing the  $g_{stoemp}$  model function to datasets from Bunce (2000) and Danielsson (2003);(b) Wheat  $f_{VPD}$  relationship shows the relative conductance decline with increasing Vapour Pressure Deficit (VPD), with empirical data from Weber (1996), Teubner (1985), and Bunce (2000) alongside the  $g_{stoemp}$  model's function; (c) Wheat  $f_{light}$  relationship depicts the relationship between relative conductance and irradiance (PPFD), including empirical observations from Machado (1994), Gruters (1995), and Bunce (2000), contrasted with the New EMEP or  $g_{stoemp}$  model's output function; (d) Spring wheat Canopy  $f_{phen}$  and leaf  $f_{phen}$  profiles within growing season" outlines the phenological development of wheat, marking the canopy and leaf  $f_{phen}$  from sowing date to end of growing season (EGS), highlighting critical growth stages like anthesis; (e)  $f_{O_3}$  function profile alongside thermal time. It shows the decline in  $f_{O_3}$  as the thermal time increases (depicting the crop growing season).

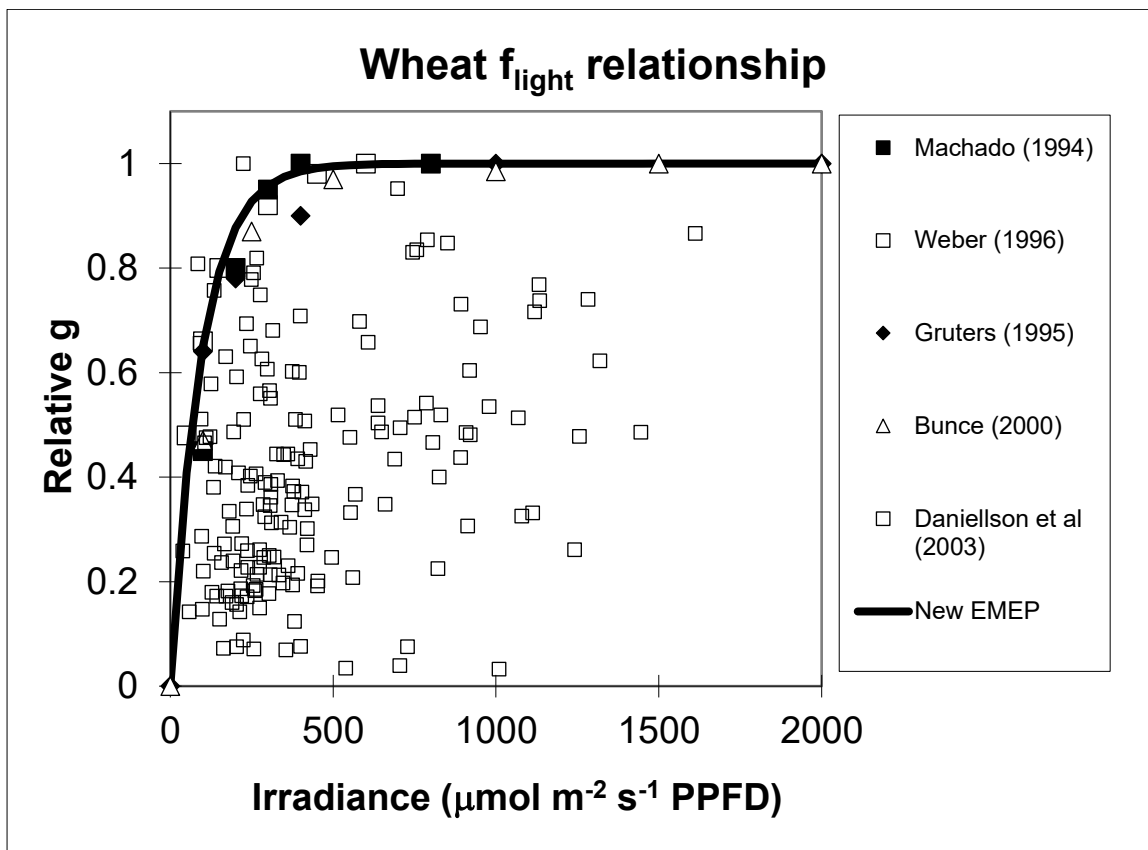
a.)



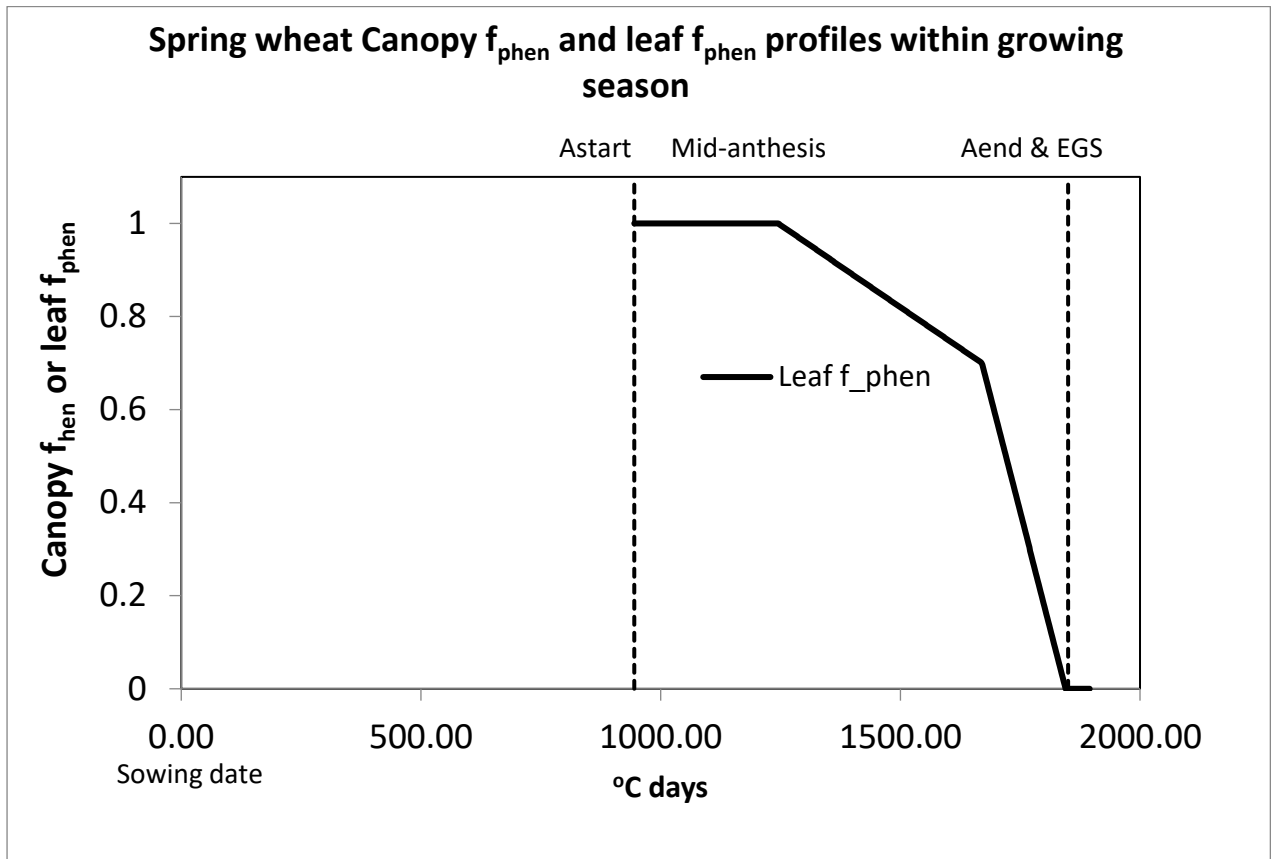
b.)



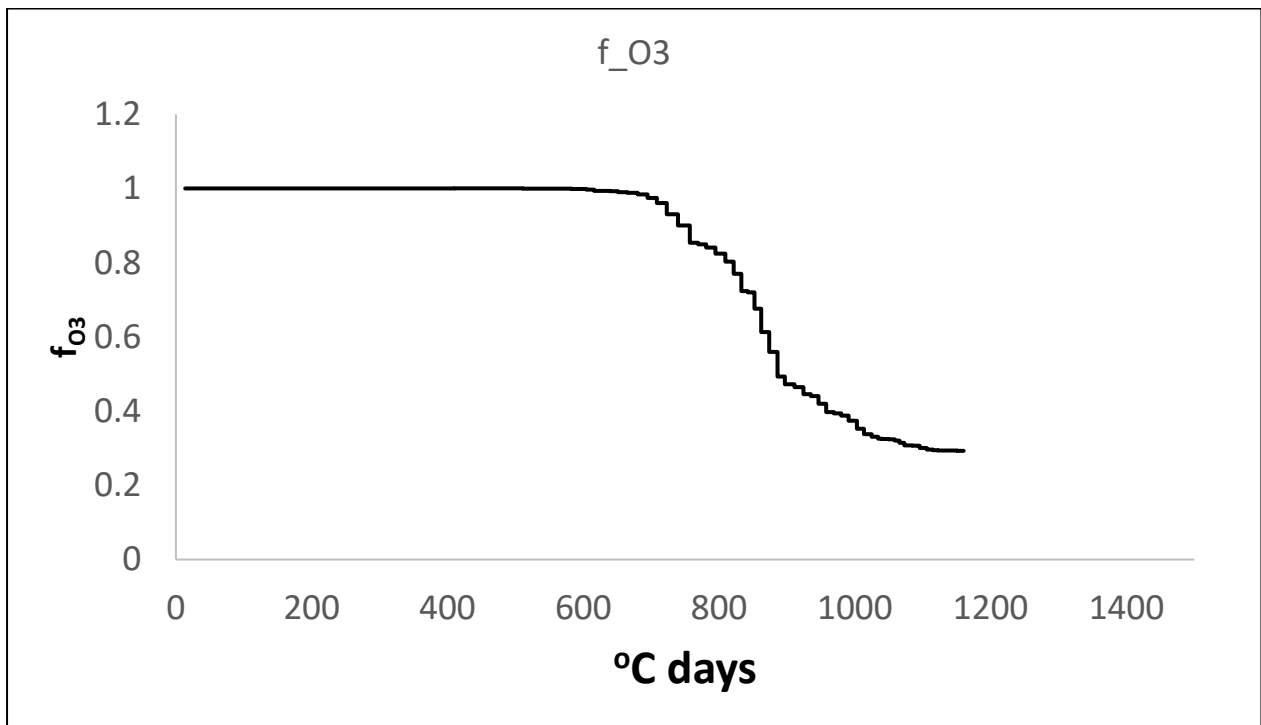
c.)



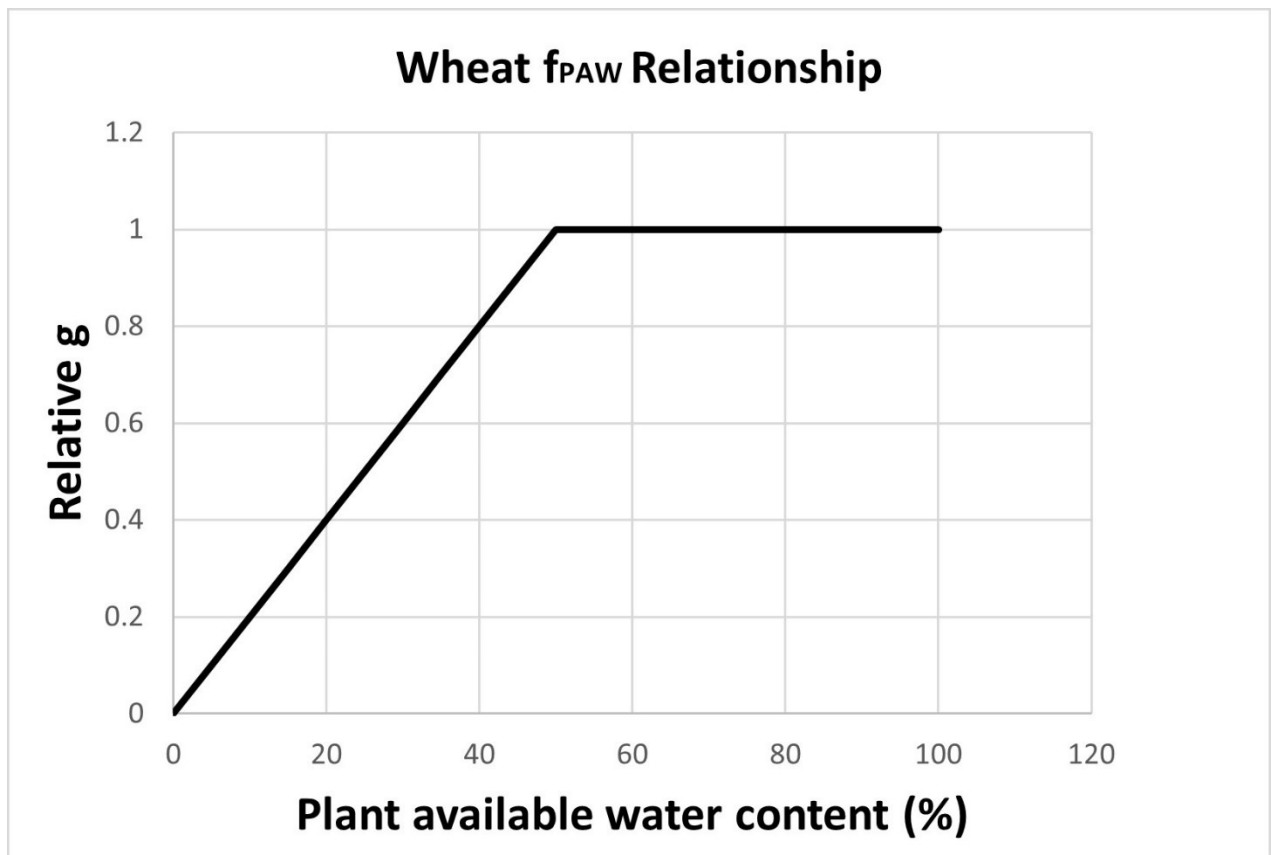
d.)



e.)



f.)



### SI.1.3 Relationship between leaf $f_{phen}$ , $f_{LS}$ and $f_{LA}$ and thermal time intervals

This section describes the link between the relationship between leaf  $f_{phen}$ ,  $f_{LS}$ , and  $f_{LA}$  and thermal time intervals of emerging ( $tl_{em}$  and mature leaf or flag leaf)

*A<sub>netgsto</sub>mech* model flag leaf phenology

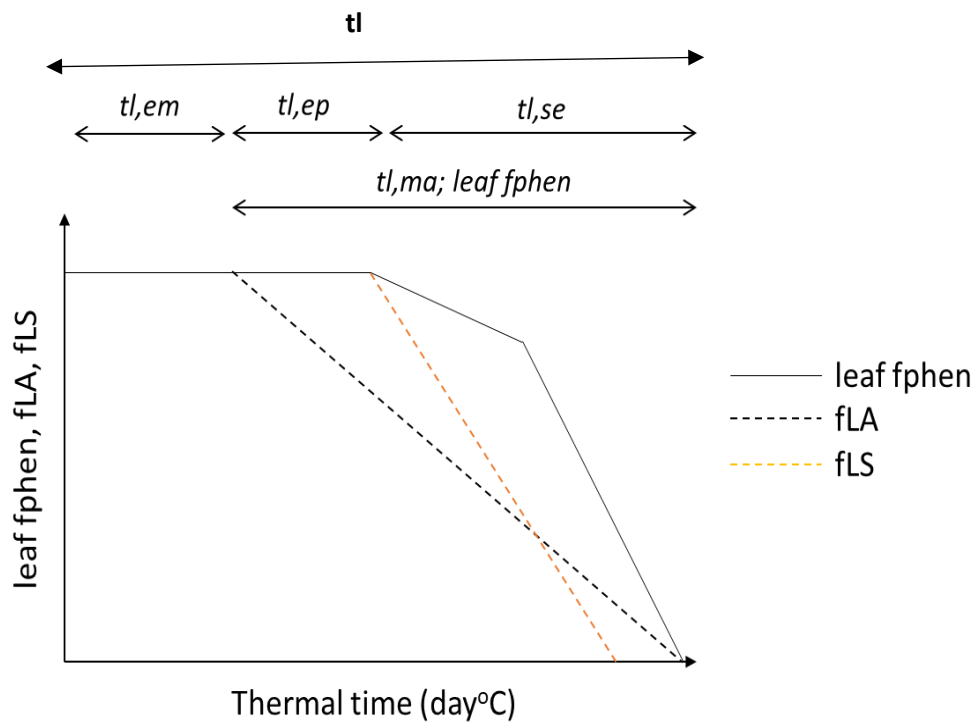
Life span of the flag leaf in the *A<sub>netgsto</sub>mech* model is defined as,

$$tl_{ma} = tl_{ep} + tl_{se}; \quad tl_{se} = 0.33 * tl_{ma}, \text{ and}; \quad tl_{ep} = tl_{ma} - tl_{se} \quad \text{Eq. SI. 6}$$

where,  $tl_{ma}$  is the total flag leaf life span and calculated as the thermal time interval from start of the anthesis to the end of the anthesis. This determined by the multiplicative 'leaf  $f_{phen}$ ' thermal time model and the  $tl_{se}$  is defined as occurring one third of the way through this period.  $tl_{ep}$  is the thermal time between start of the anthesis and start of senescence. Using the values of these thermal time intervals and the age of the leaf (in °C) corresponds are used to calculate the factor  $f_{LA}$  (unitless) and  $f_{LS}$  (unitless).  $f_{LA}$

accounts for leaf age and calculated over the lifespan of the leaf,  $t_l$ , and  $f_{LS}$  accounts for the effect of leaf senescence on  $A_c$ .

Fig. SI. 3. Relationship between  $g_{stoemp}$  model leaf phenology ( $leaf\ f_{phen}$ ) and the  $A_{net}g_{stomech}$  leaf senescence ( $f_{LS}$ ) and leaf age ( $f_{LA}$ ).  $f_{LA}$  and  $f_{LS}$  are unitless and thermal time is in  $^{\circ}C\ day$



#### SI.1.4. Dataset details:

The dataset includes thirteen field-based Open Top Chamber (OTC) studies performed between 1987 and 2015 from across Europe on field-grown spring wheat crops. The dataset incorporates 6 cultivars, 4 countries, and 14 growing seasons. Various crop responses to ozone were recorded, but all experiments and treatments assessed grain yield at harvest. These experiments were conducted using a standard protocol, i.e., the use of field-grown spring wheat cultivars, supplied fertilizers (N, P, and K) to ensure optimum soil fertility, applied insecticides and fungicides to guard against pests and diseases and irrigation to ensure the plants were not subject to water stress. The ozone filtration or fumigation process starts 15 days before anthesis with ozone treatments (i.e., filtration using charcoal filters to remove ozone (CF treatments) or application of additional ozone to enhance concentrations (NF+ treatments) applied daily between 11:00 to 18:00 local time. The datasets have previously been collected, pooled, and analysed to derive the UNECE LRTAP flux-response relationship using the multiplicative  $g_{sto}$  model only (Mapping Manual, 2017).

Additional datasets are included in this study conducted at an experimental site in Bangor, North Wales, performed for the years 2015 and 2016 in the UK on two spring wheat varieties, Mulika and Skyfall, for two different ozone concentration profiles, i.e., acute peaks and consisted of background level. Ozone fumigation starts 15 days before the start of the anthesis. In 2015, cv. Mulika and Skyfall were exposed to eight ozone treatments (i.e., 'low background' (LB), 'low peak' (LP), 'medium background' (MB), 'medium peak' (MP), 'high background' (HB), 'high peak' (HP), 'very high background, (VHB), and 'very high peak' (VHP)). In 2016, cv. Skyfall was exposed to five ozone treatments (i.e., 'low peak 1' (LP1), 'low peak 2' (LP2), MP, HP, VHP). This dataset contains variables such as Chlorophyll content Index (CCI),  $g_{sto}$ ,  $A_{net}$ ,  $V_{cmax25}$ ,  $J_{max}$ , Yield, which is used to evaluate the performance of the different models used in this study. For comprehensive details on the collection of this dataset, refer to (Osborne *et al.*, 2019). This study also incorporates supplementary CCI data derived from Ostad, Sweden, which includes measurements from charcoal-filtered (CF), non-filtered (NF), and enhanced non-filtered (NF+) treatments collected in the years 1997 and 1999.

Table. SI. 2. Details of the ozone fumigation/filtration experiments used to derive flux-response relationships using the various  $g_{sto}$  models.

Location and Country	Biogeographic biomes	Year	Experimental method	Cultivar	Treatments	Input variables & Time Step	Evaluation Data	Reference
Tervuren, Belgium	Atlantic	1996, 1995, 1994	OTCs, Field grown	Minaret	NF, CF	PPFD, Tair, VPD, u, Pa, [O3]; hourly	Yield	(Bender et al.,1999)
Ostad, Sweden	Boreal	1995, 1994, 1988, 1987	OTCs, Field grown	Dragon Darbant	CF, NF, NF+, NF++, NF+++  CF, NF, NF+, NF++,	PPFD, Tair, VPD, u, Pa, [O3]; hourly	Yield	Pleijel et.al,1999, Pleijel et.al.,1998, Pleijel et.al,1991
Jokioinen, Finland	Boreal	1993, 1992, 1991	OTCs, Field grown	Satu	CF, NF, NF+	PPFD, Tair, VPD, u, Pa, [O3]; hourly	Yield	(Ojanperä et al., 1988, 1994); (Pleijel et al.,1997)

Ostad, Sweden	Boreal	1999, 1997	OTCs, Field grown	Dragon	CF, NF, NF+, NF++, NF+++	PPFD, Tair, VPD, u, Pa, [O3]; hourly	CCI, Yield	(Gelang et al., 2000)
Bangor, UK	Atlantic	2015, 2016	Solardomes , pot grown	Mulika, Skyfall	LB, LP, MP, MP, HB, HP VHB, VHP LP1, LP2, MP, HP, VHP	PPFD, Tair, VPD, u, Pa, [O3]; hourly	CCI, $g_{sto}$ , $A_{net}$ , $V_{cmax25}$ , $J_{max}$ , Yield	(Osborne et al., 2019)

N.B: 'low background' (LB), 'low peak' (LP), 'medium background' (MB), 'medium peak' (MP), 'high background' (HB), 'high peak' (HP), 'very high background, (VHB), and 'very high peak' (VHP)), 'low peak 1' (LP1), 'low peak 2' (LP2), 'charcoal-filtered (CF), non-filtered (NF), and non-filtered air with additional ozone (NF+, NF++,NF)

### SI.1.5 Parameters: Multiplicative model

The filtration/fumigation data are from countries that are all within the Atlantic, boreal and continental region of Europe and hence only parameterisation for this region is used in this analysis even though parameterisation for wheat growing in other regions are available (e.g. Mediterranean).

Table. SI. 3. Parameters used for  $g_{stoemp}$  model (Mapping Manual, 2017)

Parameter	Units	Atlantic, boreal & continental (bread wheat)
$g_{max}$	mmol O <sub>3</sub> m <sup>-2</sup> PLA s <sup>-1</sup>	500
$f_{min}$	-	0.01
$f_{O_3}$	-	6
$f_{light}$	μmol/m <sup>2</sup> /s	0.0105
$T_{min}, T_{opt}, T_{max}$	°C	12,26,40
$VPD_{min}, VPD_{max}$	kPa	1.2,3.2
$\sum VPD_{crit}$	kPa	8
leaf $f_{phen}$	-	0.3,0.7
Flag leaf thermal time stages	°days	1605 (-200, 0, 100, 525, 700)
Leaf dimension	m	0.02

$g_{max}$  is maximum stomatal conductance. This is the maximum rate at which gases can pass through the stomata under optimal conditions. It's a characteristic of the plant species and its adaptation to its environment;  $f_{min}$  is minimum conductance factor. This sets a lower bound for stomatal conductance, ensuring that it does not fall below a certain threshold, even under adverse conditions. It represents the basal level of gas exchange that occurs even when stomata are mostly closed;  $f_{O_3}$  is ozone factor. This reflects the impact of ozone concentration on stomatal conductance. High ozone levels can lead to stomatal closure or damage, reducing gas exchange, Light factor. Stomatal conductance is influenced by light levels, as light drives photosynthesis. This factor increases conductance in the presence of light, simulating the opening of stomata during the day;  $T_{min}, T_{opt}, T_{max}$  is minimum, optimum and maximum temperature respectively;  $VPD_{min}$  and  $VPD_{max}$  is minimum and maximum vapour pressure deficit respectively;  $\sum VPD_{crit}$  is critical Vapor Pressure Deficit. leaf  $f_{phen}$  denotes the maximum fraction of  $g_{max}$  at the start of flowering or anthesis and end of anthesis.

### SI.1.6. Parameters used for the estimation of the estimation of O<sub>3</sub> uptake $f_{st}$ in $g_{stoemp}$ and $A_{net}$ models

Table. SI. 4. Parameters used for the estimation of the estimation of O<sub>3</sub> uptake ( $f_{st}$ ) in  $g_{stoemp}$ ,  $A_{net}g_{stoemp}$ , and  $A_{net}g_{stomech}$  for three different biogeographic regions (Atlantic, boreal and continental)

Parameter	Units	Atlantic, boreal & continental (bread wheat)
External plant cuticle conductance ( $g_{ext}$ )	m/s	1/2500

### SI.1.7. Literature findings: $V_{cmax25}$ and $J_{max25}$ data

Fig. SI. 4. Data extracted from literature showing the range of  $V_{cmax25}$  in Atlantic (A) and Continental (C) and Mediterranean (M) biogeographic region, and variability in the ratio of  $V_{cmax25} : J_{max25}$ .  $V_{cmax25}$  and  $J_{max25}$  data extracted from the literature grouped by biogeographic region (Mediterranean (M), 11 datapoints from Spain & Italy; Atlantic (A) and Continental (C), 238 datapoints from UK, Germany, Slovakia and Hungary). The higher number of datapoints in A&C are due to a large number coming from two published studies conducted in the UK on 64 (Silva-Pérez et al., 2020) and >80 wheat varieties respectively (McAusland et al., 2020). The Continental region shows the most extensive range in values (51-186  $\mu\text{mols CO}_2 \text{ m}^{-2} \text{ s}^{-1}$ ) ((Olsovska et al., 2016)(Harnos et.al, 2002); (Tcherkez et al., 2020) whereas, the Mediterranean region showed the least range in values (88.3-122  $\mu\text{mols CO}_2 \text{ m}^{-2} \text{ s}^{-1}$ ) with some outliers from an Italian study (Dikhoshi., 2015), where  $V_{cmax25}$  values were 190 and 240 for cultivars *Triticum durum*.

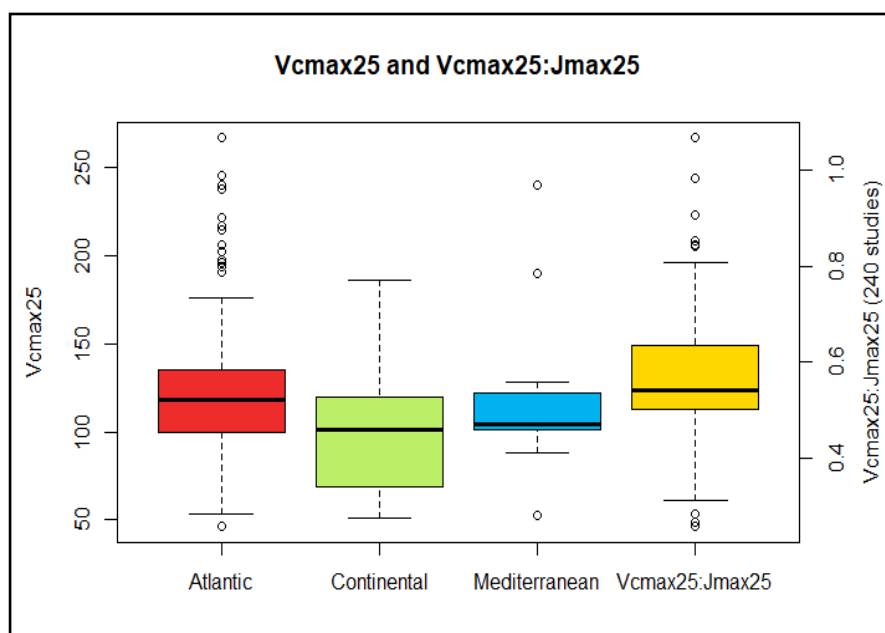


Fig. SI. 5. (a) The first figure presents a comparison of  $V_{cmax25}$  values in wheat cultivated under irrigated and rainfed conditions. The box plots display a clear demarcation of central tendency and variability, with the red line representing the mean, the black line within the boxes indicating the median, and the box edges showing the 25th and 75th percentiles. Whiskers mark the range of data, extending to the maximum and minimum values, and there are no outliers indicated.

(b) The second figure illustrates the variability in  $V_{cmax25}$  and  $J_{max25}$  for 64 varieties of wheat, measured both pre- and post-anthesis. The box plots employ the same conventions to indicate the mean (red line), median (black line), interquartile range (edges of the box), and range (whiskers). This visual comparison highlights the effects of the phenological stages on the photosynthetic parameters of wheat.

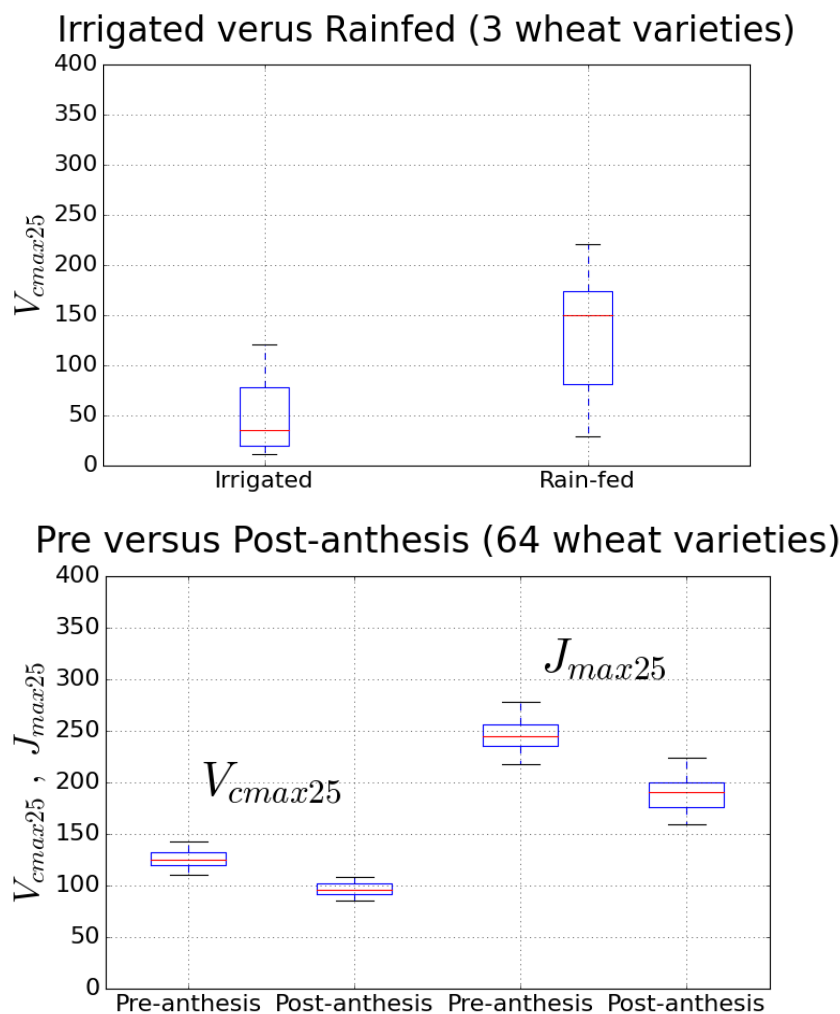
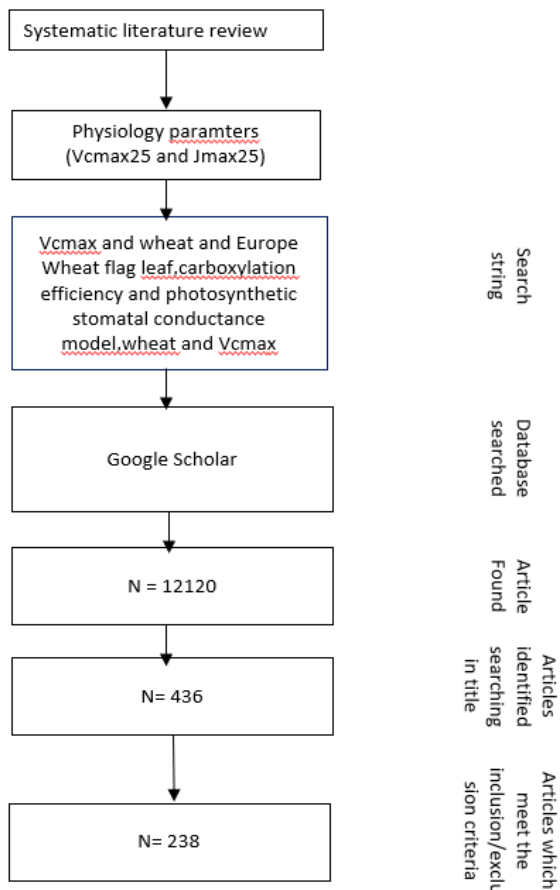


Fig. SI. 6. This diagram outlines the process of a systematic literature review focused on physiology parameters ( $V_{cmax25}$  and  $J_{max25}$ ) related to wheat. The flowchart begins with a broad systematic literature review and narrows down through various stages of filtering

and search string specificity, such as "Vcmax and wheat and Europe" and related terms. The search is conducted using Google Scholar, starting with an initial result pool of 12,120 articles. This number is refined first to 436 after further criteria are applied, and finally to 238 articles that meet the specific inclusion criteria for the review. Each step is a successive refinement aimed at isolating the most relevant studies for the physiological parameters in question.



### SI.1.8. Flag leaf senescence

Fig. SI. 7. This graph demonstrates the application of the breakpoint method to determine the onset of senescence in a Bangor low background ozone treatment study. The data points are plotted over time, with a noticeable breakpoint at the x-value of 195. This value indicates the transitional phase that signifies the start of senescence according to the model's prediction. The lines represent the fitted model's segments, both before and after the breakpoint, capturing the change in trend associated with the senescing process.

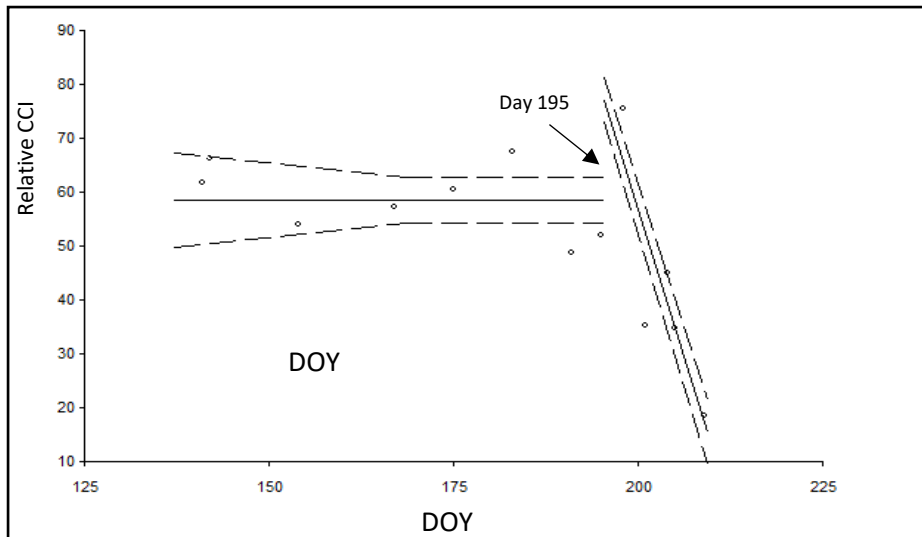


Fig. SI. 8. Leaf senescence profiles (Ostad, Sweden) simulated by the empirical (minimum of  $f_{O_3}$  and  $leaf\ f_{phen}$ ) and mechanistic ( $f_{LS}$ ) approaches compared to the start (SOS and end (EOS) of senescence as determined by the breakpoint method. Higher  $O_3$  treatment brought forwards SOS by 6 days and EOS by 12 days.

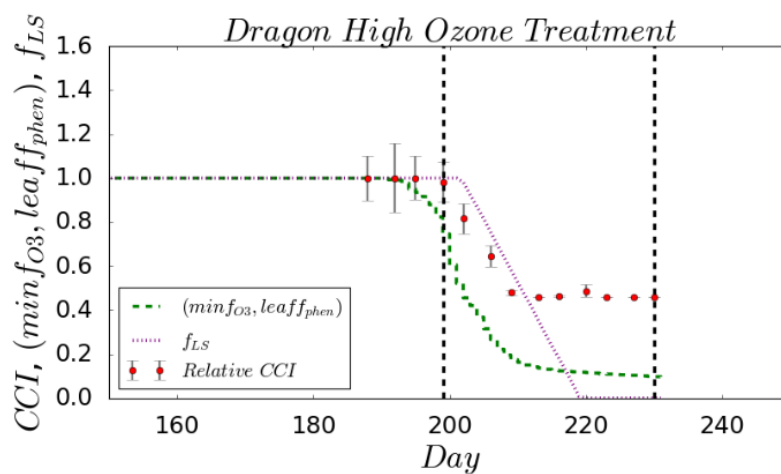
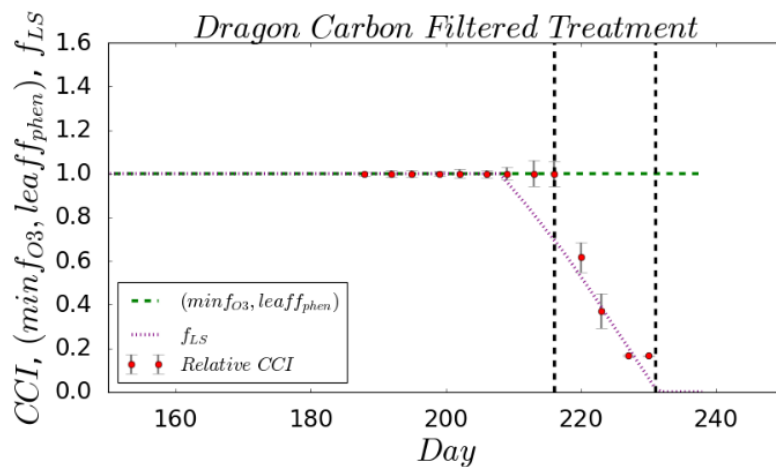


Table. Sl. 5. The SOS and EOS of the flag leaf determined from break-point analysis of the UK (Mulika and Skyfall,2015) and Swedish (Dragon,1997 and 1999) datasets

	Mulika 2015 (DOY)		Skyfall 2015	
	SOS	EOS	SOS	EOS
Bangor Treatment				
LB	195	210	204	211
LP	191	210	198	209
MB	195	210	201	210
MP	191	210	195	209
HB	195	210	201	210
HP	191	210	195	209
VHB	195	209	191	209
VHP	183	209	183	209

	Dragon 1997 (DOY)		Dragon 1999 (DOY)	
	SOS	EO S	SOS	EOS
Ostad, Sweden Treatment				
CF	216	231	224	235
NF	220	231		
NF+	216	230	209	235
NF++	200	230		
NF+++	192	230		

N.B: 'low background' (LB), 'low peak' (LP), 'medium background' (MB), 'medium peak' (MP), 'high background' (HB), 'high peak' (HP), 'very high background, (VHB), and 'very high peak' (VHP)), 'charcoal-filtered (CF), non-filtered (NF), and non-filtered air with additional ozone (NF+, NF++,NF+++). 'Start of senescence' (SOS) and 'End of senescence' (EOS).

### Sl.1.9. Training and Test datasets

Table. Sl. 6. Composition of Training and Test Data Samples (Sets 1-5) Derived via Bootstrap Resampling. Each dataset entry follows the format:

CountryCode\_Year\_CultivarAbbreviation\_TreatmentType. For instance, BE\_1994\_Mi\_CF denotes a dataset from Belgium in the year 1994, involving the Minaret cultivar, subjected to carbon-filtered treatment.

Set1			
Sample no.	Training datasets	Sample no.	Testing datasets
1	BE_1994_Mi_CF	7	FI_1993_Sa_CF
2	BE_1994_Mi_NF	11	SE_1988_Dr_NF++
2	BE_1994_Mi_NF	12	SE_1994_Dr_NF+
3	BE_1995_Mi_NF	14	SE_1995_Dr_NF
4	BE_1996_Mi_CF	18	BA_2015_Sk_LB
5	FI_1991_Sa_NF	20	BA_2015_Sk_MB
6	FI_1992_Sa_NF	23	BA_2015_Sk_HP
8	FI_1993_Sa_NF+	26	BE_1994_Mi_NF
8	FI_1993_Sa_NF+	29	BE_1996_Mi_NF
9	SE_1987_Dr_NF	32	FI_1993_Sa_NF
9	SE_1987_Dr_NF	41	SE_1999_Dr_NF+
9	SE_1987_Dr_NF	43	BA_2015_Mu_LP
10	SE_1988_Dr_NF	45	BA_2015_Mu_MP
13	SE_1994_Dr_NF+++	47	BA_2015_Mu_LP
15	SE_1997_Dr_CF	48	BA_2015_Mu_VHB
15	SE_1997_Dr_CF	49	BA_2015_Mu_VHP
15	SE_1997_Dr_CF	50	BA_2016_Sk_L1
16	SE_1997_Dr_NF++	51	BA_2016_Sk_L2
16	SE_1997_Dr_NF++	54	BA_2016_Sk_VH
17	SE_1999_Dr_CF		
19	BA_2015_Sk_LP		
21	BA_2015_Sk_MP		
22	BA_2015_Sk_HB		
22	BA_2015_SK_HB		
24	BA_2015_Sk_VHB		

25	BA_2015_Sk_VHP
25	BA_2015_Sk_VHP
25	BA_2015_Sk_VHP
27	BE_1995_Mi_NF
28	BE_1996_Mi_CF
28	BE_1996_Mi_CF
30	FI_1991_Sa_CF
31	FI_1992_Sa_NF+
33	SE_1987_Dr_CF
34	SE_1987_Dr_NF+
35	SE_1988_Dr_CF
36	SE_1988_Dr_NF+
36	SE_1988_Dr_NF+
37	SE_1994_Dr_NF
38	SE_1994_Dr_NF++
39	SE_1997_Dr_NF
39	SE_1997_Dr_NF
39	SE_1997_Dr_NF
40	SE_1997_Dr_NF++
42	BA_2015_Mu_LB
42	BA_2015_Mu_LB
44	BA_2015_Mu_MB
46	BA_2015_Mu_HB
46	BA_2015_Mu_HB
46	BA_2015_Mu_HB
52	BA_2015_Sk_M
52	BA_2016_Sk_M
53	BA_2016_Sk_VH
53	BA_2016_Sk_VH

Set 2			
Sample no.	Training datasets	Sample no.	Testing datasets

2	BE_1994_Mi_NF	1	BE_1994_Mi_CF
3	BE_1995_Mi_NF	5	FI_1991_Sa_NF
4	BE_1996_Mi_CF	7	FI_1993_Sa_CF
26	BE_1994_Mi_NF	12	SE_1994_Dr_NF+
27	BE_1995_Mi_NF	16	SE_1997_Dr_NF++
28	BE_1996_Mi_CF	19	BA_2015_Sk_LP
28	BE_1996_Mi_CF	25	BA_2015_Mu_VHP
4	FI_1991_Sa_NF	29	BE_1996_Mi_NF
6	FI_1992_Sa_NF	30	FI_1991_Sa_CF
6	FI_1993_Sa_NF+	36	SE_1988_Dr_NF+
6	FI_1993_Sa_NF+	38	SE_1994_Dr_NF++
8	FI_1993_Sa_NF+	42	BA_2015_Mu_LB
31	FI_1992_Sa_NF+	44	BA_2015_Mu_MB
31	FI_1993_Sa_NF	45	BA_2015_Mu_MP
9	SE_1987_Dr_NF	48	BA_2015_Mu_VHB
9	SE_1987_Dr_NF	52	BA_2016_Sk_M
33	SE_1987_Dr_CF	53	BA_2016_Sk_VH
33	SE_1987_Dr_CF	54	BA_2016_Sk_VH
34	SE_1987_Dr_NF+		
10	SE_1988_Dr_NF		
10	SE_1988_Dr_NF		
10	SE_1988_Dr_NF		
11	SE_1988_Dr_NF++		
35	SE_1988_Dr_CF		
50	SE_1988_Dr_NF		
13	SE_1994_Dr_NF+++		
37	SE_1994_Dr_NF		
14	SE_1995_Dr_NF		
39	SE_1997_Dr_NF		
39	SE_1997_Dr_NF		
39	SE_1997_Dr_NF		
40	SE_1997_Dr_NF++		
15	SE_1997_Dr_CF		

32	SE_1999_Dr_NF+
41	SE_1999_Dr_NF+
17	SE_1999_Dr_CF
17	SE_1999_Dr_CF
14	BA_2015_Sk_LB
18	BA_2015_Sk_LB
20	BA_2015_Sk_MB
21	BA_2015_Sk_MP
21	BA_2015_Sk_HB
22	BA_2015_Sk_HB
23	BA_2015_Sk_HP
24	BA_2015_Sk_VHB
43	BA_2015_Mu_LP
46	BA_2015_Mu_HB
46	BA_2015_Mu_VHB
47	BA_2015_Mu_LP
47	BA_2015_Mu_VHB
49	BA_2015_Mu_VHP
50	BA_2016_Sk_L1
50	BA_2016_Sk_L2
51	BA_2016_Sk_L2

Set 3			
Sample no.	Training datasets	Sample no.	Testing datasets
1	BE_1994_Mi_CF	2	BE_1994_Mi_NF
4	BE_1996_Mi_CF	3	BE_1995_Mi_NF
4	BE_1996_Mi_CF	7	FI_1993_Sa_CF
4	BE_1996_Mi_CF	8	FI_1993_Sa_NF+
26	BE_1994_Mi_NF	10	SE_1988_Dr_NF
27	BE_1995_Mi_NF	12	SE_1994_Dr_NF+
27	BE_1995_Mi_NF	18	BA_2015_Sk_LB
27	BE_1995_Mi_NF	24	BA_2015_Sk_VHB

28	BE_1996_Mi_CF	29	BE_1996_Mi_NF
5	FI_1991_Sa_NF	30	FI_1991_Sa_CF
5	FI_1991_Sa_NF	37	SE_1994_Dr_NF
5	FI_1991_Sa_NF	40	SE_1997_Dr_NF++
6	FI_1992_Sa_NF	43	BA_2015_Mu_LP
31	FI_1992_Sa_NF+	46	BA_2015_Mu_HB
32	FI_1993_Sa_NF	48	BA_2015_Mu_VHB
32	FI_1993_Sa_NF	50	SE_1988_Dr_NF
32	FI_1993_Sa_NF		
9	SE_1987_Dr_NF		
33	SE_1987_Dr_CF		
34	SE_1987_Dr_NF+		
34	SE_1987_Dr_NF+		
35	SE_1988_Dr_CF		
36	SE_1988_Dr_NF+		
11	SE_1988_Dr_NF++		
13	SE_1994_Dr_NF+++		
38	SE_1994_Dr_NF++		
38	SE_1994_Dr_NF++		
14	SE_1995_Dr_NF		
15	SE_1997_Dr_CF		
16	SE_1997_Dr_NF++		
39	SE_1997_Dr_NF		
17	SE_1999_Dr_CF		
41	SE_1999_Dr_NF+		
19	BA_2015_Sk_LP		
20	BA_2015_Sk_MB		
21	BA_2015_Sk_MP		
22	BA_2015_Sk_HB		
23	BA_2015_Sk_HP		
23	BA_2015_Sk_HP		
25	BA_2015_Mu_VHP		
25	BA_2015_Mu_VHP		

42	BA_2015_Mu_LB
42	BA_2015_Mu_LB
42	BA_2015_Mu_LB
44	BA_2015_Mu_MB
45	BA_2015_Mu_MP
47	BA_2015_Mu_VHB
49	BA_2015_Mu_VHP
51	BA_2016_Sk_L2
52	BA_2016_Sk_M
52	BA_2016_Sk_M
53	BA_2016_Sk_VH
54	BA_2016_Sk_VH
54	BA_2016_Sk_VH

Set4			
Sample no.	Training datasets	Sample no.	Testing datasets
4	BE_1996_Mi_CF	1	BE_1994_Mi_CF
4	BE_1996_Mi_CF	2	BE_1994_Mi_NF
24	BE_1996_Mi_CF	3	BE_1995_Mi_NF
28	BE_1996_Mi_NF	6	FI_1992_Sa_NF
28	BE_1996_Mi_NF	7	FI_1993_Sa_CF
29	BE_1996_Mi_NF	8	FI_1993_Sa_NF+
29	BE_1996_Mi_NF	9	SE_1987_Dr_NF
5	FI_1991_Sa_NF	10	SE_1988_Dr_NF
5	FI_1991_Sa_NF	12	SE_1994_Dr_NF+
5	FI_1991_Sa_NF	15	SE_1997_Dr_CF
31	FI_1992_Sa_NF+	19	BA_2015_Sk_LP
32	FI_1993_Sa_NF	22	BA_2015_Sk_HB
11	SE_1988_Dr_NF++	25	BA_2015_Mu_VHP
11	SE_1988_Dr_NF++	26	BE_1994_Mi_NF
11	SE_1988_Dr_NF++	27	BE_1995_Mi_NF
13	SE_1994_Dr_NF+++	30	FI_1991_Sa_CF

13	SE_1994_Dr_NF+++	34	SE_1987_Dr_NF+
14	SE_1995_Dr_NF	43	BA_2015_Mu_LP
14	SE_1995_Dr_NF	45	BA_2015_Mu_MP
16	SE_1997_Dr_NF++	47	BA_2015_Mu_VHB
17	SE_1999_Dr_CF		
17	SE_1999_Dr_CF		
33	SE_1987_Dr_CF		
35	SE_1988_Dr_CF		
35	SE_1988_Dr_CF		
35	SE_1988_Dr_CF		
36	SE_1988_Dr_NF+		
36	SE_1988_Dr_NF+		
37	SE_1994_Dr_NF		
37	SE_1994_Dr_NF		
38	SE_1994_Dr_NF++		
39	SE_1997_Dr_NF		
40	SE_1997_Dr_NF++		
41	SE_1999_Dr_NF+		
50	SE_1988_Dr_NF		
50	SE_1988_Dr_NF		
18	BA_2015_Sk_LB		
20	BA_2015_Sk_MB		
21	BA_2015_Sk_MP		
21	BA_2015_Sk_MP		
23	BA_2015_Sk_HP		
42	BA_2015_Mu_LB		
42	BA_2015_Mu_LB		
44	BA_2015_Mu_MB		
46	BA_2015_Mu_HB		
48	BA_2015_Mu_VHB		
49	BA_2015_Mu_VHP		
51	BA_2016_Sk_L2		
52	BA_2016_Sk_M		

52	BA_2016_Sk_M
53	BA_2016_Sk_VH
53	BA_2016_Sk_VH
54	BA_2016_Sk_VH
54	BA_2016_Sk_VH

Set 5			
Sample no.	Training datasets	Sample no.	Testing datasets
1	BE_1994_Mi_CF	2	BE_1994_Mi_NF
1	BE_1994_Mi_CF	3	BE_1995_Mi_NF
1	BE_1994_Mi_CF	4	BE_1996_Mi_CF
26	BE_1994_Mi_NF	5	FI_1991_Sa_NF
26	BE_1994_Mi_NF	6	FI_1992_Sa_NF
27	BE_1995_Mi_NF	10	SE_1988_Dr_NF
27	BE_1995_Mi_NF	11	SE_1988_Dr_NF++
28	BE_1996_Mi_CF	12	SE_1994_Dr_NF+
28	BE_1996_Mi_CF	13	SE_1994_Dr_NF+++
30	FI_1991_Sa_CF	14	SE_1995_Dr_NF
31	FI_1992_Sa_NF+	15	SE_1997_Dr_CF
31	FI_1992_Sa_NF+	19	BA_2015_Sk_LP
7	FI_1993_Sa_CF	20	BA_2015_Sk_MB
8	FI_1993_Sa_NF+	23	BA_2015_Sk_HP
9	SE_1987_Dr_NF	24	BE_1996_Mi_NF
16	SE_1997_Dr_NF++	25	BA_2015_Mu_VHP
16	SE_1997_Dr_NF++	29	BE_1996_Mi_NF
16	SE_1997_Dr_NF++	32	FI_1993_Sa_NF
16	SE_1997_Dr_NF++	33	SE_1987_Dr_CF
17	SE_1999_Dr_CF	40	SE_1997_Dr_NF++
34	SE_1987_Dr_NF+	42	BA_2015_Mu_LB
35	SE_1988_Dr_CF	44	BA_2015_Mu_MB
36	SE_1988_Dr_NF+	53	BA_2016_Sk_VH
36	SE_1988_Dr_NF+		

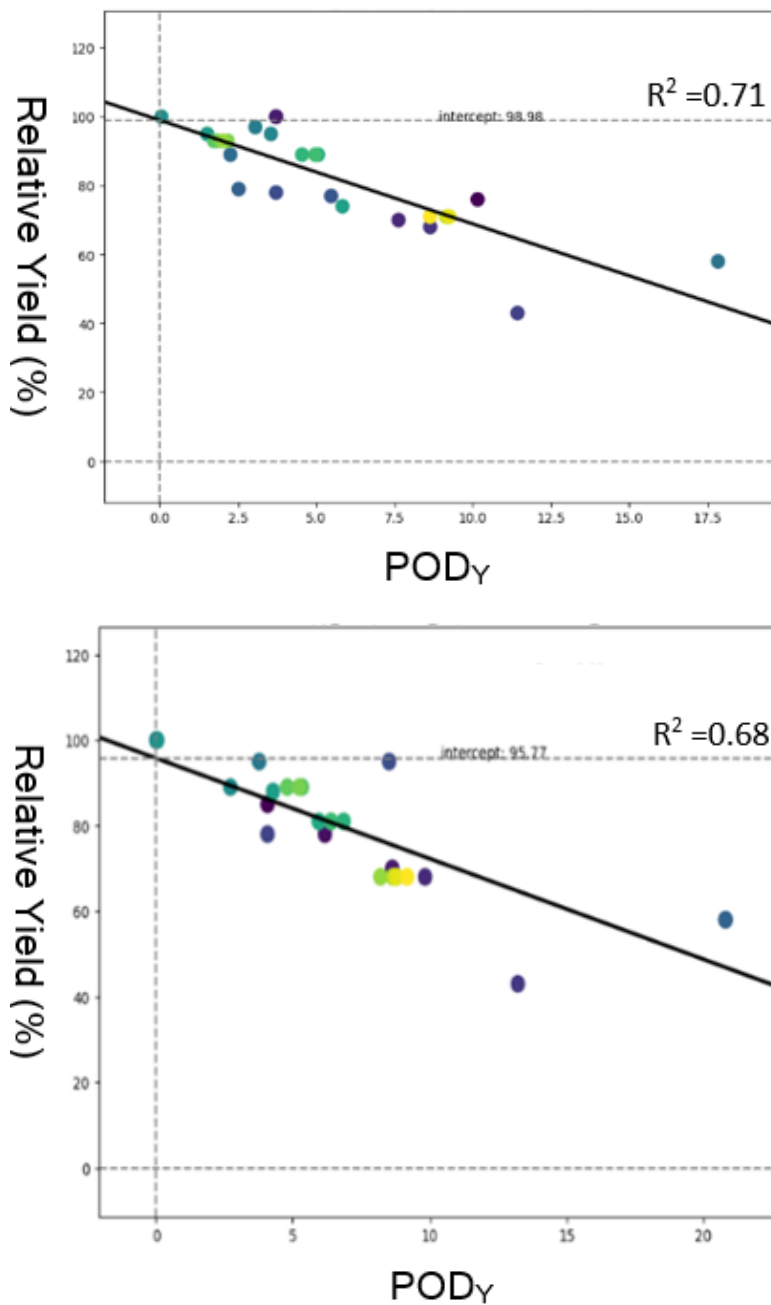
36	SE_1988_Dr_NF+
36	SE_1988_Dr_NF+
37	SE_1994_Dr_NF
38	SE_1994_Dr_NF++
39	SE_1997_Dr_NF
41	SE_1999_Dr_NF+
50	SE_1988_Dr_NF
50	SE_1988_Dr_NF
18	BA_2015_Sk_LB
21	BA_2015_Sk_MP
21	BA_2015_Sk_MP
22	BA_2015_Mu_VHP
22	BA_2015_Mu_VHP
43	BA_2015_Mu_LP
45	BA_2015_Mu_MP
46	BA_2015_Mu_HB
46	BA_2015_Mu_HB
46	BA_2015_Mu_HB
47	BA_2015_Mu_VHB
47	BA_2015_Mu_VHB
48	BA_2015_Mu_VHB
49	BA_2015_Mu_VHP
49	BA_2015_Mu_VHP
51	BA_2016_Sk_L2
51	BA_2016_Sk_L2
52	BA_2016_Sk_M
54	BA_2016_Sk_VH

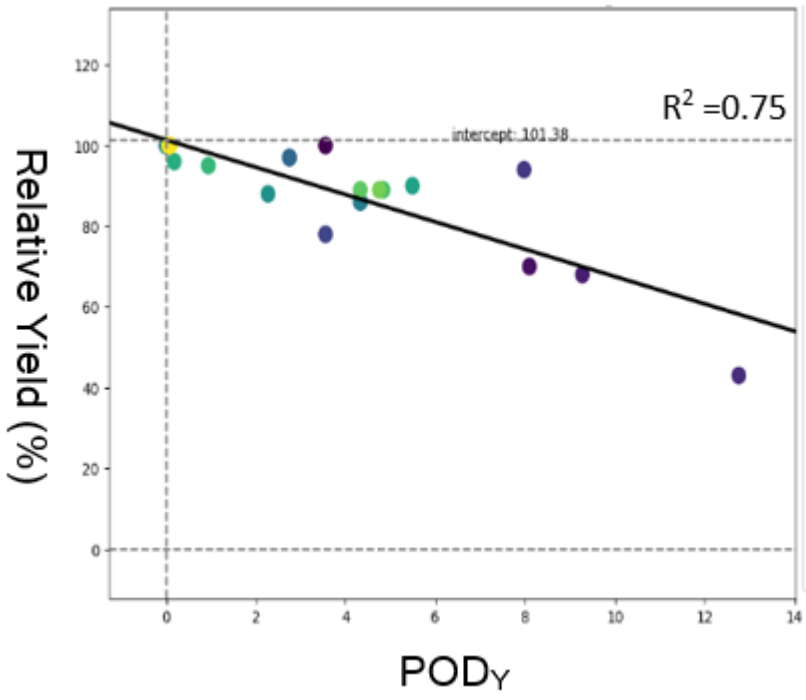
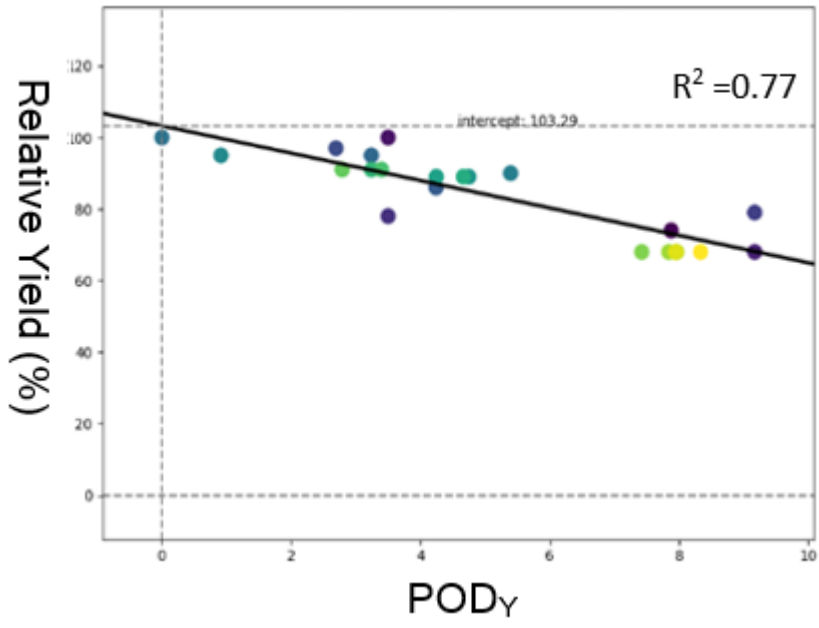
N.B.: For sets 1 -5 of training and testing, the countries included are Belgium (BE), Finland (FI), Sweden (SE), and Bangor (BA). The wheat crop cultivars studied are Minaret (Mi), Satu (Sa), Dragon (Dr), Skyfall (Sk), and Mulika (Mu). The treatments applied are categorized into: 'low background' (LB), 'low peak' (LP), 'medium background' (MB), 'medium peak' (MP), 'high background' (HB), 'high

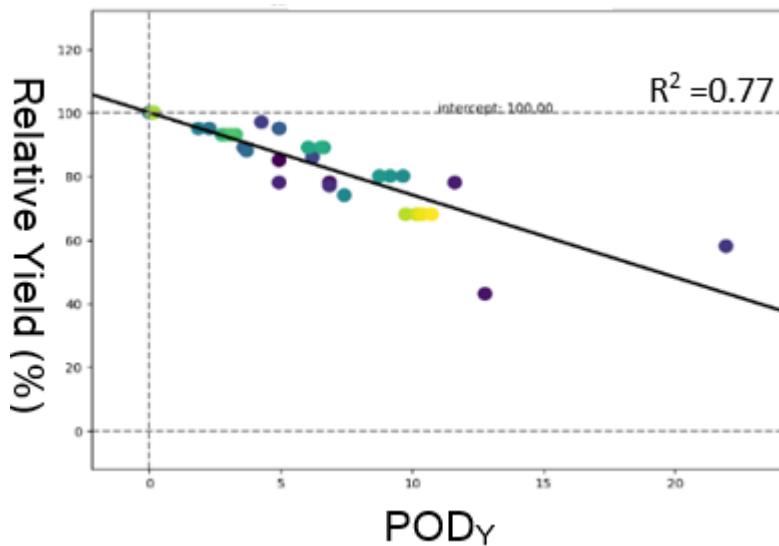
peak' (HP), 'very high background' (VHB), and 'very high peak' (VHP). 'Charcoal-filtered' (CF), 'non-filtered' (NF), and 'non-filtered air with incremental levels of added ozone' (NF+, NF++, NF+++).

SI.1.10. Flux-response relationships for relative wheat yield derived using the  $A_{net}g_{sto}mech$ .

Fig. SI. 9. Flux-response relationships for relative wheat yield derived using the  $A_{net}g_{sto}mech$  to simulate the  $POD_6$  metric.







Weighted average equation:

$$W = \frac{\sum_{i=1}^n w_i X_i}{\sum_{i=1}^n w_i} \quad \text{Eq. SI. 7}$$

Where,  $w_i$  (weight applied to  $x$  values) =  $\exp(-(\text{error}/10)^2)$  maximum error and error is calculated during the automated calibration exercise,

$n$  = number of terms to be averaged,

$X_i$  = data values to be averaged

#### SI.1.11. Diurnal and maximum $A_{net}$

Fig. SI. 10. The background and peak  $O_3$  treatments dataset for Mulika and Skyfall wheat cultivars fumigated in Bangor over the 2015 and 2016 growing seasons were used to plot a) observed against modelled  $A_{net}$  values estimated using the two different  $A_{net}g_{sto}$  models. The black dashed line is the 1:1 line, where the best match between modelled and observed values would lie. The coefficient of determination ( $R^2$ ) is provided for each model, with an  $R^2$  of 0.86 for the background and an  $R^2$  of 0.83 for the background and  $R^2$  of 0.32 and  $R^2$  of 0.56 for the peak treatments respectively for the  $A_{net}g_{sto}emp$ , (left) and  $A_{net}g_{sto}mech$  (right). b) Average daily maxima  $A_{net}$  values simulated over the flag leaf life span by the two  $A_{net}g_{sto}$  models and observed maxima  $A_{net}$  values were also shown. Red circles represent the observed data points, and black vertical lines connected to the red circles illustrate the standard error associated with the observed data.

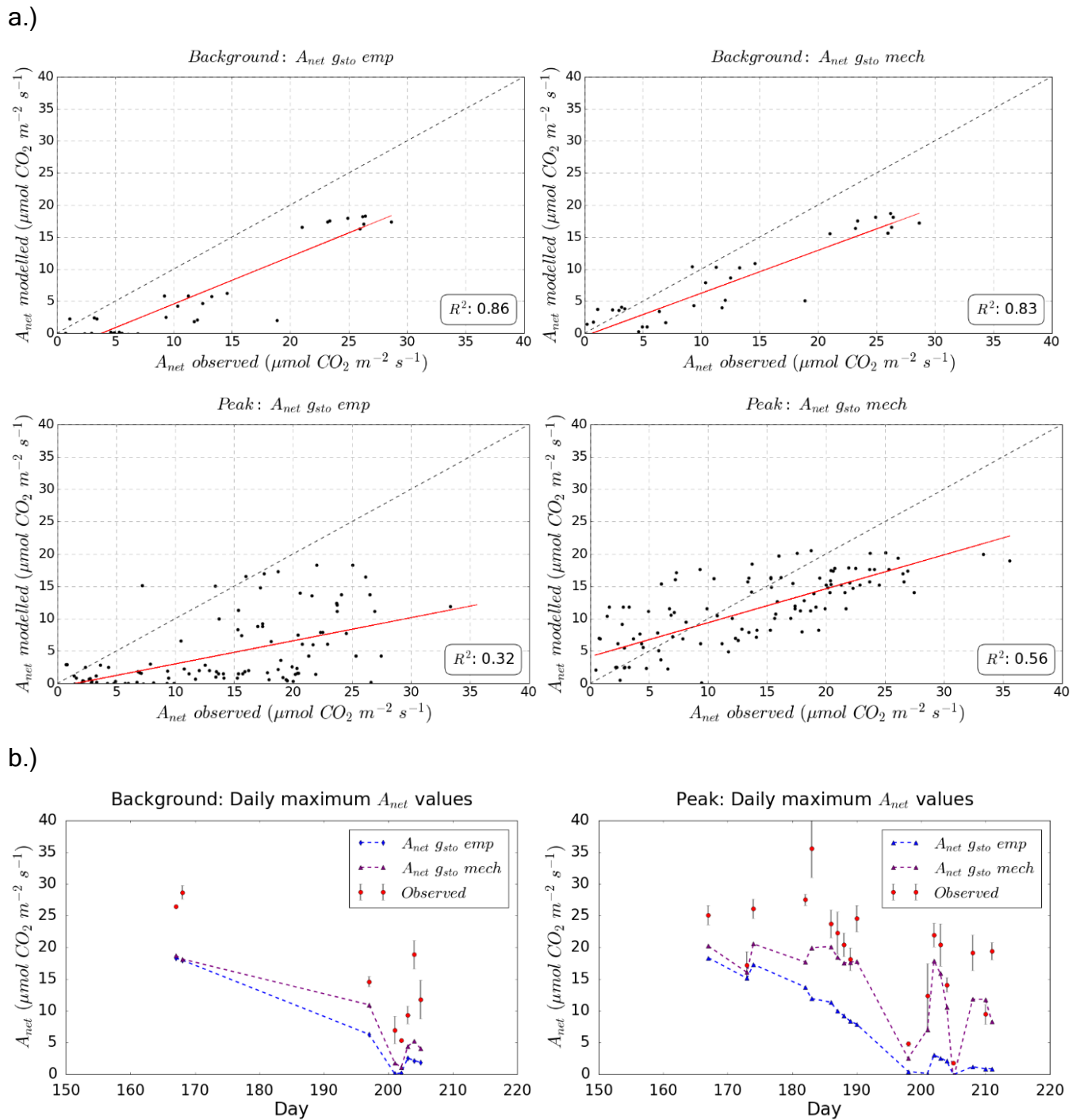


Fig. SI. 11. Average diurnal  $g_{sto}$  values simulated over the flag leaf life span by each of the three  $g_{sto}$  models for the background and peak ozone treatments for Mulika and Skyfall wheat cultivars fumigated in Bangor over the 2015 and 2016 growing season. Also shown are observed  $g_{sto}$  data collected and averaged over the same period. The observed  $g_{sto}$  values are indicated by red dots, with the standard error represented by the vertical black lines. Predicted  $g_{sto}$  values are plotted as blue and purple dashed lines, corresponding to the empirical ( $A_{net}g_{sto}emp$ ) and mechanistic ( $A_{net}g_{sto}mech$ ) stomatal conductance models, respectively.

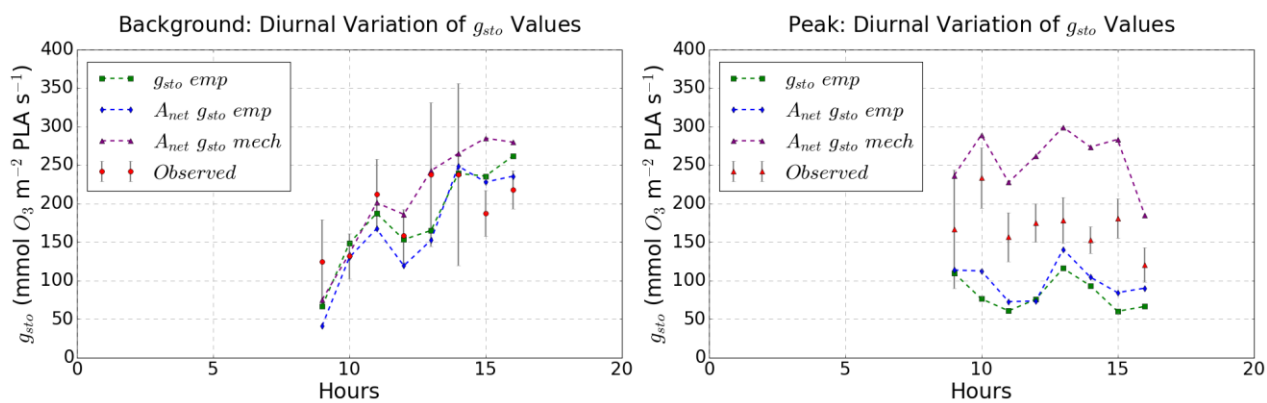
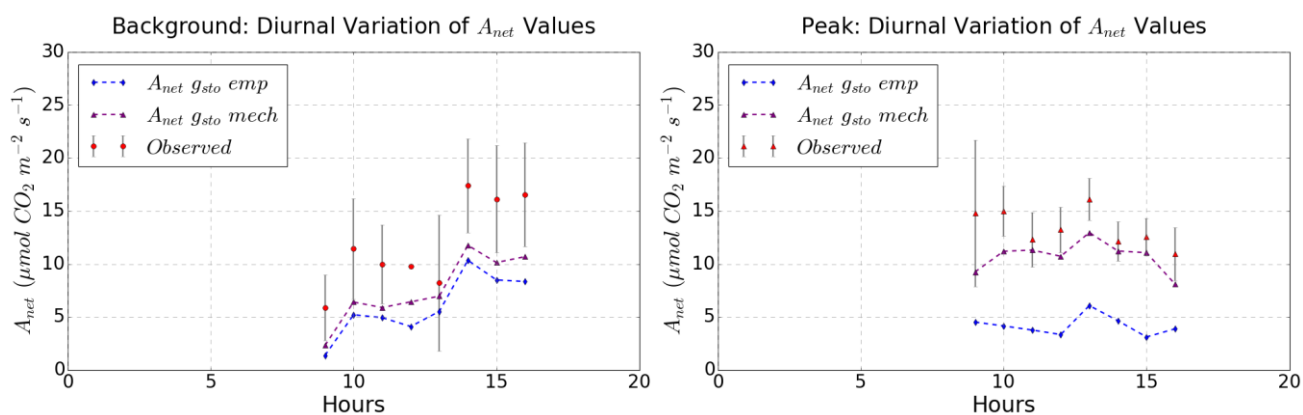


Fig. SI. 12. Average diurnal plots of  $A_{net}$  for the days 167-205 ( $n=32$ ) for background  $O_3$  treatments and 167-211 for peak  $O_3$  treatments ( $n= 112$ ) each of the two  $A_{net}g_{sto}$  models. The observed  $A_{net}$  values are indicated by red dots, with the standard error represented by the vertical black lines. Predicted  $A_{net}$  values are plotted as blue and purple dashed lines, corresponding to the empirical ( $A_{net}g_{sto}emp$ ) and mechanistic ( $A_{net}g_{sto}mech$ ) stomatal conductance models, respectively.



### 3. The development, parametrisation, and evaluation of the DO<sub>3</sub>SE Crop model for Xiaoji, China

#### 3.1 Abstract

A substantial body of empirical evidence exists to suggest that elevated O<sub>3</sub> levels are causing significant impacts on wheat yields at sites representative of highly productive arable regions of China. Here, the DO<sub>3</sub>SE model (designed to estimate total- and stomatal- O<sub>3</sub> deposition for risk assessment) was extended to incorporate a coupled  $A_{net}g_{sto}$  model to estimate O<sub>3</sub> uptake, an O<sub>3</sub> damage module (that impacts instantaneous  $A_{net}$  and the timing and rate of senescence), and a crop phenology, carbon allocation and growth model based on the JULES-Crop model. The model structure allows scaling from the leaf to the canopy to allow for multiple leaf populations and canopy layers. The DO<sub>3</sub>SE-crop model is calibrated and parametrised using O<sub>3</sub> fumigation data from Xiaoji, China for the year 2008 and for an O<sub>3</sub> tolerant and sensitive cultivar. The calibrated model can simulate key physiological variables, crop development, and yield with a good level of accuracy compared to experimental observations. DO<sub>3</sub>SE-crop accurately depicted the difference in yield reductions under ambient and elevated O<sub>3</sub> treatments for wheat cultivars Y16 (tolerant) and Y2 (sensitive) with regressions of modelled and observed absolute yields resulting in an R<sup>2</sup> of 0.99 and an RMSE of 9.27 g/m<sup>2</sup>. Further, when evaluated for 2007 and 2009 for all cultivars, the DO<sub>3</sub>SE-crop model simulated O<sub>3</sub> induced yield losses of 4-25% compared to observed yield losses of 12-34% observed, with an R<sup>2</sup> of 0.73 and an RMSE of 58.41 g/m<sup>2</sup>. Additionally, our results indicate that the variance in yield reduction is primarily attributed to the premature decrease in carbon assimilation to the grains under elevated O<sub>3</sub> exposure. This is linked to accelerated leaf senescence, which brings leaf senescence forward by 7-9 days under elevated O<sub>3</sub> treatments.

### 3.2 Introduction

Ground-level ozone ( $O_3$ ) is the most critical air pollutant causing global crop damage. Elevated  $O_3$  concentrations are particularly problematic in Asia, where decades of rapid economic growth, industrialisation, and urbanisation have seen sharp rises in pollutant emissions associated with burning fossil fuels (Lin et al., 2017). At the same time, climate change is considered a substantial threat to arable productivity through changes in average and extreme temperature and precipitation profiles across the region (IPCC, 2007 & 2014). Reductions in precipitation are considered responsible for poor harvests in recent years (Liu et al., 2010), and rising temperatures that reduce the length of the crop growing season are thought to have caused losses in crop yield (Malhi et al., 2021). There is now substantial evidence showing that stresses from ozone pollution and climate variability interact, causing either additive, synergistic, or antagonistic responses in crop development, growth, and yield (Sillmann et al., 2021). The threat posed by these stresses is a particular cause for concern in Asia since the continent contributes approximately 43% of the global wheat production, with China contributing the highest production levels at 17% (Feng et al., 2021).  $O_3$  levels are rising substantially in important wheat-growing areas in China, such as the North China Plain and the Yangtze River Delta (Li et al., 2020; Zhang et al., 2023). This led to the implementation in 2013 of a range of policies to try to reduce  $O_3$  precursor emissions across China e.g., a comprehensive management plan to control volatile organic compounds (VOCs) from key industries, an atmospheric pollution prevention and control law of the People's Republic of China and the 2020 VOCs Management Plan (Li et al., 2021). As a result, nitrogen oxide ( $NO_x$ ) emissions, an important  $O_3$  precursor, have decreased significantly from 2013 to 2017 by 21% (Li et al., 2021). By contrast, VOCs have only slightly decreased by 2% over the same time period. Since China has a VOC-limited  $O_3$  regime, the reductions in  $NO_x$  lead to rather insignificant changes in  $O_3$  concentration (Li et al., 2021), though evidence suggests that reductions in  $O_3$  may be higher in rural than urban areas (Lee et al., 2020). This implies future policies to tackle ground-level  $O_3$  pollution in China need to increase their focus on reducing VOCs along with  $NO_x$  (Lee et al., 2020).

At present, methods to assess the risk to crop productivity from changes in  $O_3$  and climate variables have used a variety of methods.  $O_3$  risk assessment methods have

in the past relied heavily on dose-response relationships, empirically derived relationships that assess changes in a response variable (most commonly yield) against an ozone exposure metric (concentration or, more recently, flux-based indices). By contrast, methods to assess the impact of climate variables (most commonly changes in temperature, precipitation, and CO<sub>2</sub> concentration) tend to use crop models since these allow the integration of the combined effect of a number of different variables acting simultaneously to affect crop development, growth and yield (Schauberger et al., 2019). There has been a growing awareness of the need to integrate the ozone effect within crop models so that a holistic assessment of the combined impacts resulting from these stressors can be achieved (Tao et al., 2017; Emberson et al., 2018; Schauberger et al., 2019).

The DO<sub>3</sub>SE model is an ozone deposition model that can be embedded within atmospheric chemistry transport models (e.g. (Simpson et al., 2012)) and uses either a multiplicative- or coupled  $A_{net}g_{sto}$  model to estimate stomatal ozone flux. Accumulated stomatal ozone flux has been successfully used as a damage metric (POD<sub>y</sub> - Phytotoxic Ozone Dose over a threshold  $y$  (LRTAP, 2017)) to predict ozone-induced yield loss (Pande et al., sub). The ability of the DO<sub>3</sub>SE model to simulate  $A_{net}$ , and the inclusion of a process-based ozone damage module for both instantaneous  $A_{net}$  and early and enhanced senescence (after (Ewert and Porter, 2000)) lends itself to the development of the DO<sub>3</sub>SE model as a process-based crop model. The inclusion of resistance algorithms that can assess the transport of O<sub>3</sub> concentrations from a reference height above a canopy down to the canopy top, means the model can easily be embedded within existing atmospheric chemistry transport schemes and hence applied for regional or global scale O<sub>3</sub> risk assessment whilst also accurately modelling O<sub>3</sub> deposition.

In this study, the development of a new 'DO<sub>3</sub>SE-Crop' model was described. The stomatal deposition component of the DO<sub>3</sub>SE model, so that both CO<sub>2</sub> uptake for carbon assimilation, as well as ozone uptake via the stomata, can be modelled consistently was modified. Further, we have incorporated the UK JULES crop model (Osborne et al., 2015) to allocate assimilated carbon to plant components (roots, leaves, stems, and harvest organs) according to the crop development stage. We also take account of the modifying effect of ozone on instantaneous  $A_{net}$  as well as the onset and rate of leaf senescence and timing of crop maturity through the

incorporation of algorithms developed by (Ewert and Porter, 2000). The UK JULES crop model is used since this is the UK land surface exchange scheme in the UK Earth System Model (UKESM) (Osborne et al., 2015), which has recently been developed to include the exchange and impact of trace gases (including O<sub>3</sub>) along with other biogeochemical cycling between the atmosphere and the land surface (Leung et al., 2020). This would allow a comparison of the UK JULES Crop model, which are based on (Sitch et al., 2007), with the alternative O<sub>3</sub> damage mechanisms used within DO<sub>3</sub>SE-crop.

In this study, DO<sub>3</sub>SE-crop model, using an experimental FACE dataset collected in Xiaoji, China, was calibrated and evaluated. This allows us to investigate the ability of the model to simulate O<sub>3</sub> damage for a global region where crop productivity is severely threatened by both ozone pollution and climate change. The key objectives of the paper are as follows: i). assess the ability of DO<sub>3</sub>SE-Crop to simulate key physiological variables (and their seasonal and diurnal profiles), crop development, biomass, and yield, ii). the ability of DO<sub>3</sub>SE-crop to simulate O<sub>3</sub> deposition for different canopy layers, iii). the ability of DO<sub>3</sub>SE-crop to estimate the difference in yield loss caused by instantaneous versus long-term O<sub>3</sub> impact, iv). the ability of the model to simulate the effects of ozone on the start and end of senescence, and v). the applicability of the prescribed UK JULES crop parameters for Chinese conditions and their ability to capture year-on-year variability in meteorology and O<sub>3</sub> and cultivar sensitivity.

### 3.3 Methods: DO<sub>3</sub>SE-Crop Model development, calibration and Evaluation

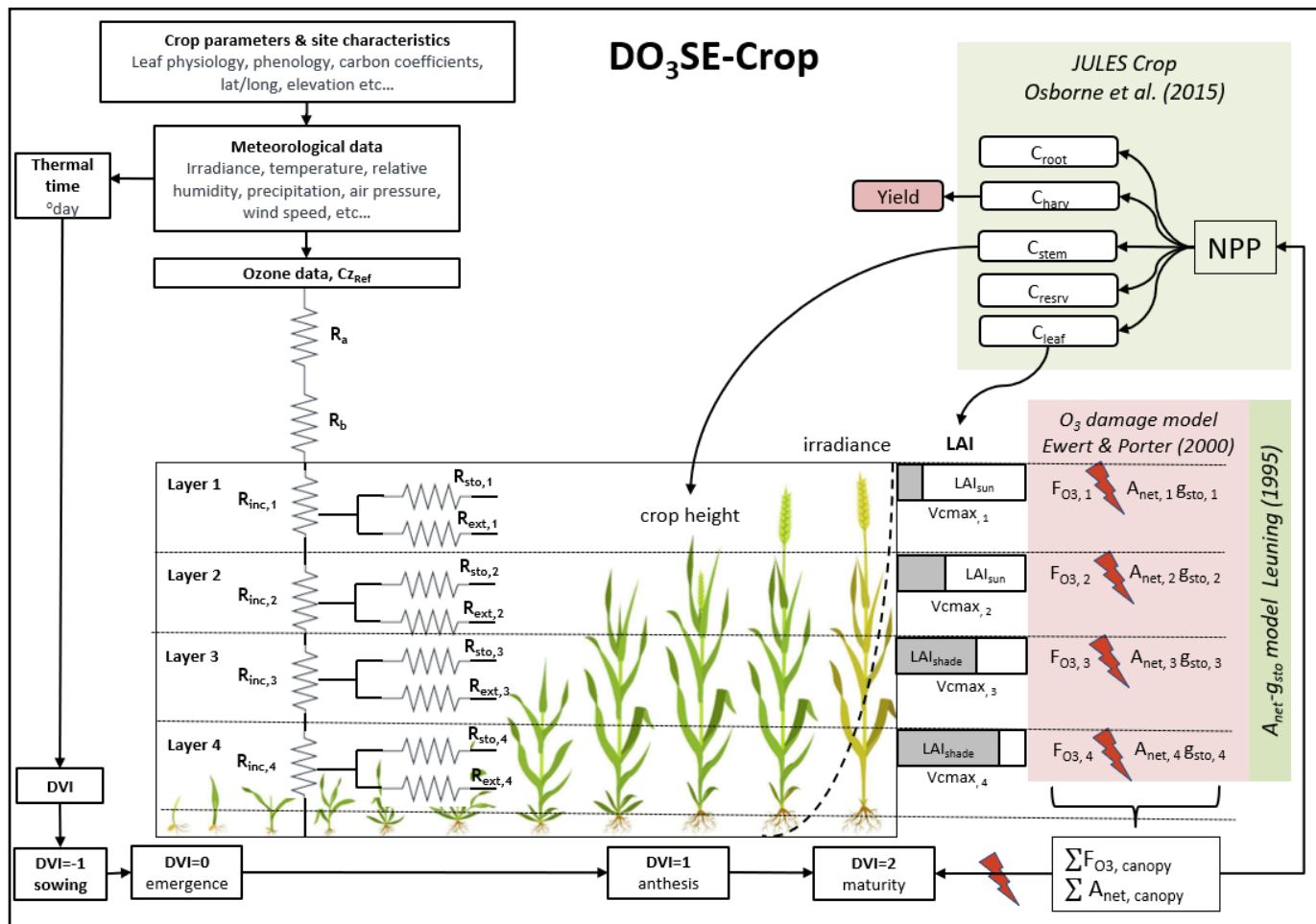
We describe the development and calibration of 'DO<sub>3</sub>SE-Crop', an ozone deposition model (Emberson et al., 2000; Simpson et al., 2012) that has been modified to simulate stomatal conductance from a coupled  $A_{net}g_{sto}$  (Leuning, 1995).  $A_{net}$  is simulated using a biochemical model (Farquhar et al., 1980; Sharkey et al., 2007). The DO<sub>3</sub>SE model has also been extended to include a photosynthetic-based crop model based on the UK JULES land surface crop model (Osborne et al., 2015) with ozone damage functions incorporated after (Ewert and Porter, 2000). DO<sub>3</sub>SE-Crop is designed to simulate O<sub>3</sub> deposition and stomatal uptake and the effects of O<sub>3</sub> and climate related variables on crop development, biomass, and yield. The DO<sub>3</sub>SE-Crop model has been developed to simulate wheat (*Triticum aestivum*) which is widely considered to be one of the most sensitive staple crops to ozone (Feng et al., 2018)

The key components of DO<sub>3</sub>SE Crop are illustrated in Fig. 18 and can be defined as i). crop phenology to ensure the correct length and timing of crop growth for carbon assimilation and ozone exposure; ii). leaf scale processes to ensure leaf level estimates of  $A_{net}$  and  $A_{net}g_{sto}$  for sunlit and shaded leaves are able to accurately model carbon assimilation and stomatal ozone flux and associated damage over the leaf life span; iii). leaf-to-canopy upscaling that incorporates a within canopy irradiance and ozone concentration gradient and iv). carbon allocation processes to ensure carbon is allocated correctly to different crop compartments (roots, leaves, stem, grain) throughout the growing season.

Fig. 8. Schematic of DO<sub>3</sub>SE-Crop model

The schematic presented encapsulates the DO<sub>3</sub>SE-Crop model. This model synthesizes site-specific agronomic parameters, including but not limited to, leaf physiology and developmental timing, alongside a suite of meteorological variables such as solar irradiance, ambient temperature, and atmospheric moisture content. The multi-layered canopy structure is modelled with discrete resistance factors for ozone influx at varying wheat crop canopy layers, facilitating a nuanced simulation of ozone dynamics relative to canopy layers. Progression through phenological phases is meticulously monitored using developmental vegetation indices (DVI), from the initiation of sowing to the crop maturity (senescence). This framework is interfaced

with the JULES-Crop model to compute the net primary productivity (NPP), with detailed partitioning across root ( $C_{root}$ ), harvest ( $C_{harv}$ ), stem ( $C_{stem}$ ), reserve ( $C_{resv}$ ), and leaf ( $C_{leaf}$ ). Embedded within this structure is an ozone damage model, informed by the methodology of Ewert & Porter (2000), which adjusts the leaf area index (LAI) and net photosynthetic rates across critical growth intervals, thereby affecting the cumulative yield output. This integrative approach is pivotal for explaining crop physiological responses under varying ozone concentrations, thereby informing adaptive management strategies in agriculture to mitigate air quality stressors.



### 3.3.1 DO<sub>3</sub>SE Crop Phenology

The DO<sub>3</sub>SE-Crop model uses thermal time ( $TT$ ) to define the rate of crop development in relation to the timing of three key developmental stages,  $TT_{emr}$  (the period from sowing to emergence),  $TT_{veg}$  (the period of emergence to start of grain filling), and  $TT_{rep}$  (the period from the start of grain filling to maturity) based on the method of Osborne et al. (2015).  $TT$  is calculated by estimating an effective temperature ( $T_{eff}$ ) using base ( $T_b$ ), optimum ( $T_o$ ), and maximum ( $T_m$ ) cardinal temperatures.

$$T_{eff} = \begin{cases} 0 & \text{for } T_{air} < T_b \\ T_{air} - T_b & \text{for } T_b \leq T_{air} \leq T_o \\ (T_o - T_b) \left(1 - \frac{T_{air} - T_o}{T_m - T_o}\right) & \text{for } T_o < T_{air} < T_m \\ 0 & \text{for } T_{air} \geq T_m \end{cases} \quad \text{Eq. 20}$$

Where,  $T_{air}$  is the surface air temperature in °C,  $T_{eff}$  is at a maximum when  $T_{air} = T_o$ , this point denotes the highest developmental rate.  $T_{eff}$  declines as the temperature falls or rises above  $T_o$ , with a linear decrease in crop development.  $T_{eff}$  is zero, i.e. no development, when  $T_{air}$  falls below  $T_b$  and or rises above  $T_m$  i.e.,  $T_m < T_{air} < T_b$ . During the sowing to emergence phase, development is dependent on  $T_b$ , whereas during the vegetative and reproductive phase, development depends on  $T_m$  or  $T_o$ .

Winter wheat requires vernalisation (a period of exposure to low temperatures during germination to accelerate flowering). Vernalisation alters the length  $TT_{veg}$  and hence flowering initiation, with subsequent effects on later growth stages such as heading. Vernalisation occurs when the minimum ( $VT_{min}$ ) and maximum ( $VT_{max}$ ) daily temperature is less than 15°C and 30°C respectively (Zheng et al., 2015). Accumulated vernalised days ( $V_{dd}$ ) are calculated as the sum of vernalised and devernalised days from emergence to the start of anthesis (Zheng et al., 2015).

$$V_{dd} = \sum(V - V_d) \quad \text{Eq. 21}$$

where;

$$V = \left( 1.4 - 0.778 * T_{air}, 0.5 + 13.44 \frac{T_{air}}{(T_{max} - T_{min} + 3)^2} \right) \text{ for } VT_{max} < 30^\circ\text{C and } VT_{min} < 15^\circ\text{C}$$

$$V_d = (\min(0.5(T_{max} - 30), V_{prev}), V_{prev}) \text{ for } VT_{max} > 30^\circ\text{C and } V_{dd} < 10 \text{ days}$$

The vernalisation factor ( $VF$ ) decreases from 1 to 0 as ( $V_{dd}$ ) increases.  $VF$  depends on a cultivar-specific vernalisation coefficient ( $PIV$ ) as described by Eq. 22.

$$VF = 1 - (0.0054545 * PIV + 0.0003) * (50 - V_{dd}) \quad \text{Eq. 22}$$

Photoperiod ( $PP$ ) or day length also affects the occurrence and timing of the flowering stage and is calculated according to latitude using standard solar geometry to estimate daylength (Jones, 1992). The photoperiod factor ( $PF$ ) represents the sensitivity to  $PP$  which decreases from 1 to 0 as the photoperiod shortens and is estimated according to a cultivar-specific photoperiod coefficient ( $PID$ ) after Tao et al. (2012) as described in Eq. 23

$$PF = 1 - \left[ \left( \frac{PID}{10000} \right) * (20 - PP)^2 \right] \quad \text{Eq. 23}$$

Crop development is related to the development index ( $DVI$ ) after (Osborne et al., 2015), which takes values of -1 upon sowing, 0 on emergence, 1 at anthesis, and 2 at crop maturity. The DO<sub>3</sub>SE-Crop model  $DVI$  equations have been modified from (Osborne et al., 2015) to take account of the photoperiod and vernalisation for winter wheat (see Eq. 24); for spring wheat these factors are omitted.

$$-1 \leq DVI < 0 \quad \text{for } td < TT_{emr}$$

$$0 \leq DVI < 1 \quad \text{for } TT_{emr} \leq td * VF * PF < TT_{veg} \quad \text{Eq. 24}$$

$$1 \leq DVI \leq 2 \quad \text{for } TT_{veg} \leq td \leq TT_{rep}$$

DO<sub>3</sub>SE-Crop allows for any number of representative leaf populations ( $pop$ ) and canopy layers ( $n$ ) to be defined over the course of the crop growing season. In this study, we used a single leaf population and 4 canopy layers (i.e.  $pop = 1$ ;  $n = 4$ ) for simplicity. The crop sowing is assumed to be at  $DVI = -1$  (start of  $TT_{emr}$ ) and emergence at  $DVI = 0$  (start of  $TT_{veg}$ ). The flag leaf is assumed to develop at  $DVI = 1$ , at the commencement of  $TT_{rep}$ , marking the initiation of anthesis ( $A_{start}$ , flowering) and flag leaf emergence, which typically occurs 4-5 days prior to the onset and is

further divided into expanding and senescing leaf periods (i.e.,  $tl_{ep}$  and  $tl_{se}$ ) with a default ratio of 0.67 to 0.33. Maturity is assumed at DVI = 2 (end of  $TT_{rep}$ ). The model allows estimation of the  $POD_y$  metric by accumulating stomatal ozone flux from the start of anthesis to maturity. The total leaf life span ( $TT_{leaf}$ ) of the crop is distributed over the DVI between 0 and 2. The relationship between these different variables is described in Fig. 9).

### 3.3.2 DO<sub>3</sub>SE-Crop leaf-level physiology

Key leaf-level physiological variables of the DO<sub>3</sub>SE-Crop model are  $A_{net}$  and  $g_{sto}$ .  $A_{net}$  is simulated using the biochemical photosynthesis-based model initially developed by (Farquhar et al., 1980) and since modified by (Sharkey et al., 2007). The coupled  $A_{net}g_{sto}$  model of (Leuning, 1995) is used to estimate  $g_{sto}$  from  $A_{net}$ , which means that  $g_{sto}$  is regulated by the demand of CO<sub>2</sub> for  $A_{net}$  on consideration of environmental conditions and crop physiology. Ozone stress, causing both instantaneous effects on  $A_{net}$  and long-term effects on leaf senescence, is simulated based on algorithms developed by (Ewert and Porter, 2000).

#### 3.3.2.1 Leaf $A_{net}$

The  $A_{net}$  model assumes that photosynthesis is constrained depending on prevailing environmental conditions according to three main mechanisms: Rubisco activity ( $A_c$ ); ribulose-1,5-bisphosphate (RuBP) regeneration, which is constrained by the speed of electron transport ( $A_j$ ); and the low rate of transfer of photosynthetic products (most frequently triose phosphate consumption) ( $A_p$ ) (Sharkey et al., 2007), and by soil water stress ( $f_{sw}$ ); the algorithm for  $A_c$  which is based on (Medlyn et al., 2002) and modified in DO<sub>3</sub>SE-crop to include the O<sub>3</sub> damage functions is given in Eq. 25.

$$A_c = V_{cmax} \cdot f_{sw} \cdot \frac{(C_i - \Gamma^*) \cdot f_{O_{3,s}}(d) \cdot f_{LS}}{C_i + K_c \left(1 + \frac{O_i}{K_o}\right)} \quad \text{Eq. 25}$$

where  $V_{cmax}$  ( $\mu\text{mol CO}_2 \text{ m}^{-2}\text{s}^{-1}$ ) is the maximum carboxylation capacity at 25°C,  $C_i$  ( $\mu\text{mol mol}^{-1}$ ) and  $O_i$  ( $\text{mmol mol}^{-1}$ ) are the intercellular CO<sub>2</sub> and O<sub>2</sub> partial pressures;  $K_c$  ( $\mu\text{mol mol}^{-1}$ ) and  $K_o$  ( $\text{mmol mol}^{-1}$ ) are the Rubisco Michaelis-Menten constants for CO<sub>2</sub> and O<sub>2</sub>;  $\Gamma^*$  ( $\mu\text{mol mol}^{-1}$ ) is the CO<sub>2</sub> compensation point in the absence of respiration;  $f_{O_{3,s}}(d)$  is the factor that accounts for the cumulative stomatal O<sub>3</sub> flux effect on  $V_{cmax}$  over the course of a day and;  $f_{LS}$  is the factor that accounts for the

cumulative stomatal O<sub>3</sub> flux effect over the course of a leaf life span on leaf senescence. Section 3.3.2.2 gives a full description of the methods used to estimate O<sub>3</sub> damage. The  $f_{PAW}$  factor (as the blue line in the figure below) is calculated by Eq. 26.

$$f_{PAW} = 1 \quad \text{for } PAW_t \leq PAW \leq 100\%,$$

$$f_{PAW} = 1 + \frac{PAW - PAW_t}{PAW_t} \quad \text{for } PAW < PAW_t \quad \text{Eq. 26}$$

Where PAW is plant available water. PAW is the amount of water in the soil (in%) which is available to the plants. At PAW=100% the soil is at field capacity, at PAW=0% the soil is at wilting point. PAW<sub>t</sub> is the threshold PAW, above which  $g_{sto}$  is at a maximum as described  $f_{PAW}$  function. The constraint on  $A_{net}$  due to the rate of electron transport  $A_j$  is described in Eq. 27.

$$A_j = J * \frac{C_i - \Gamma^*}{a * C_i + b * \Gamma^*} \quad \text{Eq. 27}$$

where  $J$  is the electron transport rate ( $\mu\text{mol CO}_2 \text{ m}^{-2}\text{s}^{-1}$ ), the parameters  $a$  and  $b$  denote the electron requirements for the formation of NADPH and ATP respectively (Sharkey et al., 2007)

Finally, the  $A_{net}$  limitation due to the low rate of transfer of photosynthetic products  $A_p$  ( $\mu\text{mol CO}_2 \text{ m}^{-2}\text{s}^{-1}$ ) is given in Eq. 28.

$$A_p = 0.5 * V_{cmax} \quad \text{Eq. 28}$$

The net leaf photosynthetic carbon uptake ( $A_{net}$ ) in  $\mu\text{mol CO}_2 \text{ m}^{-2}\text{s}^{-1}$  is calculated by Eq. 29

$$A_{net} = (A_c, A_j, A_p) - R_d \quad \text{Eq. 29}$$

Where leaf dark respiration ( $R_d$ ) in  $\mu\text{mol CO}_2 \text{ m}^{-2}\text{s}^{-1}$  is calculated as  $V_{cmax} * R_{dcoeff}$  where  $R_{dcoeff}$  is the leaf dark respiration coefficient initially set equal to 0.015 after Clark et al. (2011), a value provided for C3 grasses.

### 3.3.2.2 Short- and long-term O<sub>3</sub> damage to $A_c$

The short-term impact of O<sub>3</sub> on  $A_c$  is calculated according to the  $f_{O_3,s}(d)$  factor (between 0 and 1) which allows for an instantaneous effect of O<sub>3</sub> on  $A_{net}$  when

stomatal O<sub>3</sub> flux ( $f_{st}$ ), in nmol O<sub>3</sub> m<sup>-2</sup> s<sup>-1</sup> calculated as described later in 3.3.2.4 Stomatal ozone flux ( $f_{st}$ ), overwhelms detoxification and repair mechanisms (Betzelberger et al., 2012; Feng et al., 2022), and is estimated following (Ewert and Porter, 2000). Here,  $f_{O_3,s}(h)$  represents the relationship between  $f_{st}$  and a potential decrease in  $A_c$  calculated for every hour by Eq. 30.

$$\begin{aligned}
 f_{O_3,s}(h) &= 1; & \text{for } f_{st} \leq \frac{\gamma_1}{\gamma_2} \\
 f_{O_3,s}(h) &= 1 + \gamma_1 - \gamma_2 * f_{st} & \text{for } \frac{\gamma_1}{\gamma_2} < f_{st} < \frac{1+\gamma_1}{\gamma_2} \\
 f_{O_3,s}(h) &= 0; & \text{for } f_{st} \geq \frac{1+\gamma_1}{\gamma_2}
 \end{aligned} \tag{Eq. 30}$$

where  $\gamma_1$  (dimensionless) and  $\gamma_2$  (nmol O<sub>3</sub> m<sup>-2</sup> s<sup>-1</sup>)<sup>-1</sup> are both short-term O<sub>3</sub> damage coefficients, with  $\gamma_1$  representing the O<sub>3</sub> detoxification threshold below which no damage occurs to the photosynthetic system and  $\gamma_2$  determines the effect of  $f_{st}$  on  $A_c$  once this detoxification threshold is exceeded;  $f_{O_3,s}(d)$  and  $f_{O_3,s}(d - 1)$  i.e.  $f_{O_3,s}(d)$  at the end of the previous day, are calculated by Eq. 31.

$$\begin{aligned}
 f_{O_3,s}(d) &= f_{O_3,s}(h) * r_{O_3,s} & \text{for } hour = 0; \\
 f_{O_3,s}(d) &= f_{O_3,s}(h) * f_{O_3,s}(d - 1) & \text{for } hour = 0
 \end{aligned} \tag{Eq. 31}$$

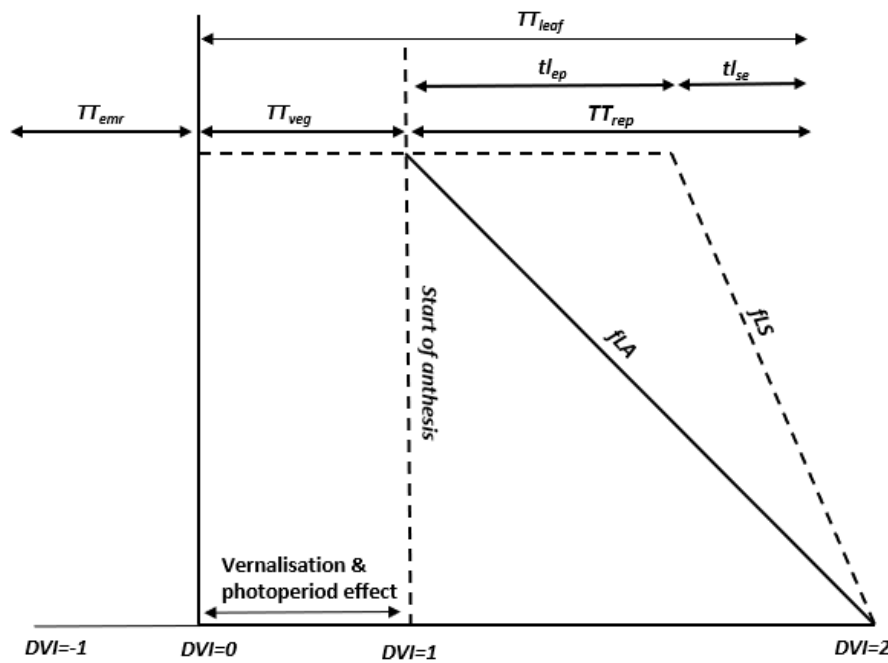
where  $r_{O_3,s}$  (dimensionless) is incomplete recovery from O<sub>3</sub> overnight which depends on leaf age according to Eq. 32.

$$r_{O_3,s} = f_{O_3,s}(d - 1) + (1 - f_{O_3,s}(d - 1)) * f_{LA} \tag{Eq. 32}$$

The long-term impact of O<sub>3</sub> on  $V_{cmax}$  represented by the  $f_{LS}$  term represents the longer-term accumulation of stomatal ozone flux ( $acc_{fst}$ ) causing degradation to the Rubisco enzyme which triggers early and enhanced senescence of mature leaves (Gelang et al., 2000b; Osborne et al., 2019). The simulation of  $f_{LS}$  (and  $f_{LA}$  used in the short-term O<sub>3</sub> effect) are related to thermal time defined periods over the course of a leaf life span  $TT_{leaf}$  as described in Fig. 9.

Fig. 9. The division of thermal time defined periods ( $TT_{emr}$ ,  $TT_{veg}$ ,  $TT_{rep}$  and  $TT_{leaf}$  and the relationship with  $f_{LA}$  and  $f_{LS}$ ). This diagram illustrates the stages of crop development in relation to thermal time and the effects of vernalization and photoperiod. Thermal time, a measure of accumulated heat, is divided into periods of

emergence ( $TT_{emr}$ ), vegetative growth ( $TT_{veg}$ ), reproduction ( $TT_{rep}$ ), and leaf lifespan ( $TT_{leaf}$ ).  $TT_{leaf}$  encompasses the thermal time from a canopy leaves full expansion to its senescence, split into active ( $tl_{ep}$ ) and senescing ( $tl_{se}$ ) phases. Vernalization and photoperiod can alter  $TT_{veg}$ , affecting the timing of flowering. Crop development correlates with the Developmental Index (DVI), ranging from -1 at sowing, 0 at emergence, 1 at anthesis, to 2 at maturity, with total leaf lifespan distributed between DVI 0 and 2. The impact of ozone ( $O_3$ ) on the maximum rate of carboxylation ( $V_{cmax25}$ ) is indicated by short-term effects ( $f_{LA}$ ), and long-term impacts ( $f_{LS}$ ).



The  $O_3$  effect on  $f_{LS}$  is first simulated by estimating a weighted accumulated  $f_{st}$  ( $fO3_l$ ) modified from (Ewert and Porter, 2000) by Eq. 33.

$$fO3_l = 1 - \max(\min(\gamma3 * (acc_{fst} - CLsO3), 1), 0) \quad \text{Eq. 33}$$

where  $\gamma3$  determines the occurrence of senescence once a critical cumulative stomatal  $O_3$  flux  $CLsO3$  (in  $mmol/m^2$ ) has been exceeded. The rate of senescence is determined by  $\gamma4$ , which determines the onset of senescence and  $\gamma5$  which determines maturity as described in Eq. 34.

$$tl_{epO_3} = tl_{ep} * (1 - ((1 - fO3_l) * \gamma4))$$

$$tl_{seO_3} = tl_{se} * \left(1 - ((1 - fO_3l) * \gamma_5)\right) + zc \quad \text{Eq. 34}$$

$$zc = tl_{ep} - tl_{epO_3}$$

Where  $tl_{ep}$  is the effective temperature ( $teff$ ) accumulated by a leaf in °C days between a fully expanded leaf and the start of leaf senescence,  $tl_{epO_3}$  is  $tl_{ep}$  with an  $O_3$  effect which may bring senescence earlier,  $tl_{se}$  is the ( $teff$ ) between the onset of senescence and maturity and  $tl_{seO_3}$  is  $tl_{se}$  with an  $O_3$  effect which may bring maturity earlier.  $f_{LS}$  is estimated by Eq. 35.

$$\begin{aligned} f_{LS} &= 1; & \text{for } teff &\leq TT_{veg} + tl_{ep} \\ f_{LS} &= 1 - \frac{TT_{eff} - TT_{veg} - tl_{epO_3}}{tl_{seO_3}}; & \text{for } TT_{veg} + tl_{ep} &< teff < TT_{leaf} \\ f_{LS} &= 0; & \text{for } teff &\geq TT_{leaf} \end{aligned} \quad \text{Eq. 35}$$

### 3.3.2.3 Stomatal conductance

The coupled  $A_{net}g_{sto}$  model based on (Leuning, 1995) and modified for vapour pressure deficit ( $VPD$ ) (Danielsson et al., 2003) is used to estimate  $g_{CO_2}$ ,  $g_{sto}$  to  $CO_2$  in  $\mu\text{mol } CO_2 \text{ m}^{-2} \text{ s}^{-1}$  as described in Eq. 36.

$$g_{CO_2} = [f_{min} + m \cdot A_{net} \cdot f_{VPD} / (c_s - \Gamma)] \quad \text{Eq. 36}$$

where  $f_{min}$  ( $\mu\text{mol m}^{-2} \text{ s}^{-1}$ ) is the minimum daytime  $g_{CO_2}$  (Leuning, 1990). The parameter  $m$  (dimensionless) is the composite sensitivity of  $g_{CO_2}$  to assimilation rate and vapour pressure deficit ( $VPD$ ) with the relationship between  $VPD$  and relative stomatal conductance ( $f_{VPD}$ ) estimated by eq. [18].  $A_{net}$  ( $\mu\text{mol m}^{-2} \text{ s}^{-1}$ ) is estimated from eq [10].  $f_{VPD}$  (Danielsson et al., 2003) is calculated by Eq. 37.

$$f_{VPD} = \left(1 + \left(\frac{VPD}{VPD_0}\right)^8\right)^{-1} \quad \text{Eq. 37}$$

where  $VPD_0$  is an empirical parameter, defined using boundary line analysis, describing the variation in relative stomatal conductance with  $VPD$  (Danielsson et al., 2003; Pleijel et al., 2007).  $c_s$  ( $\text{mmol mol}^{-1}$ ) is the external  $CO_2$  concentration at the leaf surface and is calculated from the external  $CO_2$  concentration at the upper surface of the leaf boundary layer  $c_a$  ( $\text{mmol mol}^{-1}$ ) so that  $c_s = c_a - \left(\frac{A_{net}}{g_{bCO_2}}\right)$  after

Masutomi (2023) where  $g_{bcO_2}$  is the boundary layer conductance to CO<sub>2</sub> (in mol m<sup>-2</sup> s<sup>-1</sup>), conversion factors for the boundary layer are given in the table SI. 7..

Finally,  $g_{CO_2}$  is converted to  $g_{O_3}$  in mmol O<sub>3</sub> m<sup>-2</sup> s<sup>-1</sup> by dividing by 1000 and using the conversion factor 0.96 which assumes that the ratio of the diffusivities of gases in air are equal to the inverse of the square root of the ratio of molecular weights (as described in (Campbell, G.S., Norman, 1998), see sections SI.2.1 and SI.2.2.

### 3.3.2.4 Stomatal ozone flux ( $f_{st}$ )

Stomatal O<sub>3</sub> flux  $f_{st}$  (nmol m<sup>-2</sup> s<sup>-1</sup>) is calculated after the method described in the UNECE Mapping Manual (UNECE, 2017) described in Eq. 38].

$$f_{st} = C_l * g_{O_3m/s} * \frac{r_c}{r_{b,O_3} + r_c} \quad \text{Eq. 38}$$

Where  $C_l$  is the O<sub>3</sub> at the upper surface of the laminar layer of a leaf (nmol O<sub>3</sub> m<sup>-3</sup>). Ozone concentration in ppb can be converted to nmol m<sup>-3</sup> by multiplying O<sub>3</sub> in ppb by  $P/(R*T_{air,k})$  where  $P$  is the atmospheric pressure in Pascal,  $R$  is the universal gas constant (8.31447 J/mol/K) and  $T_{air,k}$  is surface air temperature in degrees Kelvin;  $g_{O_3m/s}$  (m/s) is  $g_{sto}$  to O<sub>3</sub>, to convert  $g_{O_3}$  (mol O<sub>3</sub> m<sup>-2</sup> s<sup>-1</sup>) to  $g_{O_3m/s}$  (m/s) we assume a standard temperature  $T_{st}$ (20°C) and air pressure  $P_{st}$  (1.013 x 10<sup>5</sup> in Pascal) and divide by 41 to give the conductance value in m/s. The  $r_c/r_{b,O_3} + r_c$  term represents the O<sub>3</sub> deposition rate to the leaf through resistances  $r_b$  (the quasi-laminar resistance (s/m)) and  $r_c$  (the leaf surface resistance (s/m)), which allow for both stomatal and non-stomatal deposition to the leaf surface.  $r_c$  is  $1/(g_{O_3m/s} + g_{ext})$  where  $g_{ext}$  is 1/2500 (s/m).  $r_b$  is estimated by Eq. 39

$$r_{b,O_3} = 1.3 * 150 * \sqrt{\frac{L}{u_l}} \quad \text{Eq. 39}$$

Where the factor 1.3 accounts of the differences in diffusivity between heat and O<sub>3</sub>. and the value of 150 provides the equivalent conductance leaf layer for O<sub>3</sub> as compared to forced convection of heat (Campbell et al., 1998),  $L$  is the cross wind leaf dimension (m) and  $u_l$  is the windspeed (m/s) at the top of the leaf laminar boundary layer. The leaf boundary layer resistance to CO<sub>2</sub> is estimated using a value of 1.24 for the difference between heat and CO<sub>2</sub> in place of the 1.3 value for O<sub>3</sub> (Campbell, G.S., Norman, 1998).

### 3.3.3 DO<sub>3</sub>SE-Crop canopy

The DO<sub>3</sub>SE crop model uses a multi-layer approach to scale from the leaf to the canopy. We assume that wind, irradiance, O<sub>3</sub> concentration, and leaf nitrogen content are the key environmental conditions that change with cumulative canopy leaf area index (*LAI*) and influence leaf physiology and, therefore, canopy layer estimates of  $A_{net}$ ,  $g_{sto}$  and  $g_{ext}$ ; other environmental variables (e.g.,  $T_{air,oc}$  and  $VPD$ ) are assumed to remain constant over the canopy.

### 3.3.4 Canopy irradiance

Changes in irradiance through the canopy are described as sunlit and shaded canopy fractions and the associated quantity of direct and diffuse photosynthetically active radiation *PAR* (W/m<sup>2</sup>), these are estimated according to increasing levels of cumulative *LAI* using the methods of (Pury and Earquhar, 1997); this method requires the canopy to be divided into layers of equal *LAI* (including both green ( $LAI_G$ ) and brown ( $LAI_B$ )), see Eq. 65. More details are given in the section SI.2.3.

*PAR* absorbed per unit leaf area is divided into  $PAR_{dir}$ ,  $PAR_{diff}$  which also includes scattered (re-reflected by the canopy) beam calculated by,

$$PAR_{dir}(LAI) = (1 - \rho_{cb}(\beta)) K_b' I_b(0) \exp(-k_b' LAI) \quad \text{Eq. 40}$$

$$PAR_{diff}(LAI) = (1 - \rho_{cd}) k_d' I_d(0) \exp(-k_d' LAI) \quad \text{Eq. 41}$$

Estimates of the *LAI* fractions of sunlit ( $LAI_{sun}$ ) and shaded ( $LAI_{sh}$ ) parts of each canopy layer (*i*) are made by Eq. 42 and Eq. 43.

$$LAI_{sun,i} = \left[ 1 - \exp\left(-0.5 * \frac{LAI_i}{\sin\beta}\right) \right] * 2\sin\beta \quad \text{Eq. 42}$$

Where  $\beta$  is the solar elevation angle, description given in Table 14.

$$LAI_{sh,i} = LAI_i - LAI_{sun,i} \quad \text{Eq. 43}$$

The DO<sub>3</sub>SE-Crop model simulates *LAI* as part of the crop growth model and *LAI* is assumed to be evenly distributed across all layers.

Therefore, *PAR* for the sunlit part of each layer can be described as

$$\int_{LAI_i}^{LAI_n} PAR_{sun} = \int_{LAI_i}^{LAI_n} (LAI_{sun,i}) \cdot (PAR_{sh} + PAR_{bsun}(\beta)) dLAI \quad \text{Eq. 44}$$

Where  $\int_{LAI_i}^{LAI_n} PAR_{dir}$  can be written as  $(1 - \rho cb(\beta)) \cdot Kb' \cdot Ib(0) \cdot [\exp(-Kb' LAI_i) - \exp(-Kb' LAI_n)]$  and  $PAR_{bsun}(\beta) = (1 - \sigma)I_b(0) \frac{\cos \alpha}{\sin \beta}$

Similarly, PAR for the shaded part of each layer can be described as

$$\int_{LAI_i}^{LAI_n} PAR_{sh} = \int_{LAI_i}^{LAI_n} (LAI_{sh,i}) \cdot (PAR_{diff} + PAR_{bs}) dLAI \quad \text{Eq. 45}$$

Where  $\int_{LAI_i}^{LAI_n} (PAR_{diff}(LAI))$  can be written as  $(1 - \rho cd) \cdot Kb' \cdot Ib(0) \cdot [\exp(-k_d' LAI_i) - \exp(-k_d' LAI_n)] dL$  and  $\int_{LAI_i}^{LAI_n} PAR_{bs}(LAI)$  is  $I_b(0) [PAR_{dir} - (1 - \sigma)k_b \cdot [\exp(-k_b LAI_i) - \exp(-k_b LAI_n)]]$  Eq. 46

where  $PAR_{diff}(LAI)$  is diffuse irradiance (see eq.) and  $PAR_{bs}(LAI)$ , direct scattered beam (another form of diffuse radiation) is calculated as:

$$PAR_{bs}(LAI) = PAR_b(0) [PAR_{dir} - (1 - \sigma)k_b \exp(-k_b LAI)] \quad \text{Eq. 47}$$

### 3.3.5 Canopy [O<sub>3</sub>] concentration

O<sub>3</sub> concentration will vary as a function of O<sub>3</sub> loss to the canopy (i.e., deposition via the stomates and external plant parts) and O<sub>3</sub> replacement from ambient air concentrations above the canopy. Limited data have been collected showing how O<sub>3</sub> concentrations vary with canopy depth in semi-natural communities (Jaggi et al., 2006). These data suggest that a minimum, bottom canopy O<sub>3</sub> concentration ( $c_{zb}$ ), is about 0.2 times that at the top of the canopy ( $c_{zh}$ ) and that the O<sub>3</sub> concentration difference within the canopy is closely related to the LAI of the canopy layers.

Since each canopy layer can be assumed to be a parallel sink, the O<sub>3</sub> flux to a layer depends on the conductance (inverse of resistance) of that layer and the O<sub>3</sub> concentration at the top of the layer ( $C_i$ ; with  $C_0$  being  $c_{zh}$  (i.e., the O<sub>3</sub> concentration at height  $C_h$ , the top of the canopy)); we follow and generalise the work of Waggoner, 1971 by separating the canopy into  $nL$  leaf layers. We calculate the O<sub>3</sub> concentration for each layer,  $C_i$ , from O<sub>3</sub> intake,  $I_i$ , by,

$$C_i = r_i I_i \quad \text{Eq. 48}$$

With  $r_i$  the surface resistance for layer  $i$ .  $I_i$  is calculated as the solution to a system of linear equations. Relating  $r_i$ ,  $I_i$ , and  $R_i$ , the in-canopy aerodynamic resistance for layer  $i$ . Assuming above the canopy there is a uniform O<sub>3</sub> concentration  $C_0$ , we use

generalised equations from Waggoner, 1971 for the difference in O<sub>3</sub> concentration between the exterior air and leaf interior, which for the top layer is C<sub>0</sub> minus 0, so C<sub>0</sub> and for each lower layer the difference is 0. This O<sub>3</sub> concentration difference is calculated by,

$$C_0 = R_1 \sum_{j=1}^{nL} I_j + r_1 I_1 \quad \text{Eq. 49}$$

For the top canopy layer,

$$0 = R_i \sum_{j=i}^{nL} I_j + r_i I_i - r_{i-1} I_{i-1} \quad \text{Eq. 50}$$

For each canopy layer *i* between the top layer and the bottom layer, and,

$$0 = R_{nL+1} I_{nL+1} - r_{nL} I_{nL} \quad \text{Eq. 51}$$

For the bottom layer of the canopy, between the lowest leaf layer and the ground.

These can also be written into the matrix form as below.

$$\begin{pmatrix} r_1 + R_1 & R_1 & R_1 & \cdots & R_1 \\ -r_1 & r_2 + R_2 & R_2 & \cdots & R_2 \\ 0 & -r_2 & r_3 + R_3 & \cdots & R_3 \\ \vdots & \vdots & \vdots & \ddots & \vdots \\ 0 & 0 & 0 & \cdots & R_{nL+1} \end{pmatrix} \begin{pmatrix} I_1 \\ I_2 \\ I_3 \\ \vdots \\ I_{nL+1} \end{pmatrix} = \begin{pmatrix} C_0 \\ 0 \\ 0 \\ \vdots \\ 0 \end{pmatrix} \quad \text{Eq. 52}$$

Which can be numerically solved for *I<sub>x</sub>* when *r<sub>1</sub>* ≠ 0 and *R<sub>1</sub>* ≠ 0.

Resistances for each layer are calculated and described in the SI.2.4 using standard DO<sub>3</sub>SE deposition modelling methods (Emberson, L.D., Ashmore, M.R., Simpson, D., Tuovinen, J.-P. and Cambridge, 2001; Simpson et al., 2012).

### 3.3.6 Canopy maximum carboxylation capacity (*V<sub>cmax</sub>*)

We allow for an exponential decrease in leaf N with canopy depth, which will influence both the photosynthetic capacity (*V<sub>cmax</sub>*) and hence dark respiration (*R<sub>d</sub>*).

Photosynthetic capacity at each canopy layer *i* is calculated by Eq. 53

$$V_{cmax,i} = n_e \cdot n_0 \cdot e^{-kN \left( \frac{LAI_i}{LAI_{total}} \right)} \quad \text{Eq. 53}$$

Where *n<sub>e</sub>* (mol CO<sub>2</sub> m<sup>-2</sup> s<sup>-1</sup> kg C (kg N)<sup>-1</sup>) is a constant relating leaf nitrogen to Rubisco carboxylation capacity, *n<sub>0</sub>* (kg N[kg C]<sup>-1</sup>) is the leaf N concentration at the

top of the canopy and  $kN$  is a nitrogen profile co-efficient initially set at 0.78 after (Clark et al., 2011).

### 3.3.7 Canopy Photosynthesis ( $A_{net_c}$ )

Net canopy photosynthesis ( $A_{net_c}$ ) determines the amount of C assimilated by the entire canopy that can subsequently be allocated to different plant parts (i.e., less than the C respired for plant growth and maintenance, 3.5.1), the amount of C assimilation will ultimately determine whole plant biomass. The  $A_{net}$  for each canopy layer ( $A_{net_i}$ ) is calculated according to the LAI fraction of that layer that is sunlit ( $LAI_{sun,i}$ ) and shaded ( $LAI_{sh,i}$ ) within the layer ( $i$ ), multiplied by the  $A_{net}$  of the sunlit ( $A_{net_{sun,i,j}}$ ) and shaded leaf ( $A_{net_{sh,i,j}}$ ), respectively described by Eq. 54 and Eq. 55

$$A_{net_i} = LAI_{sun,i} * A_{net_{sun,i}} + LAI_{sh,i} * A_{net_{sh,i}} \quad \text{Eq. 54}$$

with  $A_{net_c}$  calculated by,

$$A_{net_c} = \sum_{i=1}^n A_{net_i} \quad \text{Eq. 55}$$

$A_{net_c}$  is converted from  $\mu\text{mol CO}_2 \text{ m}^{-2} \text{ s}^{-1}$  to  $\text{kg C m}^{-2} \text{ day}^{-1}$ , by multiplying by 3600 (converting from seconds to hours), multiplying by 1.2 (representing the kg of C per mol) and summing each hourly  $A_{net_c}$  over the course of a day. This  $A_{net_c}$  is used in the equation 37.

### 3.3.8 Canopy Stomatal Conductance ( $g_{sto_i}$ )

Similarly, canopy layer ( $i$ ) stomatal conductance to  $\text{O}_3$  ( $g_{O_3,i}$ ), which is converted from  $g_{CO_2}$  by assuming a diffusivity ratio of 0.96 to convert from  $\text{CO}_2$  to  $\text{O}_3$  and is calculated by Eq. 56 with whole canopy stomatal conductance calculated by Eq. 57.

$$g_{sto_i} = LAI_{sun,i} * g_{sto_{sun,i}} + LAI_{sh,i} * g_{sto_{sh,i}} \quad \text{Eq. 56}$$

$$g_{sto_c} = \sum_{i=1}^n g_{sto_i} \quad \text{Eq. 57}$$

This is converted from  $g_{sto_i}$  in eq. [33 by dividing the conductance value in  $\text{mmol m}^{-1} \text{ s}^{-1}$  by 41000 (assuming standard temperature (20°C) and air pressure ( $1.013 \times 10^5$  Pa)) to give conductance in m/s.

### 3.3.9 Crop biomass, LAI, height and yield variables

The following section describes how to estimate crop biomass, important canopy characteristics ( $LAI$  and crop height ( $h$ )), and yield variables from accumulated calculations of  $Anet_c$  over the course of the growing season following (Osborne et al., 2015).

### 3.3.9.1 Crop biomass ( $NPP$ and $GPP$ )

The simulation of crop growth requires an estimate of the net primary productivity ( $NPP$ ), which is calculated at the end of each day and summed over the growing season. Carbon is assumed to be allocated to five key crop components: root, leaf, stem, harvest, and reserve pools (Osborne et al., 2015). This carbon allocation is ultimately used to simulate leaf area index ( $LAI$ ), canopy height ( $h$ ), biomass, harvest index, and yield at the end of each day throughout the growing season.

Net primary productivity  $NPP$  ( $\text{kg C m}^{-2} \text{ day}^{-1}$ ) is accumulated throughout the day using the JULES-crop approach to model crop growth (Osborne et al., 2015) described in Eq. 58

$$NPP = GPP - R_p \quad \text{Eq. 58}$$

where  $GPP$  is the gross primary productivity ( $\text{kg C m}^{-2} \text{ day}^{-1}$ ) and  $R_p$  is plant respiration divided into maintenance ( $R_{pm}$ ) and growth ( $R_{pg}$ ) respiration ( $\text{kg C m}^{-2} \text{ day}^{-1}$ ) (Clark et al., 2011) where  $R_p = R_{pm} + R_{pg}$  and where  $R_{pg}$  is assumed to be a fixed fraction of the  $NPP$  as shown in Eq. 59

$$R_{pg} = R_{gcoeff} (GPP - R_{pm}) \quad \text{Eq. 59}$$

Where  $R_{gcoeff}$  is the growth respiration co-efficient which was initially set to 0.25 based on the value for all PFTs (i.e. forests and grasses including crops) in (Clark et al., 2011).  $GPP$  is calculated by Eq. 60

$$GPP = Anet_c + f_{sw}R_{dc} \quad \text{Eq. 60}$$

where  $Anet_c$  is net canopy photosynthesis (see eq. 28) and  $f_{sw}R_{dc}$  is the soil-moisture modified canopy dark respiration ( $\text{kg C m}^{-2} \text{ day}^{-1}$ ) where  $R_{dc} = V_{cmax,i} * R_{dcoeff}$  with  $R_{dcoeff}$  initially assumed to be 0.015 based on (Clark et al., 2011);  $V_{cmax,i}$  is the maximum carboxylation efficiency for each canopy layer  $i$  which decreases from the top to bottom of the canopy (see eq. ) and  $f_{sw}$  is calculated in Eq. 26.

Leaf maintenance respiration ( $R_{pm}$ ) is assumed equivalent to the soil moisture modified canopy dark respiration, while root and stem respiration are assumed to be independent of soil moisture but to have the same dependencies on C content (Clark et al., 2011). We assume a fixed relationship between C and N contents of these organs so that  $R_{pm}$  can be estimated by Eq. 61

$$R_{pm} = R_{dc} * \left( f_{sw} + \frac{C_{root} + C_{stem}}{C_{leaf}} \right) \quad \text{Eq. 61}$$

The C accumulating as  $NPP$  each day is divided into five carbon pools i.e. root ( $C_{root}$ ), leaf ( $C_{leaf}$ ), stem ( $C_{stem}$ ), reserve ( $C_{resv}$ ), and harvest ( $C_{harv}$ ) ( $\text{kg C m}^{-2} \text{ day}^{-1}$ ) according to partition coefficients (see Eq. 62) allowing for accumulation of C in these pools over the course of the crop growth period

$$\frac{dC_{root}}{dt} = p_{root}NPP,$$

$$\frac{dC_{leaf}}{dt} = p_{leaf}NPP,$$

$$\frac{dC_{stem}}{dt} = p_{stem}NPP (1 - \tau),$$

$$\frac{dC_{harv}}{dt} = p_{harv}NPP,$$

$$\frac{dC_{resv}}{dt} = p_{stem}NPP, \tau \quad \text{Eq. 62}$$

where  $\tau$  is the fraction of stem C that is partitioned into the reserve pool.  $p_{root}, p_{leaf}, p_{stem}, p_{harv} = 1$ . The partition coefficients are related to the crop development stage ( $DVI$ ) and hence effective thermal time ( $TT_{eff}$ ) since emergence. The partition coefficients are based on Osborne et al. (2015) and provided as a function of  $DVI$  using six parameters to continuously describe varying partition coefficients over the duration of the crop growing season. We use the same multinomial logistic as that described in (Osborne et al., 2015) to define this function according to Eq. 63

$$p_{root} = \frac{e^{\alpha_{root} + (\beta_{root} DVI)}}{e^{\alpha_{root} + (\beta_{root} DVI)} + e^{\alpha_{stem} + (\beta_{stem} DVI)} + e^{\alpha_{leaf} + (\beta_{leaf} DVI)} + 1},$$

$$p_{stem} = \frac{e^{\alpha_{stem} + (\beta_{stem} DVI)}}{e^{\alpha_{root} + (\beta_{root} DVI)} + e^{\alpha_{stem} + (\beta_{stem} DVI)} + e^{\alpha_{leaf} + (\beta_{leaf} DVI)} + 1},$$

$$p_{leaf} = \frac{e^{\alpha_{leaf} + (\beta_{leaf} DVI)}}{e^{\alpha_{root} + (\beta_{root} DVI)} + e^{\alpha_{stem} + (\beta_{stem} DVI)} + e^{\alpha_{leaf} + (\beta_{leaf} DVI)} + 1},$$

$$p_{harv} = \frac{1}{e^{\alpha_{root} + (\beta_{root} DVI)} + e^{\alpha_{stem} + (\beta_{stem} DVI)} + e^{\alpha_{leaf} + (\beta_{leaf} DVI)} + 1} \quad \text{Eq. 63}$$

Where  $DVI$  is the development index;  $\alpha$  and  $\beta$  partition parameters. These parameters describe the shape of the thermal time varying partition coefficient for leaves, roots, and stems.

Once  $C$  is no longer partitioned to stems,  $C$  from the stem reserve pool will mobilise to the harvest pool at a rate of 10% per day following (Osborne et al., 2015) described by Eq. 64.

$$C_{harv} = C_{harv} + (0.1 C_{resv}) C_{resv} = 0.9 C_{resv} \quad \text{for } p_{stem} < 0.01 \quad \text{Eq. 64}$$

Total leaf  $C$  is divided between green leaf  $C$  ( $C_{leaf,green}$ ), and brown leaf carbon ( $C_{leaf,brown}$ ). Carbon from the  $C_{leaf,green}$  will mobilise to the harvest pool at the rate of 5% per day after (Osborne et al., 2015) and to the  $C_{leaf,brown}$  at a rate of 24% per day once  $f_{LS} > 1$  as described in Eq. 65

$$\{C_{harv} = C_{harv} + (0.05 C_{leaf,green}) C_{leaf,green} = 0.86 C_{leaf} \quad C_{leaf} = 0.86 C_{leaf,green} + 0.24 C_{leaf,brown} \} \quad \text{for } f_{LS} > 1 \quad \text{Eq. 65}$$

### 3.3.9.2 Leaf area Index ( $LAI$ ) and stem height ( $h$ )

At the end of each day, the  $C$  content of the stem and leaf is used to estimate  $LAI$  by Eq. 66 and Eq. 67.

$$LAI = (C_{leaf} / f_c) * SLA \quad \text{Eq. 66}$$

$$\text{where } SLA = Y (DVI + 0.06)^\delta \quad \text{Eq. 67}$$

The values  $Y$  and  $\delta$  were determined by fitting the values to the paired values of  $DVI$  and specific leaf area ( $SLA$ ). The value of  $f_c$  is 0.5 (unitless), denotes carbon fraction of dry matter.

The amount of  $C$  in the stem is used to calculate the crop height  $h$  in m by Eq. 68

$$h = k (C_{stem} / f_c)^\lambda \quad \text{Eq. 68}$$

where  $k$  and  $\lambda$  were determined by fitting the value  $C_{stem}$  and  $h$ .

### 3.3.9.3 Yield variables

According to (Osborne et al., 2015) yield can be calculated from the C allocated to the harvest pool ( $C_{harv}$ ) at the end of the growing season as described in Eq. 69

$$Yield_{grain} = \frac{(C_{harv} \cdot (1/f_c) \cdot D_w \cdot E_g)}{1000} \quad \text{Eq. 69}$$

Where harvested C is converted to total biomass (using the conversion factor  $f_c=0.5$ ), i.e., by multiplying the harvested C by  $1/f_c$ , and then by  $1/0.84$  ( $D_w$ ) to account for the grain moisture content (Mulvaney and Devkota, 2020).  $C_{harv}$  includes both chaff and grain; however, O<sub>3</sub> fumigation experimentalists tend to only include grain when calculating total crop yield at the end of the growing season, so we assume 15% of the yield is chaff and include a grain-to-ear ratio,  $E_g$ , of 0.85. Dividing by 1000 converts yield from kg C m<sup>-2</sup> to g C m<sup>-2</sup>, the unit most often used to describe experimental yield results.

Evaluation of the DO<sub>3</sub>SE-crop model uses a variety of growth 'dry matter (DM)' metrics. Some of the most important metrics and their calculations are: 'Straw DM' which is calculated as the sum of carbon allocated to  $C_{stem}$ ,  $C_{leaf}$ , and  $C_{resv}$ ; 'Ear DM' is calculated from  $C_{harv}$  excluding the moisture content ( $D_w$ ) conversion; 'Grain DM' is calculated from  $C_{harv}$  excluding both the moisture content ( $D_w$ ) conversion and removing the chaff fraction conversion  $E_g$ ; 'Above ground DM' is the straw DM plus the Ear DM; 'Below ground DM' is converted from  $C_{root}$ ; and 'Harvest index' is the Grain DM divided by the Above ground DM. In all cases the  $f_c$  conversion factor is used to convert from e.g. g C m<sup>-2</sup> to g DM m<sup>-2</sup>.

## 3.3.10 DO<sub>3</sub>SE-Crop model calibration

### 3.3.10.1 Xiaoji China experimental dataset

The DO<sub>3</sub>SE-crop model was used to analyse the O<sub>3</sub>-FACE (Free Air Concentration Enrichment) experimental data collected in Xiaoji, Jiangsu, Jiangsu Province, China. This dataset includes four modern cultivars of winter wheat (*Triticum aestivum* L.) grown under ambient and elevated O<sub>3</sub>, with the elevated treatment being, on average, 25% above the ambient O<sub>3</sub> of 45.7 ppb for the period early March/April to

the end of May each year. Plants were grown in fully open-air field conditions for three consecutive growing seasons from 2007 to 2009. Table 6 describes the hourly meteorological and O<sub>3</sub> data that are required to run the DO<sub>3</sub>SE-Crop model, and which are provided at the Xiaoji site.

Table 6. Hourly meteorological and O<sub>3</sub> data measured at Xiaoji required to run the DO<sub>3</sub>SE-Crop

Variable	Unit	Description	Measurement height
$PAR_{total}$	W/m <sup>2</sup>	Direct and diffuse PAR at the top of the canopy	-
$T_{air}$	°C	Surface air temperature in degrees Celsius	2 m
$VPD$	kPa	Leaf to air vapour pressure deficit	2 m
$u_z$	m/s	Wind speed at a reference height $z$	2 m
$\rho_a$	Pa	Surface air pressure	2m
$O_3_z$	ppb	Ozone concentration at a reference height $z$	2 m

The wheat crop was well irrigated, so we assume there was no soil moisture stress. Any data gaps were filled following the AgMIP-O<sub>3</sub> gap filling protocol (see SI.2.10). For large [O<sub>3</sub>] data gaps (i.e. greater than 2 weeks) which occur outside the [O<sub>3</sub>] fumigation period we use scaled WFRChem (version 4.2) data for Xiaoji (Conibear et al., 2018a) to ensure consistency in model calibration and potential applications across China. The four cultivars were Yannong 19 (strong-gluten wheat, hereafter Y19), Yangmai 16 (medium-gluten wheat, hereafter Y16), Yangmai 15 (weak-gluten wheat, hereafter Y15), and Yangfumai 2 (weak-gluten wheat, hereafter Y2). The dataset provides measurements of key physiological variables for the Y2 and Y16

cultivars (i.e.,  $A_{net}$ ,  $V_{cmax}$ ,  $J_{max}$ , and  $g_{O_3}$ ) for the flag leaf which were used to evaluate the DO<sub>3</sub>SE-Crop model's simulations of these variables.

Additional data also provide measurements of chlorophyll content Index (CCI), which can be used to assess the level of senescence experienced by the leaf (Mariën et al., 2019). The dataset also provides grain yield components, including the number of ears per square meter, the number of grains per ear, and the grain dry matter (*Grain DM*) (the latter in g m<sup>-2</sup>) (Feng et al., 2011, 2016). Further experimental details are provided by (Feng et al., 2011, 2016).

### 3.3.10.2 DO<sub>3</sub>SE-Crop calibration and evaluation

The Xiaoji experimental data were split into calibration (year 2008, Y2 and Y16 cultivars) and evaluation (year 2007 & 2009, Y15 & Y19 cultivars). The calibration of DO<sub>3</sub>SE-Crop has two main steps, firstly, to calibrate for crop development and growth (i.e. phenology and C allocation). This calibration was performed using the Y2 cultivar. Secondly, the calibration of the O<sub>3</sub> damage module was calibrated using the Y2 cultivar (representing a sensitive cultivar and Y16 (representing a tolerant cultivar); these cultivar sensitivities followed the information provided by (Feng et al., 2016).

Calibration of the DO<sub>3</sub>SE-Crop model used a combination of automated (for phenology) and manual (for leaf physiology, canopy C allocation, and O<sub>3</sub> damage) calibration methods. Both methods require defining an initial parameter value and a realistic range over which the parameter value may vary. These parameter values are defined from a combination of observations from the Xiaoji experimental dataset as well as values taken from the literature (see Table. SI. 10, Table. SI. 11, and Table. SI. 12 for details). The model is calibrated until certain conditions are satisfied, as explained below.

The phenology module was calibrated using the Xiaoji 2008 dataset for the Y2 cultivar. These data were used to determine the thermal life span of the canopy from sowing to maturity ( $TT_{leaf}$ ) and calibrate key phenology parameters ( $T_b$ ,  $T_0$ ,  $T_m$ ,  $VT_{min}$ ,  $VT_{max}$ ,  $PIV$ , and  $PID$ , flag leaf emergence,  $A_{start}$ ,  $tl_{ep}$  and  $tl_{se}$ ). The phenology calibration was automated by computationally applying a genetic algorithm (Wang, 1997), an optimisation technique with gradient descent, to find the

best parameters. This uses a combination of crossover strategy (selecting parameters randomly from parameter pairings) and mutation strategy (which takes a parameter range and uses incremental step changes) to identify the parameters that give the highest  $R^2$  and lowest RMSE when compared with observations of the timing (day of year) of emergence, anthesis and maturity. The calibrated phenology parameters were tested on Y2 data for the other years (i.e., 2007 and 2009) to assess their ability to represent crop development between years.

We conducted a sensitivity analysis to pinpoint the most critical parameters within the leaf physiology, carbon (C) allocation, and ozone ( $O_3$ ) damage modules that required calibration, as recommended by Iwanaga et al. (2022). This analysis highlighted several DO3SE-crop parameters for calibration, including:

- i. Leaf photosynthesis parameters ( $V_{cmax25}, J_{max25}, kN, m, VPD_0$ );
- ii. C allocation parameters ( $\alpha_{root}, \alpha_{leaf}, \alpha_{stem}, Y, \tau$ );
- iii. Dark respiration coefficients ( $R_{dcoeff}, R_{gcoeff}$ );
- iv.  $O_3$  damage module parameters related to senescence ( $\gamma_3, \gamma_4, \gamma_5$ ).

The calibration process involved several steps, beginning with the establishment of initial leaf physiology parameters. We set targets for maximum stomatal conductance  $g_{sto}$  to range between 350-400  $mmol\ O_3\ m^{-2}\ PLA\ s^{-1}$  and for net photosynthesis  $A_{net}$  to fall between 30-35  $\mu mol\ CO_2\ m^{-2}\ s^{-1}$ . These targets align with peak values recorded in the Xiaoji dataset (Xhu et al., 2011). Subsequent calibration of C allocation parameters aimed to fulfil multiple criteria:

1. A stem-to-leaf dry matter ratio of approximately 2:1, as observed by Huang et al. (2022).
2. Relative growth of plant parts consistent with growth profiles documented in the literature (Osborne et al., 2015; de Vries et al., 1989).
3. Aboveground dry matter values within the 1200-1600  $g\ m^{-2}$  range.
4. A Leaf Area Index (LAI) between 4-7  $m^2\ m^{-2}$ .
5. Dark respiration constituting 30 to 60% of assimilated  $A_{net}$  (Amthor et al., 2019).
6. An  $R^2$  value above 0.90 when comparing modelled Grain DM against observed Grain DM.

Next, initial  $O_3$  parameters ( $\gamma_3, \gamma_4, \gamma_5$ ) were determined using senescence onset and cessation data derived through the breakpoint method (Section 3.4.1), and their

effects were analysed (Section 3.4.6).

Ultimately, we utilized training datasets to fine-tune the model for the specific conditions at the Xiaoji site. The manual calibration relied on initial values and ranges established in the steps above and corroborated by literature (Feng et al., 2011, 2016; Osborne et al., 2015). We began with the 2008 Y2 cultivar, adjusting the leaf physiology and carbon allocation parameters to match observed maximum  $g_{sto}$  and  $A_{net}$  values. Should the model output align with these targets, we proceeded to calibrate the carbon allocation parameters, which should again fulfil the multiple criteria state above; otherwise, we iterated the process, adjusting parameter values within the defined limits (refer to Table 17). This method was similarly applied for calibrating ozone parameters. However, to calibrate the model for cultivars with varying levels of tolerance to ozone, two distinct cultivars from the 2008 dataset, Y16(tolerant) and Y2 (sensitive) are used in the calibration of ozone parameters.

### 3.4 Results

We first examine the model's ability to simulate the key phenological development stages since this is key to simulating the variation in C allocation over the course of the growing season and, hence, how O<sub>3</sub> exposure will influence growth and yield, which is determined by the timing and length of the grain filling period. We also explore how DO<sub>3</sub>SE-Crop simulates within canopy O<sub>3</sub> profiles to understand which layers of the canopy are most important in determining O<sub>3</sub> response. We then examine the ability of the model to simulate leaf-level physiology and C allocation to the different parts of the crop. Lastly, the impact of both instantaneous and long-term O<sub>3</sub> damage on the crop's final grain yield is evaluated.

#### 3.4.1 Crop Phenology

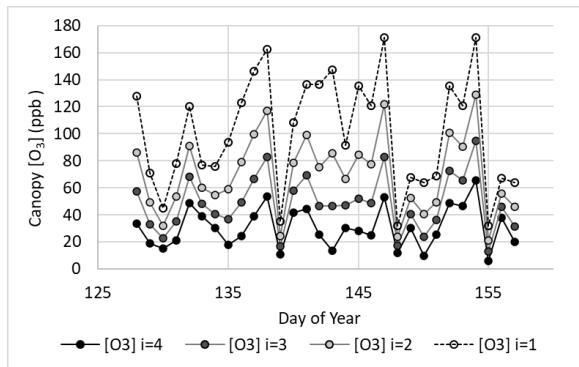
The Xiaoji dataset provides sowing and harvest dates for all cultivars for each year. However, the date of the timing of anthesis is only provided for the year 2008 for all the cultivars. We assume that DVI = 1 is equivalent to the start of anthesis, as shown in Fig. 9. The model is calibrated using the 2008 Y2 data to provide the thermal times for  $TT_{veg}$  and  $TT_{rep}$  and uses the CCI data and associated breakpoint method to estimate  $tl_{ep}$  and  $tl_{se}$ . We then assume that these values are consistent across cultivars and years. Fig. SI. 13. shows the timing of crop emergence, anthesis, and harvest in relation to simulated anthesis (i.e., at DVI=1). There is a variation of 4 to 10 days for anthesis in relation to days from crop emergence between years. The  $T_l$  ranges between 1325 and 1478 °C days for the three years with crop emergence occurring between day of year 37-45 and harvest occurring between day of year 135-151. The number of days from crop emergence to harvest was between 100 and 104 for the three years.

#### 3.4.2 Within canopy stomatal O<sub>3</sub> profile

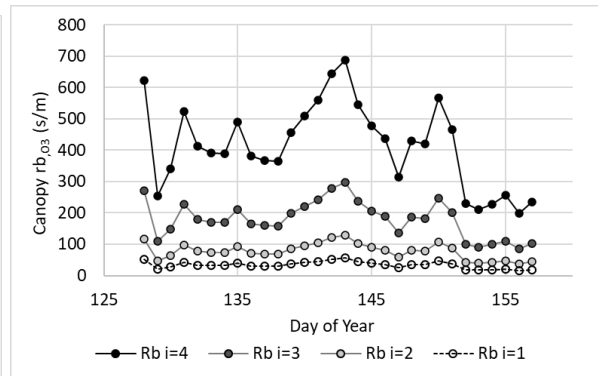
An important determinant of O<sub>3</sub> deposition and damage is stomatal O<sub>3</sub> deposition (or stomatal O<sub>3</sub> uptake), which is a function of within canopy transfer of O<sub>3</sub> and stomatal and non-stomatal deposition. The multi-layer aspect of the DO<sub>3</sub>SE-Crop model allows simulated stomatal and non-stomatal O<sub>3</sub> deposition within the canopy. Fig. 10. shows the variation in key variables that determine total and stomatal O<sub>3</sub> canopy deposition across 4 canopy layers as a mid-day average over the course of the  $tl_{ep}$  period of the flag leaf for the year 2008 and the Y2 cultivar.

Fig. 10. Plot showing variation in key  $O_3$  deposition terms as daily maxima by canopy layer (N.B.  $i = 1$  is the top canopy layer,  $n = 4$ ) a).  $[O_3]$ , b).  $rb_{O_3}$ , c).  $PAR_{sun}$  and d).  $g_{O_3}$  for the duration of the flag leaf period for the Y2 cultivar E- $O_3$  treatment 2008.

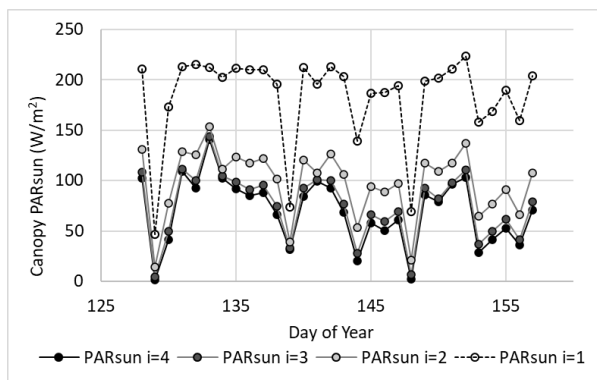
a).



b).



c).



d).

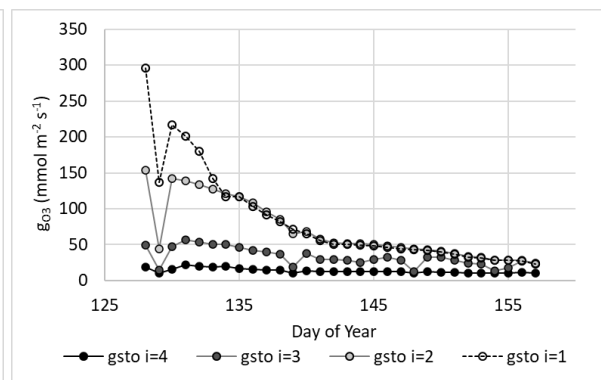
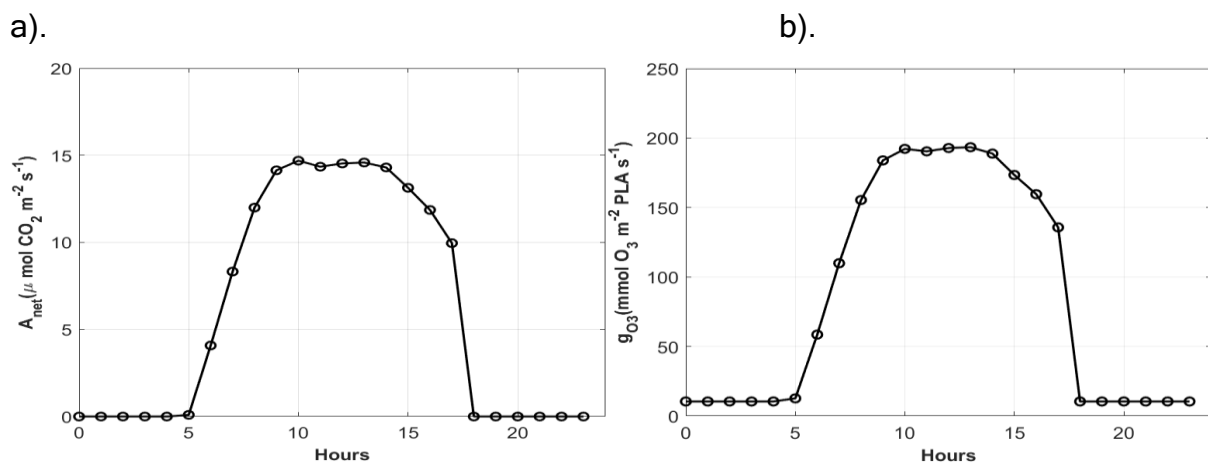


Fig. 10.a. shows a decrease within canopy  $[O_3]$  from highs of around 140 ppb to values within the range of 10 to 50 ppb between the topmost and bottom canopy layer. Similarly,  $PAR_{sun}$  reduces from maximum values of around  $200 \text{ W m}^{-2}$  to values of around  $100 \text{ W m}^{-2}$  on sunny days (see Fig. 10 b). The leaf  $rb_{O_3}$  (Fig. 10. c) also increases with canopy depth from resistances in the region of approximately  $100 \text{ s m}^{-1}$ ; and  $g_{O_3}$  (Fig. 10.d) similarly reduces from around 300 to  $20 \text{ nmol O}_3 \text{ m}^{-2} \text{ s}^{-1}$  between canopy layers, these differences reduce with the onset of senescence.

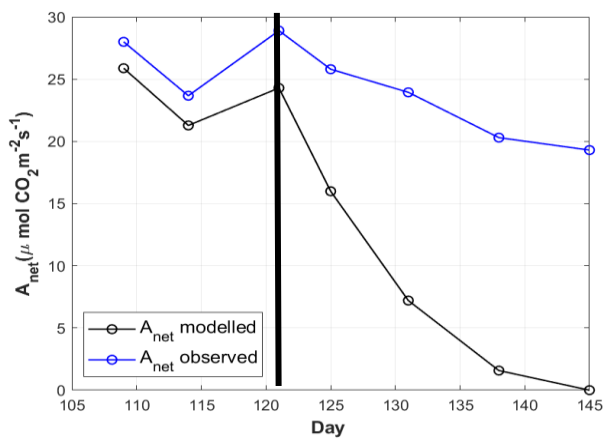
### 3.4.3 Leaf physiology variables ( $A_{net}$ , $g_{sto}$ )

The DO<sub>3</sub>SE-Crop model was able to simulate the seasonal  $A_{net}$  and  $g_{O_3}$  with values ranging from 0 and 27 and 10 and 310 for  $A_{net}$  and  $g_{O_3}$ , respectively over the course of the growing season (see Fig. 11). The simulated daily maximum values of modelled  $g_{O_3}$ , of 310 mmolm<sup>-2</sup> s<sup>-1</sup> were in the range of the observed value of 340 mmol O<sub>3</sub> m<sup>-2</sup> s<sup>-1</sup>. Similarly, the modelled maximum  $A_{net}$  is 27 μmol CO<sub>2</sub> m<sup>-2</sup> s<sup>-1</sup> compared to the observed value of 28 μmol CO<sub>2</sub> m<sup>-2</sup> s<sup>-1</sup> for the period between flag leaf emergence (Day 101) and anthesis (Day 121) for the year 2008, for both the Y2 and Y16 cultivar. Although the steep declines in modelled  $A_{net}$  and  $g_{O_3}$  values are seen as the model is showing the  $A_{net}$  and  $g_{O_3}$  canopy level (that includes all leaves, including the flag leaf), and the observed  $A_{net}$  and  $g_{O_3}$  values are at the leaf level (i.e., for the flag leaf). The flag leaf typically emerges at anthesis and is fully exposed to sunlight and, therefore, likely to show less declines because it maintains higher levels of photosynthesis for a longer period.

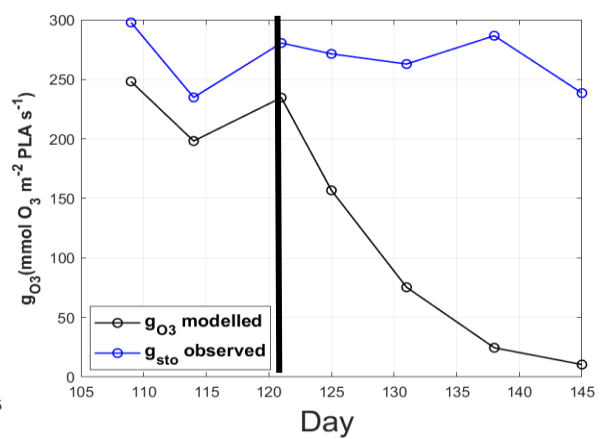
Fig. 11. DO<sub>3</sub>SE-Crop modelled diurnal profile of a).  $g_{O_3}$ , and b).  $A_{net}$  for a fully-expanded flag leaf prior to the start of senescence  $tl_{ep}$  for the ambient ozone and seasonal profile of daily maxima, with data points plotted as open circles connected by a line, representing the average daily pattern c).  $g_{O_3}$ , and d).  $A_{net}$  for the flag leaf between  $tl_{ep}$  and  $tl_{se}$  for the ambient ozone treatments. The black line showing the Start of senescence (SOS). The black line in the plot c and d shows the start of anthesis.



c).



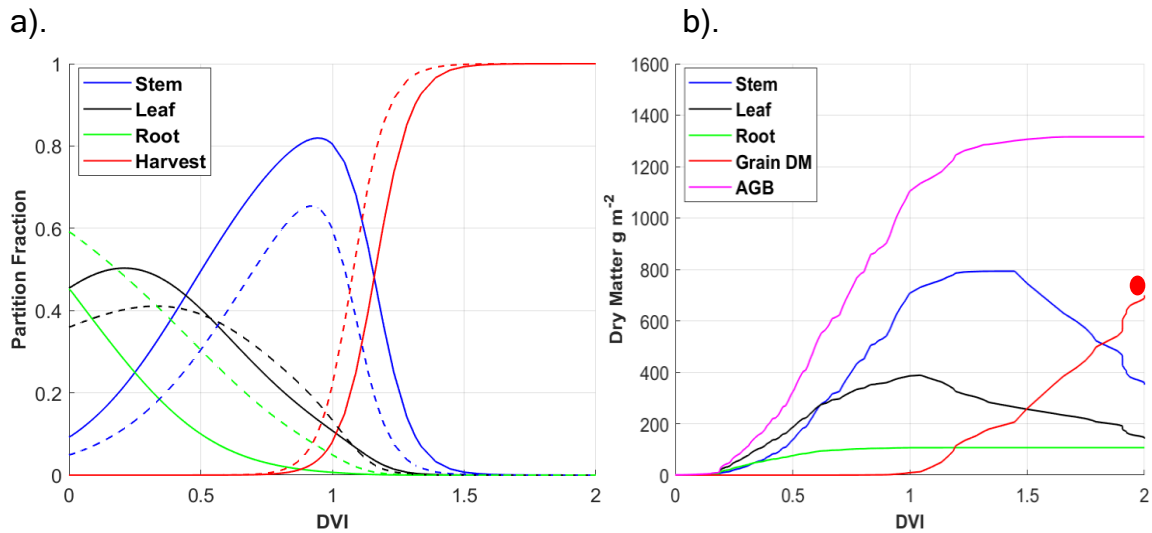
d).



### 3.4.4 Crop growth and yield.

The dry matter dynamics of the different parts of the crop are shown in Fig. 12. The modelled *Grain DM* value of  $843 \text{ g m}^{-2}$  matched the observed value of  $876 \text{ g m}^{-2}$ . The stem-to-leaf ratio is 2.1:1, in the range provided in the literature (Huang et al., 2022). Above-ground biomass values of  $1510 \text{ g m}^{-2}$  also match well against the  $1200\text{-}1600 \text{ g m}^{-2}$  range described in the literature (Huang et al., 2022; Liu et al., 2022). Further, the partition fraction profiles are consistent with those of (Osborne et al., 2015) (see Fig. 12); the main differences are that the modelled stem and root partition profiles are somewhat higher and lower, respectively, as compared to (Osborne et al., 2015).

Fig. 12. a). the partition fractions of the daily accumulated *NPP* partitioned to roots, stems, leaves, and grains for modelled (solid lines) vs. the JULES Crop model (dashed line after (Osborne et al., 2015)) plotted against *DVI*, which shows a crop development, ranging from -1 at sowing, 0 at emergence, 1 at anthesis, to 2 at maturity, with total leaf lifespan distributed between *DVI* 0 and 2 and b). the *Grain DM* of daily accumulated *NPP* partitioned to roots, stems, leaves, and grains plotted against *DVI*, the observed grain dry matter (in  $\text{g m}^{-2}$ ) is shown as a filled red circle.



### 3.4.5 Instantaneous and long-term O<sub>3</sub> impact

The  $Yield_{grain}$  is assumed to be damaged by both the instantaneous impact of O<sub>3</sub> on  $A_{net}$  as well as the long-term O<sub>3</sub> effect that can lead to enhanced senescence. To explore which of these damage mechanisms is most important, we calculated the difference between the C accumulation that would be partitioned to the grain for the AA and E-O<sub>3</sub> treatment as compared to a simulated very low [O<sub>3</sub>] treatment representing pre-industrial conditions for both the tolerant (Y16) and sensitive (Y2) cultivar for each of the three years (see Table 7). We found a negligible effect of O<sub>3</sub> (0-0.2 %) on C allocations due to the instantaneous effect of O<sub>3</sub> on  $A_{net}$  compared to a highly significant (2.86-35.85 %) impact due to the long-term O<sub>3</sub> effect *via* the enhancement of senescence on final  $Yield_{grain}$ .

Table 7. The modelled %  $Yield_{grain}$  loss compared to a pre-industrial O<sub>3</sub> scenario divided between that  $Yield_{grain}$  loss caused by the direct and instantaneous effect of O<sub>3</sub> on  $A_{net}$  and that due to the long-term O<sub>3</sub> impact on senescence. The dataset extends over a three-year period, encompassing the years 2007, 2008, and 2009. Within this framework, the analysis is applied to two wheat crop cultivars, tolerant (Y15 and Y16) and sensitive (Y2 and Y19).

Year	Tolerant: Instantaneous O <sub>3</sub> effect on % $Yield_{grain}$	Tolerant: Long-term O <sub>3</sub> effect on % $Yield_{grain}$

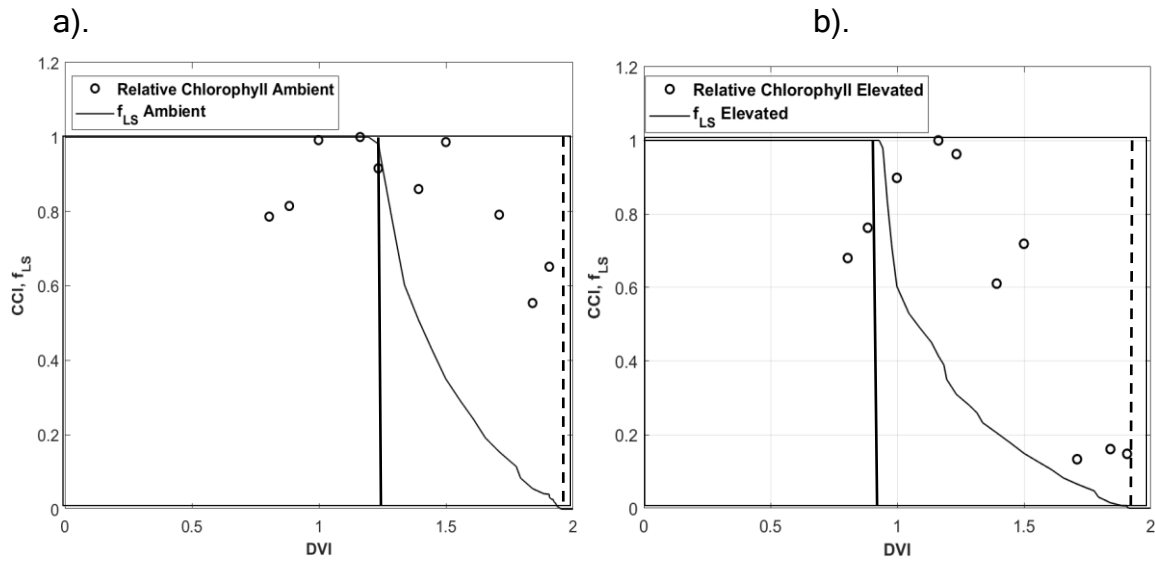
	Ambient versus pre-industrial	Elevated versus pre-industrial	Ambient versus pre-industrial	Elevated versus pre-industrial
2007	0.01	0.01	2.86	6.6
2008	0	0	3.29	17.57
2009	0.03	0.03	6.40	25.41
	Sensitive: Instantaneous O <sub>3</sub> effect on % $Yield_{grain}$		Sensitive: Long-term O <sub>3</sub> effect on % $Yield_{grain}$	
	Ambient versus pre-industrial	Elevated versus pre-industrial	Ambient versus pre-industrial	Elevated versus pre-industrial
2007	0	0.2	5.84	12.48
2008	0	0	5.21	26.5
2009	0.01	0.01	13.50	35.85

### 3.4.6 Senescence

The breakpoint method (Mariën et al., 2019) was used to determine the onset (SOS) and end (EOS) of senescence and maturity, respectively, using the chlorophyll content index (CCI) data which was available for the year 2008 and the Y2 and Y16 cultivars. Results showed (Fig. 13) that the E-O<sub>3</sub> treatment for cultivars Y2 and Y16 brought forward the SOS by 9 and 7 days, respectively, and EOS by 4 and 2 days, respectively.

Fig. 13. Leaf senescence profiles of O<sub>3</sub> induced leaf senescence for the Y2 cultivar for the a). ambient (AA) and b). elevated (E-O<sub>3</sub>) O<sub>3</sub>. The timing of the SOS (solid black line) and EOS (dashed black line) were determined by applying the breakpoint method to the CCI data and are shown in relation to the  $f_{LS}$  simulations of senescence (grey line). The observed relative CCI data are also shown (open symbols). DVI is development vegetative index, which shows the crop development,

ranging from -1 at sowing, 0 at emergence, 1 at anthesis, to 2 at maturity, with total leaf lifespan distributed between DVI 0 and 2.



### 3.4.7 Simulations across years and between cultivars

Fig. 14. shows a box plot that compares modelled versus observed grain yield ( $Yield_{grain}$ ) for both sensitive (Y2) and tolerant (Y16) wheat cultivars under ambient (AA) and elevated ozone (E-O3) conditions, spanning the years 2007, 2008, and 2009. The model accurately reflects the  $Yield_{grain}$  differential between AA and E-O3 treatments, with a simulated yield reduction of 29 g/m<sup>2</sup> for the tolerant cultivar and 49 g/m<sup>2</sup> for the sensitive cultivar under AA conditions. For the E-O3 treatment, the reduction is 131 g/m<sup>2</sup> and 196 g/m<sup>2</sup> for the tolerant and sensitive cultivars, respectively. This is in contrast to the observed reductions of 81 g/m<sup>2</sup> and 165 g/m<sup>2</sup> for tolerant cultivars and 54 g/m<sup>2</sup> and 293 g/m<sup>2</sup> for sensitive cultivars under the respective conditions. The most notable difference is that there is a larger range in the simulated  $Yield_{grain}$  losses of the modelled sensitive cultivar, though the mean value is more conservative at 610 g m<sup>-2</sup> vs an observed value of 590 g m<sup>-2</sup>.

Fig. 14. The figure presents a detailed comparison of the grain dry matter yield of wheat under two distinct ozone treatments: ambient (AA) and elevated (E-O3). The boxplots graphically summarize the distribution of both observed and simulated yield data for four wheat cultivars, categorized by their tolerance to ozone. Crosses denote the 0.01 and 0.99 percentiles, capturing the extreme values in the data set. The edges of the boxes represent the 25th and 75th percentiles, with the line inside the

box depicting the median. The solid squares indicate the mean yield, offering a direct measure of central tendency. The left cluster of boxplots under "Ambient treatment" contrasts observed yields with those simulated for ozone-tolerant cultivars Y15 and Y16 and ozone-sensitive cultivars Y2 and Y19. The right cluster, labelled "Elevated treatment," follows the same structure but under conditions of increased ozone exposure. This juxtaposition across treatments and cultivar responses—coupled with multiple years of data (2007, 2008, and 2009), provides a comprehensive view of the impact of ozone on wheat yield, illustrating the variability within and across cultivars and ozone treatments.

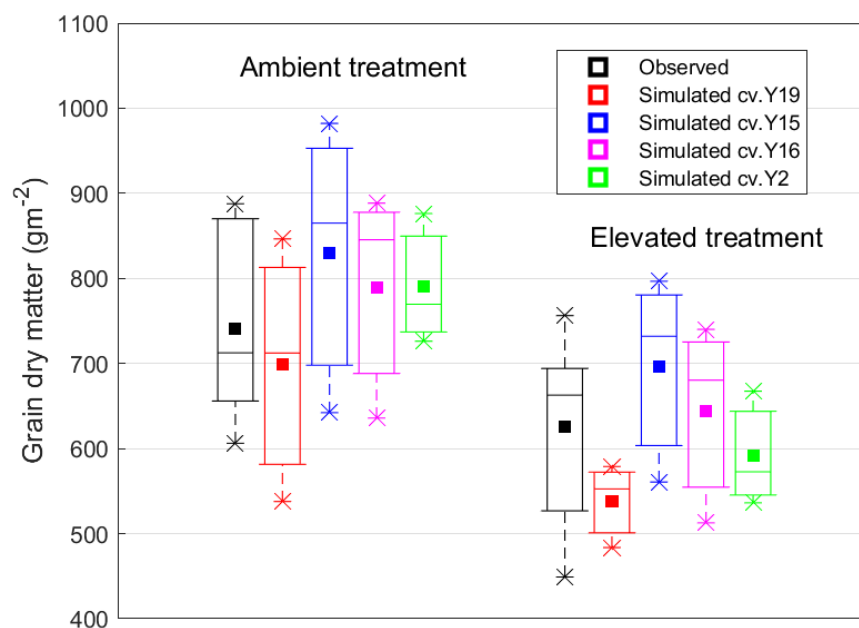
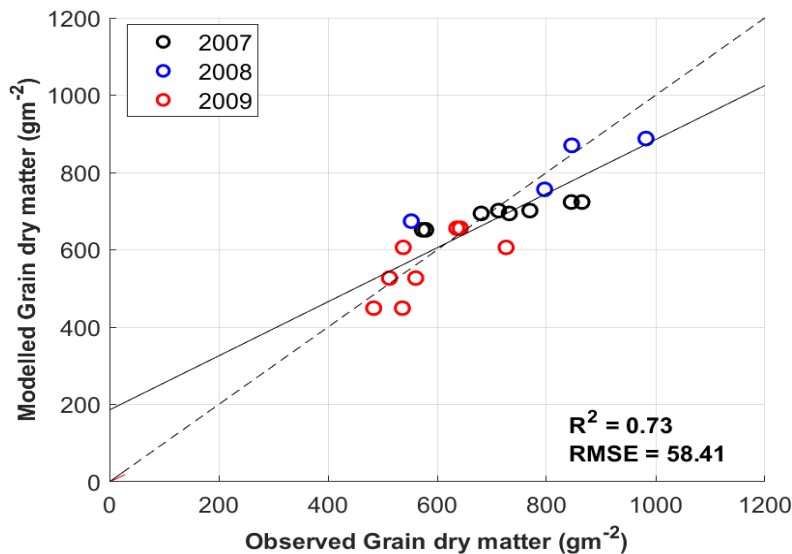


Fig. 15 shows the relationship between modelled vs. observed  $\text{Yield}_{\text{grain}}$  (in  $\text{g m}^{-2}$ ) for the years 2007, 2008, and 2009, encompassing four distinct cultivars. A linear regression through these data gives an  $R^2$  value of 0.73, indicating a moderately strong correlation between the modelled and observed yields. The data points for 2007 overestimated the  $\text{Yield}_{\text{grain}}$  for the E- $\text{O}_3$  treatments, i.e., underestimating the yield loss; this was due to the  $\text{O}_3$  treatment period being substantially shorter for the year 2007 compared to the other years (i.e., 2008 and 2009) by 38 days compared to 92 days. Additionally, in the DO3SE-crop the  $F_{\text{st}}$  (stomatal ozone flux) accumulation begins prematurely during the initial stages of leaf development, while a more realistic approach would be to start accumulating  $F_{\text{st}}$  when the leaves have developed a significant Leaf Area Index (LAI). This would represent a stage where

the canopy has developed sufficiently for meaningful gas exchange, which is crucial for a more accurate assessment of ozone's impact on yield.

Fig. 15. This scatter plot delineates the relationship between observed and modelled grain dry matter yields for wheat, aggregating data across four cultivars over three different years—2007, 2008, and 2009—as part of the Xiaoji dataset. Each year is color-coded: black for 2007, blue for 2008, and red for 2009, with respective data points plotted to illustrate the comparison on an annual basis. The dashed line represents the 1:1 correspondence between observed and modelled yields, serving as a reference for perfect model accuracy. The solid diagonal line indicates the actual regression fit between the observed and modelled data, evidencing the model's performance. The coefficient of determination ( $R^2 = 0.73$ ) suggests a substantial degree of correlation, indicating that the model can explain around 73% of the variability in observed yields. The root means square error (RMSE = 58.41) quantifies the model's prediction error, offering insight into the average magnitude of the model's residuals or prediction errors.



### 3.5 Discussion

The DO<sub>3</sub>SE-Crop model was capable of simulating O<sub>3</sub> damage to grain yield for O<sub>3</sub>-FACE conditions at the experimental site in Xiaoji, China. Simulated yield losses between ambient and elevated O<sub>3</sub> conditions for all years ranged between 4-19% and 7-25% for tolerant and sensitive cultivars respectively; these simulated values are close to equivalent observed value ranges of between 12-19% and 10-34%. However, it should be noted that the model overestimated grain dry matter for the elevated O<sub>3</sub> treatments for the year 2007 (see Fig. 15) due to a shorter exposure period. (Zhu et al., 2011) argued that despite the delayed and shorter O<sub>3</sub> fumigation period in 2007, the elevated O<sub>3</sub> levels were not much less than in other seasons and concluded this was the reason for the same level of O<sub>3</sub> impact on experimental grain yield. However, the accumulated stomatal O<sub>3</sub> flux estimated by the DO<sub>3</sub>SE-model was much higher for the elevated O<sub>3</sub> treatment for the years 2008 and 2009 (at ~ 19 mmol O<sub>3</sub> m<sup>-2</sup>) compared to 2007 (16.3 mmol O<sub>3</sub> m<sup>-2</sup>), hence the greater modelled impact on the relative grain yield loss (15-18% for 2008 and 2009 versus 4-6% for 2007). This discrepancy stems from the model's premature initiation of F<sub>st</sub> (stomatal ozone flux) accumulation during the early stages of foliar emergence rather than waiting until a significant Leaf Area Index (LAI) has been established. Such a modification would better represent the point at which the canopy is adequately developed to engage in substantial gas exchange, a critical aspect for accurately determining the impact of ozone on yield.

Overall, the DO<sub>3</sub>SE model simulation results compare favourably to results made by the MCWLA-Wheat model (Tao et al., 2017), which was also calibrated for the Xiaoji experimental conditions but without distinction between tolerant and sensitive varieties; MCWLA-Wheat absolute simulated yield varied between ~5700 and 9000 kg/ha (compared to ~5700 to 9800 kg/ha) for ambient and ~4800 to 8000 kg/ha (compared to ~5200 to 8000) for elevated O<sub>3</sub> treatments. A mean relative yield loss of 14% was simulated by the model. For context, mean relative yield losses across East Asia were estimated at 33% (with a mean range of 28-37%) by (Feng et al., 2022) according to a mean monitored O<sub>3</sub> of 30.9 ppm h expressed as AOT40 (six-month accumulated daytime O<sub>3</sub> concentration above a threshold of 40 ppb). The mean difference in AOT40 (accumulated over only 75 days) between the ambient and E-O<sub>3</sub> treatments at Xiaoji across all years was 7.8 ppm h.

Crop phenology plays a crucial role in determining the entire O<sub>3</sub> exposure period (i.e., from crop emergence to maturity), and hence O<sub>3</sub> damage since steady O<sub>3</sub> accumulation ( $acc_{fst}$ ) occurring from early on in the crop growth period can cause O<sub>3</sub> detoxification mechanisms to be overwhelmed. The DO<sub>3</sub>SE-crop model simulates the crop phenology for the three years at Xiaoji well compared to the observed dataset ( $R^2 = 0.98$ , see Fig. SI. 13). Estimating the correct timing of anthesis is crucial since the period from anthesis to crop maturity is the O<sub>3</sub> sensitive period. During this period, accumulated stomatal O<sub>3</sub> flux ( $acc_{fst}$ ) will contribute to early and enhanced senescence once the critical threshold ( $CLsO3$ ) is exceeded. This period also coincides with C accumulation in the grain (Kohut et al., 1987; Feng et al., 2008), which may be limited by O<sub>3</sub>-induced early onset or enhanced senescence. The DO<sub>3</sub>SE-crop model was developed to accommodate the full range of effects of O<sub>3</sub> on senescence with revised (Ewert and Porter, 2000) functions able to modify both the O<sub>3</sub>-induced onset of senescence as well as the O<sub>3</sub> effect on maturity. This is important since experimental evidence has shown that O<sub>3</sub> can bring forward the maturity date; for example, the flag leaf was found to have senesced 25 days earlier in a high O<sub>3</sub>, compared to a charcoal filtered, treatment (Grandjean and Fuhrer Grandjean, 1989; Gelang et al., 2000b). Ozone was also found to cause differences in the time to maturity of the flag leaf, with Shi et al., 2009 reporting that maturity was brought forward by eight days in an elevated O<sub>3</sub> (50% higher than ambient) treatment. Currently, other crop models with O<sub>3</sub> damage functions (e.g., MLCWLA-Wheat (Tao et al., 2017) and LINTULLCC-22 (Feng et al., 2022) are only able to bring the O<sub>3</sub>-induced onset of senescence earlier.

The DO<sub>3</sub>SE-crop model is also able to simulate differential O<sub>3</sub> uptake in each canopy layer. Fig. 10. shows that the majority of stomatal O<sub>3</sub> uptake occurs in the sunlit layers of the upper canopy. Similar results were found in an experimental study on a productive grassland in Switzerland (Jaggi et al., 2006), who found that different levels of O<sub>3</sub> exposure to canopy components predominantly located in the upper and lower parts of the canopy support a multi-layer approach to modelling O<sub>3</sub> uptake. Therefore, the focus on the upper canopy by flux based O<sub>3</sub> metrics (e.g., the phytotoxic ozone dose  $POD_y$  (UNECE, 2017) seems rational in the absence of multi-layer modelling. Crop models such as LINTULLCC-2 (Feng et al., 2022) also focus on estimating stomatal O<sub>3</sub> uptake at the top of the canopy to estimate O<sub>3</sub>-induced yield

losses. For wheat, such an approach is further supported by the fact that the upper canopy layers consist of the flag leaf, which plays a crucial role in  $A_{net}$  and grain filling (Pleijel et al., 2007).

Our results show that the DO<sub>3</sub>SE-crop model was able to estimate the seasonal course of  $A_{net}$  and  $g_{O_3}$  daily maxima observed at the Xiaoji site (see Fig. 11 c & d). Additionally, the model proficiently generated diurnal profiles for  $A_{net}$  and  $g_{O_3}$ , which are depicted in see Fig. 11. a & b, exhibiting consistency with documented leaf physiological variables in the scientific literature (Guan et al., 2015; Li et al., 2022). This suggests the coupled  $A_{net}g_{sto}$  model is working for Chinese conditions (having previously been applied and evaluated for European O<sub>3</sub> experimental conditions - see Pande et al. sub). The leaf physiology parameters used in this study (i.e., for Asian conditions and cultivars) are higher than the parameters for European studies. For Europe,  $V_{cmax}$  values of between 60 and 90  $\mu\text{mol CO}_2 \text{ m}^{-2} \text{ s}^{-1}$  were found in the literature (Feng et al., 2022; Pande et al., sub, Oijen and Ewert, 1999) compared to the observed mean maximum value of 137  $\mu\text{mol CO}_2 \text{ m}^{-2} \text{ s}^{-1}$  at Xiaoji which was used in this study. Similarly, European  $J_{max}$  values ranged from 160 to 180  $\mu\text{mol CO}_2 \text{ m}^{-2} \text{ s}^{-1}$  (Feng et al., 2021; Pande et al. sub, Oijen & Ewert, 1999) compared to the observed Xiaoji mean maximum value of 228  $\mu\text{mol CO}_2 \text{ m}^{-2} \text{ s}^{-1}$ .

Ensuring the seasonal variation in C allocation to the different components of the crop (i.e., roots, stem, leaves, and harvest organs) is essential for the simulation of crop growth and yield. There are few data in the literature that provide these variables, so we compare our results to the C allocation profiles described for wheat provided in the original JULES Crop model description, recognising this is intended for wheat grown globally. The DO<sub>3</sub>SE-Crop model C allocation to the stem and roots is comparatively higher than was simulated by JULES Crop ((Osborne et al., 2015); see Fig. 12 a). However, we can justify the C allocation coefficients we used for Xiaoji since the DO<sub>3</sub>SE-Crop model was able to distribute C to different plant components to produce a well-proportioned plant over the course of the growing season, this was determined by the calibration to a number of key crop variables (i.e., ratios of plant respiration,  $LAI$ , stem to leaf dry matter ratios, above-ground components and grain dry matter. Importantly, the model was found to simulate the grain dry matter for the year 2008, and the cultivar Y16 (tolerant) & Y2(sensitive)

under the ambient and elevated O<sub>3</sub> treatment to within 0.08- 2.19% of the observed values ( $R^2 = 0.99$ , RMSE=9.27 g/m<sup>2</sup>, see Fig. Sl. 14).

The DO<sub>3</sub>SE-Crop model, similar to other crop models with O<sub>3</sub> damage functions (i.e., MLCWLA-Wheat (Tao et al., 2017) and LINTULLCC-2 (Feng et al., 2022)) has the capacity to simulate both the instantaneous and long-term O<sub>3</sub> impact on wheat grain yield. The instantaneous O<sub>3</sub> effect on  $A_{net}$  may cause leaf cell damage and decrease the supply of carbohydrate precursors, which can significantly decrease  $g_{O_3}$ ,  $V_{cmax}$  and leaf chlorophyll content (Farage et al., 1991; Feng et al., 2022). Elevated O<sub>3</sub> also leads to the generation of reactive oxygen species (ROS) in plant cells, which can cause oxidative damage to various cellular components. Rubisco, the enzyme responsible for C fixation in the photosynthetic process, can be particularly susceptible to this damage, leading to a reduced carboxylation rate ( $V_{cmax}$ ). Such an ozone effect on  $V_{cmax}$  reduces  $A_{net}$  and can also induce early senescence, shortening the grain-filling period (Triboi and Triboi-Blondel, 2002).

Results from the DO<sub>3</sub>SE-crop model found a larger impact on yield due to the long-term O<sub>3</sub> impact, causing relative yield loss of between 2 to 36% compared to only 0 to 0.2% resulting from the instantaneous O<sub>3</sub> impact on  $A_{net}$ . Previous studies have also found that the long-term O<sub>3</sub> effect has a larger impact on yield compared to the instantaneous effect of O<sub>3</sub> on  $A_{net}$  (Emberson et al., 2018; Brewster et al., 2024). Senescence is an age-dependent process of degradation and degeneration that allows nutrients to be re-distributed to different plant organs (Lim et al., 2007). Under O<sub>3</sub> stress, this process is often found to occur earlier and more rapidly in leaves as well as at the whole plant or crop canopy scale (Brewster., 2024). The causes of this early and accelerated senescence are not completely understood but may be related to O<sub>3</sub>-induced enhanced expression of many genes involved in natural senescence (Miller et al., 1999). Elevated O<sub>3</sub> was also found to inhibit sugar export from leaves (Yadav et al., 2020; Feng et al., 2024), which could trigger early onset of leaf senescence.

The DO<sub>3</sub>SE-crop model accounts for the impact of O<sub>3</sub> on the Rubisco enzyme by incorporating modified (Ewert and Porter, 2000) functions for instantaneous and long-term O<sub>3</sub> impact on  $V_{cmax}$  as an important parameter used to characterize the crop photosynthetic capacity (Ewert and Porter, 2000; Osborne et al., 2019). The DO<sub>3</sub>SE-crop model assumes that the O<sub>3</sub> will only accumulate on exceedance of a

stomatal  $O_3$  flux threshold of  $6 \text{ nmol } O_3 \text{ m}^{-2} \text{ s}^{-1}$ . The  $DO_3SE$ -crop model effectively simulated the long-term impact of  $O_3$  on senescence, particularly on the  $V_{cmax}$ , as indicated by the observed reduction in leaf chlorophyll content (Fig. 13 a and b). We used the breakpoint method (Mariën et al., 2019) to estimate the SOS and EOS using measured chlorophyll content index values. It is crucial to model the timing of SOS and EOS correctly as this determines the  $O_3$  effect on the duration of the grain filling period and, hence, the difference in yield loss due to different  $O_3$  treatments. For example, we modelled a difference of 8 and 3 and 4 and 1 days in SOS & EOS respectively on average across years for the sensitive and tolerant cultivars, respectively.

China's wheat breeding programme has seen more than 1,850 varieties used across China between the 1920s and 2014, leading to increased yields from less than  $<1$  to  $>5 \text{ tonnes ha}^{-1}$  (Qin et al., 2015). Here, albeit with an extremely limited dataset, we parameterise the  $DO_3SE$ -crop model for tolerant and sensitive wheat crop cultivars since many experimental studies have shown that the response of different cultivars to  $O_3$  stress differs (Biswas et al., 2008). The data indicates that the model demonstrates a capacity to reproduce the variance in grain dry matter among the various cultivar groups over different years, with a correlation coefficient ( $R^2$ ) of 0.73; see Fig. 15. Such a cultivar sensitivity-based parametrisation can provide additional some information on the certainty of regional yield loss estimates given a large number of wheat varieties grown across China.

### 3.6 Conclusions

We have shown that the newly developed DO<sub>3</sub>SE-Crop model can be calibrated for O<sub>3</sub> tolerant and sensitive wheat varieties for O<sub>3</sub>-FACE site conditions at Xiaoaji in China. The model is able to simulate crop phenology, leaf physiology, crop growth, and yield well across different years. The model is also able to simulate the effect of O<sub>3</sub> stress on grain yield, distinguishing the extent of O<sub>3</sub> damage resulting from the same O<sub>3</sub> treatment on cultivars with differing O<sub>3</sub> sensitivities. The DO<sub>3</sub>SE-Crop model also has the advantage of simulating O<sub>3</sub> transfer and deposition dynamics within the wheat crop canopy, which could, in the future, improve our understanding of whole canopy O<sub>3</sub> effects. The ability of the model to estimate relative yield losses across years also suggests the model is 'fit for purpose' to assess the effects of O<sub>3</sub> under a variety of climate variables and O<sub>3</sub> conditions.

## SI.2 Supporting material

### SI.2.1 Resistance and diffusivity of gases across leaf boundary layers

The leaf-level quasi laminar boundary layer resistance term  $r_b$  (McNaughton and van der Hurk, 1995) incorporates empirically derived constants for heat and gas conductance (see Table 13, in mol TLA  $m^{-2} s^{-1}$ ), crosswind leaf dimension  $L$  (given in m) and the wind speed at the leaf surface  $u(h)$  (given in m/s). N.B. TLA is the Total Leaf Area.

Table. SI. 7. Empirically derived constant conductance (mol TLA  $m^{-2} s^{-1}$ ) (and resistance (PLA s/m)) values for heat and gas ( $H_2O$ ,  $CO_2$ , and  $O_3$ ) from a single leaf surface.

Matter	Conductance (mol TLA $m^{-2} s^{-1}$ )	Resistance (PLA s/m) Rounded down
Heat	0.135	150
Water vapour, $H_2O$	0.147	139
Carbon dioxide, $CO_2$	0.110	186
Ozone, $O_3$	0.105	195

The conversion of constants from conductance to resistance is achieved by multiplying by 2 to convert from single surface to PLA, dividing by 41 to convert from mol  $m^{-2} s^{-1}$  to m/s, and calculating the reciprocal to give a resistance term (e.g. for heat the conversion is  $1 / (0.135 \cdot 2) / 41$  which gives 151.85 and is then rounded down to 150).

Leaf boundary layer resistance for heat (for forced convection) ( $r_{b,heat}$ ) can be calculated according to Eq. SI. 8 after (Campbell, G.S., Norman, 1998), using the 150 values for boundary layer resistance to heat in s/m, these formulations take into account both sides of the leaf and therefore provide  $r_{b,heat}$  for PLA (Projected Leaf Area)).

$$r_{b,heat\_forced} = 150 \cdot \sqrt{\frac{L}{u(h)}} \quad \text{Eq. SI. 8}$$

To estimate boundary layer resistance values for other gases simply substitute the relevant gas constant for resistance into Eq. SI. 8

### SI.2.2 Diffusivities of gases for stomatal conductance ( $g_{sto}$ )

The conversion factors are derived from Graham's law, which assumes that the ratio of the diffusivities is equal to the inverse of the square root of the ratio of molecular weights (as described in (Campbell et al., 1998)).

$$\text{e.g. } \text{mol H}_2\text{O m}^{-2} \text{ s}^{-1} = 0.61 \text{ mol O}_3 \text{ m}^{-2} \text{ s}^{-1}$$

$$\text{mol CO}_2 \text{ m}^{-2} \text{ s}^{-1} = 0.96 \text{ mol O}_3 \text{ m}^{-2} \text{ s}^{-1}$$

Table. SI. 8. Conversion factors for H<sub>2</sub>O, CO<sub>2</sub> and O<sub>3</sub>

	Molecular weight	Ratio of molecular weights (to H <sub>2</sub> O)	Ratio of molecular weights (to CO <sub>2</sub> )	Ratio of molecular weights (to O <sub>3</sub> )	Inverse sq. root of ratio of molecular weight (to H <sub>2</sub> O)	Inverse sq. root of ratio of molecular weight (to CO <sub>2</sub> )	Inverse sq. root of ratio of molecular weight (to O <sub>3</sub> )
H <sub>2</sub> O	18	1	0.409	0.375	1	1.56	1.63
CO <sub>2</sub>	44	2.44	1	0.92	0.64	1	1.04
O <sub>3</sub>	48	2.67	1.09	1	0.61	0.96	1

### SI.2.3 Irradiance absorption by the canopy

Solar radiation is the key determinant of the productivity of any crop. The radiation absorbed (direct and diffuse) photosynthetically active radiation,  $PAR_{tot}$  (in W/m<sup>2</sup>) by crops will have a direct impact on  $A_{net_c}$  (and associated  $g_{sto}$ ) and affect crop leaf phenology and hence net primary productivity ( $NPP$ ).  $PAR$  absorbed by crops is divided into two categories, direct ( $PAR_{dir}$ ) and diffuse ( $PAR_{diff}$ ) radiation.  $PAR_{dir}$  is the  $PAR$  which reaches the crop leaf surface without being scattered, whereas  $PAR_{diff}$  can be naturally (by cloud cover and naturally occurring particles in the atmosphere) or artificially scattered (e.g., by pollutant aerosol).  $PAR$  can also be reflected by surfaces.

To estimate the total irradiance ( $PAR_{tot}$  which is equal to  $PAR_{dir} + PAR_{diff}$ ) incident on sunlit and shaded parts of the canopy we use the method (Pury and Farquhar, 1997).

### SI.2.3.1 Total Photosynthetic Active Radiation ( $PAR_{tot}$ )

$PAR$  absorbed per unit leaf area is divided into  $PAR_{dir}$ ,  $PAR_{diff}$  which also includes scattered (re-reflected by the canopy) beam calculated by,

$$PAR_{dir}(LAI) = (1 - \rho_{cb}(\beta)) K_b' I_b(0) \exp(-k_b' LAI) \quad \text{Eq. SI. 9}$$

$$\text{Where, } \rho_{cb}(\beta) = 1 - \exp\left[\frac{2\rho_h k_b}{1+k_b}\right] \quad \text{Eq. SI. 10}$$

where;  $K_b'$  is beam and scattered beam PAR extinction coefficient;  $I_b(0)$  is the initial beam irradiance, representing the intensity of direct sunlight before it interacts with the canopy.

$$PAR_{diff}(LAI) = (1 - \rho_{cd}) k_d' I_d(0) \exp(-k_d' LAI) \quad \text{Eq. SI. 11}$$

$$\text{Where, } \rho_{cd} = \frac{1}{I_d(0)} \int_0^{\frac{\pi}{2}} N_d(\alpha) \rho_{cb}(\alpha) d\alpha \quad \text{Eq. SI. 12}$$

And  $K_d'$  is diffuse and scattered diffuse PAR extinction coefficient.

The total absorbed irradiance per unit leaf area is calculated as:

$$PAR_{total} = PAR_{dir}(LAI) + PAR_{diff}(LAI) \quad \text{Eq. 70}$$

Estimations of the direct, diffuse and scattered (re-reflected) irradiance are necessary to calculate the PAR incident on the sunlit ( $LAI_{sun}$ ) and shaded ( $LAI_{shade}$ ) portions of the canopy, which are then calculated based on the equations described below:

SI.2.3.2 Total irradiance absorbed as shaded leaves ( $I_{lsh}(LAI)$ ) per unit leaf area are calculated as;

$$PAR_{sh}(LAI) = PAR_{diff}(LAI) + PAR_{bs}(LAI) \quad \text{Eq. SI. 13}$$

where  $PAR_{diff}(LAI)$  is diffuse irradiance (see eq.) and  $PAR_{bs}(LAI)$ , direct scattered beam (another form of diffuse radiation) is calculated as:

$$PAR_{bs}(LAI) = PAR_b(0) [PAR_{dir} - (1 - \sigma)k_b \exp(-k_b LAI)] \quad \text{Eq. SI. 14}$$

Total irradiance absorbed by per unit leaf area of the sunlit leaf

$$PAR_{sun}(LAI, \beta) = PAR_{sh}(LAI) + PAR_{bsun}(\beta) \quad \text{Eq. SI. 15}$$

Where;  $PAR_{sh}$  (LAI) is irradiance absorbed by shaded leaves (see equation S6) and  $PAR_{bsun}(\beta)$ , beam irradiance absorbed by sunlit leaves and calculated as below:

$$PAR_{bsun}(\beta) = (1 - \sigma)I_b(0) \frac{\cos\alpha_l}{\sin\beta} \quad \text{Eq. Sl. 16}$$

Table. Sl. 9. Variables and parameters, their definitions and units used to calculate the multi-layer canopy irradiance after De Pury and Farquhar (1997).

Parameters	Description	Value	Units
$K_b'$	Beam and scattered beam PAR extinction coefficient	$0.46/\sin\beta$	
$K_d'$	Diffuse and scattered diffuse PAR extinction coefficient	0.719	
$\rho_{cb}$	Canopy refection coefficient for beam PAR		
$\rho_{cd}$	Canopy reflection coefficient for diffuse PAR		
$\beta$	Solar elevation angle		Radians
$\delta$	Solar declination angle		Radians
$I_{lb}$ (LAI)	Absorbed beam plus scattered beam PAR per unit leaf area		$\mu\text{mol m}^{-2} \text{s}^{-1}$
$I_{ld}$ (LAI)	Absorbed diffuse plus scattered diffuse PAR per unit leaf area		$\mu\text{mol m}^{-2} \text{s}^{-1}$
$I_l$ (LAI)	Total absorbed PAR per unit leaf area		$\mu\text{mol m}^{-2} \text{s}^{-1}$
$I_b$ (LAI)	Direct PAR per unit ground area		$\mu\text{mol m}^{-2} \text{s}^{-1}$
$I_d$ (LAI)	Diffuse PAR per unit ground area		$\mu\text{mol m}^{-2} \text{s}^{-1}$
$I_d(0)$	Diffuse PAR per unit ground area at the top of the canopy		$\mu\text{mol m}^{-2} \text{s}^{-1}$
$I_b(0)$	Beam PAR per unit ground area at the top of the canopy		$\mu\text{mol m}^{-2} \text{s}^{-1}$
$I_{lbb}$ (LAI)	Absorbed beam PAR without scattering per unit leaf area		$\mu\text{mol m}^{-2} \text{s}^{-1}$

$I_{bs}$ (LAI)	Absorbed scattered beam PAR per unit leaf area		$\mu\text{mol m}^{-2} \text{s}^{-1}$
$I_{bsun}$ (LAI)	Beam PAR absorbed by sunlit leaves per unit leaf area		$\mu\text{mol m}^{-2} \text{s}^{-1}$
$I_{lsh}$ (LAI)	Beam PAR absorbed by shaded leaves per unit leaf area		$\mu\text{mol m}^{-2} \text{s}^{-1}$
$I_{lsun}$ (LAI)	Total PAR absorbed by sunlit leaves per unit leaf area		$\mu\text{mol m}^{-2} \text{s}^{-1}$
(LAI)	Cumulative leaf area index from top of canopy (L=0 at top)		$\text{m}^2\text{m}^{-2}$
$f_{1,2}$ (LAI)	Fraction of leaf area in a leaf-angle class		
$f_{sh}$ (LAI)	Fraction of leaves that are shaded		
$f_{sun}$ (LAI)	Fraction of leaves that are sunlit		
$\sigma$	Leaf scattering coefficient for PAR	0.15	
$\alpha_1$	Angle of beam irradiance to the leaf normal	0.5	Radians

## SI.2.4 O<sub>3</sub> Resistance

### Atmospheric Resistance

$$r_a = \frac{1}{K u^*} \left( \log \left( \frac{z_2}{z_1} \right) - \Psi_h \left( \frac{z_2}{L} \right) + \Psi_h \left( \frac{z_1}{L} \right) \right) \quad \text{Eq. SI. 17}$$

$u^*$  Friction velocity m/s

$K$  Von Karman's constant

$L$  Monin-Obukhov length m

$z_1$  Lower height m

$z_2$  Upper height m

$\Psi_h$  Flux-gradient stability function for heat

1. Heat flux

$$\psi_h(x) = \begin{cases} 2 \log\left(\frac{1+\sqrt{1-16x}}{2}\right) & x < 0 \\ -5x & x \geq 0 \end{cases} \quad \text{Eq. SI. 18}$$

Quasi-laminar boundary layer resistance

$$r_{b,O3} = \frac{2}{Ku^*} \left( \frac{\left(\frac{V}{diff}\right)^2}{PR} \right)^{\frac{2}{3}} \quad \text{Eq. SI. 19}$$

$u^*$  Friction velocity m/s

$K$  Von Karman's constant

$V$  Kinematic viscosity of air at 20°C m<sup>2</sup>/s

$diff$  Molecular diffusivity in air m<sup>2</sup>/s

$PR$  Prandtl number

2. In-canopy resistance

$$r_{inc} = 14 \frac{SAI h}{u^*} \quad \text{Eq. SI. 20}$$

3. External plant cuticle resistance

$$r_{ext} = \frac{2500}{SAI} \quad \text{Eq. SI. 21}$$

Stomatal resistance

$$r_{sto} = \min\left(100000, \frac{41000}{g_{sto}}\right) \quad \text{Eq. SI. 22}$$

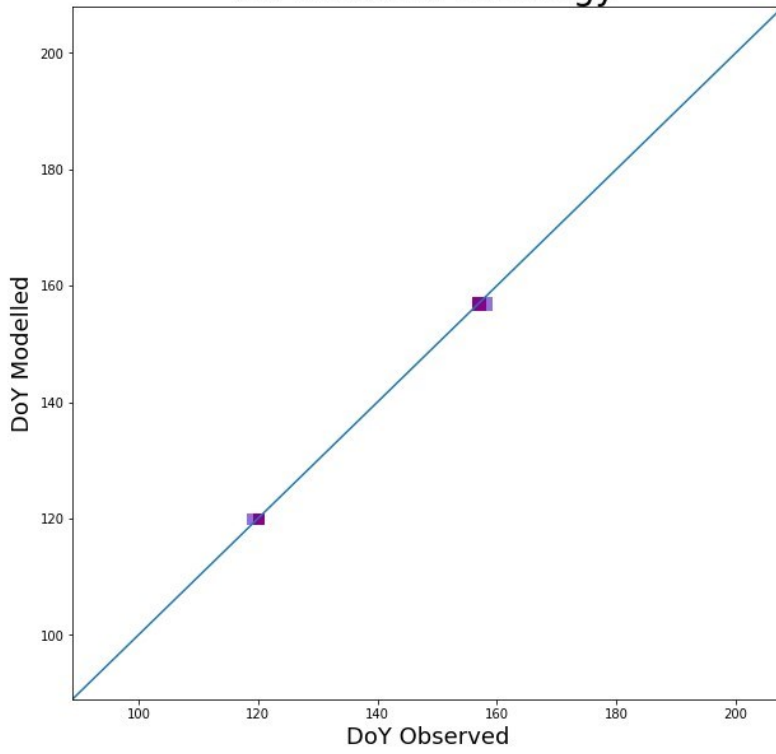
Surface resistance per layer

$$r_c = \begin{cases} r_b + \frac{1}{\left(\frac{1}{r_{sto}} + \frac{1}{r_{ext}}\right)} & LAI > 0 \\ r_b + r_{ext} & SAI > 0 \end{cases} \quad \text{Eq. SI. 23}$$

SI.2.5 The timing of crop emergence, anthesis and harvest

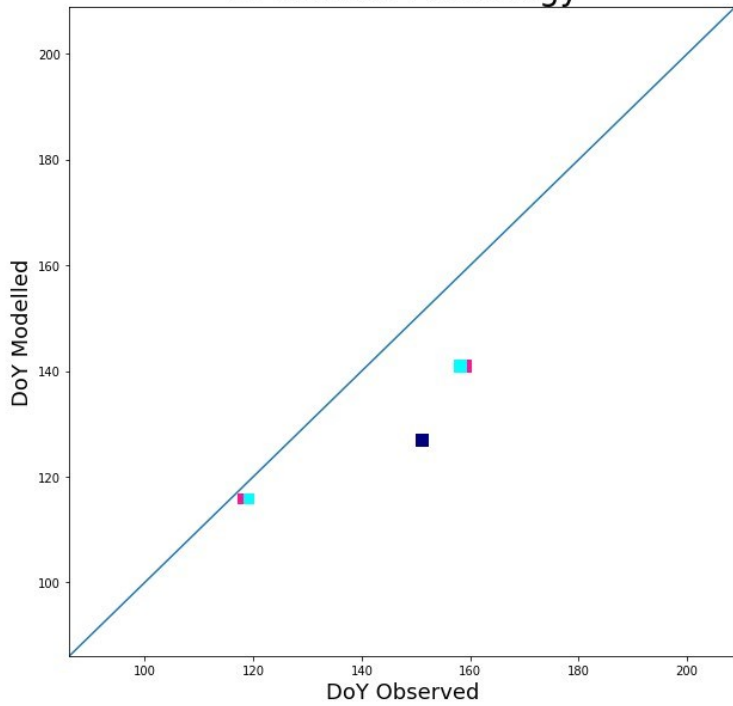
Fig. SI. 13. The Chinese FACE-O<sub>3</sub> dataset were used to plot modelled phenological stages (emergence, anthesis, and maturity) against experimental dataset for the year a) 2008 (training set, cultivar Y15, Y16, and Y2) and b) 2007 and 2009 (testing set, cultivar Y15, Y16 and Y2). The straight line shows the 1:1 line.

### All Models Phenology



- XI\_2008\_Y15\_A      ■ XI\_2008\_Y2\_A      ■ Anthesis      ■ DO3SE
- XI\_2008\_Y16\_A      ■ Emergence      ■ Maturity

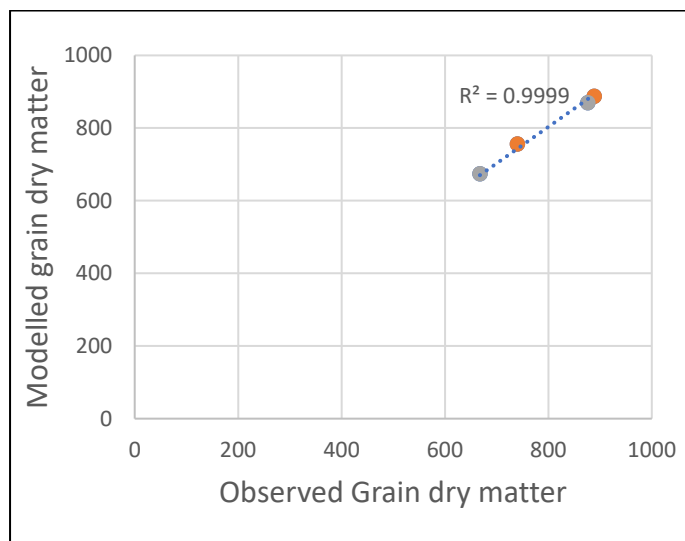
### All Models Phenology



- XI\_2007\_Y15\_A      ■ XI\_2009\_Y15\_A      ■ Emergence      ■ Maturity
- XI\_2007\_Y16\_A      ■ XI\_2009\_Y16\_A      ■ Anthesis      ■ DO3SE
- XI\_2007\_Y2\_A      ■ XI\_2009\_Y2\_A

SI.2.6 Chinese FACE-O<sub>3</sub> dataset Scatter plot: Modelled grain dry matter (g/m<sup>2</sup>) against experimental dataset for the year 2008

Fig. SI. 14. The Chinese FACE-O<sub>3</sub> dataset were used to plot modelled grain dry matter (g/m<sup>2</sup>) against experimental dataset for the year 2008 for tolerant (Y16) and sensitive cultivar (Y2) (training set). The dotted black line shows the regression line.



SI.2.7 DO<sub>3</sub>SE-Crop variables

Table. SI. 10. DO<sub>3</sub>SE-Crop variables, their description, and units.

Variable	Unit	Description
$T_{eff}$	°C days	Effective temperature accumulated between sowing to maturity
$DVI$	-	Development index
$T_{air}$	°C	Surface air temperature in degrees Celsius
$T_{air,k}$	degrees Kelvin	Surface air temperature in Kelvin
$T_{min}$	°C	Daily minimum surface air temperature
$T_{max}$	°C	Daily maximum surface air temperature
$V_{dd}$	days	Accumulated vernalised days
$V$	days	Vernalised days
$V_d$	days	Devernalised days
$VF$	-	Vernalisation factor
$PP$	hrs	Photoperiod
$PF$	-	Photoperiod factor
$A_{net}$	µmol CO <sub>2</sub> m <sup>-2</sup> s <sup>-1</sup>	Net photosynthesis or rate of CO <sub>2</sub> assimilation

$A_c$	$\mu\text{mol CO}_2 \text{ m}^{-2} \text{ s}^{-1}$	RuBP (ribulose-1,5-bisphosphate) limited $A_{net}$
$A_j$	$\mu\text{mol CO}_2 \text{ m}^{-2} \text{ s}^{-1}$	Electron transport limited $A_{net}$
$A_p$	$\mu\text{mol CO}_2 \text{ m}^{-2} \text{ s}^{-1}$	TPU (triose phosphate) limited $A_{net}$
$R_d$	$\mu\text{mol CO}_2 \text{ m}^{-2} \text{ s}^{-1}$	Dark respiration
$f_{PAW}$	-	Plant available soil water stress factor
$C_i$	$\mu\text{mol/mol}$	Intercellular $\text{CO}_2$ partial pressure
$O_i$	$\text{mmol/mol}$	Intercellular $\text{O}_2$ concentrations
$\Gamma^*$	$\mu\text{mol/mol}$	$\text{CO}_2$ compensation point in the absence of respiration
$\Gamma$	$\mu\text{mol/mol}$	$\text{CO}_2$ compensation point
$J$	$\mu\text{mol CO}_2 \text{ m}^{-2} \text{ s}^{-1}$	electron transport rate
$VPD$	kPa	Leaf to air vapour pressure deficit
$f_{st}$	$\text{nmol O}_3 \text{ m}^{-2} \text{ s}^{-1}$	Leaf level stomatal $\text{O}_3$ flux
$accf_{st}$	$\text{mmol O}_3 \text{ m}^{-2}$	Accumulated stomatal $\text{O}_3$ flux
$f_{03,s}(d)$	-	Effect of daily cumulative stomatal $\text{O}_3$ flux on $V_{C_{max}}$
$f_{03,s}(h)$	-	Effect of hourly cumulative stomatal $\text{O}_3$ flux on $V_{C_{max}}$
$f_{03,s}(d - 1)$	-	Previous days effect of cumulative stomatal $\text{O}_3$ flux on $V_{C_{max}}$
$r_{03,s}$	-	Incomplete overnight recovery of $\text{O}_3$ affected $V_{C_{max}}$
$f_{LA}$	-	Leaf age related capacity to recover from accumulated stomatal $\text{O}_3$ flux
$f_{03_t}$	-	Weighted accumulated stomatal $\text{O}_3$ flux that determines the onset of leaf senescence
$f_{LS}$	-	Accumulated stomatal $\text{O}_3$ flux effect on leaf senescence
$tl$	$^\circ\text{C days}$	Effective temperature accumulated by a leaf after emergence ( $DVI = 0$ )

$tl_{ep}$	-	Effective temperature accumulated by a leaf between full expansion and the onset of leaf senescence
$tl_{epO_3}$	-	Effective temperature accumulated by a leaf between full expansion and the onset of leaf senescence brought forward by O <sub>3</sub>
$tl_{se}$	-	Effective temperature accumulated by a leaf between the onset of leaf senescence and maturity
$tl_{seO_3}$	-	Effective temperature accumulated by a leaf between the onset of leaf senescence and maturity brought forward by O <sub>3</sub>
$g_{CO_2}$	$\mu\text{mol CO}_2 \text{ PLA m}^{-2} \text{ s}^{-1}$	Stomatal conductance to CO <sub>2</sub>
$f_{VPD}$	-	Relationship between VPD and relative stomatal conductance
$c_s$	mol CO <sub>2</sub> /mol	Leaf surface CO <sub>2</sub> concentration
$c_s$	mol CO <sub>2</sub> /mol	Quasi laminar boundary layer surface CO <sub>2</sub> concentration
$g_{bCO_2}$	$\text{mol m}^{-2} \text{ s}^{-1}$	Quasi laminar boundary layer conductance to CO <sub>2</sub>
$C_z$	$\text{nmol O}_3 \text{ m}^{-3}$	O <sub>3</sub> concentration at reference height ( $z$ )
$C_l$	$\text{nmol O}_3 \text{ m}^{-3}$	O <sub>3</sub> concentration at the upper surface of the laminar layer of a leaf
$g_{O_3}$	$\text{mmol O}_3 \text{ PLA m}^{-2} \text{ s}^{-1}$	Stomatal conductance to O <sub>3</sub> (in $\text{mmol O}_3 \text{ m}^{-2} \text{ s}^{-1}$ )
$g_{O_3 m/s}$	m/s	Stomatal conductance to O <sub>3</sub> (in m/s)
$r_c$	s/m	Leaf surface resistance to O <sub>3</sub>
$r_{b,O_3}$	s/m	Quasi laminar leaf boundary layer resistance to O <sub>3</sub>
$r_a$	s/m	Atmospheric resistance to O <sub>3</sub>
$r_{inc}$	s/m	In-canopy resistance to O <sub>3</sub>
$r_{ext}$	s/m	External plant cuticle resistance to O <sub>3</sub>

$r_{sto}$	s/m	Stomatal resistance to O <sub>3</sub>
$u_z$	m/s	Wind speed at a reference height $z$
$u_l$	m/s	Wind speed at the upper surface of the laminar layer of a leaf
$LAI$	m <sup>2</sup> m <sup>-2</sup>	Leaf Area Index
$PAR_{dir,i}$	W/m <sup>2</sup>	Direct PAR in canopy layer $i$
$PAR_{diff,i}$	W/m <sup>2</sup>	Diffuse PAR in canopy layer $i$
$PAR_{total}$	W/m <sup>2</sup>	Direct and diffuse PAR at the top of the canopy
$NPP$	kg C m <sup>-2</sup>	Net primary productivity
$GPP$	kg C m <sup>-2</sup>	Gross primary productivity
$R_p$	kg C m <sup>-2</sup>	Plant respiration
$R_{pm}$	kg C m <sup>-2</sup>	Plant maintenance respiration
$R_{pg}$	kg C m <sup>-2</sup>	Plant growth respiration
$A_{netc}$	kg C m <sup>-2</sup>	Canopy net photosynthesis
$R_{dc}$	kg C m <sup>-2</sup>	Non-water stressed canopy dark respiration
$f_{sw}R_{dc}$	kg C m <sup>-2</sup>	Water stressed modified canopy dark respiration
$C_{root}$	kg C m <sup>-2</sup>	Root C pool
$C_{leaf}$	kg C m <sup>-2</sup>	Leaf C pool
$C_{stem}$	kg C m <sup>-2</sup>	Stem C pool
$C_{resv}$	kg C m <sup>-2</sup>	Reserve C pool
$C_{harv}$	kg C m <sup>-2</sup>	Harvest pool
$P_{root}$	-	Root C pool partition coefficient
$P_{leaf}$	-	Leaf C pool partition coefficient
$P_{stem}$	-	Stem C pool partition coefficient
$P_{resv}$	-	Reserve C pool partition coefficient
$P_{harv}$	-	Harvest C pool partition coefficient
$C_{leaf,green}$	kg C m <sup>-2</sup>	Green leaf C
$C_{leaf,brown}$	kg C m <sup>-2</sup>	Brown leaf C
$SLA$	m <sup>2</sup> kg <sup>-1</sup>	Specific Leaf Area
$h$	m	Crop height

$Yield_{grain}$	$\text{g C m}^{-2}$	Grain yield
-----------------	---------------------	-------------

## SI.2.8 DO<sub>3</sub>SE-Crop parameters for wheat

Table. SI. 11. DO<sub>3</sub>SE-Crop parameters for wheat. Highlighted are the parameters (and their associated ranges) which require calibration, when applying DO<sub>3</sub>SE-Crop to varying environmental conditions.

Parameter	Unit	Default Value	Description	Reference	Range	Calibrated Parameter Value
$T_b$	°C	0	Base temperature	(Tao et.al., 2012; Osborne et al., 2015)	-0.5-3	-0.25
$T_o$	°C	20	Optimum temperature	(Tao et.al., 2012; Osborne et al., 2015)	15-25	17.79
$T_m$	°C	30	Maximum temperature	(Tao et.al., 2012; Osborne et al., 2015)	30-40	23.87
$TT_{emr}$	°C d	100	Thermal time between sowing and emergence	(Lu et al., 2018; Luo et al., 2020)	100-240	220.6
$TT_{veg}$	°C d	940	Thermal time between emergence and anthesis	Xiaoji experimental dataset	400-940	940

$TT_{rep}$	°C d	304	Thermal time between anthesis and maturity	(Wang et al., 2013); Xiaoji experimental dataset	300-650	304
$PIV$		1.5	Vernalisation coefficient	(Tao et.al., 2012; Wang et al., 2013b)	2.9-4	2.9
$PID$		40	Photoperiod coefficient	(Wang et al., 2013b; Liu et al., 2016; Zhao et al., 2020)	40-57	40
$VT_{max}$	°C	30	Maximum daily temperature for vernalisation	Zheng et.al, 2015		
$VT_{min}$	°C	15	Minimum daily temperature for vernalisation	Zheng et.al, 2015		
PAW	m <sup>3</sup> /m <sup>3</sup>	50	Plant available water below which stomatal conductance will start to reduce	Mapping Manual,2017		
$V_{cmax}$	μmol CO <sub>2</sub> m <sup>-2</sup> s <sup>-1</sup>	90	Maximum carboxylation capacity at 25°C	(Büker et al., 2012)	90-140	137

$J_{max}$	$\mu\text{mol CO}_2 \text{ m}^{-2} \text{ s}^{-1}$	180	Maximum rate of electron transport at 25°C	(Büker et al., 2012)	180-250	228
$K_c$	$\mu\text{mol/mol}$	404.9	Rubisco Michaelis-Menten constants for $\text{CO}_2$	(Medlyn et al., 2002)		
$K_0$	$\text{mmol/mol}$	278.4	Rubisco Michaelis-Menten constants for $\text{O}_2$	(Medlyn et al., 2002)		
$\Gamma^*$	$\mu\text{mol/mol}$	42.75	$\text{CO}_2$ compensation point in the absence of respiration	(Medlyn et al., 2002)		
$a$	-	4	Electron requirement for the formation of NADPH	(Sharkey et al., 2007)		
$b$	-	8	Electron requirement for the formation of ATP	(Sharkey et al., 2007)		
$R_{dcoeff}$	-	0.015	Leaf dark respiration coefficient	(Clark et al., 2011)	0.01-0.03	
$f_{min}$	$\mu\text{mol CO}_2/\text{m}^2/\text{s}$	1000	Minimum daytime stomatal conductance to $\text{CO}_2$	(Ewert and Porter, 2000)		

$m$	-	7	composite sensitivity slope constant	(Büker et al., 2012)	4-15	5
$VPD_0$	kPa	2.2	stomatal conductance sensitivity to $VPD$	UNECE, 2017; Pande et al. sub		
$\gamma_1$	-	0.027	$O_3$ short-term damage co-efficient	(Ewert and Porter, 2000)		
$\gamma_2$	$(\text{nmol } O_3 \text{ m}^{-2} \text{ s}^{-1})^{-1}$	0.0045	$O_3$ short-term damage co-efficient	(Ewert and Porter, 2000)		
$\gamma_3$	$(\mu\text{mol } O_3 \text{ m}^{-2})^{-1}$	0.0000 5	$O_3$ long-term damage co-efficient	(Ewert and Porter, 2000)	0.00001- 0.00009	0.00002
$\gamma_4$	-		$O_3$ long-term damage co-efficient determining onset of senescence		1-6	5
$\gamma_5$	-		$O_3$ long-term damage co-efficient determining maturity		0.2-0.5	0.4
$CLsO_3$	$\text{mmol } O_3 \text{ m}^{-2}$	12.9,22 .5	Critical accumulated stomatal $O_3$ flux that determines the onset of leaf senescence	(Osborne et al., 2019; Y. Feng et al., 2022)	12.9-22.5	13.5

$r_{ext}$	m/s	2500	External leaf cuticular resistance to O <sub>3</sub> uptake	UNECE, 2017		
$L$	m	0.02	Cross wind leaf dimension for wheat	UNECE, 2017		
$P_{st}$	Pa	1.013 x 10 <sup>5</sup>	Standard air pressure at 20°C	UNECE, 2017		
$T_{st}$	°C	20	Standard temperature	UNECE, 2017		
$R$	J/mol/K	8.31447	Universal gas constant	UNECE, 2017		
$n_e$	mol CO <sub>2</sub> m <sup>-2</sup> s <sup>-1</sup> kg C (kg N) <sup>-1</sup>	0.0008	Constant relating leaf nitrogen to rubisco carboxylation capacity	(Clark et al., 2011)		
$n_0$	kg N [kg C] <sup>-1</sup>	0.073	Top canopy leaf N concentration	(Clark et al., 2011)		
$kN$		0.78	Nitrogen profile coefficient	(Clark et al., 2011)		
$R_{gcoeff}$	-	0.25	Plant growth respiration coefficient	(Osborne et al., 2015)	0.15-0.25	0.16
$\alpha_{root}$	-	18.5	Coefficient for determining partitioning	(Osborne et al., 2015)	16-19	18.4

$\alpha_{stem}$	-	16.0	Coefficient for determining partitioning	(Osborne et al., 2015)	16-17	16.8
$\alpha_{leaf}$	-	18.0	Coefficient for determining partitioning	(Osborne et al., 2015)	18-19	18.4
$\beta_{root}$	--	-20.0	Coefficient for determining partitioning	(Osborne et al., 2015)	20-21	-20.9
$\beta_{stem}$	-	-15.0	Coefficient for determining partitioning	(Osborne et al., 2015)	14-16	-14.5
$\beta_{leaf}$	-	-18.5	Coefficient for determining partitioning	(Osborne et al., 2015)	18-19	-18.11
$f_c$	-	0.5	Carbon fraction of dry matter	(Osborne et al., 2015)		
$\Upsilon$	$m^{-2} kg^{-1}$	27.3	Coefficient for determining specific leaf area	(Osborne et al., 2015)	14-28	15
$\delta$	-	-0.0507	Coefficient for determining specific leaf area	(Osborne et al., 2015)		
$k$	-	1.4	allometric coefficient which relates $C_{stem}$ to $h$	(Osborne et al., 2015)		

$\tau$	-	0.4	allometric coefficient which relates $C_{stem}$ to $h$	(Osborne et al., 2015)	0.3-0.6	0.5
$D_w$	-	1/0.84	Conversion factor to allow for grain moisture content	(Mulvaney and Devkota, 2020)		
$E_g$	-	0.85	Conversion factor for grain to ear ratio	(Nagarajan et al., 1999; Kutman et al., 2011)	0.7-0.85	0.85

## SI.2.9 DO<sub>3</sub>SE-crop phenology parameters

Table. SI. 12. DO<sub>3</sub>SE-crop phenology parameters description and relation to the thermal time

Parameter	Description	% of thermal time, from start of growing season
$f_{tl,em}^a$	Crop emergence (DVI=0 <sup>b</sup> ), end of $TT_{emr}^b$	5
$f_{tl,ma}^a$	Start of anthesis to maturity <sup>a</sup> , $f_{tl,ep}^a + f_{tl,se}^a$	50
$f_{tl,ep}^a$	Start of anthesis <sup>a</sup> (DVI=1 <sup>b</sup> ) to flag leaf senescence <sup>a</sup> , flag leaf fully developed <sup>a</sup> , start of $TT_{rep}^b$	34
$f_{tl,se}^a$	Start of flag leaf senescence to harvest (DVI=2 <sup>b</sup> )	16
Mid-anthesis, start of $fphen\_3\_ETS$ , start of $fphen\_4\_ETS$	Half way through flowering	8

<sup>a</sup>(Ewert and Porter, 2000), <sup>b</sup>(Osborne et al., 2015), <sup>c</sup>Mapping manual,2007

## SI.2.10 Methodology for gap-filling and standardisation of data for AgMIP Ozone

This document describes the methodological approach that was applied in order to search for gaps and quality issues in time-series (gas concentration and meteorological) datasets, and the approach used for filling gaps.

Where gaps had already been filled by the team collecting the data then this interpolated data was left under the assumption that it would be a more accurate reflection of the experimental conditions.

Gap filling methodology for hourly data: During the data standardisation process some data gaps were identified. These ranged in size from a single hour of missing data to several consecutive hours, to several consecutive days, weeks, or even months. A requirement of input data for modellers is that it is continuous; the following gap filling methodology was therefore devised. These gap filling methods

are only applied for the duration of the plants growing season (i.e. between sowing and harvest):

Single hours of missing data were filled by taking the average of the hourly values coming the hour before, and the hour after, the missing value.

Several consecutive hours of missing data (23 hours or less) were filled by taking the average of the corresponding hour the day before, and the day after; and repeating this for each missing hour of data. If data were unavailable from that hour of the previous day, then only the value from the day after was used and vice versa. If there is no data available in either the day before or after, then the method is used (see below point 2.).

Gaps larger than 24 hours could be filled using the following methods:

1. Gaps between 24 hours and 168 hours (i.e. from 1 day up to 1 week) would be filled with the averages from that same hour of the equivalent day, the week before and the week after (i.e. averaging 2 numbers). If data were unavailable from those hours of the previous week, then only the values from the week after would be used (and vice versa).
2. Gaps longer than 1 week would be filled with the diurnal averages from one week before and after the period of missing data (i.e. potentially averaging 14 hours of data, but in cases where data is sparse then it could only be a couple of hours). Gap filled values would not be used in calculating averages. Where data is daily, i.e. some meteorological data, the average of the 7 days before and/or after is used.

There were some instances where data gaps extended for several months. For these extensive gaps, the following methods were used:

- A. All datasets from Xiaoji, China, had about a 4-month gap in meteorological and ozone data at the start of the growing season. At this stage of the growing season, plants will either have not yet emerged or have a very small LAI and therefore any ozone uptake would have been minimal. Ozone gaps were filled with the diurnal averages of the first two weeks of the ambient experimental data for each year. Meteorological data was filled using Nasa Power data (<https://power.larc.nasa.gov/data-access-viewer/>). The variables selected are

in the appendix below. In Xiaoji China, global radiation was measured, whereas the Nasa Power data platform only provides Photosynthetically Active Radiation (PAR). To convert global radiation to PAR, values were multiplied by two and divided by 24 to be comparable with global radiation in MJ/m<sup>2</sup>/hour.

- B. If the gap occurs before exposure data begins then the ambient or non-filtered treatment is gap filled using the above methodology and then this data is used for all treatments to ensure that concentrations are not overestimated. If there is no ambient treatment, then averages of the treatment closest to ambient is used. If there are gaps in gas data after the beginning of exposure date, then averages from that treatment are used (as opposed to ambient). If no date for start of exposure is provided, then exposure is assumed to start when the gas data begins (even if it is na). Similarly, once exposure has ended then only averages from the period after exposure were used. If there was not enough data to base averages on, then ambient data was used (Nottingham 1996).
- C. Any ozone values of less than 0 were treated as gaps and filled following the above methods, depending on the size of gap.
- D. If mean air temperature was not available but minimum and maximum air temperature was, the average of these two values was used and the source of the data was label 'c' for calculated.
- E. Sections of the dataset which had been gap filled were clearly identified using a categorisation system in an adjacent 'data source' column, so that these data could be identified at a later stage, and so that alternative measured or modelled data could be sought. The percentage of gap-filled data within the total time-series for each gas concentration and meteorological variable was also reported in the readme file accompanying each dataset.
- F. The Parameters downloaded from (<https://power.larc.nasa.gov/data-access-viewer/>)
- G. Hourly data was downloaded from the Nasa Power data access viewer for Xiaoji, China to fill gaps in meteorological data. The following parameters were selected: 1. Agroclimatology community; 2. Hourly; 3. Lat/long: 32.58333: 119.7; 4. Time extent: Determined by data gap in each year; 5. Format: CSV format; 6. Parameters: a) temp at 2m, b)relative humidity at 2m, c)wind speed at 2m, d) precipitation, e) radiation: "All Sky Surface

photosynthetically active radiation" (PAR Total) (MJ/m<sup>2</sup>/day). This was converted to hourly global radiation (MJ/m<sup>2</sup>/h) by dividing to 24 and multiplying with 2 because  $PAR \sim 0.5 * \text{global radiation}$ .

## **4. The ozone impact on wheat growth and yield is influenced by agro-ecological zone and cultivar sensitivity in China.**

### **4.1 Abstract**

Evidence from experimental fumigation studies has been used to develop and apply modelling methods to assess the risk posed by ozone ( $O_3$ ) under a range of climatic conditions to staple crops across China. Here, the calibration and application of the  $DO_3SE$ -Crop model, which includes  $O_3$  damage coefficients and the JULES crop model in its model construct, were described. The challenges in calibrating the phenology, leaf level physiology, carbon allocation, and  $O_3$  damage modules of  $DO_3SE$ -Crop for winter wheat growing in three productive and diverse agro-ecological zones (AEZs) across China, were explored. This study finds that the model can simulate phenology with a satisfactory degree of accuracy, with emergence and maturity dates estimated to be within a 2.5-week margin of the observed data. This study also finds that crop yield can be simulated within a  $\pm$  range of  $84 \text{ g/m}^2$  when presented as a mean yield by AEZ. However, when combining  $DO_3SE$ -Crop with WRF-Chem modelled  $O_3$  concentrations, substantial differences in estimates of  $O_3$ -induced yield losses within and between different AEZs were found. This study finds that seasonal patterns in prevailing environmental conditions (especially temperature and  $O_3$  concentration profiles, which together determine the timing of sensitive crop development stages to  $O_3$ ) are important in assessing the spatial distribution and magnitude of damage estimates, with AEZ I showing overly high  $O_3$  damage due to early accumulation of the ozone flux whilst AEZ II and IV show yield loss estimates of  $O_3$  damage more in line with other published literature and experimental studies. This work highlights the need to consider AEZ when parameterising crop models to ensure their applicability and improve their  $O_3$  damage assessment capabilities across countries and regions with diverse AEZs.

## 4.2 Introduction

Agricultural production and food security are at risk due to the dual threats of air pollution (especially ozone (O<sub>3</sub>)) and climate change; such risk has been increasing in China and India compared to other global regions over the past few decades (Schauberger et al., 2019; Burney and Ramanathan, 2014). While numerous studies have explored the effects of climate change and specific air pollutants acting on agriculture individually, there is a lack of research examining the impact of these stresses in combination (Tao et al., 2017). Climate change is altering the intensity and distribution of seasonal temperature and precipitation patterns, and this variability affects agricultural production globally, both directly and indirectly (Jägermeyr et al., 2021). Across China, the effects of climate change vary depending on the agro-ecological zone (AEZ). Changes in temperature, precipitation, and solar radiation over the past three decades have seen an increase in wheat yield in northern China (0.9 to 12.9%) but have led to reduced yields in southern China (by 1.2 to 12.9%) (Tao et al., 2014). Another major concern is the rise in O<sub>3</sub> levels, a damaging pollutant to crops, particularly in China and India (Tang et al., 2013; Tao et al., 2017). Although China has made progress in reducing primary pollutants such as aerosol and nitrogen oxides (NO<sub>x</sub>), O<sub>3</sub> levels continue to rise (Lu et al., 2021; Wang et al., 2022). This increase is believed to be linked to factors like condensed particulate matter, varying NO<sub>x</sub> emissions, and shifting meteorological conditions, as indicated by studies from Lu et al., 2021 and Li et al., 2021.

The North China Plain is an important agricultural region and a hotspot for anthropogenic pollution emissions and has recently experienced a significant upward trend in summer O<sub>3</sub> pollution. This region's summertime O<sub>3</sub> levels measured as daily 8h average maximum (MDA8), have been increasing by more than 3 ppb annually since between 2013-2019, marking one of the most rapid urban O<sub>3</sub> surges in recent years (Lu et al., 2021). Given that China is a leading producer of staple crops such as wheat, which provide a fundamental food source for 35% of the global population (Grote et al., 2021), it becomes imperative to investigate the impacts of O<sub>3</sub> and changes in meteorological conditions on wheat yields. For example, wheat yield losses could be greater when elevated O<sub>3</sub> coincides with high temperatures during the grain filling period when elevated O<sub>3</sub> causes premature leaf senescence (Long, 2012; Feng et al., 2011). Understanding and addressing these influences are crucial

for ensuring agricultural sustainability and food security both now and in the future across China (Schauberger et al., 2019).

A handful of photosynthetic-based mechanistic crop models have been developed to incorporate O<sub>3</sub> damage functions, these have the potential to enable the simulation of O<sub>3</sub> impact under diverse agro-climatic conditions. The LPJml model, described by Schauberger et al. (2019), is a big leaf model able to concurrently simulate the effects of O<sub>3</sub>, temperature, water stress, phenology, and CO<sub>2</sub> on wheat yields. The model is developed for global application but parameterised for an 'Asian' wheat type to account for the higher O<sub>3</sub> sensitivities of Asian cultivars to O<sub>3</sub>. Calibration of the O<sub>3</sub> damage module was performed for parameters that represented O<sub>3</sub> detoxification rates, O<sub>3</sub> induced-reduction in rubisco-limited photosynthesis, and O<sub>3</sub>-induced changes in senescence. However, data were not available to set these parameters directly; but rather, the model was calibrated to closely match results from seven Asian studies (and 12 experiments) that described O<sub>3</sub>-induced changes in  $A_{net}$ ,  $g_{sto}$  respiration and yield. The LPJml model was further calibrated by maximum LAI to scale absolute yield for different global regions and then applied to assess O<sub>3</sub> impacts to wheat across China between 2008 and 2010; model results estimated average yield losses of 34.2%, with up to 50% yield losses in more northerly regions. The analysis highlighted that these losses were primarily attributed to cumulative O<sub>3</sub> effect on crop senescence rather than instantaneous effects. The MCWLA-Wheat model, described by Tao et al. (2017), offers a more regionally focused approach than the LPJml model. The MCWLA-Wheat model's phenology and O<sub>3</sub> damage modules were initially calibrated and evaluated for the Xiaoji O<sub>3</sub> experimental site (Feng et al., 2011; Zhu et al., 2011). The calibrated model was then applied over eight Chinese provinces using gridded data describing wheat sowing dates and evaluated against provincial level yield data. The model was designed to assess the combined impacts of climate change, O<sub>3</sub> pollution, and CO<sub>2</sub> levels on wheat crop growth and productivity in these areas. Application of MCLWA across selected Chinese provinces during the 2000s found productivity losses of between 1.1-13.3% in the 2000s.

These mechanistic-based crop model estimates of O<sub>3</sub>-induced yield losses can be compared with the more traditional O<sub>3</sub> risk assessment methods that make use of dose-response relationships to estimate yield loss. A recent study by Feng et al.

(2022) uses an extensive and comprehensive collection of O<sub>3</sub> monitoring data from across Asia (including China) to estimate yield losses using an Asian-specific AOT40 dose-response relationship (where the AOT40 index was a six-month accumulated daytime O<sub>3</sub> over a threshold of 40 ppb). They reported an average ozone-induced relative yield loss for wheat across China at 33% from 2017 to 2019, ranging between 28% and 37%. The most significant losses were noted in the North China Plain, where they exceeded 35%. This represents a significant increase from the previous 17-18% estimates for 2015 to 2016, derived from the same ozone monitoring network. However, it is essential to note that these figures could be subject to considerable interannual variability. Taken together, these modelling studies suggest that O<sub>3</sub>-induced yield losses across China are substantial and have been increasing rapidly over recent years.

Despite the valuable insights these modelling studies provide into the effects of O<sub>3</sub> (and, in some cases, climate variables) on crop productivity, they have limitations. Arguably, the major limitation is the lack of experimental O<sub>3</sub> fumigation data to calibrate crop or dose-response models; this causes particular problems when calibrating the crop model O<sub>3</sub> damage modules since it limits the number of cultivars represented by the model. A further limitation is that these models do not calibrate for variable crop development and crop growth that will occur in different AEZs; these are known to cause substantial differences in crop growth and yield (Xiong et al., 2008) as well as the timing of sensitive crop development stages in relation to O<sub>3</sub> concentrations. These limitations highlight areas for further refinement and development in modelling to better understand how crop models could be used to infer the causes and consequences of co-occurring environmental conditions causing O<sub>3</sub> damage.

To address these challenges, the DO<sub>3</sub>SE crop model, as outlined by Pande et al. (sub), is used in this study. This process-based model is used to evaluate the impact of O<sub>3</sub> in China, examining how effects vary diurnally and seasonally due to both O<sub>3</sub> concentrations and climate variables in critical agro-ecological zones of high winter wheat production. This will help inform how sensitivity to O<sub>3</sub> varies between AEZs and infer how current and potential future climate may influence O<sub>3</sub> impacts. To achieve this, the DO<sub>3</sub>SE-Crop model is i) calibrated to develop AEZ-specific parameterisation for phenology and carbon allocation parameters, ii) calibrated for

O<sub>3</sub>-sensitive and tolerant cultivars and iii) applied to estimate O<sub>3</sub>-induced yield losses for three AEZs across China.

## 4.3 Methods

### 4.3.1 DO<sub>3</sub>SE Crop Model

The DO<sub>3</sub>SE crop model has been extensively described in Pande et al. (sub). The core of the model is the biochemical photosynthesis model (after Farquhar et al. 1989) that simulates carbon fixation and assimilation. The modelling of  $A_{net}$  assumes that photosynthesis is limited, according to prevailing environmental conditions, by three different mechanisms: i. rubisco activity (Ac); ii. the regeneration of ribulose-1,5-bisphosphate (RuBP), which is limited by the rate of electron transport (Aj), and iii. the inadequate rate of transport of photosynthetic products (most commonly triose phosphate utilization) (Ap) (Sharkey et al., 2007). Ac is modified to allow for an aging leaf (Ewert and Porter, 2000), where the effect of instantaneous O<sub>3</sub> and senescence on the rubisco-limited rate of photosynthesis (Ac) is estimated. The coupling of  $A_{net}$  with  $g_{sto}$  is used to estimate  $g_{sto}$ , and performed as described by Leuning (1995). The effect of O<sub>3</sub> on carbon assimilation is introduced via the Ac term as described in Eq. 71 after methods developed by Ewert & Porter (2000), which allows for both instantaneous and long-term cumulative effects of stomatal ozone flux on  $A_{net}$ .

$$A_c = V_{cmax} \cdot f_{sw} \cdot \frac{(C_i - \Gamma^*) \cdot f_{O_{3,s}(d)} \cdot f_{LS}}{C_i + K_c \left(1 + \frac{O_i}{K_o}\right)} \quad \text{Eq. 71}$$

where  $V_{cmax}$  is the maximum carboxylation capacity at 25°C,  $C_i$  and  $O_i$  are the intercellular CO<sub>2</sub> and O<sub>2</sub> concentrations;  $K_c$  and  $K_o$  are the Rubisco Michaelis-Menten constants for CO<sub>2</sub> and O<sub>2</sub>;  $\Gamma^*$  is the CO<sub>2</sub> compensation point in the absence of respiration;  $f_{O_{3,s}(d)}$  is the factor that accounts for the cumulative stomatal O<sub>3</sub> flux effect on  $V_{cmax}$  over the course of a day and;  $f_{LS}$  is the factor that accounts for the cumulative stomatal O<sub>3</sub> flux effect over the course of a leaf life span on leaf senescence.

The DO<sub>3</sub>SE-Crop model can be run with any number of leaf populations and canopy layers. To date, DO<sub>3</sub>SE-Crop simulations have been performed with only one representative leaf population, which ages in line with the entire canopy, which is determined by the thermal time. However, the model can use thermal time to define the period of the total leaf population life span when the flag leaf would be present, which is assumed to be from a little before anthesis to maturity. The model assumes

that leaf life spans are divided into expanding and senescing periods using a default ratio of approximately 0.66 to 0.33 thermal time of the total leaf life span. The leaf population is further divided into leaf area index (LAI) fractions depending on cumulative LAI position. The scaling of  $A_{net}$  and  $g_{sto}$  is determined by the sunlit and shaded portions of LAI estimated according to a standard light extinction profile with LAI accumulating through the canopy. DO<sub>3</sub>SE-Crop also takes account into the O<sub>3</sub> deposition occurring with depth through the canopy, which will affect the within-canopy O<sub>3</sub> concentration and, hence, the O<sub>3</sub> available for stomatal uptake by different canopy layers.

Crop phenology is defined by thermal time and divided into three key developmental stages, sowing, emergence, anthesis, and maturity, based on the method of Osborne et al. (2015). The effective temperature is calculated from three wheat-specific cardinal temperatures (T<sub>b</sub>, T<sub>o</sub>, and T<sub>m</sub>) using equations defined in the JULES-crop model (Osborne et al., 2015) modified to take account of photoperiod and vernalisation, which are important in winter wheat. Net primary productivity (NPP) is accumulated throughout the day from gross primary productivity (GPP) minus plant respiration (comprising both maintenance and growth respiration) following the JULES-crop method (Osborne et al., 2015). GPP is estimated as a function of  $A_{net,c}$  and dark respiration.

The NPP that accumulates at the end of the day is allocated to different carbon pools, i.e., root, leaf, stem, reserve, and harvest, according to the JULES Crop partition coefficients (Osborne et al., 2015), which vary with crop growth stage. Once carbon is no longer partitioned to stems, carbon from the stem reserve pool is mobilised to the harvest pool at an initial default rate of 10% per day. For senescing green leaves (when the fLS <1), carbon is mobilised towards the harvest pool at a rate of 5% per day. Finally, at the end of the day, the amount of carbon in the leaf and stem determines LAI and crop height. According to Osborne et al. (2015), crop yield is calculated from the carbon allocated to the harvest pool (which includes grain and chaff) at the end of the growing season.

Soil water is modelled using the Penman-Monteith energy balance method to drive water cycling through the soil-plant-atmosphere system with an assumption that the stomata will begin to limit transpiration once half of the plant available soil water is lost; this limitation progresses linearly until the permanent wilting point is reached

and is described by a function relating plant available soil water to stomatal conductance ( $f_{PAW}$ ). Full details of this  $f_{PAW}$  method are provided in Bueker et al. (2012); this method is used to modify the  $A_c$  term of the  $A_{net}$  model via scaling of the maximum carboxylation capacity.

For these DO<sub>3</sub>SE-Crop model runs, we set  $f_{PAW}$  equal to 1 and apply the model to irrigated winter wheat areas as defined by the gridded SPAM2010 database (Yu et al., 2020), hence we assume no limitation of soil water stress to either crop growth or O<sub>3</sub> uptake. Our focus is on winter wheat since this occupies ~ 95% of the total wheat area of China (Li et al., 2019). Much of this winter wheat production occurs in the North China Plain, which produces ~70% of the total wheat production in China (Zeng et al., 2021). Most winter wheat produced in the North China Plain is irrigated since this is also a region of water scarcity (Huang et al., 2019). Therefore our analysis focuses on crops under irrigation and captures the most productive winter wheat areas across China.

The data described in Table. SI. 13 are required to run the DO<sub>3</sub>SE-crop. These data are provided by the WRF-Chem model (describe in section 4.7.1) on a 30 km by 30 km spatial resolution across China.

#### 4.3.2 WRF-Chem model

Ozone concentrations for China between October 1st, 2017, and October 1st, 2018, were simulated using WRF-Chem (version 4.2), a fully coupled atmospheric chemistry model. The model set-up and version used in this study are the same as Graham et al. (2020, 2021). A detailed model description can be found in Conibear et al. (2018a). The model domain covered China at a 30 km horizontal resolution (190 x 170 grid boxes), with 33 vertical levels (to 10 hPa). The WRF-Chem model requires meteorology, emissions data, and boundary conditions as inputs. Meteorology data for the year 2017/2018 was taken from ERA5 (Hoffman et al., 2018), while a combination of emission databases was used as described in Table 8. Further details are provided in section SI.3.1.

Table 8. Emissions and meteorological input data used to run the WRF-Chem model for the derivation of O<sub>3</sub> concentrations for year 2017/2018.

Input Data	Input dataset input for WRF-Chem	References
Meteorology	ERA5 6-hourly 2017/2018 reanalysis, 0.1° resolution	(Hoffmann et al., 2019)
Rest of the World Anthropogenic Emissions	CAMS-GLOB-ANT 2016, monthly, 0.1° resolution  EDGARv5 2015 (aircraft emissions & PM), monthly, 0.1° resolution	(Soulie et al., 2023)  Crippa et al. (2021)
Chinese Anthropogenic Emissions	MEIC 2017, monthly, 0.25° resolution	(Li et al., 2017; Zheng et al., 2018)
Chinese Agricultural Emissions	Malley 2017, annual, 0.083° resolution	Emmons et al. (2010)
Wildfire Emissions	FINNv1.5 2017/2018, daily, 1 km resolution (fires on agricultural land removed)	(Hoelzemann et al., 2004; Akagi et al., 2011; Wiedinmyer et al., 2011) McMeeking, 2008; Andrae & Merlet, 2001
Chemical Boundary Conditions	WACCM SSP3-70 Baseline 2017/2018	(Marsh et al., 2013)

#### 4.3.2.1 WRF-Chem model evaluation

To evaluate the ability of the WRF-Chem model to predict O<sub>3</sub> concentrations, the modelled and observed M7 O<sub>3</sub> concentrations were compared at rural winter wheat locations. We use the SPAM2010 (Yu et al., 2020) winter wheat mask described in Fig. 16 to identify WRF-Chem grid cells that contain winter wheat. The mask is also

used to identify those O<sub>3</sub> monitoring sites located within winter wheat growing regions. We used observed O<sub>3</sub> concentrations collected from hourly measured data at 1,600 ground-based sites across China, Macao, Hong Kong, and Taiwan, as detailed in (Silver et al., 2018). We use population density data to determine rural areas (< 1500 people/km<sup>2</sup>). This threshold is widely used and was developed by the European Commission (World Bank, 2017). We subsample both the modelled and O<sub>3</sub> observations, keeping the data only where the population is below this threshold. This results in 386 sites from the original 1,600 ground-based sites being classified as rural winter wheat sites. We then calculate M7 for these sites, where M7 is the hourly mean O<sub>3</sub> concentration between 09:00 to 16:00 hours for each day during an 'average' winter wheat growth period from November 1<sup>st</sup>, 2017, to May 16<sup>th</sup>, 2018. Finally, we use nearest neighbour interpolation to find the nearest neighbour grid cell in the modelled data to the observations. We use several statistical measures to evaluate the WRF-Chem models' predictive capability; these are explained in SI.3.3.

#### 4.3.3 Calibration of DO<sub>3</sub>SE-Crop for O<sub>3</sub> damage in China

The DO<sub>3</sub>SE-crop model has previously been calibrated to analyse an O<sub>3</sub>-FACE experimental dataset collected in Xiaoji, Jiangsu, Jiangsu Province, China (Zhu et al., 2011). This dataset investigated the influence of O<sub>3</sub> exposures on four modern cultivars of winter wheat (*Triticum aestivum* L.) grown under ambient (AA) and elevated (E-O<sub>3</sub>). The E-O<sub>3</sub> treatment was a mean 25% enhancement above ambient O<sub>3</sub> concentrations. The plants were grown in fully open-air field conditions for three consecutive growing seasons between 2007 and 2009. The crop was well irrigated, so we assume there was no soil moisture stress. The four cultivars were Yannong 19 (strong-gluten wheat, hereafter Y19), Yangmai 16 (medium-gluten wheat, hereafter Y16), Yangmai 15 (weak-gluten wheat, hereafter Y15) and Yangfumai 2 (weak-gluten wheat, hereafter Y2). Further experimental details are provided by (Zhu et al., 2011).

The Xiaoji experimental data were split into calibration (the year 2008, Y2, and Y16 cultivars) and evaluation (the year 2007 & 2009, Y18 & Y19 cultivars). The calibration of DO<sub>3</sub>SE-Crop was first performed for crop development and growth (i.e., phenology and carbon allocation). This calibration was performed using the Y2 cultivar. Secondly, the DO<sub>3</sub>SE-Crop O<sub>3</sub> damage module was calibrated for both the Y2 (a sensitive) and Y16 (a tolerant) cultivars according to the cultivar sensitivities

assessed (Zhu et al., 2011). Full details of the calibration procedure are given in Pande et al. (sub), and the resulting DO<sub>3</sub>SE-Crop parameterisation is given in Table 9.

Table 9. The key parameterisation of the DO<sub>3</sub>SE-Crop model after calibration against the Xiaoji experimental dataset (Zhu et al., 2011).

Parameter	Value	Unit	Description (for Y2 cultivar unless stated)
Phenology parameters			
$T_b, T_o, T_m$	-0.25, 17.79, 23.8	°C	Cardinal temperatures for phenology
$fTT_{emr}, fTT_{veg}, fTT_{rep}$	0.05, 0.71, 0.23	-	Fractions of thermal time between emergence-anthesis, anthesis to start of senescence, start of senescence to maturity
$TT_{leaf}$	1325	°C days	Life span of the wheat crop canopy
Leaf physiology			
$V_{cmax25}$	137	µmol CO <sub>2</sub> /m <sup>2</sup> /s	Maximum carboxylation capacity
$J_{max25}$	228	µmol CO <sub>2</sub> /m <sup>2</sup> /s	Maximum electron transport
$D_o$	2.2	kPa	Vapour pressure deficit coefficient
$m$	4	-	Species-specific sensitivity to $A_{net}$
C allocation parameters			
$\alpha_{root}, \alpha_{root}, \alpha_{root}, \Upsilon, \tau$	18.1, 18.4, 16.8, 14, 0.5	-	Carbon allocation coefficients
$R_d$ and $r_g$	0.01, 0.16	µmol CO <sub>2</sub> /m <sup>2</sup> /s	Dark respiration and growth respiration parameters
$\lambda_3, \lambda_4$ and $\lambda_5$	0.0004, 1.2, 0.2	-	Tolerant (for Y16 cultivar)

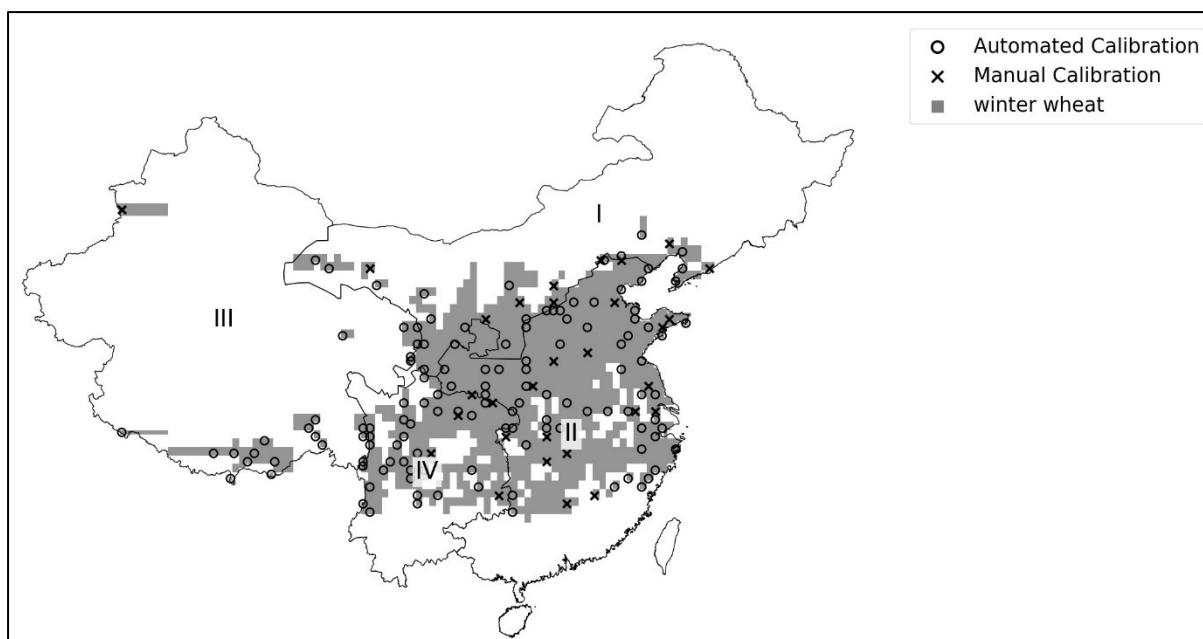
	0.00004, 2.4, 0.3	-	Sensitive (for Y2 cultivar)
--	-------------------	---	-----------------------------

N.B.  $T_b$  ( $^{\circ}\text{C}$ ) is base temperature;  $T_o$  ( $^{\circ}\text{C}$ ) is optimum temperature;  $T_m$  ( $^{\circ}\text{C}$ ) is maximum temperature;  $fTT_{emr}$  (fraction) is the fraction represents the part of the thermal time from sowing to emergence ( $TT_{emr}$ );  $fTT_{veg} = f_{tl,em}$  (fraction) is the fraction of the thermal time associated with the vegetative phase of the crop's development;  $fTT_{rep} = f_{tl,ma}$  (fraction) is the fraction corresponds to the thermal time during the reproductive phase, signified by the thermal time from emergence to maturity ( $TT_{rep}$ ); Harvest (in degree day) refers to the accumulated temperature (in degree days) required to reach the harvest stage of a crop; PIV (no units) is the vernalisation Coefficient. It quantifies the effect of vernalization on the crop's development; PID (no units) is the is the photoperiod Coefficient. It quantifies the effect of photoperiod on the crop's development;  $\alpha_{root}$  is the coefficient for determining partitioning of carbon into roots;  $\alpha_{leaf}$  is the coefficient for determining partitioning of carbon into leaves;  $\alpha_{stem}$  is the coefficient for determining partitioning of carbon into stems;  $\gamma$  ( $\text{m}^{-2} \text{kg}^{-1}$ ) is the coefficient for determining specific leaf area and  $\tau$  is the allometric coefficient which relates  $C_{stem}$  to height of the crop ( $h$ ).

#### 4.3.3.1 Calibration of DO<sub>3</sub>SE-Crop for phenology and yield under ambient O<sub>3</sub> in China

China consists of a number of agro-ecological zones (AEZs) that have particular climatic conditions affecting the development, growth, and subsequent yield of crops. Crop related studies conducted in China have classified anywhere between three to 17 different AEZs (Lin et al., 2013). In this study, we define four agro-ecological zones for winter wheat after Luo et al. (2020), as shown in Fig. 16. We calibrate the DO<sub>3</sub>SE-Crop model so that we can define a unique set of phenology and carbon coefficient parameterisations for each of the four AEZs.

Fig. 16. Winter wheat distribution across China according to SPAM2010 (Yu et al. 2020). The map divides the country into four distinct agro-ecological zones (AEZs) for winter wheat production, : I, II, III, and IV. Within these zones, 32 locations were manually selected for calibration, while 107 were chosen for automated calibration of the DO<sub>3</sub>SE-Crop model, as indicated by the respective symbols. These calibration points were extracted from the SPAM2010 database to refine the DO<sub>3</sub>SE-Crop model, ensuring it accurately reflects the conditions affecting winter wheat growth across the different ecological regions of China.



The calibration of the DO<sub>3</sub>SE-crop model is split into two parts. First, we perform a manual calibration, which uses 30 SPAM2010 sites (Yu et al., 2020) randomly selected from across China’s winter wheat production area; the number of sample sites falling into each AEZ are given in Table 10. For each of these sites, we identify the associated WFR-Chem data (N.B. the spatial resolution of WFR-Chem and SPAM2010 is such that there are, on average, four WFR-Chem grids to each SPAM2010 grid). We searched the published literature to identify suitable ranges for key phenology variables to have an initial understanding of how phenology varies across our four AEZs in China. We use an estimate of the sowing date for winter wheat which utilises a latitude model devised by Xiao et al. (2015), along with secondary spatial data describing emergence, anthesis, and maturity for each of our four AEZs. The extracted data ranges for key phenology variables, which are given in Table 10.

Table 10. The range in timings of key phenology stages (sowing, emergence, anthesis and maturity) for winter wheat across China, given in Julian day (DOY) divided by four agro-ecological zones (AEZs- as Zone1, Zone2, Zone3 and Zone 4). Also shown are the number of SPAM2010 and associated WFR-Chem sample sites used to perform a manual parameterisation of the DO<sub>3</sub>SE-Crop model.

		DOY	
--	--	-----	--

Zone	Sam ple sites	Sowing range	Emergenc e range	Anthesis range	Maturity range	References
Zone I	15	78-111	80-111	111-158	208-253	Luo et.al., 2020;
Zone II	64	270- 290	32-64	116-137	141-164	Luo et.al., 2020; Tao et.al., 2012
Zone III	1	78-89	95-111	158-180	231-253	Luo et.al., 2020;
Zone IV	10	270- 290	32-64	116-137	141-164	Luo et.al., 2020; Tao et.al., 2012

We then used these ranges in key phenological stages to calibrate the DO<sub>3</sub>SE-crop phenology model for each AEZ. This calibration was performed manually, starting from initial phenology values based on the Xiaoji calibration (see Table 11) and varying each parameter to produce modelled estimates of emergence, anthesis, and maturity broadly consistent with dates extracted from the literature (see Table 10). This method was used to fix the  $T_b$ ,  $T_o$ ,  $T_m$ ,  $fTT_{emr}$ ,  $fTT_{veg}$ , and  $fTT_{rep}$  fractions and thermal time for maturity for each AEZ, as shown in Table 11.

Table 11. Initial default and range (in brackets) of parameter values for the calibrated DO<sub>3</sub>SE-Crop phenology model.

Zone	$T_b$ (°C)	$T_o$ (°C)	$T_m$ (°C)	$fTT_{emr}$ (fraction)	$fTT_{veg} =$ $ftl_{,em}$ (fraction)	$fTT_{rep}$ $=ftl_{,ma}$ (fraction)	Harvest (in degree day)	PIV (no units)	PID (no units)
Zone I	081 1	20.1 63	331. 412	0.05	0.45	0.50	1026.77 9	2.4	40

	(-1 - 3)	(15- 25)	2.61 1 (30- 40)				(500- 2000)		
Zone II	0.23 1 (-1 - 3)	20.6 63 (15- 25)	32.6 11 (30- 40)	0.16	0.52	0.32	1700 (950- 1800)	2.9	46
Zone III	3 (-1 - 3)	21.2 07 (15- 25)	31.6 94 (30- 40)	0.05	0.15	0.80	608.981 (950- 1800)	2.4	40
Zone IV	0.14 7 (-1- 3)	19.5 37 (15- 25)	31.6 85 (30- 40)	0.18	0.50	0.32	1083.22 (950- 1800)	2.4	40

N.B.  $T_b$  (°C) is base temperature;  $T_o$  (°C) is optimum temperature;  $T_m$  (°C) is maximum temperature;  $fTT_{emr}$  (fraction) is the fraction represents the part of the thermal time from sowing to emergence ( $TT_{emr}$ );  $fTT_{veg} = f_{tl,em}$  (fraction) is the fraction of the thermal time associated with the vegetative phase of the crop's development;  $fTT_{rep} = f_{tl,ma}$  (fraction) is the fraction corresponds to the thermal time during the reproductive phase, signified by the thermal time from emergence to maturity ( $TT_{rep}$ ); Harvest (in degree day) refers to the accumulated temperature (in degree days) required to reach the harvest stage of a crop; PIV (no units) is the vernalisation Coefficient. It quantifies the effect of vernalization on the crop's development; PID (no units) is the is the photoperiod Coefficient. It quantifies the effect of photoperiod on the crop's development.

Automated calibration is then performed, allowing  $T_b$ ,  $T_o$ ,  $T_m$ , and harvest values to vary until a good agreement is reached between the modelled and observed timing of maturity for 107 randomly selected grid cells, split equally across the AEZs (nine per zone), which are not already used in the manual calibration. We aim for these key phenology stages to be simulated within +/- 1 to 2 weeks with these key crop dates.

Finally, we use the gridded SPAM2010 yield dataset to calibrate the DO<sub>3</sub>SE-Crop model ‘tolerant’ cultivar for absolute yield values along with a target LAI of 4 m<sup>2</sup>/m<sup>2</sup> for zones I and II and 3.5 for zones III and IV. This again uses automated calibration, allowing  $\alpha_{root}$ ,  $\alpha_{leaf}$ ,  $\alpha_{stem}$ ,  $\Upsilon$ , and  $\tau$  to vary until an optimised agreement between the modelled and observed yield is found (ideally to within +/-20%). An initial default and range of values for these parameters are defined from the Xiaoji experimental data (see Table. SI. 14); the resulting parameter values after the automated calibration are given in Table 12.

Table 12. Initial default and range (in brackets) of parameter values for the calibrated DO<sub>3</sub>SE-Crop yield model.

Zone	$\alpha_{root}$	$\alpha_{leaf}$	$\alpha_{stem}$	$\Upsilon$ (m <sup>-2</sup> kg <sup>-1</sup> )	$\tau$
Zone I	18.7 (16-19)	18.4 (18-19)	16.8 (16-17)	15 (15-27)	0.3 (0.3-0.6)
Zone II	18.7 (16-19)	18.4 (18-19)	16.8 (16-17)	19 (15-27)	0.3 (0.3-0.6)
Zone III	16.5 (16-19)	18.5 (18-19)	16.2 (16-17)	23 (15-27)	0.3 (0.3-0.6)
Zone IV	18.5 (16-19)	18.4 (18-19)	16.8 (16-17)	23 (15-27)	0.3 (0.3-0.6)

N.B.  $\alpha_{root}$  is the coefficient for determining partitioning of carbon into roots;  $\alpha_{leaf}$  is the coefficient for determining partitioning of carbon into leaves;  $\alpha_{stem}$  is the coefficient for determining partitioning of carbon into stems;  $\Upsilon$  (m<sup>-2</sup> kg<sup>-1</sup>) is the coefficient for determining specific leaf area and  $\tau$  is the allometric coefficient which relates  $C_{stem}$  to height of the crop ( $h$ ).

The calibrated DO<sub>3</sub>SE-Crop model parameters are then applied using the following model runs to assess the effect of O<sub>3</sub> effect on crop yield across China:

1. Current year (2018/19) meteorology and ambient O<sub>3</sub> concentration.
2. Current year (2018/19) meteorology and pre-industrial O<sub>3</sub> concentration (assumed to be 10 ppb after UNECE, 2017).

These runs will allow us to explore and evaluate the effect of O<sub>3</sub> concentrations on yield for the current year (2018/19), i.e., the yield loss that would be avoided were O<sub>3</sub> concentrations at pre-industrial levels. Here, we run the model for the SPAM2010 irrigated winter wheat locations only. We also limit our analysis to those grid cells that have an average elevation below 1600 m a.s.l. since this elevation is at the limit of the winter wheat distribution (Chen et al., 2020).

#### 4.3.4 Evaluation of the DO<sub>3</sub>SE Crop model across China.

We evaluate the DO<sub>3</sub>SE Crop model estimates of crop yield under ambient O<sub>3</sub> conditions for 2017/18 for a tolerant cultivar against the SPAM2010 yield database (Yu et al., 2020). We use the R<sup>2</sup> and RMSE statistical measures to assess the ability of DO<sub>3</sub>E-Crop to simulate yield (further details on the information provided by these measures are provided in section SI.3.3).

## 4.4 Results

In the results section, we delve into the evaluation of the WRF-Chem model's effectiveness in predicting O<sub>3</sub> concentrations during China's winter wheat growing season across different agro-ecological zones (AEZs). Initially, the focus is on comparing modelled versus observed rural M7 O<sub>3</sub> concentrations spatial plots across China, particularly over the key winter wheat areas, assessing the model's accuracy and noting any bias.

The study then transitions to a temporal comparison of the WRF-Chem modelled O<sub>3</sub> concentrations against observations, spanning from November 2017 to May 2018. This section emphasizes on the crucial phase for wheat growth, anthesis for the year 2017/18 growing season. The diurnal variations in O<sub>3</sub> concentrations are also explored, highlighting the model's performance across different times of the day and months within the growing season.

Next, the DO<sub>3</sub>SE-crop phenology model performance was evaluated, which is vital for determining the timing and length of the wheat growing season and the interplay between elevated O<sub>3</sub> exposures and crop growth stages. This section compares simulated key crop growth stages with published data, focusing on differences across four different AEZs.

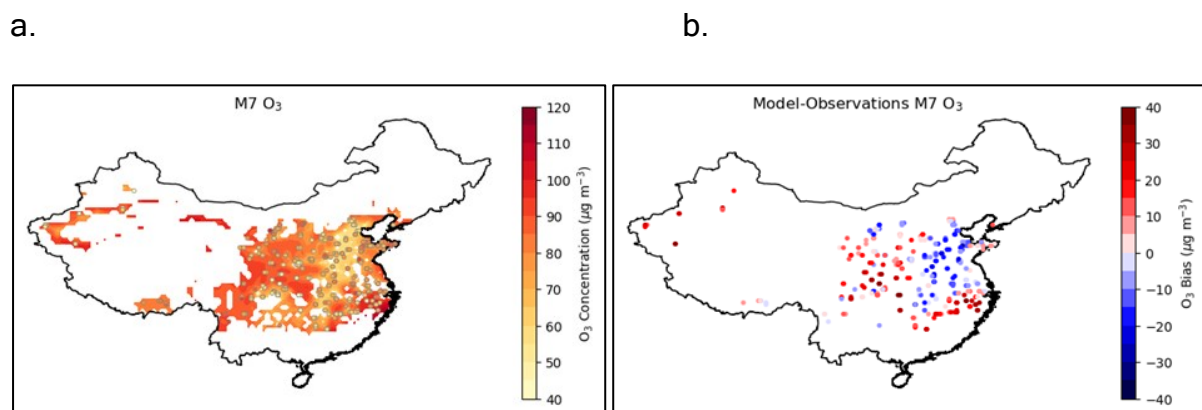
Lastly, the results encompass an analysis of winter wheat yield simulations by the DO<sub>3</sub>SE-crop model. This involves comparing modelled yield against observations from the SPAM2010 yield database, dissecting the model's performance at broader spatial scales, and examining O<sub>3</sub>-induced yield losses in different AEZs. The study also provides a nuanced look at the yield variation under current and pre-industrial O<sub>3</sub> concentrations, underscoring the differential impact of O<sub>3</sub> on crop yields across various zones. This comprehensive analysis aims to provide insights into the model's capabilities and areas for refinement in the context of agricultural and environmental planning.

### 4.4.1 WRF-Chem modelled versus observed M7-O<sub>3</sub>

The WRF-Chem model's simulations of rural M7 O<sub>3</sub> concentrations during the winter wheat growing season yielded an RMSE of 16.1 µg/m<sup>3</sup> compared to ground-based observations, indicating a quantifiable deviation with the model showing a propensity for overestimation. (RMSE: 16.1 µg/m<sup>3</sup>, NMAEF = 0.18, NMBF = 0.05) (see Fig. SI.

15). Fig. 17. a. shows the spatial distribution of modelled and observed M7 O<sub>3</sub> concentrations across China with values of 40 to 110 µg/m<sup>3</sup> across most of the productive winter wheat areas (i.e., AEZ zones II and IV, see Fig. 28). Fig. 17. b. illustrates the discrepancies between the predicted and actual M7 ozone concentrations, highlighting the model's biased forecasts. Specifically, the WRF-Chem model generally predicts lower levels than observed in zone II, the most agriculturally productive area, with a shortfall ranging from 0 to 20 µg/m<sup>3</sup>. Conversely, in zones I and IV, along with regions further south, the model tends to overpredict ozone concentrations by approximately 10-40 µg/m<sup>3</sup>, indicating significant prediction errors.

Fig. 17. Spatial plot showing (a). WRF-Chem modelled and observed M7 (09.00-16.00) O<sub>3</sub> concentrations µg/m<sup>3</sup> and (b). bias between modelled and observed M7 (09.00-16.00) O<sub>3</sub> concentrations µg/m<sup>3</sup> at observation sites. All M7 values are calculated for the period November to mid-May (rural locations only) for 2017/18.

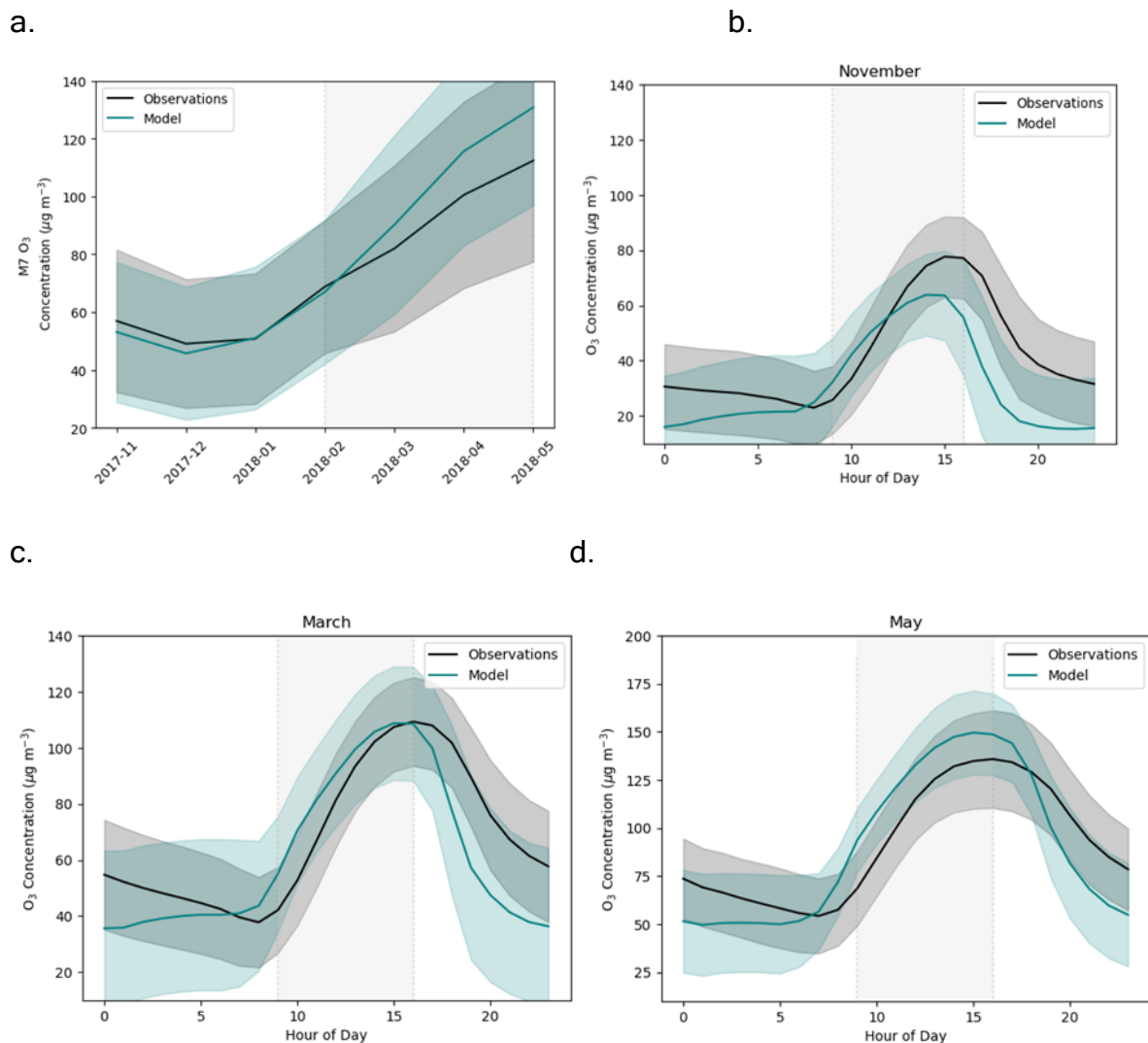


Temporal comparison of the WRF-Chem modelled O<sub>3</sub> concentrations against observations are shown in Fig. 18. (a-d) for the period November 2017 to May 2018. The approximate period of anthesis for the 2017/18 growing season for the whole of China is indicated by grey shading between mid-February and mid-May. This clearly shows that during anthesis (the most crucial time for accumulating damaging stomatal O<sub>3</sub> flux), the WRF-Chem model overestimates monthly M7 O<sub>3</sub> concentrations by around 20 µg/m<sup>3</sup> (Fig. 18.a). Fig. 18.c and d. show that this is due to WRF-Chem overestimating O<sub>3</sub> concentrations by about 15 µg/m<sup>3</sup> between 09.00 and 16.00. Earlier months in the growing season show the modelled and observed hourly concentrations are in good agreement or slightly underestimated (Fig. 18.b.) between 09:00 and 16:00. However, during the night hours (16:00-07:00), an

underestimation of hourly O<sub>3</sub> concentrations was noted in all three months shown in Fig. 18.

#### 4.4.2 Seasonal variation in modelled and observed M7

Fig. 18. (a). Seasonal variation in modelled (teal) and observed (black) M7 (mean 09.00 to 16.00 hrs) mean (line) and 1 standard deviation (shading) O<sub>3</sub> concentrations, µg/m<sup>3</sup> (for the period November 2017 to May 2018). (b-d) Modelled (teal) and observed (black) diurnal variations in hourly mean (line) and 1 standard deviation (shading) O<sub>3</sub> concentrations, µg/m<sup>3</sup> for (b). November, (c). March and (d). May, across the winter wheat growing region of China.

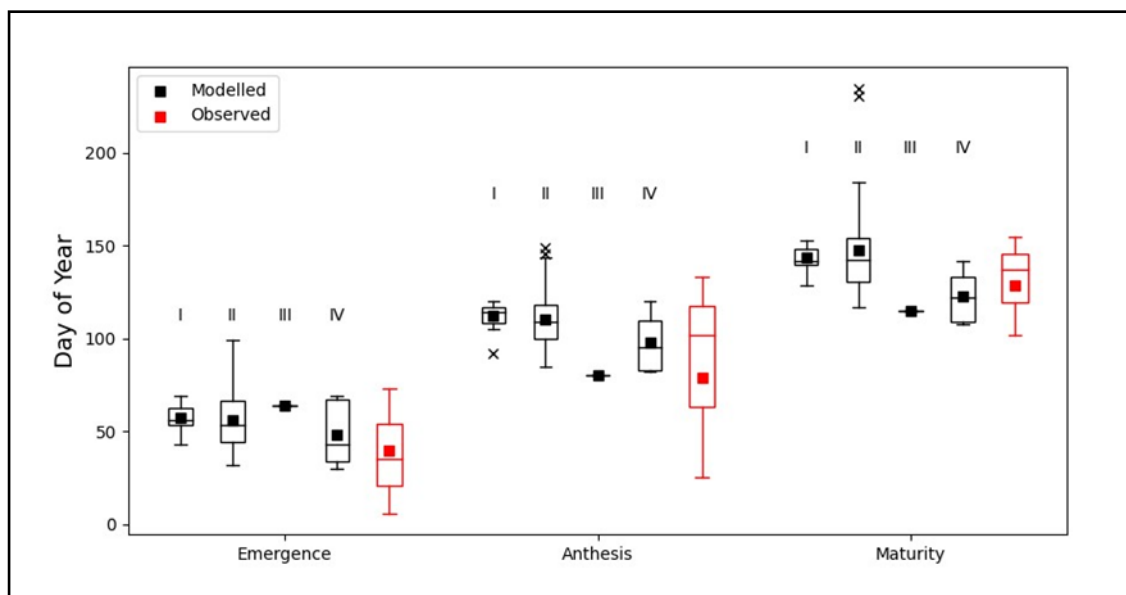


#### 4.4.3 Zone wise crop phenology versus observed

The DO<sub>3</sub>SE-crop phenology model is crucial to determining the timing and length of the growing season and the coincidence of elevated O<sub>3</sub> exposures and crop growth

stage. Fig. 19 compares the simulated timing of key crop growth stages (emergence, anthesis, and maturity) with timings derived from the published literature by AEZ; observed data are predominantly compiled for zones II and IV. Overall, the DO<sub>3</sub>SE-crop modelled values fall within the range of observations. However, it is clear that the timings of crop growth stage differ by AEZ, with zone I having a relatively short and late growth period, zone II having a longer and later growth period and zone IV having an early and shorter growth period. In zone III, only one of the randomly selected sites had an elevation of less than 1,600 m a.s.l (considered the limit for winter wheat cultivation in China (Chen et al., 2020)), so we do not consider zone III in further analysis.

Fig. 19. Boxplots (crosses: 0.01 and 0.99 percentiles; box: 0.25 quartile, median and 0.75 quartile; square: mean) comparing crop emergence, anthesis, and maturity phases of winter wheat in agro-ecological zones (AEZs) (zones I, II, III and IV; labelled black boxes) with data collected from observational studies (red boxes). Observed data are predominantly for zones II and IV.



#### 4.4.4 Scattered plot Observed (SPAM2010 data) vs calibrated DO<sub>3</sub>SE-crop modelled yield (g/m<sup>2</sup>)

Fig. 20a. shows the DO<sub>3</sub>SE-crop model's simulations of winter wheat yield (g/m<sup>2</sup>) for the tolerant cultivar, when compared against observations from the SPAM2010 yield database across various Agro-Ecological Zones (AEZs), yield an R<sup>2</sup> value of -0.398. The negative value is because the sum of square errors is larger than the observed

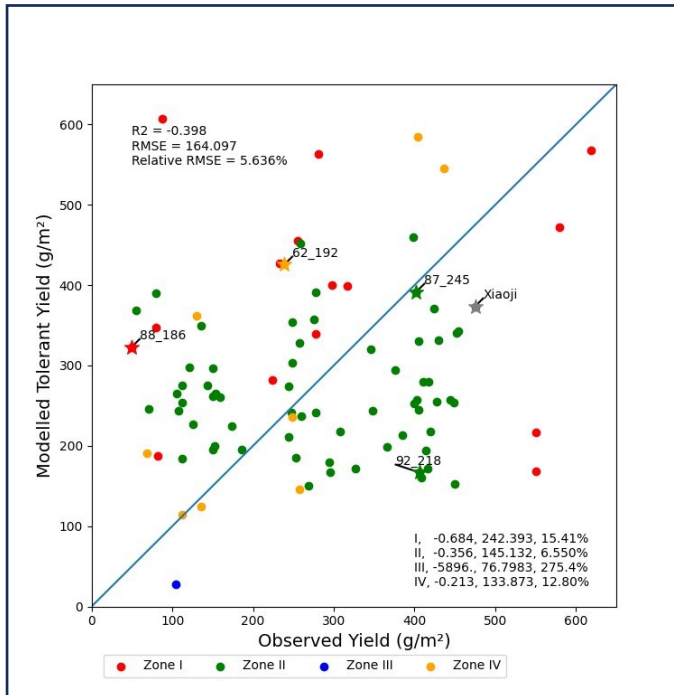
data's total sum of squares. This indicates a level of discrepancy between the modelled (SPAM data yield value) that are being used with meteorological factors generated from WRF-Chem data and observed yields.

This level of agreement is expected given that the SPAM2010 yield data are highly variable across small regions and are better suited to indicating yields between regions rather than for site-specific locations (Yu et al., 2020), in addition, the SPAM2010 data are on a coarser resolution as compared to the WRF-Chem grid (where four WRF-Chem grids comprise one SPAM grid). It is, therefore, useful to assess how the model performs at a broader spatial scale, Fig. Sl. 16 shows that the DO<sub>3</sub>SE-Crop model can simulate yields for the entire AEZs with good agreement between mean simulated vs. observed yields by AEZ (with an R<sup>2</sup> of 0.17 and RMSE of ~70 g/m<sup>2</sup>). Fig. 20.b. shows the modelled yield under current day O<sub>3</sub> concentrations vs. the modelled yield under pre-industrial O<sub>3</sub> concentrations; here we see how O<sub>3</sub>-induced yield losses are clearly very different by AEZs with zone IV (and III) experiencing minimal yield losses; zone II shows more variability with some locations showing more substantial yield losses of up to 30% and zone I with the vast majority of sites showing extreme yield losses.

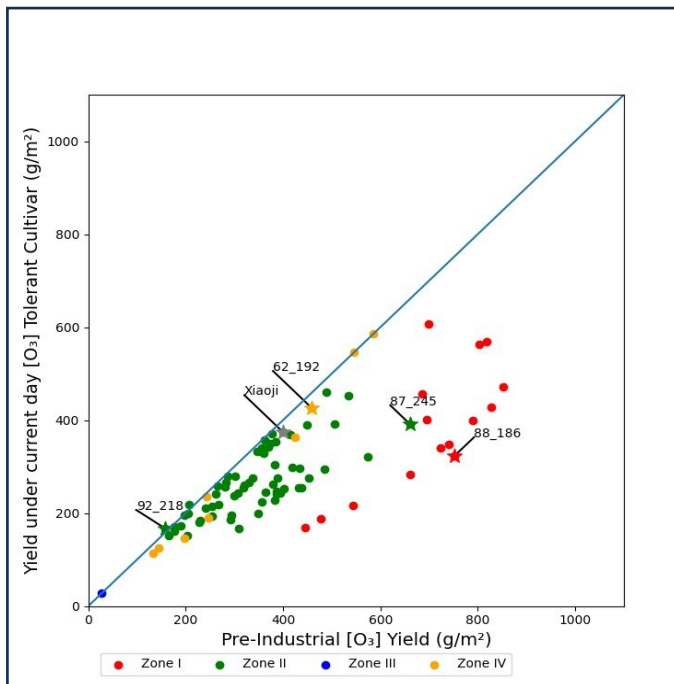
Fig. 20. This composite figure presents the analytical comparison between wheat yield data in two contexts: a. The left panel depicts the correlation between observed yield data from SPAM2010 and yield estimates modelled by the calibrated DO<sub>3</sub>SE-crop model across 89 randomly selected sites spanning four Agro-Ecological Zones (AEZs), distinguished by unique colours. The site-specific data points, identified by highlighted numbers, are earmarked for in-depth analysis later in the paper. The R<sup>2</sup> value is shown and the blue line depicts the 1:1 line.

b. The right panel contrasts the modelled yields of the current day with those from the pre-industrial era, again across the four AEZs and the same 89 sites. The data alignment along the blue diagonal 1:1 line reveals the variance between present-day and historical yield estimates, elucidating the effects of modern environmental conditions on crop production. Site codes accompanying each data point will be referenced for subsequent detailed discussions within the study.

a.



b.

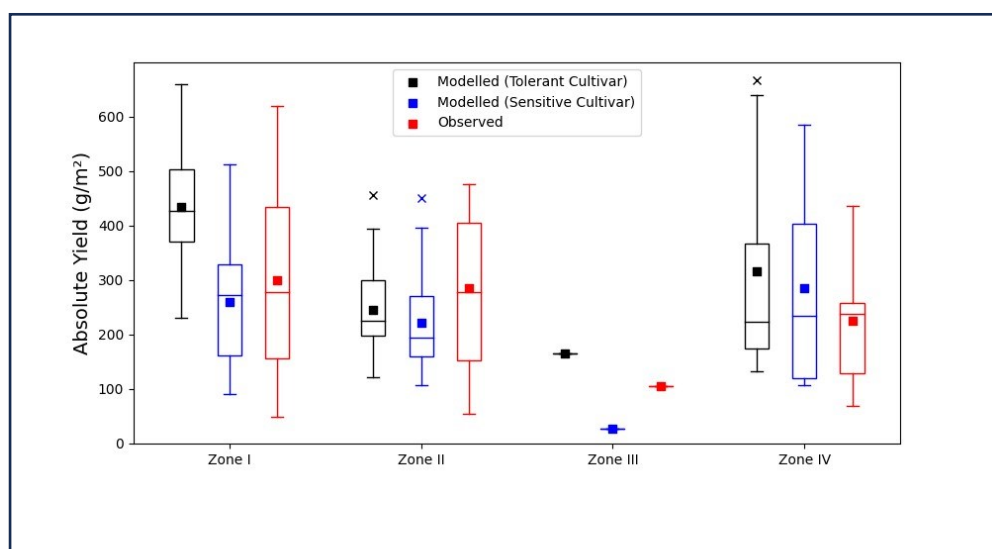


#### 4.4.5 Observed (SPAM2010 data) vs calibrated DO<sub>3</sub>SE-crop modelled yield (g/m<sup>2</sup>)

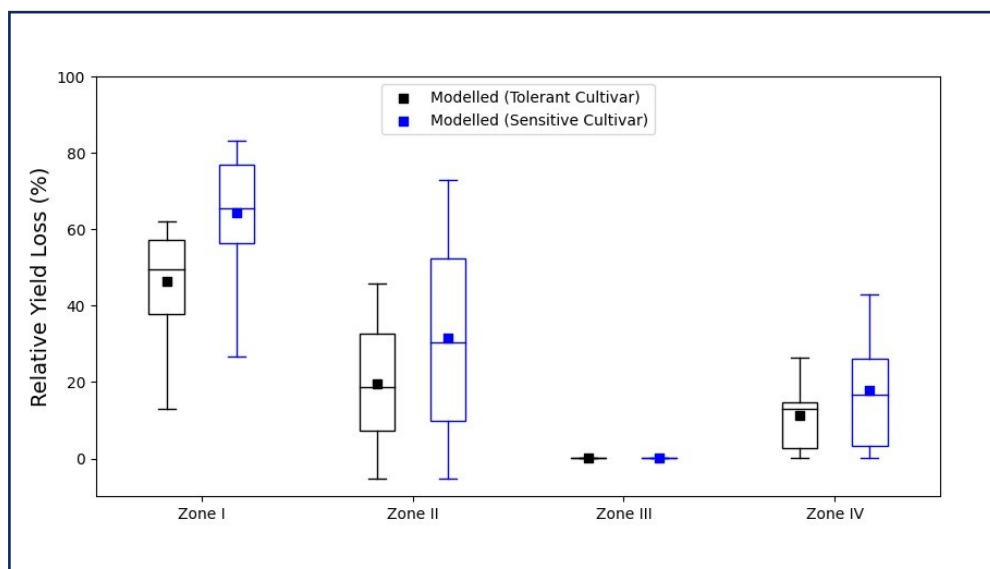
To get an idea of how well DO<sub>3</sub>SE-Crop is able to simulate absolute yield, we compare (a). the simulated yields for tolerant and sensitive cultivars for present-day O<sub>3</sub> concentrations (2017/18) with SPAM2010 observed yield (shown in Fig. 21.a). This shows that for zones I and II, modelled yields are largely within the observed yield estimates, however for zone IV modelled yields are higher by an average of ~75 g/m<sup>2</sup> for the tolerant cultivar Fig. 21.b shows relative yields using the pre-industrial O<sub>3</sub> concentrations (assumed to be constant at 10 ppb) as the reference yield. This gives an indication of the yield loss due to O<sub>3</sub> for different cultivar sensitivities by AEZ. We see that the O<sub>3</sub> influence on yield varies by AEZ and cultivar sensitivity, for tolerant cultivars, zone IV shows the lowest mean O<sub>3</sub> effect (with a mean yield loss of ~ 15%), zone II a slightly greater O<sub>3</sub> effect with a mean yield loss of ~ 20%) and zone I the greatest, and overly extreme, O<sub>3</sub> effect at ~ 50% mean yield loss.

Fig. 21. Box plots comparing the (a). absolute yield under ambient O<sub>3</sub> for 2017/18 vs observed SPAM2010 yield and (b). relative yields (i.e., current compared to pre-industrial O<sub>3</sub> for the tolerant cultivar of the four different AEZs. All for irrigated winter wheat. The mean value of the yield is indicated by the square box inside each plot, while the median value is represented by the dashed line within the box. The "whiskers" extend from the box to show the range, which includes the maximum and minimum yield values. Outliers, which are data points that differ significantly from the rest of the dataset, are marked with crosses. It is noteworthy that Zone III has only a single data point for the observed yields due to limited data availability. This single data point is represented as an outlier, which may affect the interpretation of the results for that zone.

a.



b.

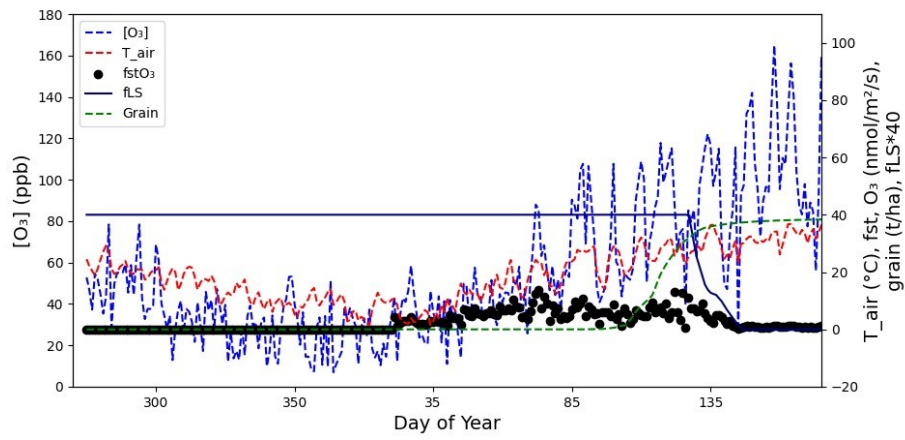


#### 4.4.6 Comparison Observed (SPAM2010 data) vs calibrated DO<sub>3</sub>SE-crop modelled yield (g/m<sup>2</sup>)

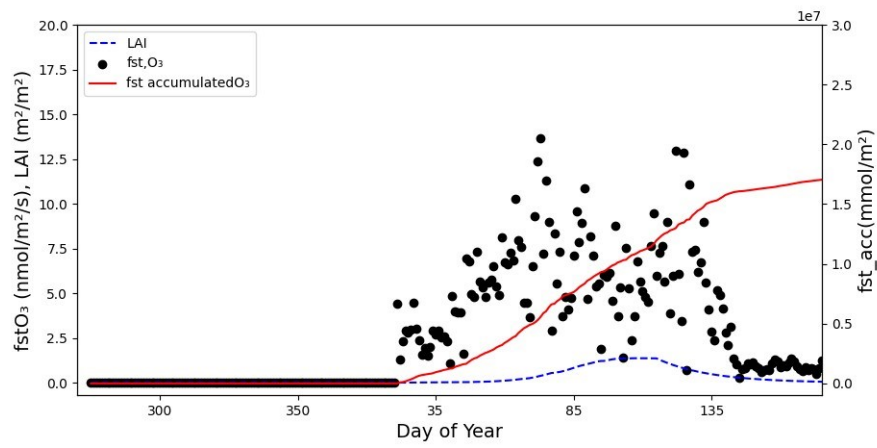
To understand which environmental conditions are driving these differences in O<sub>3</sub>-induced yield losses by AEZ, it is useful to explore specific locations in more detail. We start with the Xiaoji location since this is the site at which the DO<sub>3</sub>SE-Crop O<sub>3</sub> damage module was calibrated. Fig. 22 provides a direct comparison between the experimental data collected from the Xiaoji site and the WRF-Chem equivalents for O<sub>3</sub> and meteorological conditions. We explore how these data (and the different model parameterisations) influence the modelling of O<sub>3</sub> damage by comparing key variables selected for their importance in determining the extent of O<sub>3</sub>-induced yield losses.

Fig. 22. Comparison of WRF-Chem (a. and b.) and experimental (c. and d.) O<sub>3</sub> concentration and meteorological data on crop phenology, growth, and yield at Xiaoji for the tolerant cultivar for key variables (a. and c.) of O<sub>3</sub> concentration, surface air temperature ( $T_{air}$ ), canopy stomatal ozone flux (canopy  $f_{st}$ ), fLS and grain yield and (b. and d.) canopy  $f_{st}O_3$ , LAI and accumulated stomatal ozone flux ( $acc\_f_{st}$ ) for the period of 1<sup>st</sup> Oct (Day of Year 274) to end of June (Day of Year 540).

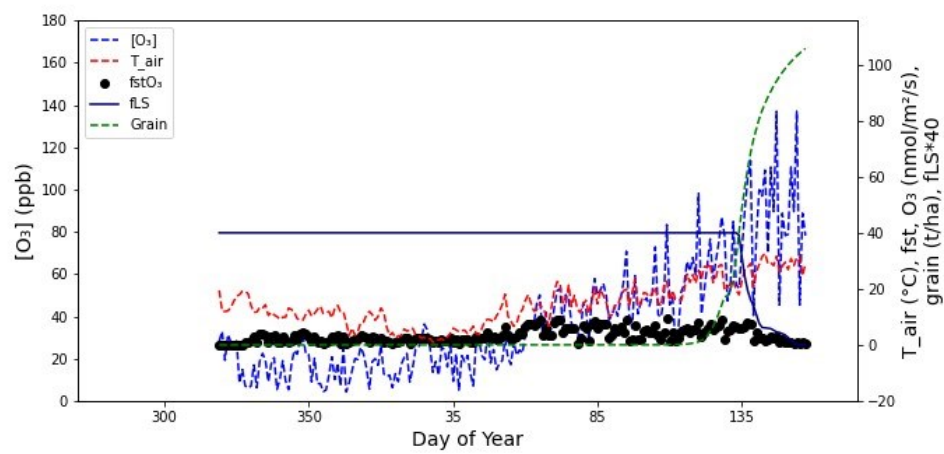
a.



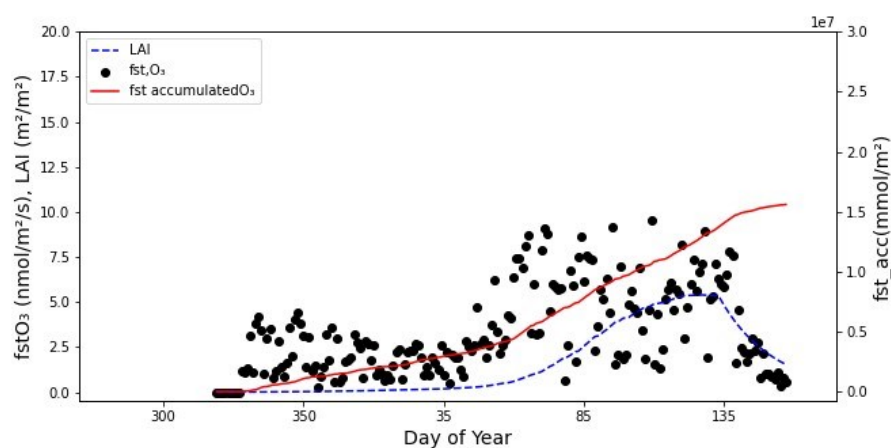
b.



c.



d.



For Xiaoji, Fig. 22 shows that WRF-chem O<sub>3</sub> concentrations peak ~ 10 ppb higher than the experimental data though the seasonal profile is fairly similar, the air temperature ( $T_{\text{air}}$ ) is around 20 °C during the during grain filling period but marginally higher (by a few °C) in the WRF-Chem data. However, the yield estimated using the WRF-chem data is 395 g/m<sup>2</sup> compared to 1000 g/m<sup>2</sup> for the experimental site (refer to figure Fig. 22 a and c by the green dashed line), this difference is driven by the low LAI for the WRF-Chem data (1.9 m<sup>2</sup>/m<sup>2</sup>) showing that the calibration of the carbon allocation coefficients driven by the regional SPAM2010 yields produces a lower yield than that derived from calibration of these same coefficients for the experimental site data where conditions are optimal for growth.

The accumulated stomatal O<sub>3</sub> flux ( $\text{acc\_fst}$ ) value is similar for both the WRF-Chem and experimental data suggesting the effect on relative yield is similar.

To understand the differences in environmental characteristics by AEZ and how these play out in influencing O<sub>3</sub> damage, it is useful to compare key characteristics between sites in different zones. We use Fig. 20 to choose sites for this analysis, selecting one from zone I (88\_186, the most extreme O<sub>3</sub> induced yield loss of all sites for which absolute modelled yield is substantially overestimated), two from zone II (92\_218 representing an underestimated modelled yield and negligible O<sub>3</sub>-induced yield loss and; 87\_245 representing an accurately modelled absolute yield and a high O<sub>3</sub>-induced yield loss) and one from zone IV (representing an overestimated modelled yield and a minimal O<sub>3</sub>-induced yield loss).

The overestimated O<sub>3</sub> induced yield losses in zone I (88\_186) seem to be primarily due to the stomatal O<sub>3</sub> flux accumulating too early in the growing season, despite minimal variation in O<sub>3</sub> concentration and temperature from year day 300 vs 320 in the zone II grid (62\_192) which has minimal yield loss due to O<sub>3</sub> (see Fig. SI. 17 a). During this early period, the Leaf Area Index (LAI) in zone I is at its minimum. However, the DO3SE-Crop model estimates ozone flux on a per square meter basis for each sunlit leaf rather than accounting for the total cumulative sunlit leaf area. This method assigns equal importance to the ozone flux for every leaf, ignoring variations in sunlit leaf area. Such an approach might not accurately capture the true impact of ozone on plant growth and yield. Therefore, before the model's extensive deployment across China, it is crucial to adjust its parameters. Specifically, the LAI should only begin to increase during the peak of the growing season, and this adjustment could be achieved by managing the relationship between crucial carbon allocation coefficients and the timing of ozone flux accumulation. Similarly, the large O<sub>3</sub>-induced yield losses seen in zone II (87\_245) are due to an early accumulation of stomatal O<sub>3</sub> flux at year day 370, with values reaching close to 2.5 mmol/m<sup>2</sup> by the time of crop maturity. This can be contrasted with the other selected zone II site (92\_218), where stomatal O<sub>3</sub> flux does not start accumulating until around year day 450 (see Fig. SI. 18. b); this is due to T<sub>air</sub> being below T<sub>b</sub> (0.8°C zone II this study, see Table 11) until day 457 for site 92\_218.

Carbon accumulation in the grain occurs towards the end of the growing season and coincides with that period when O<sub>3</sub> concentrations are increasing; the point at which the model simulates the start of a reduction in grain yield due to O<sub>3</sub> is when fLS starts to decrease from 1 (note the scalar used in the plots), the steepness of the decline in fLS shows the sensitivity to O<sub>3</sub> damage and is greatest in zones I (88\_186) and II (site 87\_245), this occurs due to the high O<sub>3</sub> concentrations caused by local conditions compounded by a delay in the timing of anthesis to later in the season (see Fig. SI. 19).

## 4.5 Discussion

The DO<sub>3</sub>SE-crop model is developed and calibrated to estimate crop yield losses due to O<sub>3</sub> across China; in this study the model has been applied for three AEZs covering the majority (~ 95%) of the cultivated area under winter wheat production. We found substantial O<sub>3</sub>-induced yield losses when comparing the current year (2017/18) with pre-industrial O<sub>3</sub> levels. These losses varied considerably by AEZ and were further modified by cultivar sensitivity. Modelled O<sub>3</sub>-induced yield losses in AEZ II and IV were 18-30% (7-32% to 10-50%) and 15-18% (3%-18% to 3-22%) as an average (and 25 and 75 percentile ranges) respectively. By comparison, AEZ I yield losses were evidently overestimated with mean values of 46-62% (and an equivalent percentile range of 38-56% to 58-78%). Comparing these results with other studies, we find that results for AEZ II and IV are within the range of yield losses estimated by (Feng et al., 2022; and Schaubberger et al., 2019) simulated yield losses of between 35 and 50% across much of the winter wheat growing region, with losses increasing northwards across the winter wheat growing region; this spatial pattern is consistent with our higher yield losses estimated in AEZ I (though our estimates are overly high). Feng et al., (2022) estimated yield losses predominantly in the range of 20 to 35%, again with higher yield loss estimates in the northern reaches of the winter wheat distribution range but also lower yield losses to the east in our AEZ IV compared to AEZ II, again consistent with our results. This east-west pattern was not seen in the (Schaubberger et al., 2019) results but was seen in the (Tao et al., 2017) results, though these estimated far lower yield losses, reaching only 13%. This discrepancy could partly be due to the latter's focus on the 2000s, particularly in light of the significant rise in yield losses from approximately 18% to 33% documented by (Feng et al., 2022) from 2015/16 to 2017/19, highlighting potential interannual variability.

Our study also shows substantial differences in yield losses dependent on cultivar sensitivity with an increase in average relative yield losses of 3%, 12 and 16% for AEZ IV, II, and I, respectively (average values are taken from the box plot in Figure 33 b; where square represents the average values of the relative yield losses). No other studies have explored the effect of cultivar sensitivity on O<sub>3</sub>-induced yield losses for China but other studies, in addition to the Xiaoji experimental study (Zhu et al., 2011) used to parameterise our cultivar sensitivity, have shown a similar

influence of cultivar on yield loss. For example, a recent study by (Feng et al., 2022) found an average yield loss of 18.7 % when 18 wheat cultivars were exposed to a season long O<sub>3</sub> concentration of 70 ppb, but considerable genotypic variation ranging from 2.7 to 44.6 %. Such cultivar variation is important, especially given that studies suggest more recently released wheat cultivars may be more sensitive to O<sub>3</sub> (Biswas et al., 2008). The fact that China tends to use more recently released cultivars (i.e., released in the 2000s) compared to other global regions has been put forward as one explanation for AOT40 dose-response relationships developed using Chinese varieties being more sensitive than those developed for cultivars from other parts of the World (Xu et al., 2024). Further experimental investigation of cultivar sensitivity is required and would also benefit from an improved understanding of the plant traits that confer sensitivity (Feng et al., 2022).

There are several elements that are crucial to accurate estimates of O<sub>3</sub>-induced yield losses. The first of these is an accurate representation of the environmental conditions, namely meteorological data and O<sub>3</sub> concentrations, both of which are supplied *via* the WRF-Chem model. Meteorological data come from ERA-5 (see Table 19) and are used as input both to DO<sub>3</sub>SE-Crop and WRF-Chem for O<sub>3</sub> concentration estimates. Other studies that have modelled O<sub>3</sub> concentrations for China found comparatively high O<sub>3</sub> concentrations with M7 values ranging from ~90 to 140 µg/m<sup>3</sup> (Wang et al., 2022); however, these M7 values are estimated for the three months prior to harvest whilst our M7 values are modelled from November to May (i.e., 7 months), the inclusion of the earlier months in the growing season with lower O<sub>3</sub> concentrations is very likely to be the reason for our lower M7 values with M7 values of between 60-110 µg/m<sup>3</sup> (see Fig. 29) for the same region during the winter wheat crop growing season. Although Our M7 estimates, while lower than those reported by (Wang et al., 2022), exhibit an overestimation of O<sub>3</sub> concentrations in the later months relative to observed data from (Silva et al., 2018). This discrepancy highlights the need for additional research to enhance the accuracy of O<sub>3</sub> concentration modelling across China.

The second important element is the modelling of crop phenology since this determines both the timing of key crop growth stages in relation to prevailing O<sub>3</sub> concentrations as well as the timing and length of the important grain-filling period that will determine yield. The extensive crop phenology dataset,

ChinaCropPhen1km, established by (Luo et al., 2020), divided the winter wheat crop growing region into four AEZs with variable timings across zones for key phenology stages (e.g., maturity was found to occur anywhere between the day of year 102 to 155 within AEZs II and IV). There are some limitations to the DO<sub>3</sub>SE-Crop's phenology module. We have limited data with which to calibrate the phenology model; the addition of more sites covering all zones (i.e., I and III) would be beneficial. In addition, our crop phenology model only uses three cardinal temperatures ( $T_b$ ,  $T_o$ , and  $T_{max}$ ), the inclusion of additional parameters that are able to distinguish the differing effects of the higher end temperatures on the progression of phenological stages (e.g. (Tao et al., 2012)) could improve the ability of the model to simulate phenology across the full diversity of AEZ conditions found across China. The importance of the growing season has been identified previously by Wang et al., 2022 who found when using the less complex dose-response type models, that the definition of the growing season was likely to have a greater impact on estimated O<sub>3</sub>-induced yield losses than small biases in O<sub>3</sub> surface concentrations.

The ability to describe the variability in crop yields across AEZs is the third element crucial to process-based crop modelling of O<sub>3</sub>-induced yield losses since these data are an important requirement for the calibration of crop models to ensure the correct allocation of biomass to the different plant parts over time. This study used the SPAM2010 crop yield dataset, which has been developed to provide a global spatially explicit dataset on agricultural production by combining census statistics with agricultural land cover maps (Yu et al 2020). This SPAM2010 dataset is seen as the most accessible and comprehensive crop distribution data to date (Liu et al., 2022). However, the SPAM2010 methodology and input data are still evolving. The dataset has faced criticism for its less precise spatial distribution of wheat yields and for using lower-resolution input data (Luo et al., 2022). For example, Luo et al. (2022) assessed two gridded map datasets, GWPMS (Global Wheat Production Mapping System) and SPAM and determined that GWPMS outperformed SPAM. GWPMS's superiority was attributed to its higher spatial accuracy and resolution in wheat distribution datasets. (Luo et al., 2022) study highlighted that the RMSE values for the SPAM dataset in the Chinese region range from 72 to 105 g/m<sup>2</sup> (years studied 2000,2005 and 2010) when comparing SPAM yield against census yield during 2007-2012. Despite these limitations in the SPAM2010 dataset, it is widely used by the crop modelling community for crop model calibration (Müller et al., 2019). In this

study, we found an RMSE of 164 g/m<sup>2</sup> when the DO<sub>3</sub>SE-Crop modelled yields were compared with the SPAM 2010 yields, which provides confidence that the model is able to broadly capture the range of the yield in the three-winter wheat AEZs.

However, even though the DO<sub>3</sub>SE-Crop model seems able to simulate yield on a broad scale, understanding the factors contributing to yield variability within AEZs is crucial, and several factors are important here. Studies have shown that low temperatures can adversely affect wheat crop emergence, causing delays in crop growth and development (Buriro et al., 2011; Lozovskaya et al., 2012). Such effects can influence yield; for example, low temperatures early in spring were found to delay plant growth and reduce grain weight per spike by 31% (Yu et al., 2022). Ensuring that the various stages of phenology are correctly related to carbon and, hence, biomass partitioning is important both for the modelling of an appropriately structured plant as well as to determining how O<sub>3</sub>-induced changes in carbon assimilation will influence biomass and yield. Ensuring the carbon allocation coefficients are suitably parameterised will produce a well-structured plant (i.e., one that has appropriate crop growth stages for the changes in LAI, above-ground biomass, and yield in relation to the prevailing AEZ environmental conditions). Our results show that there are still improvements that need to be made in these parameters, especially in AEZ I, where increases in LAI occurred seemed to occur too early. However, the variability in LAI within and between AEZs is substantial, causing difficulties in ensuring models capture LAI accurately. Efforts to assimilate satellite data with crop model estimates of yield (Huang et al., 2015) may improve this important aspect of process-based modelling in the future.

#### 4.6 Conclusions

The DO<sub>3</sub>SE-Crop model has been calibrated for winter wheat growing across three AEZs in China. The model has been shown to provide O<sub>3</sub>-induced yield loss estimates in line with other published studies for two out of three AEZs, where the model performs poorly, which seems linked to the simulation of phenology, carbon allocation, and, in particular, LAI. Our study shows that there is substantial variation both within and between AEZs both in the environmental conditions that determine crop growth as well as those that will, therefore, influence the extent and magnitude of O<sub>3</sub> damage. This study also found that cultivar sensitivity will have a substantial influence on the size of yield losses experienced. Therefore, it can be concluded that developing models capable of differentiating the influence of environmental conditions by AEZ as well as cultivar sensitivity is important to understand the drivers of enhanced O<sub>3</sub> sensitivity to crop yield loss.

## SI.3 Supporting material

### SI.3.1 WRF-Chem model

This section describes the various meteorological and emissions input datasets used to run the WRF-Chem model for 2017/18.

#### Rest of the World (ROW) Anthropogenic Emissions

Global anthropogenic emissions were taken from CAMS-GLOB-ANT v4.2-R1.1 (CAMS-GLOB-ANT) at  $0.1^\circ$  for 2016 (Soulie et al., 2023). Within CAMS-GLOB-ANT, anthropogenic emissions for China are taken from MEIC for 2016. MEIC emissions are re-gridded from  $0.25^\circ$  to  $0.1^\circ$  to match the resolution of the CAMS-GLOB-ANT dataset and are used in place of CAMS-GLOB-ANT in China. Within CAMS-GLOB-ANT, emissions for the rest of the world are taken from CEDS between 2011 and 2014 and EDGARv4.3.1 for 2010. Within CAMS-GLOB-ANT, to generate emissions for 2016, a linear trend is fitted to the  $0.5^\circ$  global CEDS data for each species between 2011 and 2014. The trends are then disaggregated to the EDGARv4.3 grid and used to project the EDGARv4.3 2010 emission estimates to the year 2016.

#### China Emissions

Anthropogenic emissions for China in the CAMS-GLOB-ANT database are from the Multi-resolution Emission Inventory for China (MEIC) (Li et al., 2017; Zheng et al., 2018); we replace the original 2016 Chinese emissions held in this database with 2017 MEIC emissions using a China shapefile to remove and replace only those emissions in China. To merge the MEIC 2017 emissions with CAMS-GLOB-ANT, we re-grid the MEIC emissions from their native grid resolution ( $0.25^\circ$  resolution) to the CAMS-GLOB-ANT resolution ( $0.1^\circ$  resolution) using conservative re-gridding.

Agricultural emissions for China were provided by the SEI Health model (Malley et al., 2021) and were estimated for all key pollutant sources: manure management, manure application, rice production, enteric fermentation, fertilizer application, and residue burning. Emissions from farm machinery were not included to avoid double counting the non-road transport sector. Emissions were estimated at  $0.083^\circ$  and re-gridded to  $0.1^\circ$  using conservative re-gridding.

Wildfire emissions are taken from the Fire Inventory from NCAR version 1.5 (FINNV1.5). The FINNV1.5 emissions dataset combines satellite observations, land

cover, biomass consumption estimates and emissions factors to calculate fire emissions globally at 1 km resolution every day. Satellite observations from the MODIS Thermal Anomalies Product provide detections of active fires with a nominal horizontal resolution of  $\sim 1$  km<sup>2</sup>. The burned area is assumed to be 1 km<sup>2</sup> for each fire identified and scaled back based on the density of vegetation from the MODIS Continuous Fields (VCF) (i.e., if 50% bare = 0.5 km<sup>2</sup> burned area). The type of vegetation burned during a detected fire is determined using the MODIS Collection 5 Land Cover Type (LCT). This assigns each fire pixel to one of 16 possible land cover/land use classes, and the density of vegetation is at 500 m resolution, scaled to 1 km. The 16 land cover types are then aggregated into 8 generic categories to which fuel loadings are applied (Wiedinmyer et al., 2011). Fuel loadings are from (Hoelzemann et al., 2004), and emissions factors are from (Akagi et al., 2011), (McMeeking, 2008), and (Andreae, 2019). We remove fire emissions on cropland using the land cover type information. This is to avoid double counting since agricultural residue burning is included in the Malley agricultural emissions dataset.

Biogenic emissions were calculated online by the Model of Emissions of Gases and Aerosols from Nature (MEGAN) (Guenther et al., 2006)

All emissions datasets were provided at monthly temporal resolution and included black carbon, organic carbon, fine (PM<sub>2.5</sub>) and coarse (PM<sub>10</sub>) particulate matter, carbon monoxide, NH<sub>3</sub>, NO<sub>x</sub>, SO<sub>2</sub>, and non-methane VOCs. VOCs were speciated according to the Model for Ozone and Related Chemical Tracers (MOZART, (Emmons et al., 2010)). Emissions sectors included land transport, residential, power, shipping, aircraft, agriculture, and industry. Sector-specific diurnal cycles were subsequently added to the emissions, using diurnal cycles from Olivier et al. (2003).

#### Initial Boundary Chemistry

Boundary conditions are required to account for the initial concentrations and movement of concentrations into and out of the China study area. Initial boundary chemistry was provided by the Whole Atmosphere Community Climate Model (WACCM) monthly mean simulation data for 2017/2018 ((Marsh et al., 2013); UCAR, 2020a). The NASA GMAO GEOS-5 model drives WACCM meteorology.

Anthropogenic emissions for 2014 from CEDS (used in CMIP6) and FINN-v1 fire

emissions are used in WACCM. Model output is given on 88 vertical levels at 0.9x1.25° (UCAR, 2020b).

### Chemical Scheme

The Model for Ozone and Related Chemical Tracers, version 4 (MOZART-4) scheme was used for gas-phase chemistry (Emmons et al., 2010), driven by model meteorology. The MOZART-4 scheme includes 85 gas-phase species, 12 bulk aerosol compounds, 109 photolysis (phot\_opt=4) reactions relevant to tropospheric and stratospheric chemistry, and 157 gas-phase reactions (Emmons et al., 2010).

### Meteorology

Meteorological conditions were initialised using ERA5 6-hourly reanalysis for 2017 and 2018 at 0.1° resolution on 38 pressure levels (Hoffmann et al., 2019). Nudging was used to keep simulated meteorology in line with the meteorological analyses. Nudging was performed for all vertical levels in the model every 6 hours. For all simulations 2017/2018, reanalysis was used.

### SI.3.2 Data required to run the DO<sub>3</sub>SE-Crop model

Table. SI. 13 Input data required by the DO<sub>3</sub>SE-Crop model and made available via the implementation of WRFChem (version 4.2).

Variable	Abbreviation	Description	Units
Day of year	DOY	Julian day from 1 <sup>st</sup> Jan	Day
Hour	hr	Hour of day (0 to 23)	Hour
Surface temperature	Tair	Air temperature at 2 m above ground level	°C
Air pressure	P	Surface air pressure at 2 m above ground level	kPa
Precipitation	Precip	Precipitation	mm

Vapour pressure deficit	VPD	Vapour pressure deficit at 2 m above ground level	kPa
Wind speed	u	Wind speed at 10 m	m/s
Ozone concentration	O3,ppb	Ozone concentration at middle of lowest WRFChem model layer (~15 m)	ppb
Surface heat flux	Hd	Surface heat flux	W/m <sup>2</sup>
Friction velocity	u*	Friction velocity at 50 m	m/s
Cloud fraction	cloud_frac	Fraction of sky covered by cloud	-

Table. Sl. 14. Final calibrated parameters by zone used for the DO3SE-Crop model runs across China. Other parameters used are same as in Table 17.

Zone	T <sub>b</sub> (°C)	T <sub>o</sub> (°C)	T <sub>m</sub> (°C)	fTT <sub>emr</sub> (-)	fTT <sub>veg</sub> = ftl <sub>,em</sub> (-)	fTT <sub>rep</sub> =ftl <sub>,ma</sub> (-)	Harvest (in °day)	PIV (no units)	PID (no units)	V <sub>cmax</sub> (μmol CO <sub>2</sub> m <sup>-2</sup> s <sup>-1</sup> ), J <sub>max</sub> (mmol m <sup>-2</sup> s <sup>-1</sup> ), m, D <sub>o</sub>	α <sub>root</sub>	α <sub>leaf</sub>	α <sub>stem</sub>	Y (m <sup>-2</sup> kg <sup>-1</sup> )	τ	γ <sub>3</sub> (μmol O <sub>3</sub> m <sup>-2</sup> ) <sup>-1</sup> , γ <sub>4</sub> , γ <sub>5</sub> [Tolerant cultivar]	CLsO <sub>3</sub> mmol O <sub>3</sub> m <sup>-2</sup>
Zone I	0.8 (-1 - 3)	20.1 (15- 25)	33.1 (30- 40)	0.05	0.45	0.50	1026.8 (500- 2000)	2.4	40	137,228 ,4,2.2	18.7 (16- 19)	18.4 (18- 19)	16.8 (16- 17)	15 (15- 27)	0.3 (0.3- 0.6)	0.00002,5[ 1.8],0.4[0.2 ]	13.5
Zone II	0.23 1 (-1 - 3)	20.7 (15- 25)	32.6 (30- 40)	0.16	0.52	0.32	1700 (950- 1800)	2.9	46	137,228 ,4,2.2	18.7 (16- 19)	18.4 (18- 19)	16.8 (16- 17)	19 (15- 27)	0.3 (0.3- 0.6)	0.00002,5[ 1.8],0.4[0.2 ]	13.5
Zone III	3 (-1 - 3)	21.2 07 (15- 25)	31.6 94 (30- 40)	0.05	0.15	0.80	608.981 (950- 1800)	2.4	40	137,228 ,4,2.2	16.5 (16- 19)	18.5 (18- 19)	16.2 (16- 17)	23 (15- 27)	0.3 (0.3- 0.6)	0.00002,5[ 1.8],0.4[0.2 ]	13.5

Zone IV	0.14 7 (-1-3)	19.5 37 (15-25)	31.6 85 (30-40)	0.18	0.50	0. 3 2	1083.22 (950-1800)	2.4	40	137,228 ,4,2.2	18.5 (16-19)	18.4 (18-19)	16.8 (16-17)	23 (15-27)	0.3 (0.3-0.6)	0.00002,5[ 1.8],0.4[0.2 ]	13.5
---------	---------------------	-----------------------	-----------------------	------	------	--------------	-----------------------	-----	----	-------------------	-----------------	-----------------	-----------------	---------------	------------------	---------------------------------	------

N.B.  $T_b$  (°C) is base temperature;  $T_o$  (°C) is optimum temperature;  $T_m$  (°C) is maximum temperature;  $fTT_{emr}$  (fraction) is the fraction represents the part of the thermal time from sowing to emergence ( $TT_{emr}$ );  $fTT_{veg} = f_{tl,em}$  (fraction) is the fraction of the thermal time associated with the vegetative phase of the crop's development;  $fTT_{rep} = f_{tl,ma}$  (fraction) is the fraction corresponds to the thermal time during the reproductive phase, signified by the thermal time from emergence to maturity ( $TT_{rep}$ ); Harvest (in degree day) refers to the accumulated temperature (in degree days) required to reach the harvest stage of a crop; PIV (no units) is the vernalisation Coefficient. It quantifies the effect of vernalization on the crop's development; PID (no units) is the photoperiod Coefficient. It quantifies the effect of photoperiod on the crop's development.  $\alpha_{root}$  is the coefficient for determining partitioning of carbon into roots;  $\alpha_{leaf}$  is the coefficient for determining partitioning of carbon into leaves;  $\alpha_{stem}$  is the coefficient for determining partitioning of carbon into stems;  $\Upsilon$  ( $m^2 kg^{-1}$ ) is the coefficient for determining specific leaf area and  $\tau$  is the allometric coefficient which relates  $C_{stem}$  to height of the crop ( $h$ ).  $\gamma_3$  determines the occurrence of senescence once a critical cumulative stomatal  $O_3$  flux  $CLS03$  (in  $mmol/m^2$ ) has been exceeded. The rate of senescence is determined by  $\gamma_4$ , which determines the onset of senescence and  $\gamma_5$  which determines maturity.

### SI.3.3. Statistical measures used to assess the WRF-Chem and DO<sub>3</sub>SE-Crop models.

$R^2$  is a measure of how the variance of the errors compares to the variance of observed data. If  $R^2$  is 0, then the modelled data is the mean of observed data, and both variances are equal. If  $R^2$  is 1 then the errors (modelled - observed) is 0. A negative  $R^2$  means the variance of the errors is larger than the variance of the observed data.

RMSE is the root mean square error which is the average 'distance' or value the modelled data is from the observed data. It is squared and the square root taken, so all means are positive, with 0 representing a perfect fit. RMSE captures the average magnitude of the error produced by the model in the same units as the data. Since errors are squared before averaging is applied, RMSE gives a higher weight to large biases. This is particularly useful when large biases are undesirable.

Relative RMSE is RMSE normalised by the range of the observed data to give a similar version of the average 'distance' the modelled data is from the observed but scaled to a percentage based upon the range of the observed i.e., if the relative RMSE is 6% then the data are on average within 6% of the range of the data to the observed values.

NMAE is the normalized mean absolute error and indicates the average magnitude of the error between the model and observations without measuring the direction of the error (relative to the observations). All values are weighted equally, unlike RMSE, which is biased towards larger errors due to the square of the error value. The NMAE uses the same scale as the data being measured so predicted values must use the same scale as observed values. An NMAE is commonly used as a measure of forecast error in time series. A NMAE of 0 would indicate no error in predictions.

NMAEF is the normalized mean absolute error factor

NMBF is the normalized mean bias factor and indicates the model bias relative to the observations. The NMBF can be interpreted in the following way: if NMBF is positive (e.g. NMBF = 1.5), the model overpredicts the observations (in this case by a factor of

2.5). Whereas, if NMBF is negative (e.g. NMBF = -0.5), the model underpredicts the observations (in this case by a factor of 1.5).

### SI.3.4 Results

Fig. SI. 15. Scatter plot showing M7 (09.00-16.00) O<sub>3</sub> concentrations  $\mu\text{g}/\text{m}^3$  comparison of observed vs modelled for rural locations only. All M7 values are calculated for the period November to mid-May (rural locations only) for 2017/18.

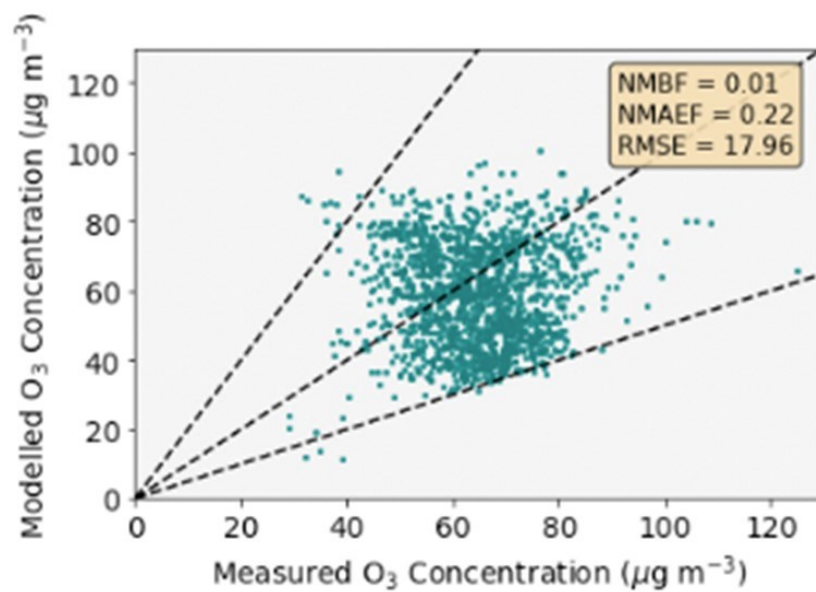
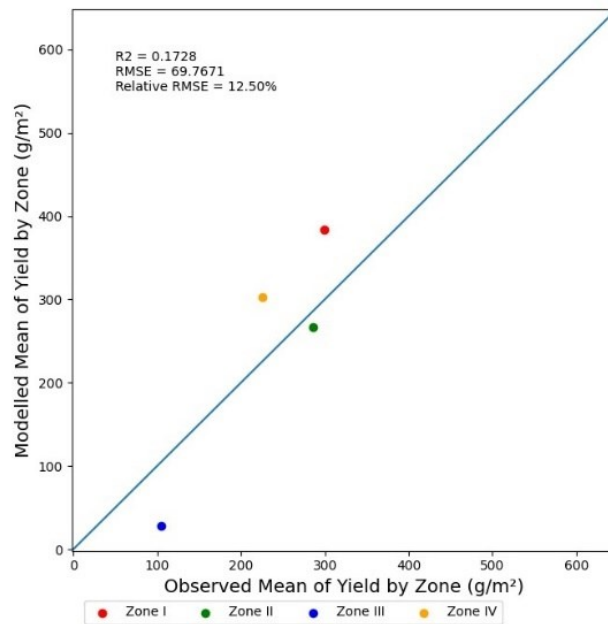


Fig. SI. 16. (a.) Mean and (b.) sum observed vs simulated yields ( $\text{g}/\text{m}^2$ ) for tolerant cultivars for each of the four AEZs.

a.



b.

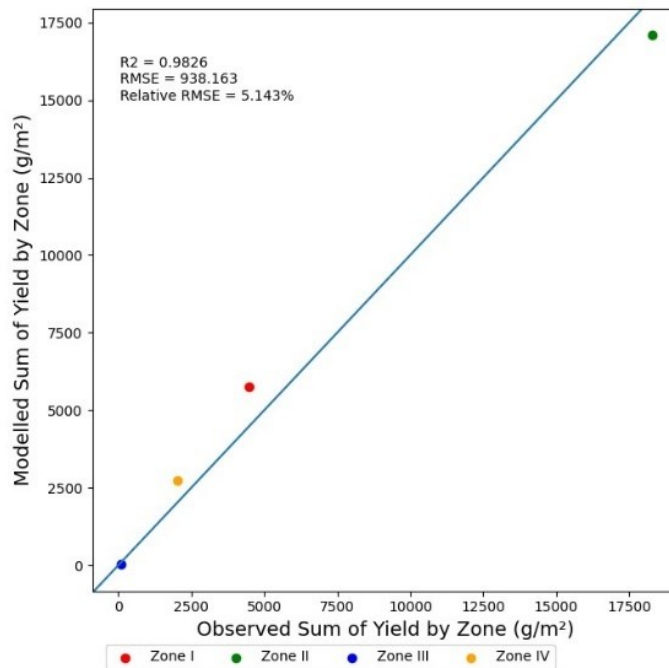
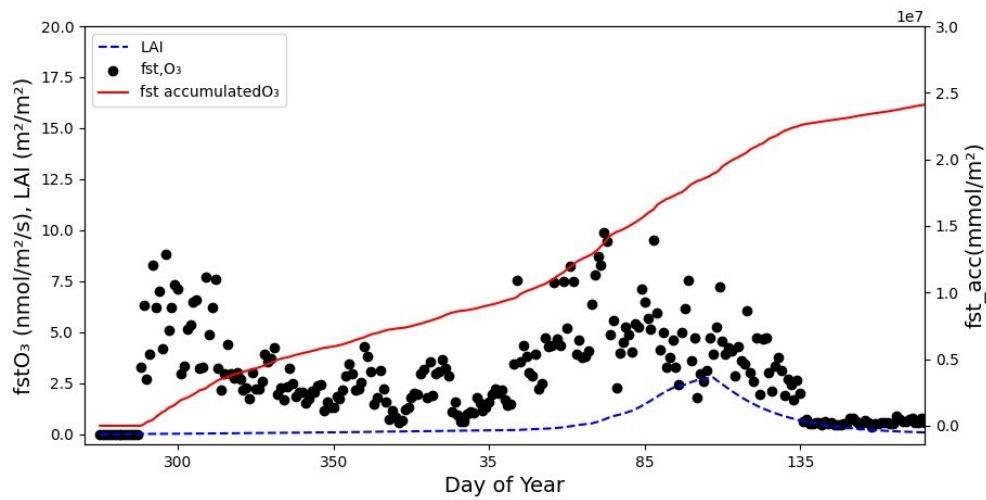


Fig. SI. 17. Comparison of (a). zone I (88\_186; with an overestimated O<sub>3</sub> induced yield loss) and (b). zone II (62\_192; with a negligible O<sub>3</sub> induced yield loss) for variables canopy fstO<sub>3</sub>, LAI and accumulated stomatal ozone flux (acc\_f<sub>st</sub>) for the period of 1st Oct (Day of Year 274) to end of June (Day of Year 540).

a.



b.

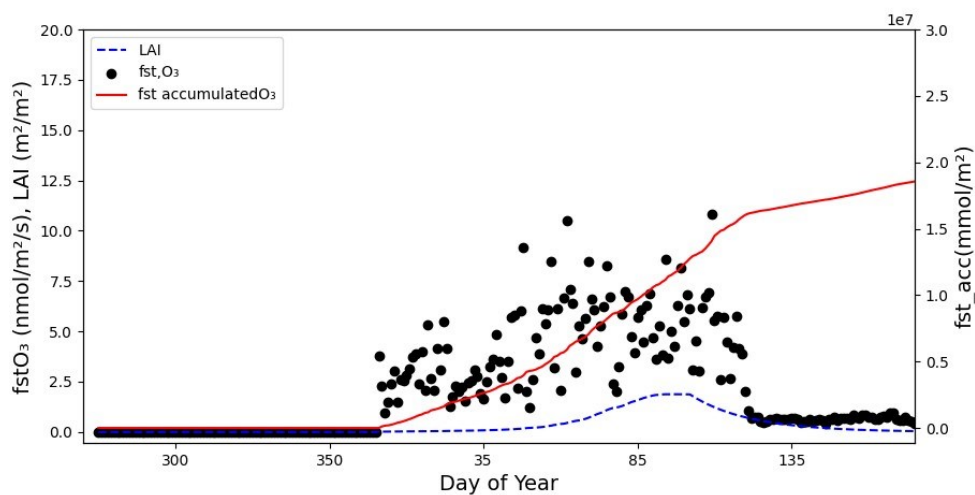
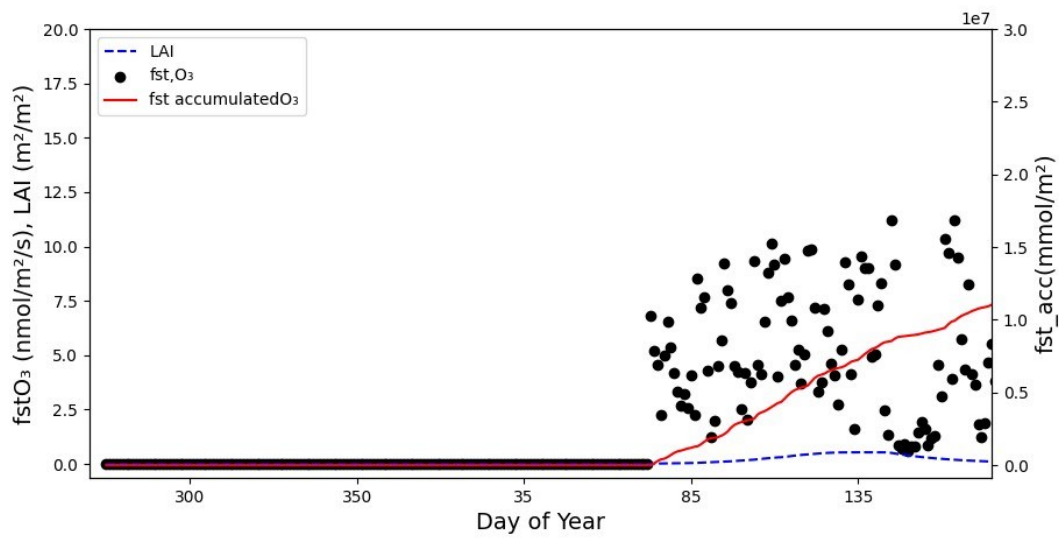


Fig. SI. 18. Comparison of (a). zone II (92\_218; with a low absolute yield and a negligible O<sub>3</sub> effect on yield) and (b). zone II (87\_245; with a high absolute yield and a substantial O<sub>3</sub> induced yield loss) for variables canopy  $\text{fstO}_3$ , LAI and accumulated stomatal ozone flux ( $\text{acc\_fst}$ ) for the period of 1st Oct (Day of Year 274) to end of June (Day of Year 540).

a.



b.

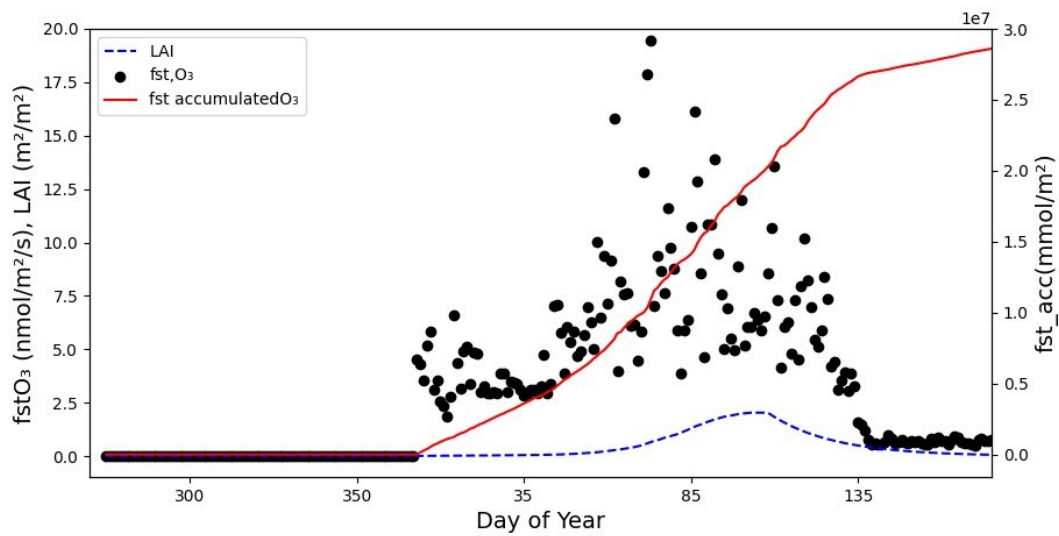
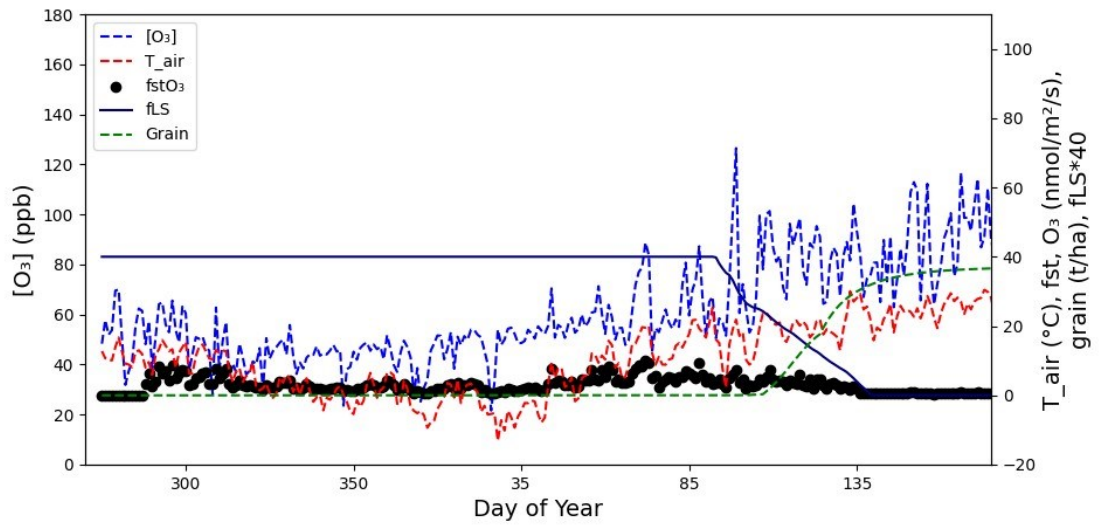
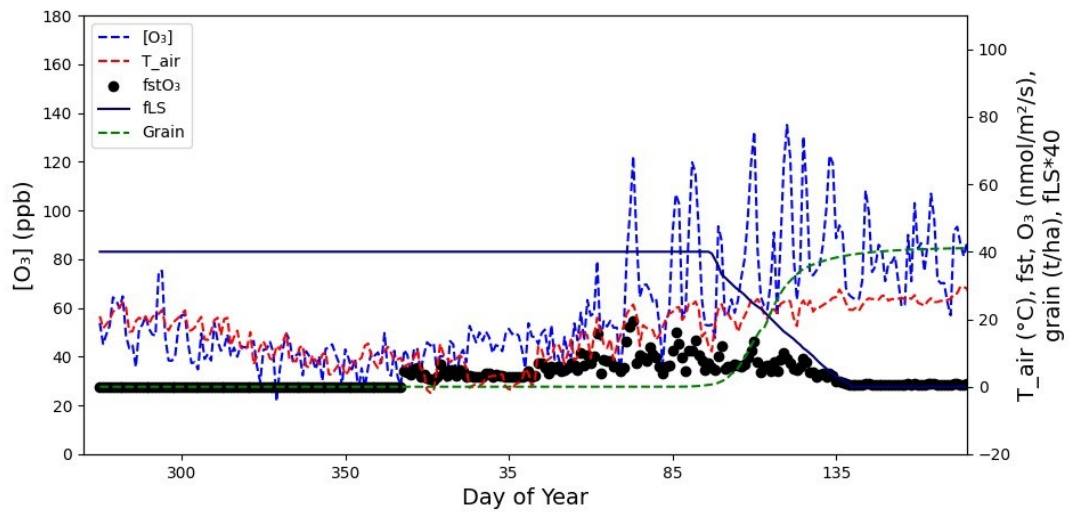


Fig. SI. 19. Comparison of (a). zone I (88\_186; with a medium absolute yield and an overestimated O<sub>3</sub> effect on yield) and (b). zone II (87\_245; with a high absolute yield and a substantial O<sub>3</sub> induced yield loss) for variables O<sub>3</sub>, Tair, f<sub>st</sub>, fLS and grain for the period of 1st Oct (Day of Year 274) to end of June (Day of Year 540).

a.



b.



## Thesis Discussion

### 5.1 Choice of $g_{sto}$ model for PODy estimates.

Numerous empirical and semi-empirical models have been developed to simulate  $g_{sto}$ . Among these, one of the earliest and most widely used is the multiplicative model proposed by Jarvis in 1976. This model reduces  $g_{sto}$  from its maximum potential based on observed responses to changing environmental conditions. Modifications to this model have added pollution as an environmental variable affecting  $g_{sto}$ . Multiplicative  $g_{sto}$  models have also been used to estimate other important plant processes such as evapotranspiration, land surface processes, and biogeochemical cycle simulations, as highlighted by (Yu et al., 2017). The multiplicative model's success stems from its ability to accurately simulate  $g_{sto}$  using a few driving environmental variables and its ease of parameterization, as noted in (Beeck et al., 2010). Furthermore, it has lower input requirements than more sophisticated  $g_{sto}$  models, such as the coupled  $A_{net}$   $g_{sto}$  model. The lower complexity of the multiplicative  $g_{sto}$  model supported its use in developing dose-response relationships and critical levels for a number of European crop species (i.e., wheat, potato, and tomato) (UNECE, 2017).

However, the multiplicative model has its limitations. As pointed out by Damour et al. (2010), it assumes that each environmental influence operates independently, which may only sometimes be accurate (especially in the case of temperature and vapour pressure deficit which are tightly coupled variables). Additionally, the model relies heavily on location and species-specific empirical data for parameterization. In regions with limited  $g_{sto}$  data, ensuring the multiplicative model gives robust  $g_{sto}$  estimates is challenging given differences in crop cultivar and crop growing conditions (which can be categorized by agro-ecological zones). (Yu et al., 2004) also criticized the approach for not considering physiological interactions or feedback that could alter stomatal movement. This results in a disconnect between estimates of  $g_{sto}$  and critical physiological processes such as  $A_{net}$ .

To address these limitations, research like that of Wong et al. in 1979 demonstrated that the current  $A_{net}$  rate directly regulates the stomatal aperture. This led to the development of semi-empirical coupled models that establish a linear relationship between  $A_{net}$  and  $g_{sto}$ , iterating to solve for both simultaneously. Beeck et al.

elaborated in 2010 that these models link  $g_{sto}$  and  $g_{sto}$  and simulate the effects of factors like O<sub>3</sub> damage on photosynthetic capacity.

The  $A_{net}g_{sto}$  model developed by Leuning (1995) is one such coupled model. In some studies, it has performed equally well as the multiplicative model, yet it is more complex due to its higher input requirements. For example, the  $A_{net}g_{sto}$  model used by Beeck et al. (2010) required 25 parameters, 20 of which were related to the  $A_{net}$  sub-model of (Farquhar et al., 1980), compared to only 12 for the Jarvis-type multiplicative model. However, (Beeck et al., 2010) also emphasized that if the multiplicative model were extended to include other important variables (e.g., CO<sub>2</sub>), this would increase the number of required parameters, potentially matching the complexity of the  $A_{net}g_{sto}$  models. Nonetheless, advancements in data acquisition methods like remote sensing data have made it easier to gather the data necessary to parameterise the  $A_{net}g_{sto}$  model, lessening the limitation of this model's higher input requirements. The coupling of the Leuning (1995)  $g_{sto}$  model to  $A_{net}$  has proven efficient and effective in predicting transpiration rates at various scales. This coupled  $A_{net}g_{sto}$  modelling approach has also been utilized in numerous models at the leaf and canopy levels and in regional and global earth system models.

Comparative studies evaluating the performance of the  $A_{net}g_{sto}$  models against multiplicative  $g_{sto}$  models have yielded mixed results. While some studies have found the  $A_{net}g_{sto}$  model superior ( $R^2= 0.71$  versus  $R^2 =0.65$ ; (Misson et al., 2004)), others suggest it is comparable or inferior in performance ( $R^2= 0.66$  versus  $R^2 =0.52$ ; (Uddling et al., 2005)). This range of outcomes suggests that the coupled  $A_{net}g_{sto}$  model could be a viable alternative for modelling  $g_{sto}$  for stomatal ozone flux calculations.

The DO<sub>3</sub>SE-crop model developed in this study, which incorporates the  $A_{net}g_{sto}$  model of Leuning (1995) and optional O<sub>3</sub> damage functions after (Ewert and Porter, 2000), provides further evidence that the  $A_{net}g_{sto}$  model can be used to provide reliable estimates of stomatal O<sub>3</sub> flux for use in the development of O<sub>3</sub> dose-response relationships (Pande et al. sub). The  $A_{net}g_{sto}$  mechanistic model was found to more accurately simulate daily and seasonal variations in  $A_{net}$  and  $g_{sto}$  when comparing against observations. This was particularly evident under varying O<sub>3</sub> treatments that were applied in the Bangor (UK) experimental fumigation, suggesting

the  $A_{net}g_{sto}$  models' superior effectiveness over the multiplicative models in these contexts. The fact that the  $A_{net}g_{sto}$  mechanistic model can be used to derive reliable dose-response relationships and critical levels makes it valuable for regional-scale risk assessments.

## 5.2 Ozone damage module: Does the DO<sub>3</sub>SE-crop model capture O<sub>3</sub> damage mechanisms correctly?

The primary impact of O<sub>3</sub> on wheat involves a reduction in  $A_{net}$ , primarily due to the enhancement of senescence. Ozone, entering the leaves through the stomata, is believed to quickly interact with the mesophyll cell wall's aqueous phase, generating highly reactive oxygen species (ROS). This oxidative stress often leads to observable effects such as accelerated senescence and leaf damage, which are detrimental to the plant. Chronic exposure to O<sub>3</sub> has been shown to reduce  $A_{net}$  and hasten senescence in two winter wheat varieties (Feng et al., 2012). In wheat crops, cultivars exhibited a reduction in green leaf area due to accelerated senescence, culminating in decreased grain yield (Burkart et al., 2013). The DO<sub>3</sub>SE-crop model integrates the effects of O<sub>3</sub> on the Rubisco enzyme by including modified functions (based on (Ewert and Porter, 2000)) for both instantaneous and long-term O<sub>3</sub> impacts on maximum carboxylation capacity ( $V_{cmax25}$ ), a key parameter that describes crop photosynthetic rate (Ewert and Porter, 2000; Osborne et al., 2019). The model revealed a more pronounced yield reduction due to long-term O<sub>3</sub> exposure, leading to earlier senescence of the flag leaf in high O<sub>3</sub> scenarios compared to low O<sub>3</sub> conditions (for example, senescence occurring 6 days earlier in very high peak (VHP) versus low background (LB) O<sub>3</sub> treatments in Bangor (UK); 7 days earlier in high (NF++) compared to carbon-filtered (CF) treatments in Ostad (Sweden), and 3-8 days earlier in Xiaoji (China) for tolerant and sensitive cultivars). The DO<sub>3</sub>SE-crop model also considers O<sub>3</sub> impacts on the end of senescence (i.e., can bring forward maturity). For example, the model estimated maturity to occur 12 days earlier in the VHP compared to the LB O<sub>3</sub> treatment in Bangor (UK) and 1-4 days earlier in the elevated o3 treatment in Xiaoji (China)). For the Xiaoji site, the DO<sub>3</sub>SE-crop model showed that relative yield loss is significantly higher due to long-term O<sub>3</sub> (2-36%) compared to the instantaneous impact of O<sub>3</sub> (0-0.02%) on  $A_{net}$ .

However, there are other mechanisms that might also be important in determining O<sub>3</sub> damage. Some studies have indicated additional, less anticipated effects of O<sub>3</sub> on

stomata. For instance, (Lombardozzi et al., 2012), in an open-top chamber experiment with tulip poplar, found that the rate of  $A_{net}$  declined more rapidly than  $g_{sto}$  under  $O_3$  exposure. This led to the hypothesis that  $O_3$  might cause a 'decoupling' between these two physiological processes. Given that  $A_{net}g_{sto}$  crop simulation and  $O_3$  effect modelling methods rely on the tight coupling between  $g_{sto}$  and  $A_{net}$ , this potential decoupling is a crucial factor for those engaged in applying and refining these models. Another observed impact of  $O_3$  on stomata, as identified in several experiments, is a delayed or 'sluggish' response by stomatal to environmental changes or stress, such as the slowed stomatal reaction to high light intensity in the Mediterranean broadleaf tree *Arbutus unedo* under chronic  $O_3$  exposure, as found by (Paoletti, 2005). Additionally, impaired stomatal response to drought conditions in grassland species has been documented, attributed to a decreased sensitivity to the plant hormone abscisic acid (ABA), posing a significant threat to plant resilience during water shortages, as suggested by (Wilkinson and Davies, 2010; Lim et al., 2015). Further research is necessary to determine if such impaired stomatal control due to  $O_3$  is also prevalent in crop species, and if so,  $A_{net}g_{sto}$  models would ideally be modified to incorporate this effect.

### 5.3 The importance of leaf vs. canopy stomatal $O_3$ uptake on the damage.

Traditionally, research has focused primarily on the canopy's top layer, particularly the flag leaf in wheat, as the part of the canopy that is most important in determining  $O_3$  damage from stomatal  $O_3$  uptake. This focus assumes that the flag leaf, positioned at the canopy's apex, is the most exposed to sunlight and  $O_3$  and also plays a pivotal role in providing photosynthate to the grain during the grain-filling phase (Pleijel et al., 2007). However, the significance of the  $O_3$  uptake to lower canopy leaves in causing damage should not be ignored. The  $DO_3SE$ -crop model structure provides a mechanism to explore this, given its ability to simulate  $O_3$  uptake by cumulative leaf area index layer accounting for changes in wind speed,  $O_3$  concentration, and irradiance with canopy height. It is posited that understanding the role that  $O_3$  plays in modifying leaf nitrogen content may be more important than overall yield, which is likely to be strongly related to those leaves that provide the bulk of the photosynthate. This suggests a shift from traditional yield-centric evaluations of agricultural success towards a more nuanced understanding of crop health, particularly in terms of leaf nitrogen content which is essential for

photosynthesis and overall vitality. Such a perspective underscores the importance of considering the effects of O<sub>3</sub> not just on the yield-contributing upper canopy leaves but also on the lower canopy leaves. These lower leaves, though not directly contributing to yield, are integral to the plant's overall development and resilience against environmental stressors like O<sub>3</sub> pollution, thus highlighting the complex interplay between environmental factors and crop physiology. For example, Brewster et al. (2024) observed that higher O<sub>3</sub> levels and leaf aging caused more harm to the second, third, and fourth leaves during anthesis and the early grain-filling stage in comparison to the flag leaf. A study also reported significant visible damage to the lower leaf layers in two wheat varieties after three days of increased O<sub>3</sub> exposure following anthesis. Other research assessed the impact of O<sub>3</sub> on  $A_{net}$  efficiency, utilizing Fv/Fm chlorophyll fluorescence measurements at the ear emergence stage in the flag, second, third, and fourth leaves and found reductions in chlorophyll levels and, as a result, reduction in photosynthetic capacity (Soja, 1995). Whole canopy  $A_{net}$  determines grain yields: in both laminar and non-laminar organs, throughout all growth stages (Araus et al., 2021). Therefore, these findings underscore the importance of considering O<sub>3</sub> uptake and potential effects on all leaf cohorts in crop modelling, as focusing solely on the flag leaf data can conceal the effects of O<sub>3</sub> on overall canopy chlorophyll levels and canopy-wide carbon/nitrogen assimilation.

In this context, the DO<sub>3</sub>SE crop model, which is set up to allow the modelling of multiple leaf populations and canopy layers, offers the flexibility to investigate the variability in stomatal O<sub>3</sub> uptake over the crop growing season and across the crop canopy. The DO<sub>3</sub>SE-crop model has proven effective in simulating various factors across these dimensions, such as the reduction in photosynthetically active radiation (PAR) with canopy depth and the associated reduction in  $A_{net}$  (which reduces from around 300 to 20  $\mu\text{mol O}_3 \text{ m}^{-2} \text{ s}^{-1}$  between canopy layers), and  $g_{sto}$  (also reducing from about 300 to 20  $\text{nmol O}_3 \text{ m}^{-2} \text{ s}^{-1}$  between layers), in different wheat canopy layers. Thus, the availability of models like DO<sub>3</sub>SE-crop enables a more nuanced exploration of the dynamics of O<sub>3</sub> damage across different wheat canopy layers, which could be complemented with targeted experimental studies.

Perhaps more importantly, this structure also allows the variability in stomatal (and non-stomatal) deposition that occurs across the growing season as canopy height varies and across the canopy depth to be estimated. This should improve O<sub>3</sub>

deposition estimates that are an important component of atmospheric chemistry models which are used to estimate the mass balance of O<sub>3</sub> concentrations remaining the atmosphere after deposition to the vegetation sink (Clifton et al., 2020).

#### 5.4 Model Calibration - Manual vs. Automated Methods.

Calibration plays a crucial role in the modelling process, as it aligns numerical model results with real-world data, ensuring their reliability in various applications (Wallach et al., 2021). This process is standard across diverse fields that rely on process-based models, such as hydrology (Badham et al., 2019), pest and disease dynamics (Donatelli et al., 2017), and agriculture (Seidel et al., 2018). Model calibration typically involves fine-tuning parameters to minimize the discrepancy between model outputs and empirical data. In crop modelling, calibration is often performed manually through trial and error, as noted by (Seidel et al., 2018). While potentially more time-consuming and labour-intensive than automated methods, this manual approach offers greater control and insight into the model's workings and the interplay of its parameters. Manual calibration is instrumental in complex systems where automated algorithms are unable to grasp intricate details of the model construct and feedback.

Our studies with the DO<sub>3</sub>SE-Crop model began using automated calibration while adjusting the DO<sub>3</sub>SE-crop model at the leaf level, as detailed in section 3.6.2.

Initially, we identified key parameters ( $V_{cmax25}$ ,  $J_{max25}$ , and  $m$ ) from literature since only a few experimental studies (e.g., Bangor (UK) and Xiaoji (China)) provided observational data. We also employed the 'breakpoint method' (Mariën et al., 2019) to determine the onset and conclusion of senescence more objectively from observed chlorophyll content data. However, as the model's complexity increased from a single leaf to the entire canopy, we noticed that the automated calibration sometimes failed to capture all nuances of the model system. For instance, issues such as unrealistically high yield predictions for very low Leaf Area Index (LAI) and low grain dry matter for stems and leaves emerged. We attempted to address this issue by focussing the automated calibration on the Leaf Area Index (LAI), which succeeded in aligning LAI values within a more plausible range of 3-6 m<sup>2</sup> m<sup>-2</sup>.

However, this adjustment did not resolve discrepancies in the magnitudes of other canopy components. These discrepancies in obtaining an overall balanced crop architecture necessitated the reversion to manual calibration to align the model with realistic values from the literature and available experimental data.

As mentioned in section 3.6.2, an essential aspect of calibration of the DO<sub>3</sub>SE-crop model is deciding which observed variables to include in the best-fit criteria used to train the model. From a modelling perspective, incorporating a broad range of variables for calibration decreases the likelihood of achieving accurate results for some variables while misrepresenting others crucial for understanding the system's behaviour (Wallach et al., 2021). An additional challenge is potential errors in the observed data, which can complicate the calibration process; the availability of more experimental and observed data would go a long way to overcome these problems but requires far more resources to be targeted to experimental investigation.

This study faced a similar limitation regarding the need for more observed datasets. For instance, parameters related to leaf physiology, such as  $A_{net}$ ,  $g_{sto}$ ,  $V_{cmax25}$ ,  $J_{max25}$ , and CCI data, were only available from a location in Bangor (UK), and Xiaoji (China), the site in Ostad (Sweden) provided data only for CCI data. These data were limited to the flag leaf and for a period spanning mid-anthesis to ten days pre-maturity. Although the Bangor (UK) site provides hourly data for these critical parameters, only daily data are available from Xiaoji (China). This restricts our ability to validate the DO<sub>3</sub>SE-crop model's diurnal  $g_{sto}$  and  $A_{net}$  predictions, hampering efforts to enhance model robustness. However, the Bangor (UK) dataset, which did provide hourly flag leaf data, indicates effective model performance in capturing diurnal variations.

Another issue is the sparse data on dry matter content across various plant parts, such as stem, leaves (green and brown), and roots, from both the literature as well as the experimental studies explored here (i.e., there was no availability of dry matter content data from the Xiaoji study for which the DO<sub>3</sub>SE-crop canopy model is calibrated). This necessitates reliance on data collected from studies conducted in different regions (and likely agro-ecological zones), posing a challenge in creating robust parameterisations for particular growing conditions. Comprehensive data from a single site would increase model robustness for that site, but data describing variability in key parameters by agro-ecological zone is required to calibrate or test the model under a range of growth conditions (see section 1.5).

Furthermore, this study examines the impact of O<sub>3</sub> on wheat yield, noting O<sub>3</sub>-induced early senescence and potentially earlier maturity as the key reasons for the significant decrease in yield under elevated O<sub>3</sub> treatments. Here, chlorophyll

concentration index (CCI) data from some of the experimental studies are crucial to track the timing and extent of senescence. However, only 11, 13, and 7 CCI data points are provided for O<sub>3</sub> treatments in Bangor (UK), Ostad (Sweden), and Xiaoji (China), respectively. In addition, these limited data only cover a brief phase of wheat growth (mid-anthesis to ten days before maturity). More evenly distributed CCI data across the critical growth period would significantly enhance our understanding of the effect of O<sub>3</sub> on wheat senescence and maturity.

### 5.5 AEZs and Cultivar-Specific Parametrization

Scaling the model from a site-specific application to a regional or global level results in an observed increase in calibration error. This issue is partly due to the limited number of coordinated O<sub>3</sub> experimental (or even other types of crop physiology and crop growth) studies across different climatic regions, especially in countries like China. Accurately modelling crop dynamics requires precise phenology, leaf physiology, and canopy structure data. However, obtaining robust data from the literature is challenging because environmental conditions that influence crop growth such as temperature, atmospheric humidity and O<sub>3</sub> levels vary across different geographical zones. These zones may also have a range of crop cultivars (suited to particular climatic conditions) with varying levels of O<sub>3</sub> sensitivity, from highly sensitive to tolerant or intermediate. Unfortunately, acquiring comprehensive experimental data sets for robust modelling may take many years of coordinated research. To address this challenge, there's a need for the design of standardized experimental and O<sub>3</sub> fumigation protocols which would be designed to ensure the collection of data that O<sub>3</sub> risk assessment models require. Modellers have attempted to bridge this gap by employing satellite imagery and crop statistics, mainly for assessing phenology and yield (Luo et al., 2020; Yu et al., 2020) but more recently to relate changes in NPP to O<sub>3</sub> concentration (Yue et al., 2017). For instance, a 1 km gridded crop phenological dataset for three crops, including wheat, from 2000-2015 has been produced based on the Global Land Surface Satellite (GLASS) LAI products, called ChinaCropPhen1km (Luo et al., 2020). For yield, the SPAM database products globally gridded maps of agricultural production at an 8.88 km resolution. We have used results from (Luo et al., 2020), which describe differences in developmental stages in the key AEZs across China. Such datasets have shown how phenology and yields vary across regions and therefore emphasise the need to

calibrate models to produce AEZ specific parametrisations as well as O<sub>3</sub> cultivar sensitivity parameterisations that take into account the variation in cultivars within and across AEZs. For the latter, we explore the possibility of defining tolerant, intermediate, and sensitive cultivars that might be used in the future to assess the uncertainty in O<sub>3</sub> risk assessments.

The DO<sub>3</sub>SE-crop model has been calibrated for winter wheat crops in four distinct Agro-Ecological Zones (AEZs) across China to enable the estimation of key phenological stages with improved accuracy. This calibration aligns with the gridded phenology outputs presented by Lu et al. (2020), i.e., within a 2.5-week margin of the observed data. The model is simultaneously calibrated for yield by changing the carbon allocation coefficients so that the modelled yield values match the observed SPAM yields. In crops such as wheat, the allocation of carbon to different plant parts is significantly influenced by the crop's phenological stages, including emergence, vegetative, and reproductive phases. For example, during the early season, particularly the emergence and vegetative stages, a greater proportion of carbon is allocated to the leaves and stems to support growth. However, as the plant transitions into the reproductive stage, the focus of carbon allocation shifts towards the grains. Therefore, the calibration of these allocation coefficients is crucial to ensure that crop models accurately reflect these dynamic changes throughout the growing season (Osborne et al., 2015). In China, given the variability in phenology across the four agro-ecological zones, the calibration of carbon allocation parameters is particularly essential to capture regional differences in crop development accurately.

The DO<sub>3</sub>SE-crop model can simulate the key stages of phenology within a range of that observed (see Fig. SI. 13, section 4.4.3). Accurate representation of these stages is essential; inaccuracies could cause significant errors in the timing of the O<sub>3</sub>-sensitive crop growth period in relation to the prevailing O<sub>3</sub> concentrations that would adversely affect the estimates of relative yield losses due to O<sub>3</sub>. For example, a 10-day discrepancy in the anthesis stage, coinciding with peak O<sub>3</sub> levels, could lead to overstated or understated yield loss predictions. This issue is particularly relevant as the grain-filling phase in wheat often overlaps with periods when high O<sub>3</sub> concentrations are experienced across China. Understanding these dynamics is

crucial for effective agronomic management, particularly in mitigating impacts from O<sub>3</sub> episodes (Teixeira et al., 2013).

However, the DO<sub>3</sub>SE-Crop model performance in yield prediction, when plotted against SPAM yield data, reveals both strengths and weaknesses. While the model successfully captures the variation in yield across different AEZs, a noticeable deviation in accuracy is indicated by an RMSE of 164, see Fig. 20. This figure implies that, on average, the model's yield predictions deviate from actual values by  $\pm 164$  g/m<sup>2</sup>. Further, the accuracy range of mean yield by AEZ is  $\pm 84$  g/m<sup>2</sup>, see Fig. Sl. 15. Recognizing this discrepancy opens up avenues for further refinement. The model can be fine-tuned by undergoing additional calibration to enhance its predictive accuracy. Such calibration would aim to bring the data points closer to the ideal 1:1 line, thereby reducing the RMSE. This step is crucial for improving the model's reliability and precision in yield prediction, ultimately contributing to a more robust and dependable agricultural forecasting tool.

Furthermore, various crop models have also been used to forecast global wheat yield losses due to future projected O<sub>3</sub> concentrations, but only a select few, including LINTULCC-2, have included the distinct responses of O<sub>3</sub>-tolerant and sensitive wheat genotypes (Feng et al., 2022). Research indicates that different wheat cultivars exhibit unique reactions to O<sub>3</sub>, evidenced by alterations in both enzymatic and non-enzymatic antioxidants, impacting various physiological aspects and overall yield. For example, in the O<sub>3</sub>-tolerant cultivar Kharchiya 65, levels of antioxidative metabolites like abscisic acid (AsA), total thiol (both non-protein and protein), and glutathione (GSH) were significantly higher under elevated O<sub>3</sub> stress compared to cultivars with sensitive or intermediate sensitivity (Fatima et al., 2019). This genetic variability lays the groundwork for developing wheat varieties with enhanced O<sub>3</sub> tolerance, which could be crucial in reducing yield losses and securing a consistent food supply. At the moment, DO<sub>3</sub>SE-crop model estimates of cultivar sensitivity are all based on empirical data, but there may be opportunities in the future to model this based on studies that have tried to identify the key processes and traits involved in O<sub>3</sub> detoxification (e.g. (Roberts et al., 2022))

The DO<sub>3</sub>SE-crop model provides a model structure that has the capacity to be parameterized for wheat cultivars with differential sensitivity to O<sub>3</sub> in terms of O<sub>3</sub> uptake, carbon allocation and  $A_{net}$  and senescence ozone damage mechanisms. In

this study, the model effectively simulates the variance in grain yield between the ambient and elevated O<sub>3</sub> treatments and cultivars. DO<sub>3</sub>SE-Crop estimates a decrease in grain yield of 29 and 131 g/m<sup>2</sup>, which aligns closely with the observed reductions of 81 and 165 g/m<sup>2</sup> for the tolerant cultivars. Similarly, for the sensitive cultivars, the model predicts reductions of 49 and 196 g/m<sup>2</sup>, which are close to the observed values of 54 and 293 g/m<sup>2</sup>, respectively. Additional calibration data for different wheat cultivars, growing under a wider range of environmental conditions, would allow improved model calibration as well as the capabilities of the model to be further tested.

## 5.6 Future work

The DO<sub>3</sub>SE-crop model is still a relatively immature crop model and will benefit from further calibration and testing across different global regions and AEZs. This will help to define a more focussed range of key parameters for calibration that will result in the correct plant structure (e.g., ensuring LAI, biomass of different crop components (i.e., leaves, roots, stem), and yields are aligned. For example, refining and applying the DO<sub>3</sub>SE-crop model for different AEZs across China requires a multifaceted approach, beginning with further calibration to understand how variations in the LAI influence crop yields. The current DO<sub>3</sub>SE-crop estimated LAI values for different AEZs range between 2-4 m<sup>2</sup>/m<sup>2</sup>; these align with literature describing LAI in the zone II AEZ but are lower than minimum LAI values observed in zones I and IV. The DO<sub>3</sub>SE-crop model could then benefit from more efficient automated calibration having established a more restrictive LAI range tailored explicitly for Chinese AEZs, thereby reducing the time needed for calibration iterations. Another aspect of this process involves adjusting leaf physiology parameters such as  $V_{cmax25}$  and  $J_{max25}$ , which are currently fixed based on data from Xiaoji, China. Recognizing that these parameters most likely vary with temperature and light, it is imperative to account for these variations across different AEZs.

The DO<sub>3</sub>SE-Crop model also can model the influence of soil water stress on crop growth, yield, and O<sub>3</sub> damage (Nguyen et al., 2024). In this study, we have concentrated on assessing the O<sub>3</sub> effect on irrigated, highly productive winter wheat since this is the most important wheat for food supply across China (Ma et al., 2021) and also allows easier assessment of the ability of the model to simulate growth and yield in the absence of additional stressors, of which soil water stress is key

especially in the Northern part of China (Liang et al., 2016). Once we are confident that DO<sub>3</sub>SE-Crop is giving reliable results under more optimum conditions for crop growth and yield, it will be interesting to use the model to explore the extent to which different key abiotic stressors (i.e., soil water and temperature stress) compare with O<sub>3</sub> stress to understand which environmental conditions might enhance, or reduce, O<sub>3</sub> impacts. This will realise one of the key benefits to the development and application of crop models over more empirical O<sub>3</sub> risk assessments performed using dose-response relationships (Emberson et al., 2018).

Moving forward, the DO<sub>3</sub>SE-crop model's capability to simulate the effect of O<sub>3</sub> under future emission scenarios and associated projections of O<sub>3</sub> concentration could play an important role in proactive environmental management and policy development. For instance, simulations of O<sub>3</sub> concentrations for the 2030s, using the WRF-Chem model under the SSP3-7.0 emission scenario, planned for 2024, will provide valuable insights into the potential impact of O<sub>3</sub> concentrations and how these relate to emission pathways and potential emission reductions.

### 5.7 Policy recommendations

There are essentially two approaches to alleviating the adverse effects of O<sub>3</sub> pollution on crop growth and yield. First, mitigation of O<sub>3</sub> precursor emissions that reduce O<sub>3</sub> concentrations and hence crop exposure to harmful O<sub>3</sub> concentrations. The second is in developing adaptation approaches that might reduce the impact of O<sub>3</sub> concentrations on crops. The DO<sub>3</sub>SE-crop model has the potential to support the development of both approaches.

In terms of mitigation, DO<sub>3</sub>SE-Crop could be applied nationally, regionally, or globally (given appropriate calibration for application at these different scales) to assess both the current and potential future (in combination with emission projections and the modelling of atmospheric chemistry) impacts of O<sub>3</sub> on crop yields. This would help identify the regions and environmental conditions that enhance O<sub>3</sub> risk. Such information would potentially be useful for policymakers to develop effects-based emission reduction strategies (similar to those supported by the UNECE LRTAP Convention (Emberson, 2020)). Useful approaches to utilise this aspect of the DO<sub>3</sub>SE-Crop model include model ensemble methods whereby a number of crop models (that also include O<sub>3</sub> damage functions) can be applied to standardised current and projected future estimates of changing O<sub>3</sub> and climate variables so that

mean model results, which are arguably more robust, can be used to inform policy. Such crop model ensemble studies are planned within the AgMIP-ozone activity (Emberson et al., 2018). The ability of DO<sub>3</sub>SE-Crop to simulate damage for a range of cultivar sensitivities to O<sub>3</sub> will contribute to an assessment of the uncertainties of this type of risk assessment modelling.

In terms of adaptation, the DO<sub>3</sub>SE-crop model could be useful in developing adaptation options for agricultural management. For example, recent studies have shifted focus toward the effect of sowing times and early vs. late maturing varieties on improving wheat yields under stresses (especially temperature stress) since these management options can produce growing seasons that avoid periods of extreme stress. Similar stress avoidance can occur for O<sub>3</sub> exposures since high temperatures coincide with high O<sub>3</sub> concentrations that occur towards the grain-filling part of the crop growth period. A good example of the benefit this can afford to reduce O<sub>3</sub> impacts is given by the study of (Yadav et al., 2020), which investigated the effects of early and late sowing on wheat cultivars under ambient and elevated O<sub>3</sub> levels. The study found that early-sown cultivars exhibited a more robust defensive response and less grain yield loss than their late-sown counterparts, attributed to a more pronounced increase in enzymatic and non-enzymatic antioxidants in the early-sown varieties.

The versatility of the DO<sub>3</sub>SE-crop model is further highlighted by its capacity to simulate the effects of varying sowing dates on wheat crop yields. This feature is pivotal in understanding the underlying reasons for yield variances, such as the alignment of the anthesis and grain filling period with high O<sub>3</sub> concentrations. The insights gained from this model regarding cultivar-specific parametrization and sowing time flexibility may be useful in developing adaptation options for arable crop management. Importantly, the model's comprehensive approach to considering multiple stresses extends to resource management, providing guidance on optimizing irrigation schedules. This ensures that irrigation schedules are monitored and applied at critical growth stages to maximize efficiency and support crop development under varying environmental conditions. Such detailed insights will also offer strategies for adapting to climate change, encompassing a holistic approach to improving resilience and sustainability in crop production.

Finally, components of the DO<sub>3</sub>SE-crop model could be used in the development of more mechanistic dose-response relationships (in place of dose-response relationships that rely on the multiplicative  $A_{net}$  model). This may help to develop relationships that are more suitable for application across different climatic regions as the  $A_{net}g_{sto}$  model detailed approach can offer efficient and nuanced insights into leaf-level physiological processes. This advancement is particularly significant as it could lead to the establishment of air quality guidelines (AQGs), especially for regions like China and other Asian countries. These AQGs could serve as benchmarks to determine thresholds below which crop damage is not anticipated and provide a scientific foundation for establishing safety standards, regulatory limits, and intervention thresholds, thereby contributing significantly to sustainable agriculture, environmental protection, along with co-benefits for human health and climate change (Emberson, 2020)

In this thesis, the intricacies of the DO<sub>3</sub>SE-crop model were explored, underscoring its pivotal role in advancing our understanding of the interplay between ozone pollution and crop growth and yield, particularly in the context of China's diverse agro-ecological zones (AEZs). Through rigorous calibration and testing, this research has highlighted the model's potential to offer nuanced insights into crop responses under varying environmental stressors, laying a foundational framework for mitigating ozone's adverse effects and enhancing agricultural resilience through informed adaptation strategies.

This thesis underscored the critical need for further refinement of the model, particularly in parameter calibration across different AEZs, to ensure accuracy in predicting crop outcomes. This refinement, coupled with the model's capacity to simulate the impacts of soil water stress and the effects of future ozone emission scenarios, provides an invaluable tool for proactive environmental management and policy formulation. By aligning model simulations with future emission trajectories, this work sets the stage for informed decision-making that could significantly mitigate the risks associated with ozone pollution on vital food crops, thereby enhancing food security.

The policy recommendations derived from the findings of this thesis advocate for a dual approach, emphasizing both emission mitigation and the development of adaptive agricultural practices. By harnessing the unique capabilities of the DO<sub>3</sub>SE-

crop model, policymakers and stakeholders can devise strategies that address the immediate challenges posed by ozone pollution and contribute to the long-term sustainability of agricultural systems in the face of climatic uncertainties. This underscores the model's role as a practical tool in guiding policy decisions.

In conclusion, this thesis represents a significant step forward in our collective efforts to safeguard food security against environmental challenges. The continued development and application of the DO3SE-crop model stand as a testament to the potential of scientific innovation in bridging the gap between research and practical, policy-oriented solutions. As we progress, the insights garnered from this work will undoubtedly play a crucial role in shaping a more resilient and sustainable agricultural future.

## References

- Ainsworth, E. A. *et al.* (2012) 'The Effects of Tropospheric Ozone on Net Primary Productivity and Implications for Climate Change \*', *Annu. Rev. Plant Biol*, 63, pp. 637-661. doi: 10.1146/annurev-arplant-042110-103829.
- Akagi, S. K. *et al.* (2011) 'Emission factors for open and domestic biomass burning for use in atmospheric models', *Atmospheric Chemistry and Physics*, 11(9), pp. 4039-4072. doi: 10.5194/acp-11-4039-2011.
- Andreae, M. O. (2019) 'Emission of trace gases and aerosols from biomass burning - An updated assessment', *Atmospheric Chemistry and Physics*, 19(13), pp. 8523-8546. doi: 10.5194/acp-19-8523-2019.
- Araus, J. L., Sanchez-Bragado, R. and Vicente, R. (2021) 'Improving crop yield and resilience through optimization of photosynthesis: Panacea or pipe dream?', *Journal of Experimental Botany*, 72(11), pp. 3936-3955. doi: 10.1093/jxb/erab097.
- Archibald, A. T. *et al.* (2020) 'Tropospheric ozone assessment report: A critical review of changes in the tropospheric ozone burden and budget from 1850 to 2100', *Elementa*, 8(1), pp. 1-53. doi: 10.1525/elementa.2020.034.
- Asseng, S. *et al.* (2015) 'Rising temperatures reduce global wheat production', *Nature Climate Change*, 5(2), pp. 143-147. doi: 10.1038/nclimate2470.
- Avnery, S. *et al.* (2011) 'Global crop yield reductions due to surface ozone exposure: 2. Year 2030 potential crop production losses and economic damage under two scenarios of O<sub>3</sub> pollution', *Atmospheric Environment*. Elsevier Ltd, 45(13), pp. 2297-2309. doi: 10.1016/j.atmosenv.2011.01.002.
- Badham, J. *et al.* (2019) 'Effective modeling for Integrated Water Resource Management: A guide to contextual practices by phases and steps and future opportunities', *Environmental Modelling & Software*. Elsevier, 116, pp. 40-56. doi: 10.1016/J.ENVSOF.2019.02.013.
- Barten, J. G. M. *et al.* (2021) 'Role of oceanic ozone deposition in explaining temporal variability in surface ozone at High Arctic sites', *Atmospheric Chemistry and Physics*, 21(13), pp. 10229-10248. doi: 10.5194/acp-21-10229-2021.
- Op De Beeck, M. *et al.* (2010) 'A comparison of two stomatal conductance models for ozone flux modelling using data from two Brassica species', *Environmental Pollution*. Elsevier Ltd, 158(10), pp. 3251-3260. doi: 10.1016/j.envpol.2010.07.026.
- Bender, J., Hertstein, U. and Black, C. R. (1999) 'Growth and yield responses of spring wheat to increasing carbon dioxide, ozone and physiological stresses: A statistical analysis of "ESPACE-wheat" results', *European Journal of Agronomy*. Elsevier, 10(3-4), pp. 185-195. doi: 10.1016/S1161-0301(99)00009-X.
- Betzberger, A. M. *et al.* (2012) 'Ozone exposure response for U.S. soybean cultivars: Linear reductions in photosynthetic potential, biomass, and yield', *Plant Physiology*. American Society of Plant Biologists, 160(4), pp. 1827-1839. doi: 10.1104/pp.112.205591.
- Biswas, D. K., Xu, H., Li, Y. G., *et al.* (2008) 'Assessing the genetic relatedness of higher ozone sensitivity of modern wheat to its wild and cultivated

progenitors/relatives', *Journal of experimental botany*. J Exp Bot, 59(4), pp. 951-963. doi: 10.1093/JXB/ERN022.

Biswas, D. K., Xu, H., Li, Yong Ging, *et al.* (2008) 'Genotypic differences in leaf biochemical, physiological and growth responses to ozone in 20 winter wheat cultivars released over the past 60 years', *Global Change Biology*, 14(1), pp. 46-59. doi: 10.1111/j.1365-2486.2007.01477.x.

Biswas, D. K. *et al.* (2013) 'Modification of photosynthesis and growth responses to elevated CO<sub>2</sub> by ozone in two cultivars of winter wheat with different years of release', *Journal of Experimental Botany*, 64(6), pp. 1485-1496. doi: 10.1093/jxb/ert005.

Boleti, E. *et al.* (2020) 'Temporal and spatial analysis of ozone concentrations in Europe based on timescale decomposition and a multi-clustering approach', *Atmospheric Chemistry and Physics*, 20(14), pp. 9051-9066. doi: 10.5194/acp-20-9051-2020.

Brás, T. A. *et al.* (2021) 'Severity of drought and heatwave crop losses tripled over the last five decades in Europe', *Environmental Research Letters*, 16(6). doi: 10.1088/1748-9326/abf004.

Brewster, C., Fenner, N. and Hayes, F. (2024) 'Chronic ozone exposure affects nitrogen remobilization in wheat at key growth stages', *Science of The Total Environment*. Elsevier B.V., 908(August 2023), p. 168288. doi: 10.1016/j.scitotenv.2023.168288.

Brewster, C., Hayes, F. and Fenner, N. (2019) 'Ozone Tolerance Found in *Aegilops tauschii* and Primary Synthetic Hexaploid Wheat', *Plants 2019, Vol. 8, Page 195*. Multidisciplinary Digital Publishing Institute, 8(7), p. 195. doi: 10.3390/PLANTS8070195.

Broberg, M. C. *et al.* (2015) 'Ozone effects on wheat grain quality - A summary', *Environmental Pollution*. Elsevier Ltd, 197(January), pp. 203-213. doi: 10.1016/j.envpol.2014.12.009.

Buchner, P. *et al.* (2015) 'Expression patterns of C- and N-metabolism related genes in wheat are changed during senescence under elevated CO<sub>2</sub> in dry-land agriculture', *Plant Science*. Elsevier Ireland Ltd, 236, pp. 239-249. doi: 10.1016/j.plantsci.2015.04.006.

Büker, P. *et al.* (2007) 'Comparison of different stomatal conductance algorithms for ozone flux modelling', *Environmental Pollution*, 146(3), pp. 726-735. doi: 10.1016/j.envpol.2006.04.007.

Büker, P. *et al.* (2012) 'DO 3SE modelling of soil moisture to determine ozone flux to forest trees', *Atmospheric Chemistry and Physics*, 12(12), pp. 5537-5562. doi: 10.5194/acp-12-5537-2012.

Buriro, M. *et al.* (2011) 'Wheat Seed Germination Under the Influence of Temperature Regimes', *Sarhad J. Agric.*, 27(4), pp. 539-543. Available at: <https://www.researchgate.net/publication/266463463>.

Burkart, S. *et al.* (2013) 'Effects of Ozone on Leaf Senescence, Photochemical Efficiency and Grain Yield in Two Winter Wheat Cultivars', *Journal of Agronomy and Crop Science*, 199(4), pp. 275-285. doi: 10.1111/jac.12013.

- Campbell, G.S., Norman, J. M. (1998) *An introduction to Environmental Biophysics*. Second. Springer.
- Challinor, A. J. *et al.* (2014) 'A meta-analysis of crop yield under climate change and adaptation', *Nature Climate Change*, 4(4), pp. 287-291. doi: 10.1038/nclimate2153.
- Chang, K.-L. *et al.* (2017) 'Regional trend analysis of surface ozone observations from monitoring networks in eastern North America, Europe and East Asia', *Elem Sci Anth*. University of California Press, 5(0), p. 50. doi: 10.1525/elementa.243.
- Chen, F., Wang, M. and Pu, Z. (2022) 'The impact of technological innovation on air pollution: Firm-level evidence from China', *Technological Forecasting & Social Change*, 177, p. 121521. doi: 10.1016/j.techfore.2022.121521.
- Chen, S. *et al.* (2020) 'Spatiotemporal dynamics of the northern limit of winter wheat in China using MODIS time series images', *Remote Sensing*, 12(15). doi: 10.3390/RS12152382.
- Chen, Y. *et al.* (2016) 'Identifying the impact of multi-hazards on crop yield-A case for heat stress and dry stress on winter wheat yield in northern China', *European Journal of Agronomy*. Elsevier B.V., 73, pp. 55-63. doi: 10.1016/j.eja.2015.10.009.
- Chutteang, C. *et al.* (2016) 'Biochemical and physiological processes associated with the differential ozone response in ozone-tolerant and sensitive soybean genotypes', *Plant biology (Stuttgart, Germany)*. Plant Biol (Stuttg), 18 Suppl 1, pp. 28-36. doi: 10.1111/PLB.12347.
- Clark, D. B. *et al.* (2011) 'The Joint UK Land Environment Simulator (JULES), model description - Part 2: Carbon fluxes and vegetation dynamics', *Geoscientific Model Development*, 4(3), pp. 701-722. doi: 10.5194/gmd-4-701-2011.
- Clifton, O. E. *et al.* (2020) 'Dry Deposition of Ozone Over Land: Processes, Measurement, and Modeling', *Reviews of Geophysics*, 58(1). doi: 10.1029/2019RG000670.
- Cooper, O. R. *et al.* (2014) 'Global distribution and trends of tropospheric ozone: An observation-based review', *Elementa*, 2, pp. 1-28. doi: 10.12952/journal.elementa.000029.
- Danielsson, H. *et al.* (2003) 'Ozone uptake modelling and flux-response relationships - An assessment of ozone-induced yield loss in spring wheat', *Atmospheric Environment*. Pergamon, 37(4), pp. 475-485. doi: 10.1016/S1352-2310(02)00924-X.
- Derwent, R. G. *et al.* (2004) 'Intercontinental transport and the origins of the ozone observed at surface sites in Europe', *Atmospheric Environment*. Pergamon, 38(13), pp. 1891-1901. doi: 10.1016/J.ATMOENV.2004.01.008.
- Emberson, L.D., Ashmore, M.R., Simpson, D., Tuovinen, J.-P. and Cambridge, H. M. (2001) 'Modelling and mapping ozone deposition in Europe', *Water, Air and Soil Pollution*, pp. 577-582.
- Emberson, L. (2020a) 'Effects of ozone on agriculture, forests and grasslands: Improving risk assessment methods for O<sub>3</sub>', *Philosophical Transactions of the Royal Society A: Mathematical, Physical and Engineering Sciences*, 378(2183). doi: 10.1098/rsta.2019.0327.
- Emberson, L. (2020b) 'Effects of ozone on agriculture, forests and grasslands',

- Philosophical Transactions of the Royal Society A: Mathematical, Physical and Engineering Sciences*. The Royal Society Publishing, 378(2183), p. 20190327. doi: 10.1098/rsta.2019.0327.
- Emberson, L. D. *et al.* (2000) 'Modelling stomatal ozone flux across Europe', *Environmental Pollution*, 109(3), pp. 403-413. doi: 10.1016/S0269-7491(00)00043-9.
- Emberson, L. D. *et al.* (2018) 'Ozone effects on crops and consideration in crop models', *European Journal of Agronomy*. Elsevier, 100(May), pp. 19-34. doi: 10.1016/j.eja.2018.06.002.
- Emmons, L. K. *et al.* (2010) 'Description and evaluation of the Model for Ozone and Related chemical Tracers, version 4 (MOZART-4)', *Geoscientific Model Development*, 3(1), pp. 43-67. doi: 10.5194/gmd-3-43-2010.
- Ewert, F., Van Oijen, M. and Porter, J. R. (1999) 'Simulation of growth and development processes of spring wheat in response to CO<sub>2</sub> and ozone for different sites and years in Europe using mechanistic crop simulation models', *European Journal of Agronomy*. Elsevier, 10(3-4), pp. 231-247. doi: 10.1016/S1161-0301(99)00013-1.
- Ewert, F. and Porter, J. R. (2000) 'Ozone effects on wheat in relation to CO<sub>2</sub>: Modelling short-term and long-term responses of leaf photosynthesis and leaf duration', *Global Change Biology*, 6(7), pp. 735-750. doi: 10.1046/j.1365-2486.2000.00351.x.
- Farage, P. K. *et al.* (1991) 'The sequence of change within the photosynthetic apparatus of wheat following short-term exposure to ozone', *Plant Physiology*, 95(2), pp. 529-535. doi: 10.1104/pp.95.2.529.
- Farquhar, G.D., von Caemmerer, S., Berry, J. A. (1980) 'A biochemical model of photosynthetic CO<sub>2</sub> assimilation in leaves of C<sub>3</sub> species', *Planta*, 149, pp. 78-90.
- Farquhar, G. D., Caemmerer, S. and Berry, J. A. (1980) 'A biochemical model of photosynthetic CO<sub>2</sub> assimilation in leaves of C<sub>3</sub> species', *Planta*, 149(1), pp. 78-90-90. Available at: <http://dx.doi.org/10.1007/BF00386231>.
- Fatima, A. *et al.* (2019) 'Assessment of ozone sensitivity in three wheat cultivars using ethylenediurea', *Plants*. MDPI AG, 8(4). doi: 10.3390/plants8040080.
- Feng, Y. *et al.* (2022) 'Identifying and modelling key physiological traits that confer tolerance or sensitivity to ozone in winter wheat', *Environmental Pollution*. Elsevier Ltd, 304(April), p. 119251. doi: 10.1016/j.envpol.2022.119251.
- Feng, Y. *et al.* (2024) 'Alteration of carbon and nitrogen allocation in winter wheat under elevated ozone', *Plant Science*. Elsevier, 338, p. 111924. doi: 10.1016/J.PLANTSCI.2023.111924.
- Feng, Z. *et al.* (2011a) 'Differential responses in two varieties of winter wheat to elevated ozone concentration under fully open-air field conditions', *Global Change Biology*. John Wiley & Sons, Ltd, 17(1), pp. 580-591. doi: 10.1111/J.1365-2486.2010.02184.X.
- Feng, Z. *et al.* (2011b) 'Differential responses in two varieties of winter wheat to elevated ozone concentration under fully open-air field conditions', *Global Change Biology*, 17(1), pp. 580-591. doi: 10.1111/J.1365-2486.2010.02184.X.

- Feng, Z. *et al.* (2012a) 'A stomatal ozone flux-response relationship to assess ozone-induced yield loss of winter wheat in subtropical China', *Environmental Pollution*. Elsevier Ltd, 164, pp. 16-23. doi: 10.1016/j.envpol.2012.01.014.
- Feng, Z. *et al.* (2012b) 'A stomatal ozone flux-response relationship to assess ozone-induced yield loss of winter wheat in subtropical China', *Environmental Pollution*. Elsevier, 164, pp. 16-23. doi: 10.1016/J.ENVPOL.2012.01.014.
- Feng, Z. *et al.* (2016a) 'Differential effects of ozone on photosynthesis of winter wheat among cultivars depend on antioxidative enzymes rather than stomatal conductance', *The Science of the total environment*. Sci Total Environ, 572, pp. 404-411. doi: 10.1016/J.SCITOTENV.2016.08.083.
- Feng, Z. *et al.* (2016b) 'Differential effects of ozone on photosynthesis of winter wheat among cultivars depend on antioxidative enzymes rather than stomatal conductance', *Science of the Total Environment*. Elsevier B.V., 572, pp. 404-411. doi: 10.1016/j.scitotenv.2016.08.083.
- Feng, Z. *et al.* (2018) 'Comparison of crop yield sensitivity to ozone between open-top chamber and free-air experiments', *Global Change Biology*. Blackwell Publishing Ltd, 24(6), pp. 2231-2238. doi: 10.1111/gcb.14077.
- Feng, Z. *et al.* (2021) 'Emerging challenges of ozone impacts on asian plants: actions are needed to protect ecosystem health'. doi: 10.1080/20964129.2021.1911602.
- Feng, Z. *et al.* (2022) 'Ozone pollution threatens the production of major staple crops in East Asia', *Nature Food*. Springer US, 3(1), pp. 47-56. doi: 10.1038/s43016-021-00422-6.
- Feng, Z., Kobayashi, K. and Ainsworth, E. A. (2008) 'Impact of elevated ozone concentration on growth, physiology, and yield of wheat (*Triticum aestivum* L.): A meta-analysis', *Global Change Biology*, 14(11), pp. 2696-2708. doi: 10.1111/j.1365-2486.2008.01673.x.
- Fuhrer, J. (2009) 'Ozone risk for crops and pastures in present and future climates', *Naturwissenschaften*, 96(2), pp. 173-194. doi: 10.1007/s00114-008-0468-7.
- Fukase, E. and Martin, W. (2020) 'Economic growth, convergence, and world food demand and supply', *World Development*. Elsevier Ltd, 132, p. 104954. doi: 10.1016/j.worlddev.2020.104954.
- Gago, J. *et al.* (2016) 'Relationships of leaf net photosynthesis, stomatal conductance, and mesophyll conductance to primary metabolism: A multispecies meta-analysis approach', *Plant Physiology*, 171(1), pp. 265-279. doi: 10.1104/pp.15.01660.
- Gaudel, A. *et al.* (2018) 'Tropospheric Ozone Assessment Report: Present-day distribution and trends of tropospheric ozone relevant to climate and global atmospheric chemistry model evaluation', *Elementa*. University of California Press, 6. doi: 10.1525/ELEMENTA.291/112811.
- Gelang, J. *et al.* (2000a) 'Rate and duration of grain filling in relation to flag leaf senescence and grain yield in spring wheat (*Triticum aestivum*) exposed to different concentrations of ozone', *Physiologia Plantarum*, 110(3), pp. 366-375. doi: 10.1111/j.1399-3054.2000.1100311.x.

- Gelang, J. *et al.* (2000b) 'Rate and duration of grain filling in relation to flag leaf senescence and grain yield in spring wheat (*Triticum aestivum*) exposed to different concentrations of ozone', *Physiologia Plantarum*, 110(3), pp. 366-375. doi: 10.1111/J.1399-3054.2000.1100311.X.
- Ghosh, A. *et al.* (2020) 'Assessment of growth, physiological, and yield attributes of wheat cultivar HD 2967 under elevated ozone exposure adopting timely and delayed sowing conditions', *Environmental Science and Pollution Research*. Environmental Science and Pollution Research, 27(14), pp. 17205-17220. doi: 10.1007/s11356-020-08325-y.
- Godde, C. M. *et al.* (2021) 'Impacts of climate change on the livestock food supply chain; a review of the evidence', *Global Food Security*. Elsevier B.V., 28(December 2020), p. 100488. doi: 10.1016/j.gfs.2020.100488.
- Grandjean, A. and Fuhrer Grandjean, J. (1989) *Growth and leaf senescence in spring wheat (Triticum aestivum) grown at different ozone concentrations in open-top field chambers*.
- Grote, U. *et al.* (2021) 'Food Security and the Dynamics of Wheat and Maize Value Chains in Africa and Asia', *Frontiers in Sustainable Food Systems*. Frontiers Media S.A., p. 617009. doi: 10.3389/fsufs.2020.617009.
- Graham, A. M. *et al.* (2020) 'Impact on air quality and health due to the Saddleworth Moor fire in northern England', *Environmental Research Letters*, 15(7). doi: 10.1088/1748-9326/ab8496.
- Graham, A. M. *et al.* (2021) 'Impact of the 2019/2020 Australian Megafires on Air Quality and Health', *GeoHealth*, 5(10), pp. 1–17. doi: 10.1029/2021GH000454.
- Konduri, V. S. *et al.* (2020) 'Data Science for Weather Impacts on Crop Yield', *Frontiers in Sustainable Food Systems*, 4(May). doi: 10.3389/fsufs.2020.00052.
- Guan, X. K. *et al.* (2015) 'Effect of Drought on the Gas Exchange, Chlorophyll Fluorescence and Yield of Six Different-Era Spring Wheat Cultivars', *Journal of Agronomy and Crop Science*, 201(4), pp. 253-266. doi: 10.1111/jac.12103.
- Guarin, J. R. *et al.* (2019) 'Impacts of tropospheric ozone and climate change on Mexico wheat production', *Climatic Change*, 155(2), pp. 157-174. doi: 10.1007/s10584-019-02451-4.
- Guenther, A. *et al.* (2006) 'Estimates of global terrestrial isoprene emissions using MEGAN (Model of Emissions of Gases and Aerosols from Nature)', *Atmospheric Chemistry and Physics*. European Geosciences Union, 6(11), pp. 3181-3210. doi: 10.5194/ACP-6-3181-2006.
- Han, H. *et al.* (2019) 'Foreign influences on tropospheric ozone over East Asia through global atmospheric transport', *Atmospheric Chemistry and Physics*, 19(19), pp. 12495-12514. doi: 10.5194/acp-19-12495-2019.
- Hansen, E. M. Ø. *et al.* (2019) 'The impact of ozone exposure, temperature and CO<sub>2</sub> on the growth and yield of three spring wheat varieties', *Environmental and Experimental Botany*. Elsevier B.V., 168. doi: 10.1016/J.ENVEXPBOT.2019.103868.
- Heyneke, E. *et al.* (2019) 'Effect of senescence phenotypes and nitrate availability on wheat leaf metabolome during grain filling', *Agronomy*, 9(6). doi:

10.3390/agronomy9060305.

Hoelzemann, J. J. *et al.* (2004) 'Global Wildland Fire Emission Model (GWEM): Evaluating the use of global area burnt satellite data', *Journal of Geophysical Research D: Atmospheres*, 109(14). doi: 10.1029/2003JD003666.

Hoffmann, L. *et al.* (2019) 'From ERA-Interim to ERA5: The considerable impact of ECMWF's next-generation reanalysis on Lagrangian transport simulations', *Atmospheric Chemistry and Physics*, 19(5), pp. 3097-3214. doi: 10.5194/acp-19-3097-2019.

Hsu, N. C. *et al.* (2012) 'Global and regional trends of aerosol optical depth over land and ocean using SeaWiFS measurements from 1997 to 2010', *Atmospheric Chemistry and Physics*, 12(17), pp. 8037-8053. doi: 10.5194/acp-12-8037-2012.

Huang, H. *et al.* (2022) 'A dataset of winter wheat aboveground biomass in China during 2007-2015 based on data assimilation', *Scientific Data*. Springer US, 9(1), pp. 1-11. doi: 10.1038/s41597-022-01305-6.

Huang, J. *et al.* (2015) 'Improving winter wheat yield estimation by assimilation of the leaf area index from Landsat TM and MODIS data into the WOFOST model', *Agricultural and Forest Meteorology*. Elsevier, 204, pp. 106-121. doi: 10.1016/J.AGRFORMET.2015.02.001.

Huang, L. *et al.* (2016) 'The impact of drought on ozone dry deposition over eastern Texas', *Atmospheric Environment*. Pergamon, 127, pp. 176-186. doi: 10.1016/J.ATMOSENV.2015.12.022.

lii, W. T. S. and Cheung, A. C. (1960) 'Carbon Monoxide: Residence Time in the Atmosphere Spectrographic Detection of Topographic Features on Mars', 166, pp. 3-4.

Ishaque, W. *et al.* (2023) 'Quantifying the impacts of climate change on wheat phenology, yield, and evapotranspiration under irrigated and rainfed conditions', *Agricultural Water Management*. Elsevier, 275, p. 108017. doi: 10.1016/J.AGWAT.2022.108017.

Jaggi, M. *et al.* (2006) 'Environmental control of profiles of ozone concentration in a grassland canopy', *Atmospheric Environment*, 40(28), pp. 5496-5507. doi: 10.1016/j.atmosenv.2006.01.025.

Jarvis, P. G. (1976) 'The interpretation of the variations in leaf water potential and stomatal conductance found in canopies in the field', *Philosophical Transactions of the Royal Society of London. B, Biological Sciences*, 273(927), pp. 593-610. doi: 10.1098/rstb.1976.0035.

Jones, H. G. (1992) *Plants and microclimate: A quantitative approach to environmental plant physiology*. Cambridge University Press.

Karlsson, P. E. *et al.* (2017) 'Past, present and future concentrations of ground-level ozone and potential impacts on ecosystems and human health in northern Europe', *Science of The Total Environment*. Elsevier, 576, pp. 22-35. doi: 10.1016/J.SCITOTENV.2016.10.061.

Kittipornkul, P. *et al.* (2021) 'Mechanisms of ozone responses in sensitive and tolerant mungbean cultivars', *Science of The Total Environment*. Elsevier, 800, p.

149550. doi: 10.1016/J.SCITOTENV.2021.149550.

Kleinman, I. *et al.* (2001) 'precursors', 28(15), pp. 2903-2906.

Kobayashi, K. (2015) 'FACE-ing the challenges of increasing surface ozone concentration in Asia', *Journal of Agricultural Meteorology*, 71(3), pp. 161-166. doi: 10.2480/agrmet.D-15-00100.

Kohut, R. J., Amundson, R. G. and Laurence, J. A. (1987) 'Effects of ozone and sulfur dioxide on yield of winter wheat', *Phytopathology*, 77(1), pp. 71-74. doi: 10.1094/Phyto-77-71.

Konduri, V. S. *et al.* (2020) 'Data Science for Weather Impacts on Crop Yield', *Frontiers in Sustainable Food Systems*, 4(May). doi: 10.3389/fsufs.2020.00052.

Kumari, S., Lakhani, A. and Kumari, K. M. (2020) 'First observation-based study on surface O<sub>3</sub> trend in Indo-Gangetic Plain: Assessment of its impact on crop yield', *Chemosphere*. Pergamon, 255, p. 126972. doi: 10.1016/J.CHEMOSPHERE.2020.126972.

Kutman, U. B., Yildiz, B. and Cakmak, I. (2011) 'Effect of nitrogen on uptake, remobilization and partitioning of zinc and iron throughout the development of durum wheat', *Plant and Soil*. Springer, 342(1-2), pp. 149-164. doi: 10.1007/S11104-010-0679-5/METRICS.

Lee, J. D. *et al.* (2020) 'UK surface NO<sub>2</sub> levels dropped by 42% during the COVID-19 lockdown: Impact on surface O<sub>3</sub>', *Atmospheric Chemistry and Physics*, 20(24), pp. 15743-15759. doi: 10.5194/acp-20-15743-2020.

Lefohn, A. S. *et al.* (2018) 'Tropospheric ozone assessment report: Global ozone metrics for climate change, human health, and crop/ecosystem research', *Elementa*, 6. doi: 10.1525/elementa.279.

Leung, F. *et al.* (2020) 'Calibrating soybean parameters in JULES 5.0 from the US-Ne2/3 FLUXNET sites and the SoyFACE-O<sub>3</sub> experiment', *Geoscientific Model Development*. Copernicus GmbH, 13(12), pp. 6201-6213. doi: 10.5194/GMD-13-6201-2020.

Leuning, R. (1990) 'MODELING STOMATAL BEHAVIOR AND PHOTOSYNTHESIS OF EUCALYPTUS-GRANDIS', *AUSTRALIAN JOURNAL OF PLANT PHYSIOLOGY*, 17(2), pp. 159-175.

Leuning, R. (1995) 'A critical appraisal of combine stomatal model C<sub>3</sub> plants', *Plant, Cell & Environment*, 18, pp. 339-355. Available at: <http://www.unc.edu/courses/2010spring/geog/595/001/www/Leuning95b-PCE.pdf%0Apapers2://publication/uuid/B8B998AB-EB42-4E09-A609-B192084D13EE>.

Li, A., Zhou, Q. and Xu, Q. (2021) 'Prospects for ozone pollution control in China: An epidemiological perspective', *Environmental Pollution*. Elsevier Ltd, 285. doi: 10.1016/J.ENVPOL.2021.117670.

Li, D. *et al.* (2022) 'Surface ozone impacts on major crop production in China from 2010 to 2017', *Atmospheric Chemistry and Physics*, 22(4), pp. 2625-2638. doi: 10.5194/acp-22-2625-2022.

Li, H. *et al.* (2019) 'Wheat breeding in northern China: Achievements and technical

- advances', *The Crop Journal*. Elsevier, 7(6), pp. 718-729. doi: 10.1016/J.CJ.2019.09.003.
- Li, K. *et al.* (2020) 'anthropogenic and meteorological influences', *Atmos. Chem. Phys*, 20, pp. 11423-11433. doi: 10.5194/acp-20-11423-2020.
- Li, M. *et al.* (2017) 'Special Topic: Air Pollution and Control Anthropogenic emission inventories in China: a review', *National Science Review*, 4, pp. 834-866. doi: 10.1093/nsr/nwx150.
- Li, P. *et al.* (2023) 'Source attribution of near-surface ozone trends in the United States during 1995-2019', *Atmospheric Chemistry and Physics*, 23(9), pp. 5403-5417. doi: 10.5194/acp-23-5403-2023.
- Liang, H. *et al.* (2016) 'An integrated soil-crop system model for water and nitrogen management in North China', *Scientific Reports*. Nature Publishing Group, 6(December 2015), pp. 1-20. doi: 10.1038/srep25755.
- Lim, C. W. *et al.* (2015) 'Function of ABA in Stomatal Defense against Biotic and Drought Stresses', *Int. J. Mol. Sci*, 16, pp. 15251-15270. doi: 10.3390/ijms160715251.
- Lin, M. *et al.* (2017) 'US surface ozone trends and extremes from 1980 to 2014: Quantifying the roles of rising Asian emissions, domestic controls, wildfires, and climate', *Atmospheric Chemistry and Physics*, 17(4), pp. 2943-2970. doi: 10.5194/acp-17-2943-2017.
- Lin, Y. *et al.* (2013) 'Impacts of future climate changes on shifting patterns of the agro-ecological zones in China', *Advances in Meteorology*, 2013. doi: 10.1155/2013/163248.
- Liu, B. *et al.* (2016) 'Testing the responses of four wheat crop models to heat stress at anthesis and grain filling', *Global Change Biology*. John Wiley & Sons, Ltd, 22(5), pp. 1890-1903. doi: 10.1111/GCB.13212.
- Liu, C. and Shi, K. (2021) 'A review on methodology in O<sub>3</sub>-NO<sub>x</sub>-VOC sensitivity study', *Environmental Pollution*. Elsevier, 291, p. 118249. doi: 10.1016/J.ENVPOL.2021.118249.
- Liu, J. *et al.* (2008) 'Protein degradation and nitrogen remobilization during leaf senescence', *Journal of Plant Biology*, 51(1), pp. 11-19. doi: 10.1007/BF03030735.
- Liu, S. *et al.* (2010) 'Crop yield responses to climate change in the Huang-Huai-Hai Plain of China', *Agricultural Water Management*. Elsevier, 97(8), pp. 1195-1209. doi: 10.1016/J.AGWAT.2010.03.001.
- Liu, T., Wang, Z. and Cai, T. (2016) 'Canopy Apparent Photosynthetic Characteristics and Yield of Two Spike-Type Wheat Cultivars in Response to Row Spacing under High Plant Density', *PLoS ONE*, 11(2), pp. 1-16. doi: 10.1371/journal.pone.0148582.
- Liu, Z. *et al.* (2022) 'Tropospheric ozone changes and ozone sensitivity from the present day to the future under shared socio-economic pathways', *Atmospheric Chemistry and Physics*. Copernicus GmbH, 22(2), pp. 1209-1227. doi: 10.5194/ACP-22-1209-2022.
- Lombardozzi, D. *et al.* (2012) 'Predicting photosynthesis and transpiration responses

- to ozone: decoupling modeled photosynthesis and stomatal conductance', *Biogeosciences*, 9, pp. 3113-3130. doi: 10.5194/bg-9-3113-2012.
- Lozovskaya, M. V *et al.* (2012) 'The effect of high temperature stress on the phenology, growth and yield of five wheat (*Triticum aestivum* L.) genotypes The Asian and Australasian Journal of Plant Science and Biotechnology The Effect of High Temperature Stress on the Phenology, Growth an', *Asian and Australasian Journal of Plant Science and Biotechnology*, 6(1), pp. 14-23. Available at: <https://www.researchgate.net/publication/283557698>.
- Lu, X. *et al.* (2018) 'Lower tropospheric ozone over India and its linkage to the South Asian monsoon', *Atmospheric Chemistry and Physics*, 18(5), pp. 3101-3118. doi: 10.5194/acp-18-3101-2018.
- Lu, X., Zhang, L. and Shen, L. (2019) 'Meteorology and Climate Influences on Tropospheric Ozone: a Review of Natural Sources, Chemistry, and Transport Patterns', *Current Pollution Reports*. Current Pollution Reports, 5(4), pp. 238-260. doi: 10.1007/s40726-019-00118-3.
- Luo, Y. *et al.* (2020) 'ChinaCropPhen1km: a high-resolution crop phenological dataset for three staple crops in China during 2000-2015 based on leaf area index (LAI) products', *Earth System Science Data*. Copernicus GmbH, 12(1), pp. 197-214. doi: 10.5194/ESSD-12-197-2020.
- Luo, Y. *et al.* (2022) 'Accurately mapping global wheat production system using deep learning algorithms', *International Journal of Applied Earth Observation and Geoinformation*. Elsevier B.V., 110(May), p. 102823. doi: 10.1016/j.jag.2022.102823.
- Ma, M. *et al.* (2021) 'Current Situation and Key Parameters for Improving Wheat Quality in China', *Frontiers in Plant Science*, 12(February), pp. 1-9. doi: 10.3389/fpls.2021.638525.
- Ma, X. *et al.* (2021) 'Rapid increase in summer surface ozone over the North China Plain during 2013-2019: A side effect of particulate matter reduction control?', *Atmospheric Chemistry and Physics*, 21(1), pp. 1-16. doi: 10.5194/acp-21-1-2021.
- Malhi, G. S., Kaur, M. and Kaushik, P. (2021) 'Impact of Climate Change on Agriculture and Its Mitigation Strategies: A Review', *Sustainability 2021, Vol. 13, Page 1318*. Multidisciplinary Digital Publishing Institute, 13(3), p. 1318. doi: 10.3390/SU13031318.
- Malley, C. S. *et al.* (2021) 'Integrated assessment of global climate, air pollution, and dietary, malnutrition and obesity health impacts of food production and consumption between 2014 and 2018', *Environmental Research Communications*. IOP Publishing, 3(7). doi: 10.1088/2515-7620/ac0af9.
- Mariën, B. *et al.* (2019) 'Detecting the onset of autumn leaf senescence in deciduous forest trees of the temperate zone', *New Phytologist*. John Wiley & Sons, Ltd, 224(1), pp. 166-176. doi: 10.1111/NPH.15991.
- Marsh, D. R. *et al.* (2013) 'Climate change from 1850 to 2005 simulated in CESM1(WACCM)', *Journal of Climate*, 26(19), pp. 7372-7391. doi: 10.1175/JCLI-D-12-00558.1.
- Massman, W. J. (2004) 'Toward an ozone standard to protect vegetation based on effective dose: a review of deposition resistances and a possible metric',

*Atmospheric Environment*. Pergamon, 38(15), pp. 2323-2337. doi: 10.1016/J.ATMOSENV.2003.09.079.

Mauzerall, D. L. and Wang, X. (2001) 'PROTECTING AGRICULTURAL CROPS FROM THE EFFECTS OF TROPOSPHERIC OZONE EXPOSURE: Reconciling Science and Standard Setting in the United States, Europe, and Asia'. Available at: [www.annualreviews.org](http://www.annualreviews.org) (Accessed: 11 October 2021).

McAusland, L. *et al.* (2020) 'Variation in key leaf photosynthetic traits across wheat wild relatives is accession dependent not species dependent', *New Phytologist*, 228(6), pp. 1767-1780. doi: 10.1111/nph.16832.

Medlyn, B. E. *et al.* (2002) 'Temperature response of parameters of a biochemically based model of photosynthesis. II. A review of experimental data', *Plant, Cell and Environment*, 25(9), pp. 1167-1179. doi: 10.1046/j.1365-3040.2002.00891.x.

Meng, Q. *et al.* (2012) 'Responses on Photosynthesis and Variable Chlorophyll Fluorescence of *Fragaria ananassa* under Sound Wave', *Energy Procedia*, 16, pp. 346-352. doi: 10.1016/j.egypro.2012.01.057.

Mertens, M. *et al.* (2024) 'The contribution of transport emissions to ozone mixing ratios and methane lifetime in 2015 and 2050 in the Shared Socioeconomic Pathways (SSPs)', (February), pp. 1-45.

Miller, J. D., Arteca, R. N. and Pell, E. J. (1999) 'Senescence-Associated Gene Expression during Ozone-Induced Leaf Senescence in Arabidopsis', *Plant Physiology*. Oxford University Press, 120(4), p. 1015. doi: 10.1104/PP.120.4.1015.

Mills, G. *et al.* (2007) 'A synthesis of AOT40-based response functions and critical levels of ozone for agricultural and horticultural crops', *Atmospheric Environment*. Pergamon, 41(12), pp. 2630-2643. doi: 10.1016/J.ATMOSENV.2006.11.016.

Mills, G. *et al.* (2011) 'New stomatal flux-based critical levels for ozone effects on vegetation', *Atmospheric Environment*. Pergamon, 45(28), pp. 5064-5068. doi: 10.1016/J.ATMOSENV.2011.06.009.

Mills, G., Sharps, K., Simpson, D., Pleijel, H., Frei, M., *et al.* (2018) 'Closing the global ozone yield gap: Quantification and cobenefits for multistress tolerance', *Global Change Biology*, 24(10), pp. 4869-4893. doi: 10.1111/gcb.14381.

Mills, G., Sharps, K., Simpson, D., Pleijel, H., Broberg, M., *et al.* (2018) 'Ozone pollution will compromise efforts to increase global wheat production', *Global Change Biology*, 24(8), pp. 3560-3574. doi: 10.1111/gcb.14157.

Mina, U. *et al.* (2019) 'Quantitative assessment of individual and combined impact of ozone and aerosols on wheat cultivar: Growth, development, biochemical, physiological and yield attributes', *Agricultural and forest meteorology*. doi: 10.1016/j.agrformet.2019.107817.

Mina, U., Kumar, P. and Varshney, C. (2010) 'Effect of ozone exposure on growth, yield and isoprene emission from tomato (*Lycopersicon esculentum* L.) plants', *Vegetable Crops Research Bulletin*, 72(1), pp. 35-48. doi: 10.2478/v10032-010-0004-0.

Misson, L., Panek, J. A. and Goldstein, A. H. (2004) 'A comparison of three approaches to modeling leaf gas exchange in annually drought-stressed ponderosa

- pine forests', *Tree Physiology*, 24(5), pp. 529-541. doi: 10.1093/treephys/24.5.529.
- Monks, P. S. *et al.* (2015) 'Tropospheric ozone and its precursors from the urban to the global scale from air quality to short-lived climate forcer', *Atmospheric Chemistry and Physics*, 15(15), pp. 8889-8973. doi: 10.5194/acp-15-8889-2015.
- Muhie, S. H. (2022) 'Novel approaches and practices to sustainable agriculture', *Journal of Agriculture and Food Research*. Elsevier B.V., 10(August), p. 100446. doi: 10.1016/j.jafr.2022.100446.
- Müller, C. *et al.* (2019) 'The Global Gridded Crop Model Intercomparison phase 1 simulation dataset', *Scientific Data*, 6(1), pp. 1-22. doi: 10.1038/s41597-019-0023-8.
- Mulvaney, M. J. and Devkota, P. J. (2020) 'Adjusting Crop Yield to a Standard Moisture Content', *EDIS*. University of Florida George A Smathers Libraries, 2020(3). doi: 10.32473/EDIS-AG442-2020.
- Nagarajan, S. *et al.* (1999) 'Effect of post-anthesis water stress on accumulation of dry matter, carbon and nitrogen and their partitioning in wheat varieties differing in drought tolerance', *Journal of Agronomy and Crop Science*, 183(2), pp. 129-136. doi: 10.1046/j.1439-037X.1999.00326.x.
- Nguyen, D. H. *et al.* (2022) 'Tropospheric ozone and NOx: A review of worldwide variation and meteorological influences', *Environmental Technology and Innovation*, 28(x). doi: 10.1016/j.eti.2022.102809.
- Nguyen, T. H. *et al.* (2024) 'Assessing the spatio-temporal tropospheric ozone and drought impacts on leaf growth and grain yield of wheat across Europe through crop modeling and remote sensing data', *European Journal of Agronomy*. Elsevier, 153, p. 127052. doi: 10.1016/J.EJA.2023.127052.
- Van Oijen, M. and Ewert, F. (1999) 'The effects of climatic variation in Europe on the yield response of spring wheat cv. Minaret to elevated CO<sub>2</sub> and O<sub>3</sub>: an analysis of open-top chamber experiments by means of two crop growth simulation models', *European Journal of Agronomy*. Elsevier, 10(3-4), pp. 249-264. doi: 10.1016/S1161-0301(99)00014-3.
- Ojanperä, K., Pätsikkä, E. and Ylärinta, T. (1998a) 'Effects of low ozone exposure of spring wheat on net CO<sub>2</sub> uptake, Rubisco, leaf senescence and grain filling', *New Phytologist*. John Wiley & Sons, Ltd, 138(3), pp. 451-460. doi: 10.1046/J.1469-8137.1998.00120.X.
- Ojanperä, K., Pätsikkä, E. and Ylärinta, T. (1998b) 'Effects of low ozone exposure of spring wheat on net CO<sub>2</sub> uptake, Rubisco, leaf senescence and grain filling', *New Phytologist*. John Wiley & Sons, Ltd, 138(3), pp. 451-460. doi: 10.1046/J.1469-8137.1998.00120.X.
- Olsovka, K. *et al.* (2016) 'Genotypically identifying wheat mesophyll conductance regulation under progressive drought stress', *Frontiers in Plant Science*, 7(AUG2016), pp. 1-14. doi: 10.3389/fpls.2016.01111.
- Osborne, S. *et al.* (2019) 'New insights into leaf physiological responses to ozone for use in crop Modelling', *Plants*, 8(4). doi: 10.3390/plants8040084.
- Osborne, T. *et al.* (2015) 'JULES-crop: A parametrisation of crops in the Joint UK Land Environment Simulator', *Geoscientific Model Development*, 8(4), pp. 1139-

1155. doi: 10.5194/gmd-8-1139-2015.

Paoletti, E. (2005) 'Ozone slows stomatal response to light and leaf wounding in a Mediterranean evergreen broadleaf, *Arbutus unedo*', *Environmental Pollution*. Elsevier, 134(3), pp. 439-445. doi: 10.1016/J.ENVPOL.2004.09.011.

Paoletti, E. *et al.* (2019) 'Importance of Detoxification Processes in Ozone Risk Assessment: Need to Integrate the Cellular Compartmentation of Antioxidants?', *Frontiers in Forests and Global Change / www.frontiersin.org*, 1, p. 45. doi: 10.3389/ffgc.2019.00045.

Pleijel, H. *et al.* (2007) 'Ozone risk assessment for agricultural crops in Europe: Further development of stomatal flux and flux-response relationships for European wheat and potato', *Atmospheric Environment*. Pergamon, 41(14), pp. 3022-3040. doi: 10.1016/J.ATMOENV.2006.12.002.

Pleijel, H., Danielsson, H. and Broberg, M. C. (2022) 'Benefits of the Phytotoxic Ozone Dose (POD) index in dose-response functions for wheat yield loss', *Atmospheric Environment*. Pergamon, 268, p. 118797. doi: 10.1016/J.ATMOENV.2021.118797.

Pommier, M. (2023) 'Estimations of NO<sub>x</sub> emissions, NO<sub>2</sub> lifetime and their temporal variation over three British urbanised regions in 2019 using TROPOMI NO<sub>2</sub> observations', *Environmental Science: Atmospheres*. RSC, 3(2), pp. 408-421. doi: 10.1039/D2EA00086E.

Porter, J. R. (1984) 'A model of canopy development in winter wheat', *The Journal of Agricultural Science*, 102(2), pp. 383-392. doi: 10.1017/S0021859600042714.

Pun, B. K., Wu, S. Y. and Seigneur, C. (2002) 'Contribution of biogenic emissions to the formation of ozone and particulate matter in the Eastern United States', *Environmental Science and Technology*, 36(16), pp. 3586-3596. doi: 10.1021/es015872v.

Pury, D. G. G. D. E. and Farquhar, G. D. (1997) 'Simple scaling of photosynthesis from leaves to canopies without the errors of big-leaf models', pp. 537-557.

De Pury, D. G. G. and Farquhar, G. D. (1997) 'Simple scaling of photosynthesis from leaves to canopies without the errors of big-leaf models', *Plant, Cell and Environment*. Blackwell Publishing Ltd, 20(5), pp. 537-557. doi: 10.1111/j.1365-3040.1997.00094.x.

Qin, X. *et al.* (2015) 'Wheat yield improvements in China: Past trends and future directions', *Field Crops Research*. Elsevier B.V., 177, pp. 117-124. doi: 10.1016/j.fcr.2015.03.013.

Ragothaman, A. and Id, W. A. A. (2017) 'environments Air Quality Impacts of Petroleum Refining and Petrochemical Industries'. doi: 10.3390/environments4030066.

Rai, R. and Agrawal, M. (2012) 'Impact of tropospheric ozone on crop plants', *Proceedings of the National Academy of Sciences India Section B - Biological Sciences*. Springer, pp. 241-257. doi: 10.1007/s40011-012-0032-2.

Reid, N., Yap, D. and Bloxam, R. (2008) 'The potential role of background ozone on current and emerging air issues: An overview', *Air Quality, Atmosphere and Health*,

1(1), pp. 19-29. doi: 10.1007/s11869-008-0005-z.

Roberts, H. R. *et al.* (2022) 'Chronic tropospheric ozone exposure reduces seed yield and quality in spring and winter oilseed rape', *Agricultural and Forest Meteorology*, 316, p. 108859. doi: 10.1016/j.agrformet.2022.108859.

Russo, M. R. *et al.* (2023) 'Seasonal, interannual and decadal variability of tropospheric ozone in the North Atlantic: comparison of UM-UKCA and remote sensing observations for 2005-2018', *Atmospheric Chemistry and Physics*. Copernicus Publications, 23(11), pp. 6169-6196. doi: 10.5194/ACP-23-6169-2023.

Sarkar, M. *et al.* (2021) 'Impact of tropospheric ozone pollution on wheat production in Southeast Asia: an update', *Global Climate Change*. Elsevier, pp. 235-266. doi: 10.1016/B978-0-12-822928-6.00008-3.

Schauberger, B. *et al.* (2019) 'Global historical soybean and wheat yield loss estimates from ozone pollution considering water and temperature as modifying effects', *Agricultural and Forest Meteorology*, 265(October 2018), pp. 1-15. doi: 10.1016/j.agrformet.2018.11.004.

Seidel, S. J. *et al.* (2018) 'Towards improved calibration of crop models - Where are we now and where should we go?', *European Journal of Agronomy*. Elsevier B.V., 94, pp. 25-35. doi: 10.1016/J.EJA.2018.01.006.

Shah, S. H. *et al.* (2019) 'Does Household Capital Mediate the Uptake of Agricultural Land, Crop, and Livestock Adaptations? Evidence From the Indo-Gangetic Plains (India)', *Frontiers in Sustainable Food Systems*, 3(January). doi: 10.3389/fsufs.2019.00001.

Sharkey, T. D. *et al.* (2007) 'Fitting photosynthetic carbon dioxide response curves for C3 leaves', *Plant, Cell and Environment*, 30(9), pp. 1035-1040. doi: 10.1111/j.1365-3040.2007.01710.x.

Sharma, A. *et al.* (2016) 'Influence of ozone precursors and particulate matter on the variation of surface ozone at an urban site of Delhi, India', *Sustainable Environment Research*. Elsevier Ltd, 26(2), pp. 76-83. doi: 10.1016/j.serj.2015.10.001.

Sharma, D. K. *et al.* (2015) 'Wheat cultivars selected for high F v /F m under heat stress maintain high photosynthesis, total chlorophyll, stomatal conductance, transpiration and dry matter', *Physiologia Plantarum*, 153, pp. 284-298. doi: 10.1111/ppl.12245.

Shi, G. *et al.* (2009) 'Impact of elevated ozone concentration on yield of four Chinese rice cultivars under fully open-air field conditions', *Agriculture, Ecosystems and Environment*, 131(3-4), pp. 178-184. doi: 10.1016/J.AGEE.2009.01.009.

Sicard, P. *et al.* (2017) 'Projected global ground-level ozone impacts on vegetation under different emission and climate scenarios', *Atmos. Chem. Phys*, 17, pp. 12177-12196. doi: 10.5194/acp-17-12177-2017.

Sicard, P. *et al.* (2021) 'Urban population exposure to air pollution in Europe over the last decades', *Environmental Sciences Europe 2021 33:1*. SpringerOpen, 33(1), pp. 1-12. doi: 10.1186/S12302-020-00450-2.

Sillmann, J. *et al.* (2021) 'Combined impacts of climate and air pollution on human health and agricultural productivity', *Environmental Research Letters*, 16(9). doi:

10.1088/1748-9326/ac1df8.

Silva-Pérez, V. *et al.* (2020) 'Genetic variation for photosynthetic capacity and efficiency in spring wheat', *Journal of Experimental Botany*, 71(7), pp. 2299-2311. doi: 10.1093/jxb/erz439.

Silver, B. *et al.* (2018) 'Substantial changes in air pollution across China during 2015-2017', *Environmental Research Letters*. IOP Publishing, 13(11). doi: 10.1088/1748-9326/aae718.

Simpson, D. *et al.* (2012) 'The EMEP MSC-W chemical transport model &ndash; Technical description', *Atmospheric Chemistry and Physics*, 12(16), pp. 7825-7865. doi: 10.5194/acp-12-7825-2012.

Singh, A. A. *et al.* (2018) 'Assessment of ozone toxicity among 14 Indian wheat cultivars under field conditions: growth and productivity', *Environmental Monitoring and Assessment*. Springer International Publishing, 190(4), pp. 1-14. doi: 10.1007/s10661-018-6563-0.

Singh Yadav, D. *et al.* (2020) 'Responses of an old and a modern Indian wheat cultivar to future O<sub>3</sub> level: Physiological, yield and grain quality parameters \*'. doi: 10.1016/j.envpol.2020.113939.

Singla, V. *et al.* (2011) 'Ozone formation and destruction at a sub-urban site in North Central region of India', *Atmospheric Research*. Elsevier B.V., 101(1-2), pp. 373-385. doi: 10.1016/j.atmosres.2011.03.011.

Sinha, B. *et al.* (2015) 'Assessment of crop yield losses in Punjab and Haryana using 2 years of continuous in situ ozone measurements', *Atmos. Chem. Phys*, 15, pp. 9555-9576. doi: 10.5194/acp-15-9555-2015.

Sitch, S. *et al.* (2007) 'Indirect radiative forcing of climate change through ozone effects on the land-carbon sink', 448. doi: 10.1038/nature06059.

Soulie, A. *et al.* (2023) 'Global Anthropogenic Emissions (CAM5-GLOB-ANT) for the Copernicus Atmosphere Monitoring Service Simulations of Air Quality Forecasts and Reanalyses', *Earth System Science Data Discussions*, 2023(August), pp. 1-45. Available at: <https://essd.copernicus.org/preprints/essd-2023-306/>.

Szopa, S. *et al.* (2013) 'Aerosol and ozone changes as forcing for climate evolution between 1850 and 2100', *Climate Dynamics*. Springer Verlag, 40(9), pp. 2223-2250. doi: 10.1007/s00382-012-1408-y.

Tamaoki, M. (2008) 'The role of phytohormone signaling in ozone-induced cell death in plants', *Plant Signaling and Behavior*, 3(3), pp. 166-174. doi: 10.4161/psb.3.3.5538.

Tao, F. *et al.* (2014) 'Responses of wheat growth and yield to climate change in different climate zones of China, 1981-2009', *Agricultural and Forest Meteorology*. Elsevier, 189-190, pp. 91-104. doi: 10.1016/J.AGRFORMET.2014.01.013.

Tao, F. *et al.* (2017) 'Effects of climate change, CO<sub>2</sub> and O<sub>3</sub> on wheat productivity in Eastern China, singly and in combination', *Atmospheric Environment*. Elsevier Ltd, 153, pp. 182-193. doi: 10.1016/j.atmosenv.2017.01.032.

Tao, F., Zhang, S. and Zhang, Z. (2012) 'Spatiotemporal changes of wheat phenology in China under the effects of temperature, day length and cultivar thermal

- characteristics', *European Journal of Agronomy*. Elsevier B.V., 43, pp. 201-212. doi: 10.1016/j.eja.2012.07.005.
- Tcherkez, G. *et al.* (2020) 'Elevated CO<sub>2</sub> has concurrent effects on leaf and grain metabolism but minimal effects on yield in wheat', *Journal of Experimental Botany*, 71(19), pp. 5990-6003. doi: 10.1093/jxb/eraa330.
- Teixeira, E. *et al.* (2011) 'Limited potential of crop management for mitigating surface ozone impacts on global food supply', *Atmospheric Environment*. Pergamon, 45(15), pp. 2569-2576. doi: 10.1016/J.ATMOENV.2011.02.002.
- Teixeira, E. I. *et al.* (2013) 'Global hot-spots of heat stress on agricultural crops due to climate change', *Agricultural and Forest Meteorology*, 170, pp. 206-215. doi: 10.1016/j.agrformet.2011.09.002.
- Tibrewal, K., Maithel, S. and Venkataraman, C. (2019) 'A State-Level Methodology for Estimating Present-Day Emissions of Short-Lived Climate Pollutants from Fired Brick Production in India', *Climate Change Signals and Response*, pp. 211-229. doi: 10.1007/978-981-13-0280-0\_13.
- Triboi, E. and Triboi-Blondel, A. M. (2002) 'Productivity and grain or seed composition: A new approach to an old problem - Invited paper', *European Journal of Agronomy*, 16(3), pp. 163-186. doi: 10.1016/S1161-0301(01)00146-0.
- Turnock, S. T. *et al.* (2019) '300 years of tropospheric ozone changes using CMIP6 scenarios with a parameterised approach', *Atmospheric Environment*. Elsevier, 213(April), pp. 686-698. doi: 10.1016/j.atmosenv.2019.07.001.
- Uddling, J. *et al.* (2005) 'Measuring and modelling stomatal conductance and photosynthesis in mature birch in Sweden', *Agricultural and Forest Meteorology*, 132(1-2), pp. 115-131. doi: 10.1016/j.agrformet.2005.07.004.
- Uddling, J. and Pleijel, H. (2006) 'Changes in stomatal conductance and net photosynthesis during phenological development in spring wheat: Implications for gas exchange modelling', *International Journal of Biometeorology*, 51(1), pp. 37-48. doi: 10.1007/s00484-006-0039-6.
- Wallach, D. *et al.* (2021) 'The chaos in calibrating crop models: Lessons learned from a multi-model calibration exercise', *Environmental Modelling & Software*. Elsevier, 145, p. 105206. doi: 10.1016/J.ENVSOFT.2021.105206.
- Wang, H. *et al.* (2022) 'Global tropospheric ozone trends, attributions, and radiative impacts in 1995-2017: An integrated analysis using aircraft (IAGOS) observations, ozonesonde, and multi-decadal chemical model simulations', *Atmospheric Chemistry and Physics*. Copernicus Publications, 22(20), pp. 13753-13782. doi: 10.5194/ACP-22-13753-2022.
- Wang, J. *et al.* (2013a) 'Phenological trends of winter wheat in response to varietal and temperature changes in the North China Plain', *Field Crops Research*. Elsevier, 144, pp. 135-144. doi: 10.1016/J.FCR.2012.12.020.
- Wang, J. *et al.* (2013b) 'Phenological trends of winter wheat in response to varietal and temperature changes in the North China Plain', *Field Crops Research*. Elsevier B.V., 144, pp. 135-144. doi: 10.1016/j.fcr.2012.12.020.
- Wang, Q. J. (1997) 'Using genetic algorithms to optimise model parameters',

- Environmental Modelling and Software*. Elsevier Ltd, 12(1), pp. 27-34. doi: 10.1016/S1364-8152(96)00030-8.
- Wang, T. *et al.* (2009) 'Increasing surface ozone concentrations in the background atmosphere of Southern China, 1994-2007', *Atmospheric Chemistry and Physics*, 9(16), pp. 6217-6227. doi: 10.5194/acp-9-6217-2009.
- Wang, X. *et al.* (2007) 'Assessing the impact of ambient ozone on growth and yield of a rice (*Oryza sativa* L.) and a wheat (*Triticum aestivum* L.) cultivar grown in the Yangtze Delta, China, using three rates of application of ethylenediurea (EDU)', *Environmental Pollution*. Elsevier, 148(2), pp. 390-395. doi: 10.1016/J.ENVPOL.2006.12.014.
- Wang, Y. *et al.* (2022) 'Reductions in crop yields across China from elevated ozone', *Environmental Pollution*, 292(April 2021). doi: 10.1016/j.envpol.2021.118218.
- Wiedinmyer, C. *et al.* (2011) 'The Fire INventory from NCAR (FINN): A high resolution global model to estimate the emissions from open burning', *Geoscientific Model Development*, 4(3), pp. 625-641. doi: 10.5194/gmd-4-625-2011.
- Wilkinson, S. *et al.* (2012) 'How is ozone pollution reducing our food supply?', *Journal of Experimental Botany*, 63(2), pp. 527-536. doi: 10.1093/jxb/err317.
- Wilkinson, S. and Davies, W. J. (2010) 'Drought, ozone, ABA and ethylene: new insights from cell to plant to community', *Plant, Cell and Environment*, 33(4), pp. 510-525. doi: 10.1111/J.1365-3040.2009.02052.X.
- Wolff, G. T. *et al.* (2001) 'Ozone air quality over north america: Part I—A review of reported trends', *Journal of the Air and Waste Management Association*, 51(2), pp. 273-282. doi: 10.1080/10473289.2001.10464270.
- Xiao, G. *et al.* (2005) 'Effects of temperature increase and elevated CO<sub>2</sub> concentration, with supplemental irrigation, on the yield of rain-fed spring wheat in a semiarid region of China', *Agricultural Water Management*. Elsevier, 74(3), pp. 243-255. doi: 10.1016/J.AGWAT.2004.11.006.
- Xu, J. *et al.* (2020) 'Understanding the formation of high-ozone episodes at Raoyang, a rural site in the north China plain', *Atmospheric Environment*. Elsevier Ltd, 240(July), p. 117797. doi: 10.1016/j.atmosenv.2020.117797.
- Xu, W. *et al.* (2016) 'Long-term trends of surface ozone and its influencing factors at the Mt Waliguan GAW station, China-Part 1: Overall trends and characteristics', *Atmos. Chem. Phys*, 16, pp. 6191-6205. doi: 10.5194/acp-16-6191-2016.
- Xu, X. *et al.* (2008) 'Long-term trend of surface ozone at a regional background station in eastern China 1991-2006: Enhanced variability', *Atmospheric Chemistry and Physics*, 8(10), pp. 2595-2607. doi: 10.5194/acp-8-2595-2008.
- Xu, Y., Kobayashi, K. and Feng, Z. (2024) 'Wheat yield response to elevated O<sub>3</sub> concentrations differs between the world's major producing regions', *Science of The Total Environment*. Elsevier, 907, p. 168103. doi: 10.1016/J.SCITOTENV.2023.168103.
- Yadav, D. S., Agrawal, S. B. and Agrawal, M. (2021) 'Ozone flux-effect relationship for early and late sown Indian wheat cultivars: Growth, biomass, and yield', *Field Crops Research*. Elsevier B.V., 263(January), p. 108076. doi:

10.1016/j.fcr.2021.108076.

Yadav, M. *et al.* (2019) 'Source apportionment of particulate matter, gaseous pollutants, and volatile organic compounds in a future smart city of India', *Urban Climate*. Elsevier, 28(March), p. 100470. doi: 10.1016/j.uclim.2019.100470.

Yang, L. *et al.* (no date) 'Mathematical Programming for Piecewise Linear Regression Analysis'.

Yao, Y. *et al.* (2023) 'Urban Surface Ozone Concentration in Mainland China during 2015-2020: Spatial Clustering and Temporal Dynamics', *International Journal of Environmental Research and Public Health*, 20(5). doi: 10.3390/ijerph20053810.

Yoshida, S. *et al.* (2006) 'Cytosolic dehydroascorbate reductase is important for ozone tolerance in *Arabidopsis thaliana*', *Plant and Cell Physiology*, 47(2), pp. 304-308. doi: 10.1093/pcp/pci246.

Young, P. J. *et al.* (2018) 'Tropospheric ozone assessment report: Assessment of global-scale model performance for global and regional ozone distributions, variability, and trends', *Elementa*, 6. doi: 10.1525/elementa.265.

YU, L. *et al.* (2017) 'Towards a more flexible representation of water stress effects in the nonlinear Jarvis model', *Journal of Integrative Agriculture*. Chinese Academy of Agricultural Sciences, 16(1), pp. 210-220. doi: 10.1016/S2095-3119(15)61307-7.

Yu, Q. *et al.* (2004) 'Simulation of the stomatal conductance of winter wheat in response to light, temperature and CO<sub>2</sub> changes', *Annals of Botany*, 93(4), pp. 435-441. doi: 10.1093/aob/mch023.

Yu, Q. *et al.* (2020) 'A cultivated planet in 2010-Part 2: The global gridded agricultural-production maps', *Earth System Science Data*. Copernicus GmbH, 12(4), pp. 3545-3572. doi: 10.5194/ESSD-12-3545-2020.

Yu, X. *et al.* (2022) 'Cytological and molecular characteristics of delayed spike development in wheat under low temperature in early spring', *Crop Journal*. Crop Science Society of China, 10(3), pp. 840-852. doi: 10.1016/j.cj.2021.08.008.

Yue, X. *et al.* (2017) 'Ozone and haze pollution weakens net primary productivity in China', *Atmospheric Chemistry and Physics*, 17(9), pp. 6073-6089. doi: 10.5194/acp-17-6073-2017.

Zhang, X. *et al.* (2023) 'First long-term surface ozone variations at an agricultural site in the North China Plain: Evolution under changing meteorology and emissions', *Science of The Total Environment*. Elsevier, 860, p. 160520. doi: 10.1016/J.SCITOTENV.2022.160520.

Zhao, H. *et al.* (2020) 'Evaluating the effects of surface O<sub>3</sub> on three main food crops across China during 2015-2018', *Environmental Pollution*. Elsevier Ltd, 258. doi: 10.1016/J.ENVPOL.2019.113794.

Zheng, B. *et al.* (2018) 'Trends in China's anthropogenic emissions since 2010 as the consequence of clean air actions', *Atmospheric Chemistry and Physics*, 18(19), pp. 14095-14111. doi: 10.5194/acp-18-14095-2018.

Zhu, X. *et al.* (2011) 'Effects of elevated ozone concentration on yield of four Chinese cultivars of winter wheat under fully open-air field conditions', *Global Change Biology*. John Wiley & Sons, Ltd, 17(8), pp. 2697-2706. doi: 10.1111/J.1365-

2486.2011.02400.X.

Zhu, Z. *et al.* (2015) 'Ozone concentrations, flux and potential effect on yield during wheat growth in the Northwest-Shandong Plain of China', *Journal of Environmental Sciences (China)*. Elsevier B.V., 34, pp. 1-9. doi: 10.1016/j.jes.2014.12.022.